Anion Manipulation in Perovskite-Related Materials

by

Eirin Courtney Sullivan

A thesis submitted to

The University of Birmingham

for the degree of

Doctor of Philosophy

School of Chemistry

The University of Birmingham

August 2009

Abstract

$Sr_2Co_2O_5$ with the perovskite-related brownmillerite structure has been synthesised *via* quenching, with the orthorhombic unit cell parameters a = 5.4639(3) Å, b = 15.6486(8) Å and c = 5.5667(3) Å based on refinement of NPD data collected at 4K. Electron microscopy revealed L-R-L-R- intralayer ordering of chain orientations which requires a doubling of the unit cell along the c-parameter, consistent with the assignment of the space group *Pcmb*. However, on the length scale pertinent to NPD, no long-range order is observed and the disordered space group *Imma* appears more appropriate.

Low-temperature fluorination of this material and the related brownmillerite phases Sr_2CoFeO_5 and $Sr_2Fe_2O_5$ has been found to give different products depending on the starting material. $Sr_2Co_2O_5$ and Sr_2CoFeO_5 are amenable to fluorine insertion reactions with corresponding oxidation of transition metal cations, forming cubic perovskite phases of the nominal compositions $SrCoO_{2.5}F_{0.5}$ (a = 3.8574(3) Å) and $SrCo_{0.5}Fe_{0.5}O_{2.5}F_{0.5}$ (a = 3.872(2) Å). Fluorination of $Sr_2Fe_2O_5$, however, results in a 1:1 mixture of two phases that were assigned to $SrFeO_2F$ (a = 3.9481(3) Å) and $SrFeO_{3-\delta}$ (a = 3.8775(3) Å).

Fluorine insertion into the oxygen defect superstructure manganite $Sr_2MnO_{3.5+x}$ has been shown by TEM to result in two levels of fluorination. In the higher fluorine content sections, the fluorine anions displace oxygen anions from their apical positions into the equatorial vacancies, thus destroying the superstructure and giving a K_2NiF_4-type structure (a = 3.8210(1) Å and c = 12.686(1) Å).

$Ce_2MnN_3F_{2-\delta}$ with tetragonal symmetry (*P4/nmm* a = 3.8554(4) Å and c = 13.088(4) Å based on neutron powder diffraction) and a structure related to

$LaSrMnO_4F$ has been synthesised *via* low-temperature fluorination of the ternary nitride Ce_2MnN_3. Two F^- anions are inserted but no F^-/N^{3-} substitution takes place, instead a structural rearrangement whereby one F^- expands the manganese coordination from four to six occurs and the second F^- inserts in alternate layers of interstitial sites, in a staged fashion. The effective magnetic moment in $Ce_2MnN_3F_{2-\delta}$, μ_{eff} = 5.38 μ_B, is consistent with an intermediate value between that of Mn^{3+} (4.9 μ_B) and Mn^{2+} (5.9 μ_B) supporting the proposed stoichiometry, $Ce_2MnN_3F_{2-\delta}$.

Acknowledgments

I would like to express my gratitude to my supervisor Professor Colin Greaves for his expert guidance and counsel during the course of my PhD. I have learnt so much from him (about chemistry, and along the way the appreciation of a few good wines) and I would like to thank him for all his encouragement. I feel privileged to have had the pleasure of working for Colin.

I would like to thank Dave Headspith and Dr M. Grazia Francesconi for the opportunity to collaborate on a very exciting project, which certainly provided me with more than its fair share of challenges!

I would also like to thank Dr Joke Hadermann for her superb electron microscopy work and for some interesting and thought-provoking discussions. I am also grateful to all the instrument scientists who have provided experimental assistance collecting NPD data, in particular Dr Emma Suard and Dr Ron Smith.

I have really enjoyed working with the Materials Chemistry group and would like to thank the past and present inhabitants of the fifth floor for making every day a little more fun. In particular, I'd like to thank Jenny for encouraging me to take regular coffee breaks, and Emma, Debbie and Amanda for hours of fun spent poking around the fluorine line. In addition, thanks are also due to Terry Green for his fearless technical support!

I count myself very lucky to have made some wonderful friends whilst at university and would like to thank Charlotte, Ulrike, Sean, Rob, Mike, Alexandra, Sung Jin, Woo and Hanno for all the fun times we've had - long may they continue!

Thank you, Dr Ian Gameson and The Glyndurs for being such amazing friends, and Ian, all your informal advice and support has been of great value to me and I really appreciate it.

I would like to express my gratitude to my parents for being so supportive during my education and for encouraging me to reach for the stars.

Finally, I would like to thank my husband, Anthony McBride, who has always been there for me during all the ups and downs of my project. Thank you so much for motivating me and helping me to believe in myself.

Table of Contents

Chapter Two: Experimental Techniques

Abbreviations

AFM	Antiferromagnetic
BCS	Bardeen Cooper Schrieffer
BVS	Bond valence sum
CMR	Colossal magnetoresistance
DFT	Density functional theory
DTA	Differential thermal analysis
FC	Field-cooled
FM	Ferromagnetic
H_c	Critical magnetic field
HREM	High resolution electron microscopy
HS	High spin
IS	Intermediate spin
J_c	Critical current density
LS	Low spin
MR	Magnetoresistance
MSPS	Magnetic property measurement system
NPD	Neutron powder diffraction
PPMS	Physical property measurement system
SQUID	Superconducting quantum interference device
T_c	Critical temperature
T_C	Curie temperature
TGA	Thermogravimetric analysis
T_N	Néel temperature
TOF	Time of flight
XANES	X-ray absorption near edge structure
XRD	X-ray diffraction
XRF	X-ray fluorescence

Chapter One

Introduction

The focus of this thesis is the synthesis and characterisation of novel perovskite-related materials, focusing on oxygen-defect structures and oxy-fluorides and the exploitation of anion stoichiometry to control the structure and properties of such materials. Perovskite-related structures were selected for this study, as a significant portion of research in the field of solid state chemistry has been dedicated to perovskites and it is well-documented that this structure-type can tolerate both sub- and super-stoichiometry leading to many useful properties. This chapter introduces the perovskite-related materials investigated in this thesis and gives an overview of the electromagnetic properties exhibited by perovskites.

1.1 The Relationship Between Structure and Properties of Solid State Materials

Materials that crystallise with a perovskite or perovskite-related structure have been widely studied, particularly after the discovery of colossal magnetoresistance [1, 2] and high-temperature superconductivity [3, 4] in layered perovskite-related ceramics. Moreover, perovskite-related materials have been shown to exhibit an extensive variety of valuable physical properties and thus are suitable for use in a wide range of applications such as electronic conductors (in particular semiconductors), ferroelectrics, ionic conductors, thermoelectric devices and battery materials.

The composition of perovskite-related materials is highly flexible, allowing huge scope for both the structure and the physical properties of the material to be controlled by exploiting the structure-property relation. Commonly, the manipulation of non-stoichiometry and substitution of cations or anions is used to control the transition metal oxidation state and to optimise the useful properties of the material.

In this chapter, perovskite and the perovskite-related structures K_2NiF_4, the Ruddlesden-Popper series of phases and brownmillerite will be introduced; followed by a discussion of key electrical and magnetic properties exhibited by such materials.

1.2 Perovskite and Related Structures

1.2.1 The Perovskite Structure

The earliest description of the common atomic arrangement having the general formula ABX_3 and a simple cubic structure was for the mineral known as perovskite, $CaTiO_3$ [5]. The structure of $CaTiO_3$ was later found to adopt a distorted perovskite lattice and thus an orthorhombic unit cell [6], however the term perovskite has been universally adopted to describe the structure of ABX_3 compounds. Indeed, most structures described as perovskites are essentially orthorhombic yet still assume the ideal simple cubic unit cell at elevated temperatures.

The ideal cubic perovskite structure (shown in *Figure 1.1* and *Figure 1.2*) comprises the body centre occupied by the A cation with the B cations situated on the corners of the unit cell and the X anions located halfway along each edge of the unit cell. The A cation tends to be larger than the B cation, as the A cation is coordinated with 12 anions whilst the B cation is coordinated with 6. The larger A cations tend to be either alkaline earth or lanthanide cations, whilst the smaller B cations are

generally transition metal cations. Commonly the X anion is oxide, but halide and nitride anions are also readily accommodated.

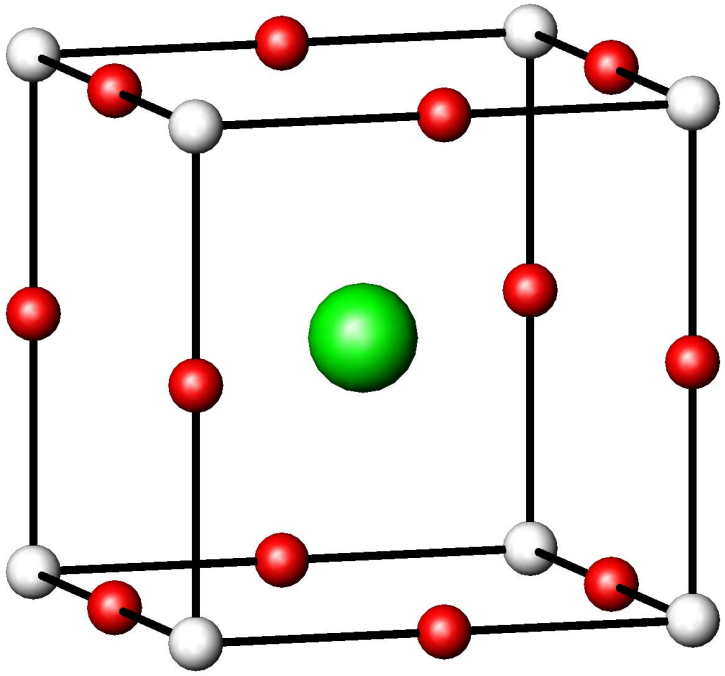

Figure 1.1 The perovskite unit cell ABX_3 where the larger A cation is depicted in green, the B cations are shown in white and the X anions are shown in red.

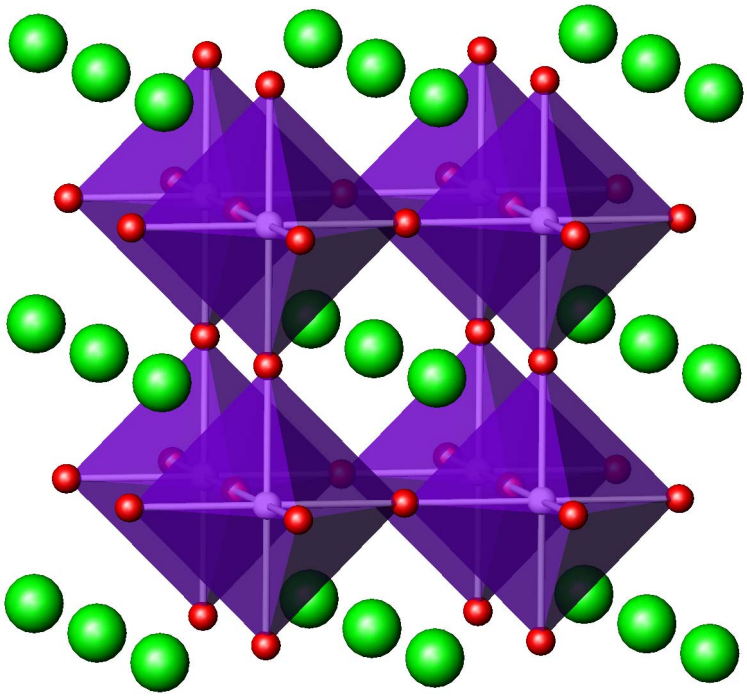

Figure 1.2 An expanded view of the perovskite structure, with white lines showing the B-X bonds and the BX_6 octahedra highlighted in purple.

Within the ABX_3 perovskite structure, there is contact between A, B and X only if the ionic radii of its constituent atoms satisfy the condition expressed in *Equation 1.1* (where R = ionic radii of A, X, and B ions, respectively).

$$R_A + R_X = \sqrt{2}(R_B + R_X)$$

(*Equation 1.1*)

For a proposed composition, the perovskite structure is usually feasible if the Goldschmidt tolerance factor, t, is in the range $0.8 < t \leq 1.0$ [5]. *Equation 1.2* expresses the Goldschmidt tolerance factor as a function of the ionic radii of A, B, and X ions.

$$t = \frac{(R_A + R_X)}{\sqrt{2}(R_B + R_X)}$$

(*Equation 1.2*)

A tolerance factor t = 1 would ordinarily result in an ideal simple cubic perovskite structure consisting of spherical ions of sufficient ionic radii to make slight contact with their nearest neighbours. Any deviation from the model result of t = 1 leads to a distortion of the cubic structure to orthorhombic, tetragonal or rhombohedral symmetry.

For perovskites with t < 1, the ionic radii of the B cations are too large relative to the ionic radii of the A cations, thus compressing the B-X bonds and putting the A-X bonds under tension. In this scenario, it is often the case that some degree of tilting of the BX_6 octahedra will arise in order to relieve these stresses by optimising the cation coordination environments. For perovskites with t > 1, the ionic radii of the B cations are too small relative to the ionic radii of the A cations. In this case, the B cations have been observed to be displaced from the centre of the BX_6 octahedra such that the B-X bonding may be slightly improved. Displacement of the B cation towards an apex of the octahedra is known as a tetragonal displacement, whilst displacement

towards an equatorial edge of the octahedra is an orthorhombic displacement and displacement towards a face of the octahedra is known as a rhombohedral displacement. Much empirical research has been carried out quantifying the correlation between ionic radii and stability of the perovskite-type structure [7] and charting the variation of the perovskite structure with changes in ionic radii and charge [8]. Aside from incompatible cationic radii, deviation from simple cubic symmetry in perovskites can also be caused by anion non-stoichiometry and Jahn-Teller distortions.

1.2.2 The Crystallographic Structure of K_2NiF_4

The crystal structure of K_2NiF_4 was initially determined by Balz [9] in 1953 and was assigned the space group *I*4/*mmm*. In their 1955 study of mixed metal fluorides and oxides, Balz and Plieth [10] reported that several compounds forming the ABX_3 perovskite structure also adopted an A_2BX_4 form analogous to that of K_2NiF_4. The crystal structure of K_2NiF_4 is highly similar to perovskite, consisting of single perovskite type layers of NiF_6 octahedra alternating with layers of KF possessing the rock salt structure.

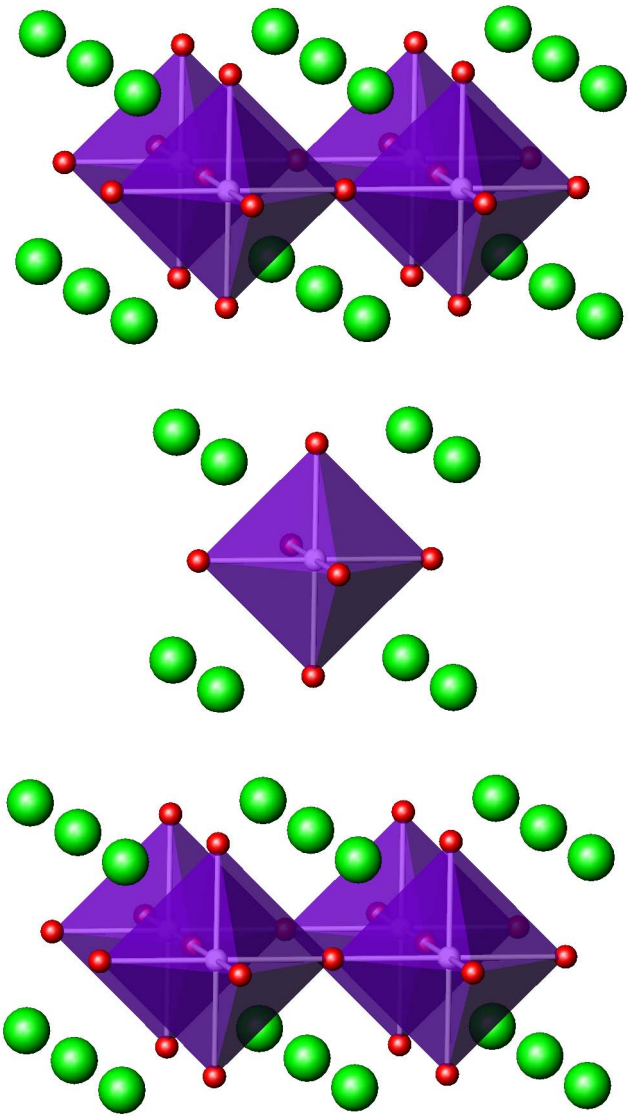

Figure 1.3 The perovskite-related A_2BX_4 structure (known as the K_2NiF_4 structure), with the A cations shown in green, B cations and B-X bonds shown in white, X anions shown in red and the BX_6 octahedra highlighted in purple.

1.2.3 The Ruddlesden-Popper Series of Phases

In 1958, Ruddlesden and Popper [11] reported the synthesis and characterization of the novel layered mixed metal oxide $Sr_3Ti_2O_7$. Its structure was described as an intermediate between $SrTiO_3$ (a perovskite) and Sr_2TiO_4 [12] (with the K_2NiF_4 [10] type structure). The crystal structure of $Sr_3Ti_2O_7$ was solved in the space group *I*4/*mmm* with the lattice parameters a = 3.90 Å and c = 20.38 Å. The crystal

structure consisted of double perovskite layers of corner linked TiO_6 octahedra interwoven with layers of SrO and is illustrated in *Figure 1.4*.

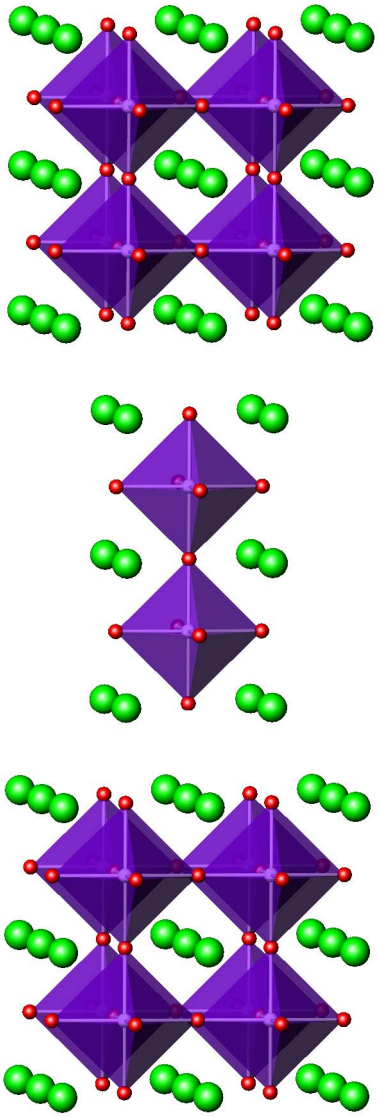

Figure 1.4 The n=2 Ruddlesden-Popper structure ($A_3B_2X_7$) as exhibited by $Sr_3Ti_2O_7$, with the A cations shown in green, B cations and B-X bonds shown in white, X anions shown in red and the BX_6 octahedra highlighted in purple.

Ruddlesden and Popper also proposed the existence of related compounds and simultaneously reported the discovery of one such phase, $Sr_4Ti_3O_{10}$. This too was found to crystallize in the *I*4/*mmm* space group with the lattice parameters a = 3.90 Å

and c = 28.1 Å [11]. The crystal structure of $Sr_4Ti_3O_{10}$ (as shown in *Figure 1.5*) was closely allied to $Sr_3Ti_2O_7$, albeit containing treble as opposed to double layers of perovskite.

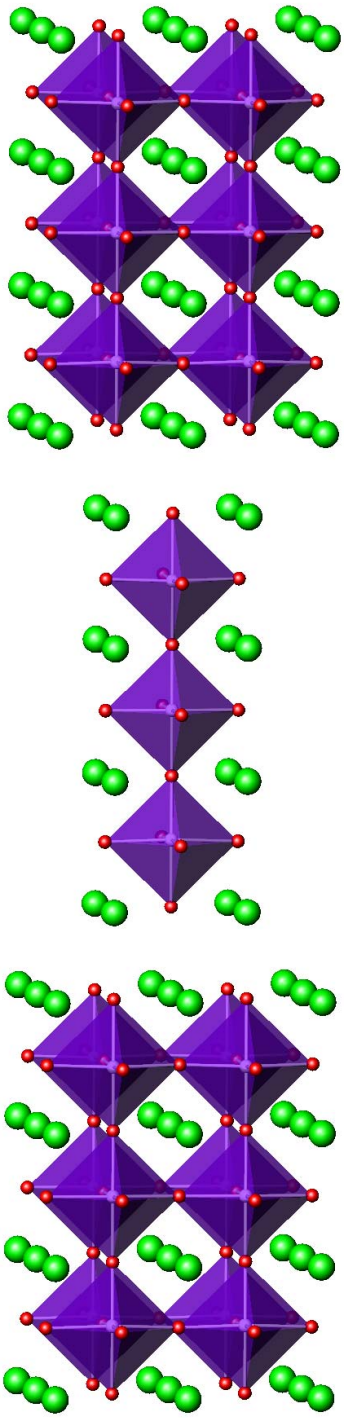

Figure 1.5 The n=3 Ruddlesden-Popper structure ($A_4B_3X_{10}$) as exhibited by $Sr_4Ti_3O_{10}$, with the A cations shown in green, B cations and B-X bonds shown in white, X anions shown in red and the BX_6 octahedra highlighted in purple.

$Sr_3Ti_2O_7$ and $Sr_4Ti_3O_{10}$ represent two examples of a series of related layered perovskite intergrowth materials known as the Ruddlesden-Popper family. The general formula for Ruddlesden-Popper phases is $A_{n+1}B_nX_{3n+1}$ with n layers of BX_6 octahedra separated by layers of AX adopting the rock salt structure. As demonstrated by Sr_2TiO_4, the n = 1 Ruddlesden-Popper phase A_2BX_4 has the K_2NiF_4 structure. Likewise, $Sr_3Ti_2O_7$ and $Sr_4Ti_3O_{10}$ are the first homologous examples of n = 2 and n = 3 members of the Ruddlesden-Popper series. The end member phase with $n = \infty$ has an infinite number of layers of BX_6 octahedra and corresponds to the simple perovskite structure ABX_3.

1.2.4 The Brownmillerite Structure

The brownmillerite structure is of perovskite-type with ordered oxygen defects such that the overall structure comprises a characteristic stacking of alternate layers of corner-sharing tetrahedra and octahedra with the orthorhombic brownmillerite unit cell related to the basic perovskite unit cell by $a_b \approx 2\sqrt{a_p}$, $b_b \approx 4a_p$, $c_b \approx 2\sqrt{a_p}$. This structure can be described as a perovskite with half of the anions from alternate BX_2 layers removed to form layers of the composition BX, resulting in anion deficient layers of BX_4 tetrahedra centred at y = 0.25 and y = 0.75 alternating with layers of BX_6 octahedra (centred at y = 0 and y = 0.5) [13-15]. *Figure 1.6* is a schematic of the perovskite structure for comparison with *Figure 1.7* depicting the brownmillerite section at y = 0.25 and *Figure 1.8* which shows the brownmillerite section at y = 0.75.

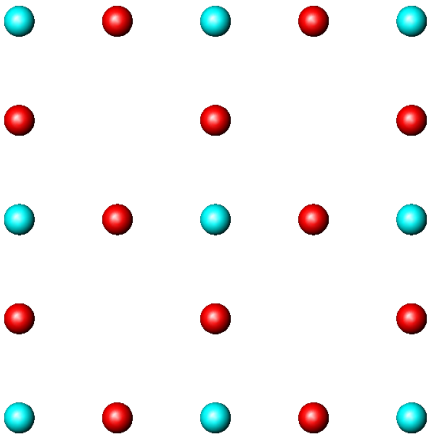

Figure 1.6 Schematic of the perovskite structure at y = 0 with B cations shown in light blue and X anions shown in red.

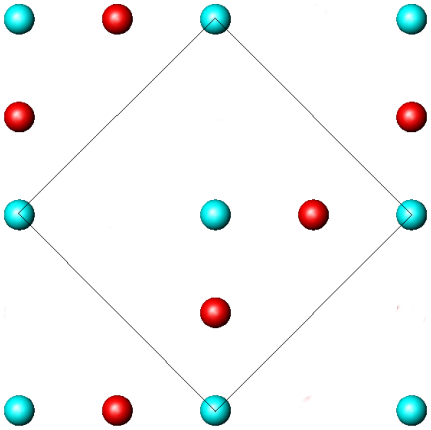

Figure 1.7 Schematic of brownmillerite structure at y = 0.25 with ordered vacancies in half of the anion sites.

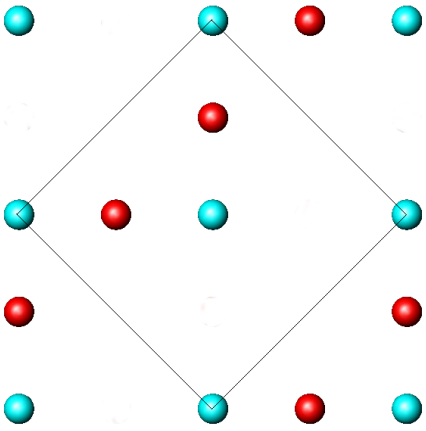

Figure 1.8 Schematic of brownmillerite structure at y = 0.75 with ordered vacancies in half of the anion sites such that a staggered anion defect structure is produced.

Hence, the generic formula often used for brownmillerites $A_2BB'X_5$ (where B = transition metal cation with octahedral co-ordination and B′ = transition metal cation with tetrahedral co-ordination) differentiates between the two transition metal co-ordination environments that are ordered throughout the structure. The layer stacking sequence can thus be described -(BX_2)-(AX)-(B′X□)-(AX)-(BX_2)- and the overall structure is shown in *Figure 1.9*.

Materials adopting the brownmillerite structure can consist of a single B cation or of two different B cations, which are commonly disordered over both octahedral and tetrahedral sites or may be ordered according to transition metal cation preference for a particular co-ordination environment.

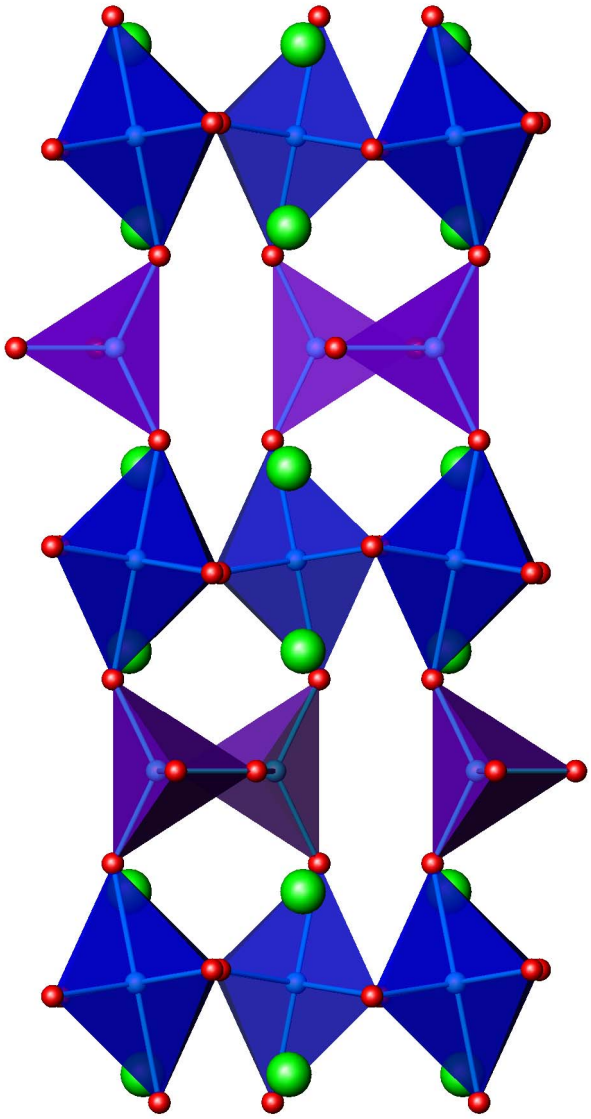

Figure 1.9 The crystallographic structure of brownmillerite $A_2BB'X_5$ where A cations are shown in green, B cations are shown in light blue and X anions are shown in red. BX_6 octahedra are highlighted in blue whilst $B'X_4$ tetrahedra are highlighted in purple.

The following section of this chapter summarises some fundamental principles of electricity and magnetism to help elucidate some of the properties exhibited by perovskite-related materials, moving on to a more in-depth discussion of some of these phenomena such as colossal magnetoresistance, superconductivity and types of magnetic ordering.

1.3 Electrical Properties and Types of Dielectric Materials

1.3.1 Current and Charge

Electromagnetism, united by Maxwell's relations, is one of the four known fundamental forces (strong, weak, electromagnetic and gravitational). Thus, when evaluating the properties of matter it should be borne in mind that the phenomena of electricity and magnetism are, to all intents and purposes, inextricable.

Atoms are electrically neutral and, although the masses of their constituent protons and electrons are vastly different, they have equal and opposite charge. The fundamental unit of charge is $e = 1.60217733 \times 10^{-19} C$ [16] where the coulomb is defined as the amount of charge flowing in 1 second through an infinitely thin wire with a current of 1 ampere (A). To clarify, the current refers to the rate of flow of electric charge through a cross-sectional area of a conducting material. *Equation 1.3* summarizes the relationship between charge, Q, in coulombs (C) and current, I, in amperes (A).

$$I = \frac{\Delta Q}{\Delta t}$$

(*Equation 1.3*)

The charge on a proton or an electron is always +e or –e respectively and like mass and spin, charge is an intrinsic property of such particles. As electrical charge is quantized, the only permissible values for any electric charge are integral multiples of e. The electric potential is the change in electric potential energy per unit charge and the potential difference between two points is measured in volts where $1\ V = 1\ JC^{-1}$ (where V = volts, J = joules and C = coulombs). In order for electric charge to travel across a difference in electric potential within a material, it must contain entities (normally electrons) that are able to move freely. The band theory of solids describes a conductor as having a valence band partially filled by electrons of the atom thus

conduction electrons are easily excited to nearby allowed energy states. A typical insulating material has a prohibitively large energy gap between the filled valence band and the conduction band.

1.3.2 Resistance and Resistivity

Resistance to the flow of an electrical current is usually caused by scattering of the free electrons in the system. This scattering is either caused by other electrons in the material, by imperfections in the lattice, or by elementary excitations in the system such as lattice vibrations known as phonons. In simple terms, the overall effect of electrical resistance is to cause a drop in the electrical potential of a conductor hence reducing the total energy flowing through the material. As the free electrons within an electrical conductor are constantly colliding, all such materials bar superconductors display some electrical resistance. Quantitatively, resistance R, measured in ohms (Ω), is simply the ratio of the drop in potential difference V to the electrical current, as shown in *Equation 1.4*.

$$R = \frac{\Delta V}{I}$$

(*Equation 1.4*)

The resistivity of a material is defined as the constant of proportionality between the resistance of a conducting wire and its length and cross-sectional area [16-18]. *Equation 1.5* shows resistivity ρ (Ωm) as a function of resistance R (Ω), length L (m) and cross-sectional area of conducting wire A (m^2). The extent of electron scattering by phonons or other electrons depends on the material itself thus these effects give rise to what is termed as the intrinsic electrical resistivity. Extrinsic

electrical resistivity is caused by defects in the lattice of the material, such as those caused by impurities.

$$\rho = R\frac{A}{L}$$

(*Equation 1.5*)

1.3.3 Dielectric Materials: Ferroelectric, Antiferroelectric, Ferrielectric, and Piezoelectric Behaviour

The electrical properties of a material are categorized by the behaviour of the electric dipole moments of its constituent atoms upon the application of an external electric field. Despite the fact that the application of a potential difference across a dielectric material does lead to some charge polarization, a dielectric is still unable to conduct electric charge. This is because each electron within it is bound tightly to an atom thus prohibiting the long-range movement of these electrons necessary to facilitate conduction. However, a dielectric material will support an electrostatic field.

Paraelectric behaviour is a result of unpaired electrons whereby each atom possessing an unpaired electron will act as an electric dipole. These dipoles are randomly arranged and do not interact with each other. Upon the application of an external electric field, the dipole moments attempt to align but are hindered as thermal vibrations favour a random arrangement.

Unlike dielectrics, ferroelectric materials retain a remnant polarization after an applied electric field is removed. Ferroelectric materials contain domains within which the electric dipoles are aligned in the same direction, hence the analogy with ferromagnetism. This behaviour occurs at low temperatures; once the temperature is raised above the Curie temperature T_C, the increase in thermal energy disrupts the order of displacements and destroys the domain structure. Hence, at the ferroelectric

Curie temperature, a transition occurs between ferroelectric and paraelectric behaviour. The ferroelectric effect refers to a material that exhibits a spontaneous permanent dipole moment in an applied electric field, which may only be removed by the application of an electric field of sufficient magnitude to reverse the polarisation.

Antiferroelectric behaviour results when the dipole moments within the material align in an anti-parallel fashion. The effect of this is that there is no net dipole moment. An antiferroelectric material will adopt this ordering at a temperature below the Néel temperature T_N. As with ferroelectric materials behaviour, anti-ferroelectric materials display paraelectric behaviour above this temperature.

The term ferrielectric describes a material in which the dipole moments have anti-ferroelectric alignment but are incongruent. Thus, the overall effect of the ordering is ferroelectric behaviour but it is achieved *via* antiferroelectric alignment.

Piezoelectric materials are a class of dielectric material that generate an electric charge when subjected to mechanical deformation, and conversely undergo mechanical deformation in the presence of an electric field [19-21].

1.4 Magnetic Properties and the Different Forms of Bulk Magnetism

1.4.1 Magnetisation and Magnetic Susceptibility

It has been experimentally observed that a moving charged object within a magnetic field experiences a force proportional to its charge and velocity [16]. *Equation 1.6* expresses the magnetic force, $\vec{F}$, on a charge as the cross product of its velocity multiplied by charge, $q\vec{v}$, and the magnetic induction, $\vec{B}$.

$$\vec{F} = q\vec{v} \times \vec{B}$$

(*Equation 1.6*)

This expression also tells us that a point charge in motion, such as an electron, induces a magnetic field itself. The intrinsic magnetic dipole moment associated with electron spins causes atoms to possess magnetic dipole moments.

The strength of a magnetic field is denoted H and the magnetic flux is often pictorially represented by lines indicating the strength and direction of the field. Magnetic induction is the term given to the response caused by the magnetic field in a volume of space. The magnetic induction, B, measured in tesla (T), is also known as the flux density and is mathematically related to the strength of the magnetic field, H, as shown in *Equation 1.7* [16] (where μ = permeability of the volume, or permeability of free space, μ_0, if in a vacuum).

$$B = \mu H$$

(*Equation 1.7*)

As there is a magnetic induction associated with the motion of the electrons within a material, an interaction between the material and the applied field exists. Hence the magnetization term, M, is introduced into the expression for magnetic induction, taking into account the field of the material itself within the applied field H, as is shown by *Equation 1.8*.

$$B = \mu H + \mu M$$

(*Equation 1.8*)

Magnetization is simply the net magnetic dipole moment per unit volume of the material. Diamagnetic materials possess a negative magnetization whilst paramagnetic materials have a positive value of magnetization, as will be further discussed in Section 1.4.2.

When characterizing the properties of matter, rather than considering magnetization, the magnetic susceptibility is often discussed, as it is more specific to the material in question. Susceptibility is simply a measure of the response of a material to an applied magnetic field and is related to magnetization by *Equation 1.9*, where χ = magnetic susceptibility, M = magnetization and H = applied magnetic field strength (A m^{-1}).

$$\chi = \frac{M}{H}$$

(*Equation 1.9*)

Often, the mass magnetic susceptibility (χ_{mass}) and the molar magnetic susceptibility (χ_{mol}) are used, and may be calculated using *Equation 1.10* and *Equation 1.11*, where ρ = density and *M* = molar mass.

$$\chi_{mass} = \frac{\chi}{\rho}$$

(*Equation 1.10*)

$$\chi_{mol} = \chi_{mass} M$$

(*Equation 1.11*)

When a magnetic field is generated, a force acts upon any electric charges encompassed by the volume in which the field is present. A material can be categorized according to the behaviour of the magnetic moments of its constituent atoms upon the application of an external magnetic field [19-22].

1.4.2 Magnetic Properties Arising From Non-Interacting Magnetic Ions

Diamagnetism is produced by the motion of electrons in their orbitals and is present in all substances but as it is weak, it is not usually observed if other effects are present. In general, non-interacting atoms with closed shells reduce the flux density

within the diamagnet thus are repelled from an applied external magnetic field, thus displaying a negative magnetic susceptibility.

Paramagnetism is caused by the randomly arranged magnetic moments of each atom possessing unpaired electrons. Although these moments are isolated from each other, upon the application of an external magnetic field they are independently attracted towards the centre of the field, increasing the flux density within the paramagnet. However, thermal energy favours the random arrangement of moments, hindering their alignment. Paramagnetic materials therefore have a positive magnetic susceptibility.

The randomising effect of thermal energy on the magnetic susceptibility of paramagnetic materials is described by the Curie Law (*Equation 1.12*) where C = Curie constant, defined by the magnetic moment corrected for diamagnetism and T = temperature (K).

$$\chi = \frac{C}{T}$$

(*Equation 1.12*)

In order to describe the high temperature paramagnetic behaviour of materials containing interacting magnetic ions, the Curie law was modified to the Curie-Weiss law (*Equation 1.13*) by the inclusion of the constant, θ, which is dependent on the type of interaction, correcting for magnetic order [19-22]:

$$\chi = \frac{C}{T - \theta}$$

(*Equation 1.13*)

1.4.3 Co-Operative Interactions Between Magnetic Ions: Ferromagnetism, Antiferromagnetism and Ferrimagnetism

Diamagnetism and paramagnetism arise from non-interacting magnetic ions, but interactions between ions occur and can result in several types of magnetic order.

Ferromagnetic (FM) interactions result when the magnetic dipole moments within the material align their spin in the same direction. This spontaneous magnetization occurs in zero applied magnetic field below the Curie temperature T_C, with $\theta > 0$. Above the Curie temperature, the ferromagnetic ordering of spins reverts to a random arrangement thus the material displays paramagnetic behaviour.

Anti-ferromagnetic (AFM) behaviour arises when the magnetic dipole moments within the material align their spins in an anti-parallel fashion. This type of ordering occurs below the Néel temperature T_N at which χ decreases, with $\theta < 0$. Similarly to ferromagnetic ordering, once the Neel temperature is exceeded, thermal disordering effects remove the antiferromagnetic alignments of spins such that the material behaves as a paramagnet.

The generic temperature dependence of the magnetic susceptibility of diamagnetic, paramagnetic, ferromagnetic and anti-ferromagnetic materials is illustrated in *Figure 1.10*, whilst *Figure 1.11* shows the temperature dependence of inverse magnetic susceptibility.

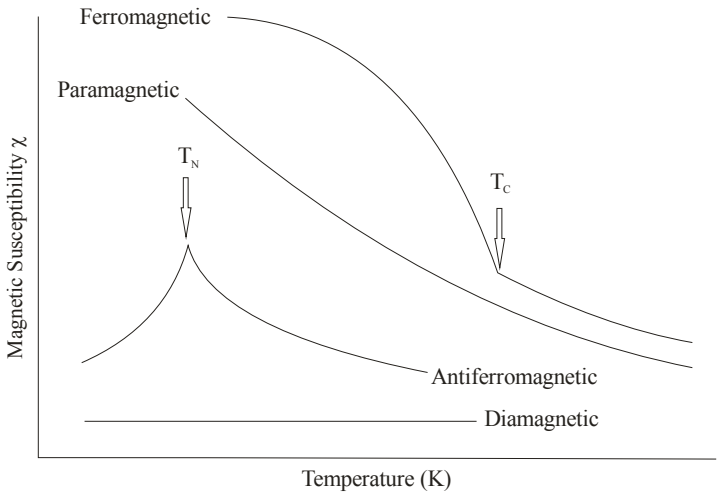

Figure 1.10 Diagram to illustrate the generic temperature dependence of diamagnetic, paramagnetic, ferromagnetic and anti-ferromagnetic materials.

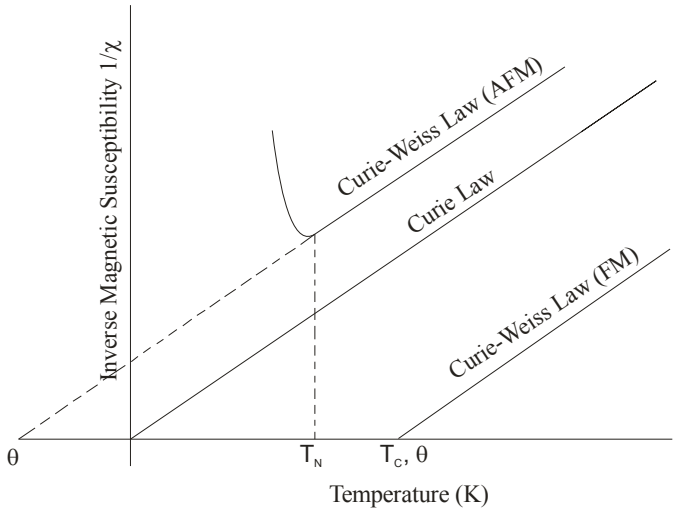

Figure 1.11 Diagram of inverse magnetic susceptibility against temperature (K) showing the Curie Law, the Curie-Weiss Law for ferromagnetic behaviour and the Curie-Weiss Law for anti-ferromagnetic behaviour respectively

The term ferrimagnetic describes what is essentially a net ferromagnetic moment but one that has arisen from the anti-ferromagnetic interactions of dissimilar moments. When moments are aligned antiferromagnetically but are not arranged in a co-linear fashion, the resulting net ferromagnetic moment is said to arise from canted antiferromagnetism. In some materials, spin glass type behaviour is observed below the Curie temperature whereby the spins are randomly orientated in a manner

reminiscent of the positional ordering present in chemical glasses. Spin glass behaviour is typified by non-exponential decay over time of the remnant magnetisation after cooling in a magnetic field and usually occurs as a result of magnetic frustration (*i.e.* degenerate magnetic systems where spins are geometrically unable to align so as to minimise interactions) [19-22].

Co-operative behaviour of spins to produce long-range magnetic order suggests that d-electrons on the transition metal cations interact, but ionic bonding in solids requires the electrons to be localised. Direct exchange interactions may occur between electrons on neighbouring ions where there is sufficient overlap but often magnetic ions are clearly separated by intervening non-magnetic ions. Hence, alternative quantum mechanical exchange mechanisms involving the electron orbitals of the non-magnetic ions are required to explain the presence of long-range magnetic order in ionic solids.

1.4.3.1 Superexchange Interactions

The superexchange interaction describing magnetic coupling mechanisms between magnetic cations *via* intermediate non-magnetic ions was proposed by Kramers [23] and Anderson [24, 25]. In ionic solids where the d-orbitals of the magnetic cations overlap with the outer orbitals of the intermediate diamagnetic ion, a degree of covalency is introduced and the overall energy of the system is lowered *via* orbital mixing/hybridisation. The overlap for superexchange may occur through linear overlap (σ-type) directed along the M-X-M bond (where M = magnetic cation, X = intermediate non-magnetic ion) or lateral overlap orthogonal to the M-X-M bond (π-type). In either case, a favourable superexchange interaction requires the electrons

in the magnetic cation d-orbital and the overlapping lobe of the non-magnetic intermediate to possess opposite spins.

A commonly cited example of how the superexchange mechanism may be used to explain antiferromagnetic ordering is NiO. The Ni^{2+} ion is situated in an octahedral environment with a d^8 electron configuration, thus it has filled t_{2g} ($3d_{xy}$, $3d_{xz}$, $3d_{yz}$) orbitals and singly occupied e_g orbitals (d_{z^2} and $d_{x^2-y^2}$). If one considers the linear 180º overlap between the Ni $3d_{x^2-y^2}$ and the O $2p_x$ orbitals (as depicted in *Figure 1.12*), it is clear that the unpaired electrons in the e_g orbitals of the Ni^{2+} cations are able to couple magnetically with the electrons in the p-orbitals of the O^{2-} anions in order to form the lowest possible energy state.

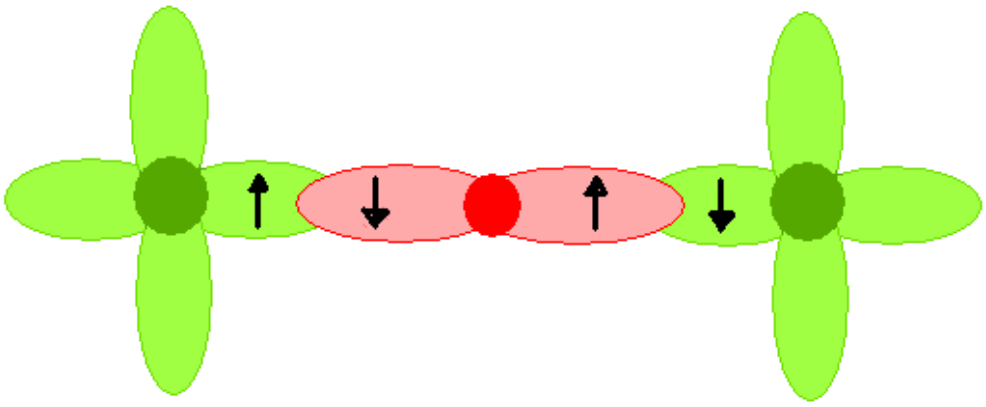

Figure 1.12 An illustration of how superexchange interactions between the Ni $3d_{x^2-y^2}$ orbitals (shaded in light green) and the O $2p_x$ orbitals (shaded in pink) give rise to antiferromagnetic ordering in NiO.

In general, σ-type interactions are stronger. The type of long-range magnetic ordering produced by superexchange depends on both the electronic configuration of the magnetic cation and the angle of the M-X-M interactions (usually 180º or 90º). Whether superexchange culminates in long-range ferromagnetic or antiferromagnetic ordering can in most cases be predicted by the Goodenough-Kanamori rules [26-28].

1.4.3.2 Double-Exchange Interactions

The double-exchange mechanism, as proposed by Zener [29, 30], predicts that it is facile for electrons to move from one species to another provided that the spin of the transferred electron is conserved thus obeying Hund's rules. Double-exchange may occur between mixed valent magnetic cations *via* an intermediate anion. Indirect magnetic coupling *via* double-exchange occurs when the additional electron in the cationic species with the lower valency 'hops' to the diamagnetic intermediate, simultaneously accompanied by an electron 'hopping' from said intermediate to the neighbouring magnetic cation.

The double-exchange mechanism can be used to explain how indirect ferromagnetic coupling between Mn^{3+} and Mn^{4+} in $La_{1-x}A_xMnO_{3-\delta}$ (A = Ca, Sr, Ba) [31, 32] results in this group of materials acing as ferromagnetic conductors upon cooling. This behaviour is only apparent when the A cation site is occupied by both di- and tri-valent cations, or the oxygen stoichiometry is such that the material contains mixed Mn^{3+} and Mn^{4+}; the end members $LaMnO_3$ and $AMnO_3$ are antiferromagnetic insulators, behaviour which has been shown to arise from superexchange interactions. In $La_{1-x}A_xMnO_{3-\delta}$ (A = Ca, Sr, Ba), the Mn^{3+} ion has a d^4 electron configuration, thus it has half-filled t_{2g} ($3d_{xy}$, $3d_{xz}$, $3d_{yz}$) orbitals and a single electron in the e_g orbitals. The Mn^{4+} ion has a d^3 co-ordination and its e_g orbitals are unoccupied. The Mn^{3+} electron is able to 'hop' to the vacancy in the Mn^{4+} e_g orbitals *via* an intervening O^{2-} anion (as depicted in *Figure 1.13*) provided that the hopping electrons do not have to change their spin direction. In this example, in order for electron spins to be conserved, the t_{2g} electrons on the Mn^{4+} cation must be ferromagnetically aligned with the t_{2g} electrons on the Mn^{3+} cation.

As a consequence of double-exchange interactions, conduction electrons are able to move through the material in a metallic manner due to their coupling with incomplete d-orbitals possessing parallel spin, inferring spin polarised conduction.

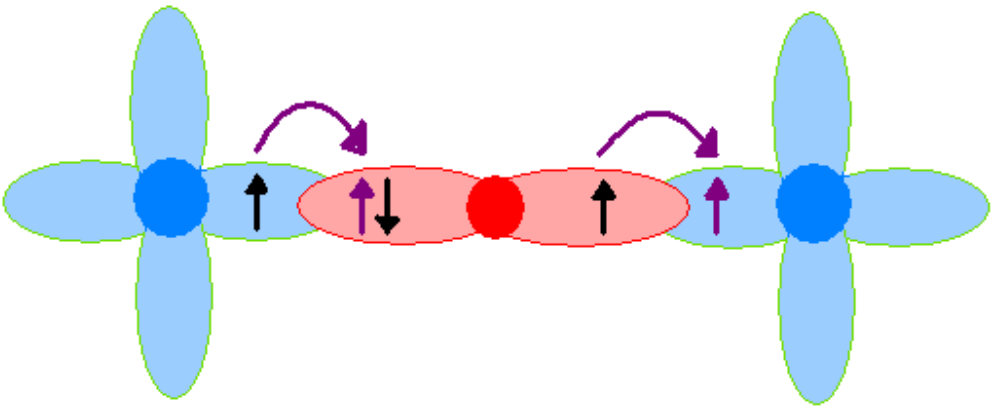

Figure 1.13 A schematic representation of the double-exchange mechanism between the $d_{x^2-y^2}$ orbitals of the Mn^{3+} cation (on the left) and the Mn^{4+} cation on the right (both shaded in light blue) *via* the intermediate O 2p orbital (shaded in pink). The positions of the electrons after 'hopping' are shown in purple.

1.5 Complex Magnetoelectric Phenomenon with Functional Applications

1.5.1 Colossal Magnetoresistance

Upon the application of a magnetic field, an alteration in the electrical resistance of the material is induced. The relative change in resistivity is termed 'magnetoresistance' and is described by the *Equation 1.14* [16] where MR = magnetoresistance, $\Delta\rho$ = change in resistivity, $\rho(0)$ = resistivity at a given temperature in the absence of any applied magnetic field and $\rho(H)$ = resistivity at a given temperature with applied magnetic field, H.

$$MR = \left[\frac{\Delta\rho}{\rho(0)}\right] = \frac{[\rho(H) - \rho(0)]}{\rho(0)}$$

(*Equation 1.14*)

Typically, most materials will have a small magnetoresistance but certain materials display significantly larger magnetoresistance and these are classified according to the magnitude of this effect. Materials containing magnetic multilayers often give rise to around 20% more magnetoresistance than conventional materials, earning the term 'giant magnetoresistance', a phenomenon that was first observed in thin film structures of alternating ferromagnetic and non-magnetic layers [33, 34]. In the absence of an applied magnetic field, there is weak antiferromagnetic coupling between the adjacent strata of ferromagnetic materials (separated by a non-magnetic layer), thus a conduction electron travelling through this spacer layer will have opposite spin to the site it is moving to. Hence the electrical resistivity of a material exhibiting giant magnetoresistance is at a maximum with zero external magnetic field. If a magnetic field of sufficient magnitude is applied, all the spins in the ferromagnetic layers will align in a parallel fashion such that the inter-layer coupling is also ferromagnetic. In this case, conduction electrons may propagate easily through the spacer layers and the resistance is lowered.

Von Helmolt *et al.* [35] reported values of magnetoresistance for the perovskite $La_{2/3}Ba_{1/3}MnO_x$ that were several orders of magnitude larger than normal magnetoresistance. Materials exhibiting this behaviour defy comparison with other forms of magnetoresistance hence are defined as colossal magnetoresistance (CMR) materials [1, 2, 35, 36]. The large changes in resistance in response to magnetic field associated with magnetoresistive materials can be exploited to record binary information onto magnetic surfaces. Magnetoresistance is highly prevalent in manganites of perovskite-type structure and has extensive applications including the read heads of hard disk drives, magnetic sensors, random access memory and a new branch of electronics known as spintronics, which exploits the spin orientation of

conduction electrons and their associated magnetic moments rather than simply their charge.

1.5.2 Superconductivity

The initial discovery of the phenomenon of superconductivity was made by Kamerlingh-Onnes during his investigations into the resistivity of pure metals at low temperatures whereby a dramatic fall in the resistance of mercury to $< 10^{-6}$ Ω at just over 4.2K [37, 38] was noted. After repeating the measurement of the resistance of mercury, Kamerlingh-Onnes reported that the electrical resistance of mercury had, to all intents and purposes, vanished.

Upon cooling below a certain temperature, superconducting materials undergo an abrupt transition to the superconducting state that permits infinite conductance of electricity with zero resistance. This temperature is unique to the superconductor and is termed its critical temperature, denoted T_c. As the resistivity of a material in the superconducting state is zero, once an electrical current has been established in a closed loop of superconducting material, it will theoretically continue for all eternity. Kamerlingh-Onnes himself in 1914 reportedly set up a permanent current (or as he termed it a 'persistent supercurrent') in a superconducting coil of lead [38].

In addition to displaying potentially infinite electrical conductivity, superconductors are often described as 'perfect diamagnets'. This arose from the observation that upon placing a material in the superconducting state in a magnetic field, H, there is complete expulsion of all magnetic field within that material (H = 0), provided that the applied field does not exceed the critical magnetic field H_c for the material in question. Should the magnetic field exceed H_c, magnetic flux will enter the superconductor, restoring it to the normal non-superconducting state. This behaviour

was first discovered by Meissner and Ochsenfeld in 1933 [39] and is not entirely explained by Faraday's law of induction. Moreover, if the electrical current carried by a superconducting wire exceeds the critical current density J_c (Am^{-2}), then the magnetic field induced equals H_c and superconductivity is destroyed. Thus, there is a natural upper limit on the magnetic field a superconducting magnet can generate and the electrical current a superconducting wire can carry.

In 1957, the BCS Theory of Conventional Superconductivity was proposed by Bardeen, Cooper and Schrieffer [40, 41], describing the pairing of single-electron states known as Cooper pairs. The basis of the theory was that in order for the interaction between electrons resulting from the virtual exchange of phonons with energy $\hbar\omega$ to be attractive, the energy difference between the electrons states involved must be less than the phonon energy. Simply put, a Cooper pair is an energetically favourable bound state containing two electrons, each with an equal and opposite spin, the overall effect of which is that the pair acts as a single particle with zero spin. The electrons forming a Cooper pair are in a single quantum state and thus the momentum of the pair must be conserved at all times. Any scattering of one electron will be mirrored by the scattering of the second electron with equal magnitude and opposite direction to that of the first. Hence, due to the conservation of momentum, the interactions of Cooper pairs ensure that there is no net electron scattering and consequently a state of zero resistance. At the critical temperature, the lattice has enough energy to overcome the gap and the Cooper pairs dissipate.

Research into superconducting materials had focused primarily on alloys such as Nb_3Ge as synthesized by Gavaler [42] with $T_c = 23.2K$. For over a decade progress was slow and it was predicted that the maximum critical temperature for any superconducting material could never exceed 30K [38]. This theory was disproved by

the groundbreaking discovery of superconductivity with an onset temperature in the unprecedented 30K range in the Ba-La-Cu-O system in 1986 by Bednorz and Müller [3, 4]. This incited a shift in the focus of research from intermetallic compounds to copper perovskites.

Shortly after the observation of superconductivity around 30K, superconductivity was reported at 93K in the oxygen deficient perovskite $YBa_2Cu_3O_{7-\delta}$ [43]. This was a crucial development as it exceeded the boiling point of liquid nitrogen, thus overcoming a significant barrier to practical applications of superconducting technology. Following this innovation, a plethora of novel superconducting materials based on copper oxide perovskites were synthesized. These materials were unlike conventional BCS superconductors and evidently entered the superconducting state *via* an alternative mechanism. The distinction from BCS superconductors was clear; hence, these new materials were designated the term 'High Temperature Superconductors'.

Although the exact mechanism of high T_c superconductivity is unknown, evidence shows that it is a distinct phenomenon from BCS superconductivity. Two front-running theories are the weak-coupling approximation [44] and the interlayer tunnelling model [45].

In general, high T_c superconductors possess common structural and electronic traits. These empirically compiled similarities appear to constitute a fundamental prerequisite for high T_c superconductivity, although no definite link has been shown between such factors and an underlying interaction inducing superconductivity. All high T_c superconductors are layered structures, consisting of alternating insulating metal oxide layers and superconducting planes. The presence of mixed oxidation states of transition metal cations in the superconducting planes allows electron

migrations between the metal centres. Such mixed oxidation states are usually attained by the substitution of cations with a suitable valency or manipulation of the anion content.

For many years, high-temperature superconductivity had only been observed in materials with superconducting planes of composition CuO_2, however high-temperature superconductivity has recently been discovered in Fe-based materials [46]. This supports the view that the high T_c values observed in superconducting cuprates are related to the strong electron correlation associated with transition metal cations, thus new non-cuprate materials may provide the key to our understanding of the mechanism of high-temperature superconductivity and facilitate attaining higher transition temperatures. Superconducting materials are currently used in a massive range of applications including magnetic levitation for transport, magnetic resonance imaging (MRI), superconducting quantum interference devices (SQUID, see Section 2.9) and superconducting magnets used in the Large Hadron Collider at CERN.

1.5.3 Charge, Spin and Orbital Ordering

The electromagnetic properties of perovskite-related materials often arise from complex interactions between charge, spin- and orbital ordering of electron spins. The spin ordering present within such materials gives rise to the overall magnetic structure. Wollan and Koehler [47] carried out a detailed study of the magnetic properties of the $La_{1-x}Ca_xMnO_3$ series including the end members $LaMnO_3$ and $CaMnO_3$ using neutron diffraction in order to determine their magnetic structures. Phases of the composition $LaMnO_3$, $CaMnO_3$, and $La_{0.2}Ca_{0.8}MnO_3$ were found to display antiferromagnetic behaviour arising from different magnetic structures, whilst a narrow composition range around $La_{0.65}Ca_{0.35}MnO_3$ was ferromagnetic. The F-type

pure ferromagnetic structure is illustrated in *Figure 1.14*, whilst *Figures 1.15-1.17* show the most common types of ordering corresponding to antiferromagnetic structures in perovskites.

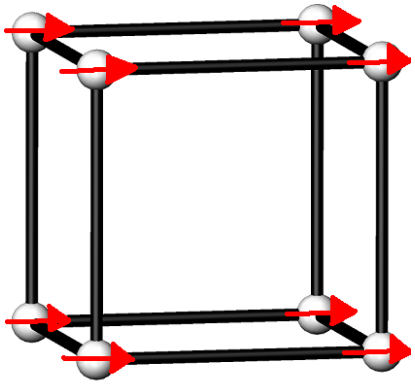

Figure 1.14 F-type ferromagnetic structure, as exhibited by $La_{0.65}Ca_{0.35}MnO_3$.

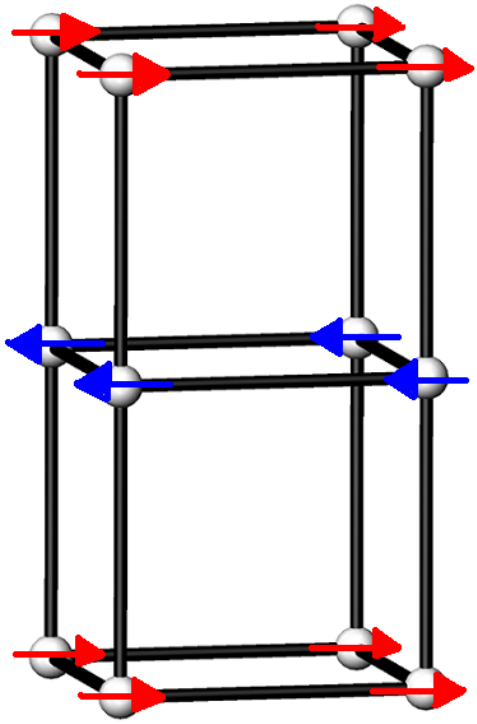

Figure 1.15 A-type antiferromagnetic structure as exhibited by $LaMnO_3$.

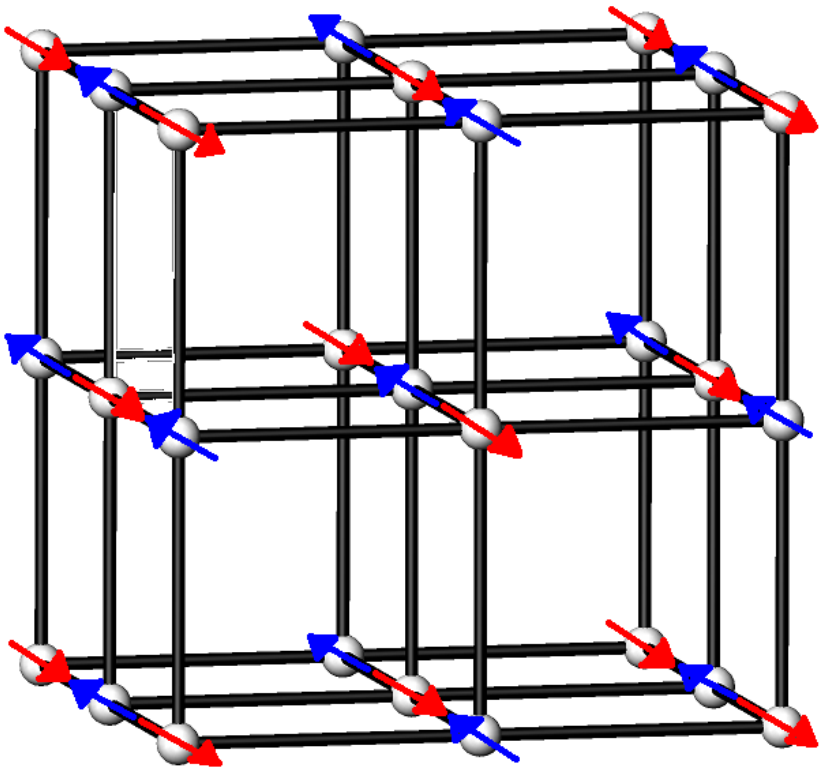

Figure 1.16 G-type antiferromagnetic structure as exhibited by $CaMnO_3$.

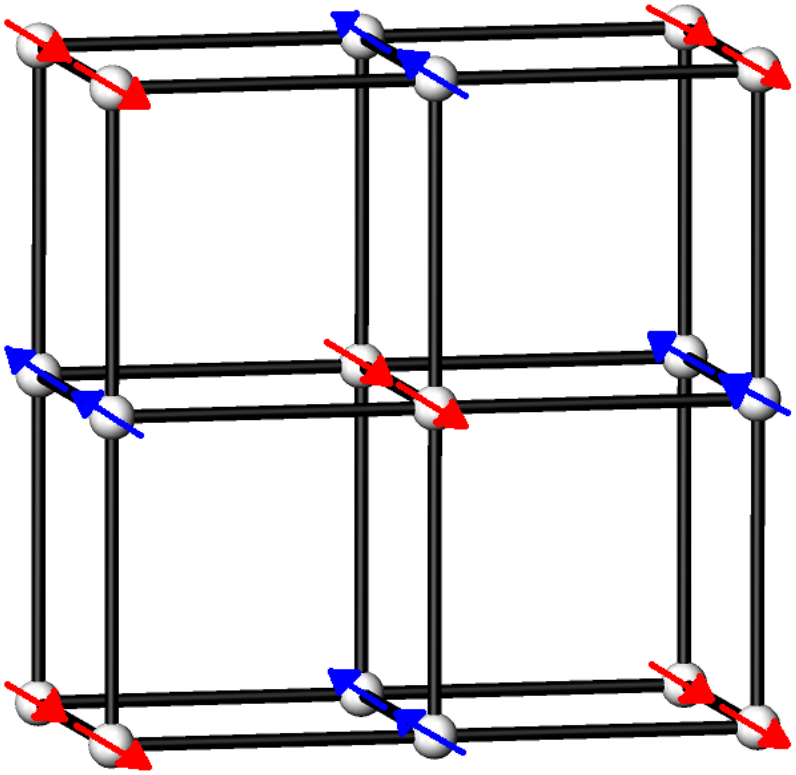

Figure 1.17 C-type antiferromagnetic structure as exhibited by $La_{0.2}Ca_{0.8}MnO_3$.

Charge ordering is also sometimes observed in perovskite-related materials containing B cations with different charges whereby the differently charged cations discretely occupy specific lattice sites. Such materials are insulators as the charge ordering causes electrons to become localised [48].

Orbital ordering has been observed to resolve spin frustration in geometrically frustrated electron systems. Electrons in d-orbitals are able to align in such a way as to favour or hinder the existing super or double exchange interactions, leading to a spin-orbital coupled state [49].

1.6 Aims of This Project

The generic aim of this research is to synthesize and characterize novel compounds exhibiting interesting magnetic ordering or properties such as superconductivity or colossal magnetoresistance. Evidence has been empirically compiled that suggests such electromagnetic properties are predominantly displayed by materials adopting a structure within the Ruddlesden-Popper series of phases, in particular the perovskite and K_2NiF_4 structures. In addition, since the advent of high temperature superconductivity and the ensuing flurry of investigations into increasingly complex layered structures, lower dimensional materials have been somewhat overlooked. Thus, it is the intention of this study to explore the structure and physical properties of some low dimensional mixed metal oxides.

A common method for inducing electromagnetic properties in perovskites is substituting some of the cations for cations with dissimilar valences, for example replacing some La^{3+} with M^{2+} in La_2CuO_4 has been shown to produce superconducting phases of the composition $La_{2-\delta}M_\delta CuO_4$ [50]. However, manipulating the anion content of perovskites is an equally versatile method of introducing mixed B

cation oxidation states [51], as shown by the induction of mixed Cu^{2+} and Cu^{3+} valency in La_2CuO_4 [52] *via* oxygen insertion reactions to form superconducting $La_2CuO_{4+\delta}$. In the same vein, the insertion of fluorine as opposed to oxygen [53, 54] into mixed copper oxides has proved to be an extremely valuable method for producing new materials with advantageous properties such as superconductivity or colossal magnetoresistance. There are four possible outcomes of successful fluorine insertion: substitution of F^- for O^{2-}, substitution of $2F^-$ for O^{2-}, interstitial F^- insertion and structural rearrangement [55-57] and these processes can occur individually or concurrently. Substitution of $2F^-$ for O^{2-} when occurring singly will not induce mixed cation valency, however substitution of F^- for O^{2-} or interstitial F^- insertion will necessitate some transition metal cations gaining or losing electrons in order to balance the charge.

Brownmillerite materials exhibit a distinctive perovskite-related ordered oxygen-vacancy structure, with subtle nuances in symmetry arising from the rotation of tetrahedral chains in the vacancy layers. A detailed structural and magnetic characterisation of the brownmillerite $Sr_2Co_2O_5$ is presented in Chapter 3 with a discussion of the relation between chain ordering and symmetry.

The brownmillerite structure provides an ordered vacancy lattice into which fluorine anions should easily be accommodated, with full occupation of the vacant sites resulting in a simple perovskite structure. Low-temperature fluorine insertion reactions with the brownmillerite $Sr_2Co_2O_5$ have been investigated. The synthesis and characterisation of the fluorinated brownmillerite and the results of preliminary studies on fluorine insertion reactions with the related materials Sr_2CoFeO_5 and $Sr_2Fe_2O_5$ are presented in Chapter 4.

The reduced single-layer manganite $Sr_2MnO_{3.5+x}$ is a low-dimensional perovskite-related material exhibiting an oxygen-vacancy superstructure. This material is formed *via* the reduction of Sr_2MnO_4 (with the K_2NiF_4) structure and although it is stable in air, it will revert to this composition upon heating in a stream of $O_{2(g)}$. Thus, low-temperature fluorine insertion reactions with $Sr_2MnO_{3.5+x}$ were carried out in order to ascertain whether it would be possible to accommodate fluorine onto the oxygen vacancy sites in order to produce an ordered fluorine array. This would induce a mixed Mn^{3+}/Mn^{4+} valency, which could potentially exhibit charge-ordering behaviour depending on the positions adopted by the fluorine anions. The synthesis, characterisation and physical properties of the new material $Sr_2MnO_{3.5+x}F_y$ are discussed in Chapter 5.

The focus of Chapter 6 is the synthetically difficult low-temperature fluorination of Ce_2MnN_3, a ternary nitride of particular interest on account of being isostructural with Sr_2CuO_3, which has previously been shown to be amenable to fluorine insertion reactions [58]. This chapter reports the synthesis and characterisation of the novel quaternary nitride-fluoride $Ce_2MnN_3F_{2-\delta}$ including a discussion of the positions adopted by the inserted fluorine anions and their influence upon the structure of this material.

1.7 References

1. B. Raveau, A. Maignan and V. Caignaert (1995) *Journal of Solid State Chemistry* **117** 424.
2. A. P. Ramirez (1997) *Journal of Physics: Condensed Matter* **9** 8171.
3. J. G. Bednorz and K. A. Müller (1986) *Zeitschrift für Physik B: Condensed Matter* **64** 189.
4. K. A. Müller and J. G. Bednorz (1987) *Science* **237** 1133.
5. F. S. Galasso (1969) *Structure, Properties and Preparation of Perovskite-type Compounds* London: Pergamon Press.
6. H. D. Megaw (1946) *The Proceedings of the Physical Society* **58** 2 132.
7. C. Li, K. C. K. Soh and P. Wu (2004) *Journal of Alloys and Compounds* **372** 40.
8. H. L. Yakel (1955) *Acta Crystallographica* **8** 394.
9. D. Balz (1953) *Die Naturwissen* **40** 241.
10. D. Balz and K. Plieth (1955) *Zeitschrift für Elektrochemie* **59** 6 545.
11. S. N. Ruddlesden and P. Popper (1958) *Acta Crystallographica* **11** 54.
12. S. N. Ruddlesden and P. Popper (1957) *Acta Crystallographica* **10** 538.
13. E. F. Bertaut, P. Blum and A. Sagnières (1959) *Acta Crystallographica* **12** 149.
14. P. Berastegui, S.-G. Eriksson and S. Hull (1999) *Materials Research Bulletin* **34** 2 303.
15. A. Abakumov, A. S. Kalyuzhnaya, M. G. Rozova, E. V. Antipov, J. Hadermann and G. Van Tendeloo (2005) *Solid State Sciences* **7** 801.
16. P. A. Tipler (1999) *Physics for Scientists and Engineers* 4th edition (first published 1976) New York: W. H. Freeman and Company.
17. J. R. Hook and H. E. Hall (2001) *Solid State Physics* 2nd edition (first published 1974) Wiley.
18. C. Kittel (1996) *Introduction to Solid State Physics* 7th edition (first published 1953) Wiley.
19. L. E. Smart and E. A. Moore (2005) *Solid State Chemistry: An Introduction* 3rd edition (first published 1992) Boca Raton: Taylor & Francis.

20. A. R. West (1985) *Solid State Chemistry and its Applications* John Wiley & Sons (Asia).
21. M. T. Weller (1996) *Inorganic Materials Chemistry* (first published 1994) New York: Oxford University Press.
22. A. F. Orchard (2003) *Magnetochemistry* New York: Oxford University Press.
23. H. A. Kramers (1934) *Physica* **1** 182.
24. P. W. Anderson (1950) *Physical Review* **79** 350.
25. P. W. Anderson (1950) *Physical Review* **79** 705.
26. J. B. Goodenough (1958) *Journal of the Physics and Chemistry of Solids* **6** 287.
27. J. Kanamori (1959) *Journal of the Physics and Chemistry of Solids* **10** 87.
28. J. B. Goodenough (1963) *Magnetism and the Chemical Bond* John Wiley & Sons.
29. C. Zener (1951) *Physical Review* **81** 4 440.
30. C. Zener (1951) *Physical Review* **82** 3 403.
31. G. H. Jonker and J. H. van Santen (1950) *Physica* **16** 3 337.
32. J. H. van Santen and G. H. Jonker (1950) *Physica* **16** 7-8 599.
33. G. Binasch, P. Grünberg, F. Saurenbach and W. Zinn (1989) *Physical Review B* **39** 7 4828.
34. M. N. Baibich, J. M. Broto, A. Fert, F. Hguyen Van Dau, F. Petroff, P. Etiene, G. Creuzet, A. Friedrich and J. Chazelas (1988) *Physical Review Letters* **61** 21 2472.
35. R. von Hemolt, J. Wecker, B. Hollzapfel, L. Schultz and K. Samwer (1993) *Physical Review Letters* **71** 14 2331.
36. R. Raveau (1998) *Colossal Magnetoresistance, Charge Ordering and Related Properties of Manganese Oxides* World Scientific Publishing Co.
37. H. Kamerlingh-Onnes (1912) *Communicatioins from the Physical Laboratory at Leiden University* **122b** 13.
38. P. F. Dahl (1992) *Superconductivity* American Institute of Physics.
39. W. Meissner and R. Ochsenfield (1933) *Die Naturwissenschaften* **21** 787.
40. J. Bardeen, L. N. Cooper and J. R. Schrieffer (1957) *Physical Review Letters* **106** 162.

41. J. Bardeen, L. N. Cooper and J. R. Schrieffer (1957) *Physical Review* **108** 5 1175.
42. J. R. Gavaler (1973) *Applied Physics Letters* **23** 480.
43. M. K. Wu, J. R. Ashburn, C. J. Tornj, P. H Hor, R. L. Meng, L. Gao, Z. J. Huang, Y. Q. Wang and C. W. Chu (1987) *Physical Review Letters* **58** 9 908.
44. P. Monthoux, A. V. Balatsky and D. Pines (1992) *Physical Review B* **46** 22 14803.
45. S. Chakravarty, A. Sudbø, P. W. Anderson and S. Strong (1993) *Science* **261** 337.
46. Y. Kamihara, H. Hiramatsu, M. Hirano, R. Kawamura, H. Yanagi, T. Kamiya and H. Hosono (2006) *Journal of the American Chemical Society* **128** 10012.
47. E. O. Wollan and W. C. Koehler (1955) *Physical Review* **100** 2 545.
48. C. N. R. Rao (2000) *Journal of Physics: Condensed Matter* **12** R83.
49. K. Terakura (2007) *Progress in Materials Science* **52** 388.
50. D. E. Cox, S. C. Moss, R. L. Meng, P. H. Hor and C. W. Chu (1988) *Journal of Materials Research* **3** 1327.
51. C. Greaves, M. Al-Mamouri, P. R. Slater and P. P. Edwards (1994) *Physica C* 235.
52. J. M. Longo and P. M. Raccah (1972) *Journal of Solid State Chemistry* **6** 526.
53. B. M. Tissue, K. M. Cirillo, J. C. Wright, M. Daeumling and D. C. Larbalestier (1988) *Solid State Communications* **65** 1 51.
54. J. M Chen, P. Nachimuthu, R. S. Liu, S. T. Lees, K. E. Gibbons, I. Gameson, M. O. Jones and P. P. Edwards (1999) *Physical Review B* **60** 9 6888
55. C. Greaves and M. G. Francesconi (1998) *Current Opinion in Solid State and Materials Science* **3** 132.
56. C. Greaves, J. L. Kissick, M. G. Francesconi, L. D. Aikens and L. J. Gillie (1999) *Journal of Materials Chemistry* **9** 111.
57. E. E. McCabe and C. Greaves (2007) *Journal of Fluorine Chemistry* **128** 448.

58. M. Al-Mamouri, P. P. Edwards, C. Greaves and M. Slaski (1994) *Nature* **369** 382.

Chapter Two

Experimental Techniques

2.1 Synthesis of Materials

2.1.1 Solid State Reactions

In order to synthesise extended lattice materials *via* a solid state reaction it is necessary to build or modify a complete crystal structure hence high energy conditions are required. Polycrystalline powders (typical particle size <10 μm) of suitable reagents are ground together in the correct stoichiometric proportions using an agate pestle and mortar. For the work presented here, high purity binary oxides or carbonates of the appropriate cations were used. This results in a homogenous mixture of reactant particles and void space. At elevated temperatures there is sufficient energy for the constituent ions (predominantly cations) to migrate and where an interface exists between crystal faces of reactant particles a product particle begins to form. Solid state reactions are slow as they require sufficient energy not only for the breaking/reforming of bonds and migration of ions over significant atomic distances but also usually a considerable rearrangement of crystal structure between the reactants and product is required. As the solid state reaction proceeds, the product grains increase in size forming a layer of product between the reactant interfaces, hence the rate of reaction slows as the diffusion path lengths for reacting ions increases. Frequent re-grinding between successive heat treatments augments the rate

of reaction by providing new interfaces between reactant particles and thus shorter diffusion paths.

The rate of a solid state reaction may be improved by pressing the reagent mixture into a pellet, hence reducing empty space or by increasing the reaction temperature such that the rates of diffusion of the various ions are increased, although this temperature is limited by the melting points of the reagents [1-3].

It is often necessary to apply certain modifications to this basic method in order to synthesise a product with a target structure or composition. An unusual oxidation state can often be attained by the use of an oxidising or reducing atmosphere during solid state reaction. If the reagents or target product are sensitive to air or water, the reaction can be carried out in evacuated sealed tubes. Metastable structures can sometimes be stabilised at room temperature by rapid quenching from a temperature at which they are stable, although some phases such as diamond can only be synthesised with the application of high pressure [3].

2.1.2 Fluorination Reactions

Preliminary fluorination reactions in the solid state were carried out using stoichiometric amounts of $CuF_{2(s)}$ as a source of fluoride anions. Nickel crucibles were used for the reaction vessels as nickel is resistant to attack by $F_{2(g)}$. The reactions were typically conducted at temperatures between 250-300ºC for twelve hours. All fluorinated oxides produced *via* this method contain a CuO impurity as a by-product of the reaction with $CuF_{2(s)}$.

The majority of the oxy-fluorides discussed in this body of work were prepared *via* a solid-gas reaction of the starting oxide material with a mixture of $10\%F_{2(g)}/90\%N_{2(g)}$ used as the gaseous fluorinating agent. The apparatus used for

these fluorinations is illustrated in *Figure 2.1*. Due to the propensity of $F_{2(g)}$ to form HF upon contact with moisture in the air, the $N_{2(g)}$ was dried by flowing through a desiccant (silica gel) and all gases were purified before entering the reaction tube by passing over NaF pellets which acts to remove any traces of HF by reacting to form $NaHF_2$. All components of the apparatus such as tubing, valves or taps were constructed from nickel, copper or polytetrafluoroethylene (PTFE) to avoid deterioration of such items in the presence of $F_{2(g)}$ or HF [4, 5]. A diagram of the fluorination apparatus layout is illustrated in *Figure 2.1* whilst *Figure 2.2* is a photograph depicting the *in situ* laboratory set-up of the fluorine line.

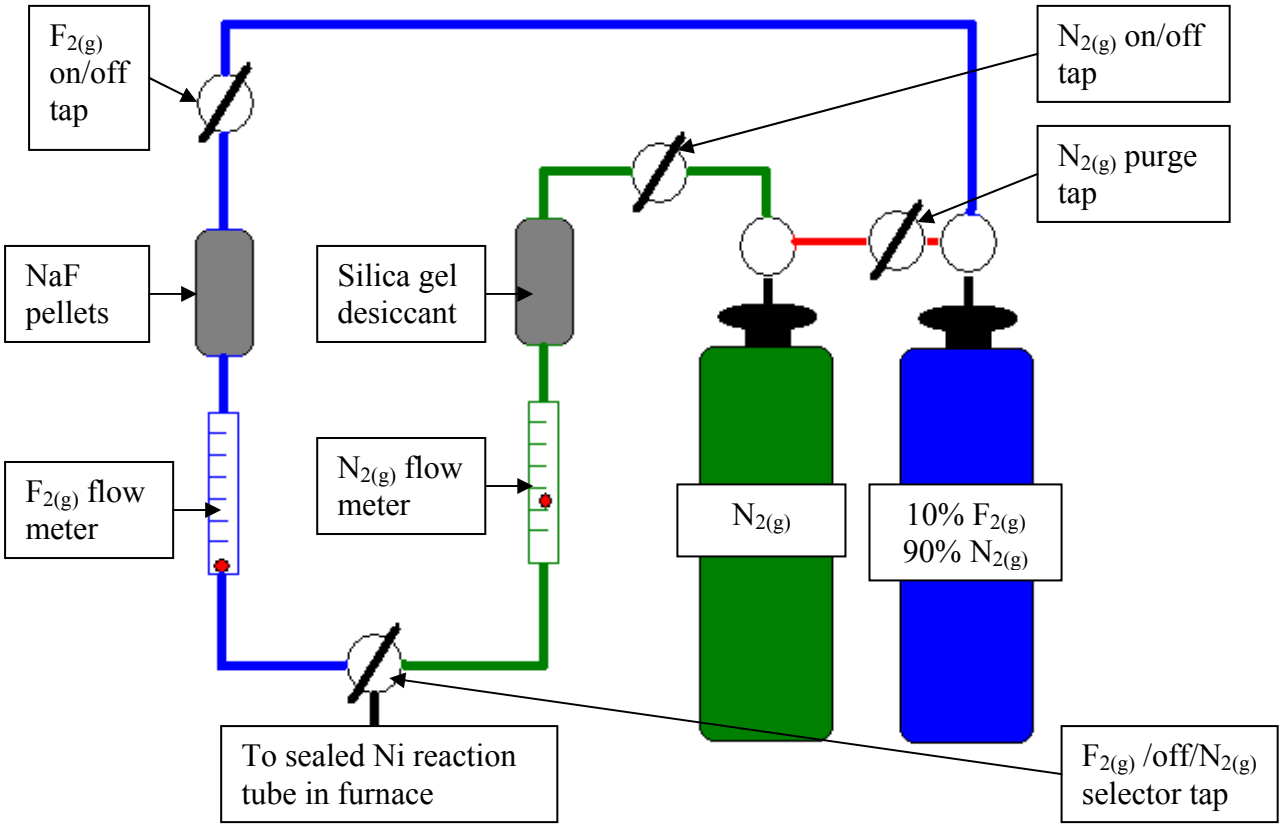

Figure 2.1 Schematic illustration of the apparatus used for solid-gas fluorination reactions. Empty circles denote gas cylinder regulators, circles with a line through them are taps. The $N_{2(g)}$ line is highlighted in green, the $10\%F_{2(g)}/90\%N_{2(g)}$ line is shown in blue and the $N_{2(g)}$ purge line is shaded red up until the point where it joins the blue $10\%F_{2(g)}/90\%N_{2(g)}$ line.

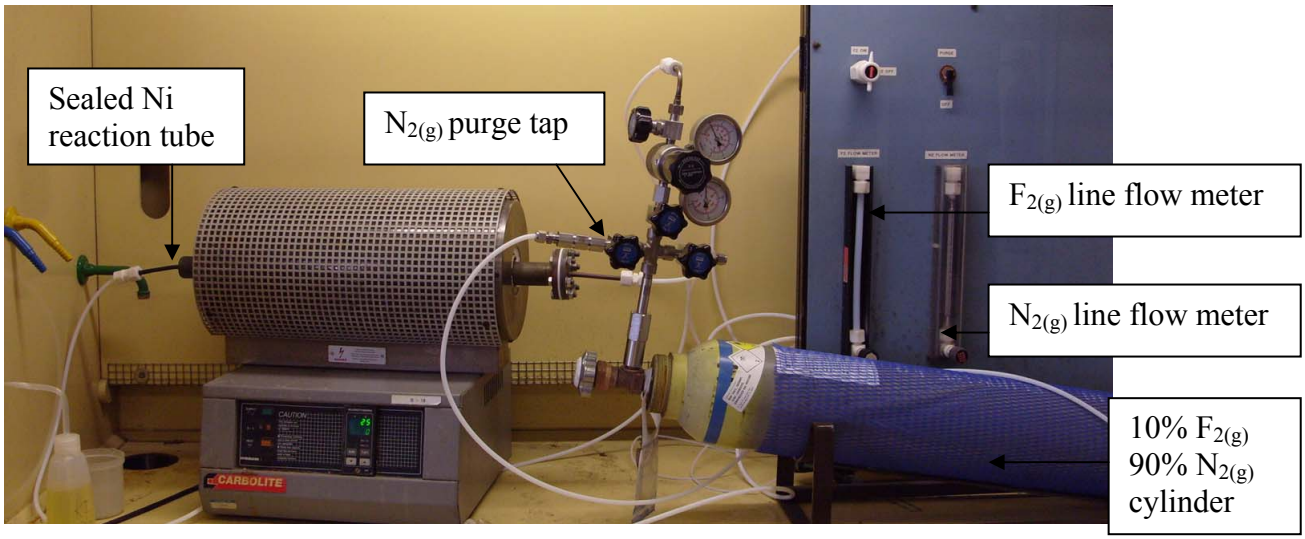

Figure 2.2 Solid-gas fluorination apparatus situated within a fume cupboard at The University of Birmingham School of Chemistry.

2.1.2. (a) Pulse method

In order to produce a timed pulse of flowing $10\%F_{2(g)}/90\%N_{2(g)}$, firstly the apparatus was flushed with $N_{2(g)}$ to ensure that the furnace was dry. Then the $10\%F_{2(g)}/90\%N_{2(g)}$ mixture was passed through the system until the presence of $F_{2(g)}$ was detected. As $F_{2(g)}$ is a powerful oxidising agent, it readily oxidises $I^-_{(aq)}$ to form $I_{2(aq)}$, thus a tissue soaked in $KI_{(aq)}$ placed at the end needle valve exhibits a visible brown colouration as soon as $F_{2(g)}$ is present. At this point, the flow rate was adjusted so as to be correct for the solid-gas reaction. Then the $10\%F_{2(g)}/90\%N_{2(g)}$ cylinder and F_2/off/N_2 tap was closed (leaving the $F_{2(g)}$ flow meter open so that the flow rate was fixed) and the furnace tube was flushed with $N_{2(g)}$ so that the sample could be safely placed into the furnace tube. Once the furnace tube had been sealed, flushed with $N_{2(g)}$ again and had been raised to reaction temperature, the $10\%F_{2(g)}/90\%N_{2(g)}$ mixture was allowed to pass through the furnace again for a set period of time. At the end of this time, $N_{2(g)}$ was passed through the furnace once more at the same rate at which the $10\%F_{2(g)}/90\%N_{2(g)}$ mixture was flowing. Only when the KI test at the end needle valve was negative for $F_{2(g)}$ was the furnace temperature decreased, thus ensuring that

the furnace remained at reaction temperature for the entire length of the $10\%F_{2(g)}/90\%N_{2(g)}$ pulse.

In the course of the work presented here, this method was primarily employed for the fluorination studies of Ce_2MnN_3 with reactions typically carried out between 90-115ºC using timed pulses of 10-20 minutes in length. However, this nitride was particularly sensitive to the presence of $F_{2(g)}$ hence the temperature range described here is far lower than would be necessary for the fluorination of ternary oxides using this method.

2.1.2 (b) Reactions with Static Fluorine

A solid-gas reaction using a static mixture of $10\%F_{2(g)}/90\%N_{2(g)}$ is slightly less harsh than using the pulse method. Samples produced using this method were heated to reaction temperature under flowing $N_{2(g)}$. Once the temperature of the furnace was stable, the $10\%F_{2(g)}/90\%N_{2(g)}$ mixture was allowed to flow through the furnace until $F_{2(g)}$ was detected at the end needle valve. At this point, the end needle valve and the F_2/off/N_2 tap were closed, thus trapping the gaseous mixture in the furnace tube. After the desired reaction time had passed, the furnace was allowed to cool down before flushing the system with $N_{2(g)}$.

Several static fluorine treatments of 2 hours were used both for the fluorination of brownmillerites and the oxygen defect perovskite $Sr_2MnO_{3.5+x}$. The reactions temperatures at which these samples were prepared varied between 200-265ºC.

2.2 Powder X-ray Diffraction

2.2.1 The Motion of Waves Incident Upon Obstacles

When a wave encounters a boundary surface between two different mediums, part of the wave is reflected within the incident medium and part is transmitted into the second medium. The angle between the incident wave and the normal to the boundary surface is equal to the angle made by the reflected wave and the normal. The part of the wave that is transmitted through the surface is attenuated due to the different wave speed in the second medium, this process is known as refraction.

Diffraction is the bending of a wave, which is observed when a wave front is incident upon an obstacle such as a boundary surface or an aperture. The extent to which a wave is diffracted is dependent on the magnitude of its wavelength relative to the object encountered. If the wavelength is far greater than the size of the barrier the diffraction effects are large, whereas if the wavelength is of a similar or smaller magnitude in relation to the barrier, the effect of diffraction is minimal.

Interference is the phenomenon that occurs at a single point in space where two or more waves meet with the resultant wave being a product of the superposition of these waves. In the case where the waves are from a coherent source and hence have the same frequency and wavelength, the amplitude of the wave resulting from their combination will depend solely upon their phase difference. If the phase difference is zero or $n360^{o}$ (where n = any integer), the waves are in phase and therefore interfere constructively. Thus where there is superposition of waves with zero phase difference the resultant amplitude of the combined wave is the sum of the amplitudes of the individual waves. If the phase difference is $n180^{o}$ (where n = any odd integer) the waves are out of phase at the point in space where they meet and therefore interfere destructively, resulting in zero amplitude.

The phase difference of interfering waves from a coherent source is often due to a difference in path length when the waves are diffracted by an obstacle. A path difference of a single wavelength is equivalent to a phase difference of 360º; therefore 2 waves both possessing wavelength λ with a path difference of $n\lambda$ (where n = any integer) are in phase and will interfere constructively. Likewise, waves with a path difference of $(n\lambda)/2$ (where n = any integer) are 180º out of phase so will interfere destructively [6].

In general, a path difference of Δr will give a phase difference of δ, given by:

$$\delta = \left\{ \frac{(\Delta r)}{\lambda} 2\pi \right\} = \left\{ \frac{(\Delta r)}{\lambda} 360° \right\}$$

(*Equation 2.1*)

2.2.2 Principles of Powder X-ray Diffraction

The principles of diffraction and interference of waves form the basis of the technique of powder X-ray diffraction (XRD). X-rays are high energy electromagnetic waves with relatively short wavelengths (*c.a.* 10^{-11}-10^{-8} m or 0.1-100 Å [7]) and high frequencies (*c.a.* 10^{16}-10^{20} Hz [6]) thus are highly penetrating. Like all electromagnetic waves, they exhibit diffraction when incident upon an obstacle and interference when two or more X-rays meet at the same point in space. Applying these basic principles of wave physics to the incidence of X-rays upon a polycrystalline material, it follows that X-rays will be scattered by the electron density about the periodically distributed atoms within the disordered crystallites. In order to use diffraction to probe a crystal structure it is necessary to use radiation with a wavelength comparable with atomic dimensions, hence the wavelengths commonly used are *c.a.* 0.5-2.5 Å [7]. X-rays produced by the bombardment of an anode

composed of an element with atomic number between 24-42 (*i.e.* Cr-Mo) fulfil this criterion, as do 'thermal' neutrons produced *via* nuclear fission (so named as they are in thermal equilibrium with the moderator of the reactor) (see Section 2.3) and electrons with suitable energy (see Section 2.5). These X-ray, neutron and electron beam radiations are all of a suitable wavelength for diffraction studies of crystals, albeit interacting with different scattering centres. Neutron radiation is scattered by nuclei whilst electron beams are scattered *via* interaction with the electrostatic potential of an atom. However as nuclei, core electron density and their electrostatic potentials have similar distribution within a given crystal structure the intensities of beams diffracted by the different types of radiation used for diffraction studies varies mostly due to the way in which the radiation interacts with their respective scattering centres [8, 9].

In essence, powder X-ray diffraction is the study of the pattern of radiation scattered by a polycrystalline material, based upon the premise that all atoms within a crystal are located on discrete planes with regular spacing. Bombardment of a crystal structure with X-ray radiation results in the scattering of the incident X-rays to some extent by the electrons in the outer shells of the constituent atoms of the crystal structure (coherent scattering). In addition to scattering, there is also partial absorption of the incident X-rays, thus they will penetrate to different planes in the crystal before reflection occurs. Because the atoms are part of an infinite regular lattice, the X-rays diffracted from different planes of atoms within the crystal may or may not be in phase with each other. The diffracted X-ray which are in phase with each other produce a very intense diffracted X-ray, and using these we can determine information about the crystal structure [7, 8].

2.2.3 The Bragg Equation

Diffraction of waves by an object results in the scattered radiation forming a pattern of intensity maxima and minima. The Bragg equation quantifies this by treating the diffracted X-rays as reflections from planes within the crystal lattice.

A plane surface within a crystal can be described by a simple set of 3 integers known as its Miller indices and are denoted (*hkl*). These can be determined by considering two parallel planes, one of which encompasses a point regarded to be the origin of the unit cell. The *x*, *y* and *z* vectors emanating from this origin will at some point be cut by the other plane and these intercepts are at some fraction of the unit cell dimensions *a*, *b*, and *c*. The Miller indices used to generically describe such a plane would be calculated as follows:

$$h = \frac{a}{x}$$

(*Equation 2.2*)

$$k = \frac{b}{y}$$

(*Equation 2.3*)

$$l = \frac{c}{z}$$

(*Equation 2.4*)

Hence the Miller indices of a plane are determined by the reciprocal on the intercept made on the axes by the plane nearest the origin [10, 11].

The spacing between parallel planes described by the Miller indices (*hkl*) is called the *d*-spacing and is denoted d_{hkl}. Thus, the *d*-spacing between a set of planes (*hkl*) within an orthogonal crystal with lattice parameters *a*, *b* and *c* is given by *Equation 2.5*.

$$\frac{1}{d_{hkl}^{\ 2}} = \frac{h^2}{a^2} + \frac{k^2}{b^2} + \frac{l^2}{c^2}$$

(*Equation 2.5*)

The Bragg conditions for x-ray diffraction are easily derived by considering two parallel X-rays incident at an angle of θ upon two parallel planes, as illustrated in *Figure 2.3*.

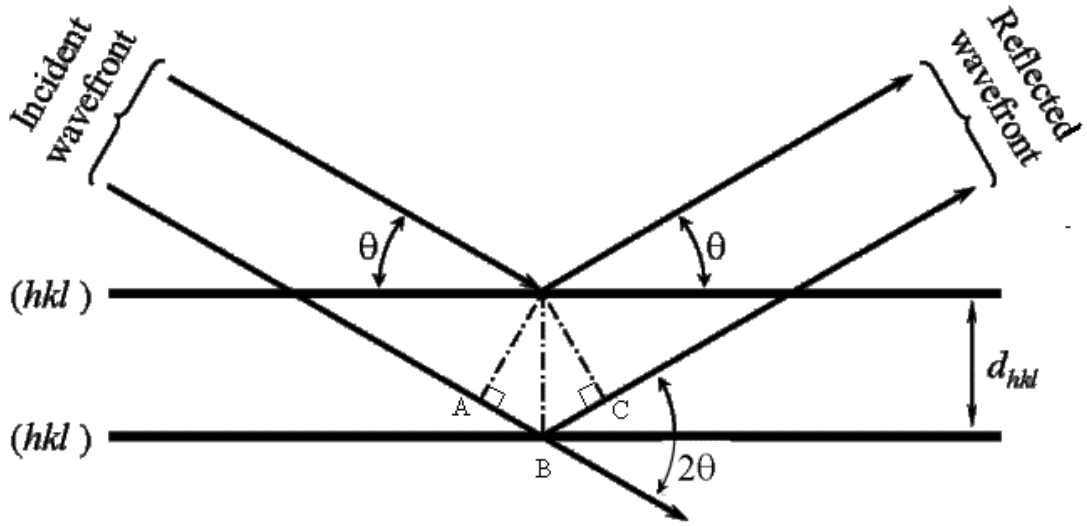

Figure 2.3 Diagram to illustrate the geometric derivation of the Bragg condition for constructive interference of X-rays diffracted by parallel planes, reproduced from [8].

By geometry, $\sin\theta = \frac{AB}{d_{hkl}}$ and $\sin\theta = \frac{BC}{d_{hkl}}$, therefore the path difference between the reflected X-rays from the two successive layers is given by

$$AB + BC = 2d_{hkl}\sin\theta$$

(*Equation 2.6*)

In order for the X-rays emerging from these planes to be in phase with each other, they must have a path difference of an integer multiple of the wavelength of the

incident X-rays, $n\lambda$. This gives the Bragg conditions [12] for constructive interference of X-rays:

$$2d_{hkl}\sin\theta = n\lambda$$

(*Equation 2.7*)

where d_{hkl} is the spacing between parallel planes of atoms, θ is the angle of the incident X-rays, *n* is any integer and λ is the wavelength of the incident X-rays.

More often than not, n is simply considered as n = 1. As n represents the n^{th} order reflection from the (*hkl*) planes, the beam can be thought of as the (*nh nk nl*) reflection. For instance, the 2^{nd} order reflection from the (111) planes where n = 2, is simply described as the (222) reflection.

X-rays scattered from Bragg planes will be in phase with each other if they have a path difference of $n\lambda$. This instigates a peak in the intensity of reflected X-ray radiation detected for each value of 2θ at which constructive interference occurs. X-rays out of phase with each other interfere destructively and annul one another. Thus, intensity peaks will be detected for different values of 2θ depending on the symmetry of the crystal being studied. This is because all X-rays detected are a direct result of the interference of incident X-rays reflected from separate planes. The X-ray diffraction pattern for a crystal is directly correlated with the size and symmetry of that crystal and is quite distinctive [7-11].

In this body of work, X-ray diffraction has been used as a characterization technique to measure the intensity of reflected X-rays from powder preparations as a function of 2θ. From this information, the lattice type and unit cell dimension of the crystal can be deduced by assigning (*hkl*) values to each peak. The basic processing of this data was facilitated by the use of the computer programs "INDEX" [13], "DSPACE" [14] and "CELL" [15].

2.2.4 Production of X-rays

X-rays are produced by the continuous bombardment of a metal anode with high-energy electrons. Upon reaching the metal anode, these electrons are decelerated by the electrons in the metal target. This produces a broad continuous spectrum of X-rays known by the original German term bremsstrahlung, from 'bremsen' (to brake) and 'strahlung' (radiation) thus translating literally as 'braking radiation' [16]. The bremsstrahlung spectrum is dependent only on the energy of the bombarding electrons.

The energy of these bombarding electrons is of sufficient energy to excite an n = 1 (K shell) electron to a higher, unoccupied state. Whenever a core electron makes an electronic transition from the n = 1 state to an unoccupied state, it leaves a vacancy in the K shell. Thus, electrons in the n = 2 (L shell) or n = 3 (M shell) are able to make a transition into the K shell, simultaneously emitting electromagnetic radiation with energies of several keV. These quantized electronic transitions give rise to a discrete spectrum of sharp peaks in the intensity of X-rays at specific wavelengths and are characteristic of the anode metal. Transitions from the n = 2 (L) shell to the n = 1 (K) shell gives rise to the Kα line, whilst the Kβ is a result of transitions from the n = 3 (M) shell to the n = 1 (K) shell. In addition to the K-series (transitions to the K shell), transitions to a vacancy in the n = 2 shell form the L-series. The lines produced by these transitions are actually unresolved doublets, for example the Kα line consists of two lines corresponding to Kα1 and Kα2 radiation resulting from two L to K transitions with similar energy, differing only due to the spin multiplicity of the 2p electrons [1, 3, 7, 8].

2.2.5 Instrumentation for Powder X-ray Diffraction

All room temperature powder X-ray diffraction data presented in this work was collected using a Siemens D5000 diffractometer operating in transmission mode with θ-2θ geometry. The X-ray beam that this instrument generates contains Cu $K\alpha_1$, $K\alpha_2$ and Kβ radiation besides background radiation. Hence, the diffractometer is fitted with a curved primary beam germanium monochromator in order to select only the $K\alpha_1$ line (λ = 1.5406 Å) so the X-rays used were of a single wavelength, as this is preferable for diffraction studies. The diffracted X-ray radiation was detected using a position sensitive detector with Δ2θ = 8˚ and a step size of 0.02˚.

Variable temperature powder X-ray diffraction data were collected using a Siemens D5005 diffractometer operating in reflection mode with θ-θ geometry fitted with an Anton Parr HKT1200 high temperature stage. This diffractometer was fitted with a Göbel mirror to produce a parallel beam of Cu $K\alpha_1$ and $K\alpha_2$ radiation (λ = 1.5404 Å, λ = 1.5443 Å).

2.2.6 Integrated Intensity of Diffracted X-ray Radiation

The observed integrated intensity of X-ray radiation I_{hkl} diffracted by a reciprocal lattice point *hkl* is determined *via* numerical integration over all data points within the range of the Bragg peak as follows:

$$I_{hkl} = \sum_{i=1}^{j} (y_i - b_i)$$

(*Equation 2.8*)

where *j* denotes the total number of data points constituting the Bragg peak, y_i is the measured profile intensity and b_i is the background contribution at a measured data point *i*.

The calculated integrated intensity in powder diffraction studies I_{hkl} is primarily dependent on the crystal structure of the material thus is proportional to the structure factor F_{hkl}. The structure factor incorporates the contribution to the integrated intensity of scattered radiation arising from the atomic species contained within the material and thus their scattering power, their thermal motions, atomic co-ordinates and distribution over different lattice sites.

The structure factor F_{hkl} is a mathematical description of the scattering of X-rays by all atoms within a unit cell n for a given reflection hkl. It depends on the positions of each atom and their respective atomic scattering factors, containing contributions from the structure amplitude, population factor, temperature factor and phase angle. The structure amplitude is a complex function used to express the amplitude of the wave scattered by a unit cell containing multiple atoms with different scattering factors. The indices hkl for a Bragg reflection are represented by the vector $\mathbf{h} = (h, k, l)$ whilst the fractional co-ordinates of the j^{th} atom in the unit cell are represented by the vector $\mathbf{x}_j = (x_j, y_j, z_j)$ with their scalar product $\mathbf{h}.\mathbf{x}_j = hx_j + ky_j + lz_j$. Using this, following expression describes the structure amplitude $\mathbf{F}_{hkl}$ for j atoms within a crystal containing n unique symmetrically equivalent atoms in the unit cell (known as the asymmetric unit):

$$\mathrm{F}_{hkl} = \sum_{\mathrm{j}=1}^{n} g_{\mathrm{j}} t_{\mathrm{j}}(s) f_{\mathrm{j}}(s) \exp\left[2\pi \mathrm{i}\left(hx_{\mathrm{j}} + ky_{\mathrm{j}} + lz_{\mathrm{j}}\right)\right]$$

(*Equation 2.9*)

where g_j is the population factor of the j^{th} atom, usually expressed as a site occupancy such that a fully occupied site has $g_j = 1$, t_j is the atomic displacement parameter of the j^{th} atom (also known as temperature factor, despite t_j being the combined total of several effects in addition to thermal motion such as deformation of

electron density due to chemical bonding) , $f_j(s)$ denotes the atomic scattering factor which describes the interaction of the X-ray with the atomic species upon which it is incident as a function of s, where $s = \frac{\sin\theta_{hkl}}{\lambda}$ and $\mathrm{i} = \sqrt{-1}$.

The isotropic approximation for the atomic displacement parameter t_j of the j^{th} atom describes the influence of the motion of atoms about their equilibrium positions upon the structure factor and is given by the following expression:

$$\mathrm{t}_j = \exp\left(-\mathrm{B}_j \frac{\sin^2\theta}{\lambda^2}\right)$$

(*Equation 2.10*)

where B_j is the isotropic displacement parameter for the j^{th} atom. This approximation assumes that an atom has an equal probability to be displaced in any direction. The isotropic displacement parameter is dependent upon the root mean square deviation of the j^{th} atom from its equilibrium position (x, y, z), $\sqrt{(\overline{u^2})_j}$ and is calculated (in Å^2) as follows:

$$\mathrm{B}_j = 8\pi^2(\overline{u^2})_j$$

(*Equation 2.11*)

For crystal structure determination *via* powder X-ray diffraction, in addition to the structure factor it is necessary to quantify all contributing instrumental, experimental and geometrical factors, thus the total calculated integrated intensity for each reflection is given by the following expression:

$$I_{hkl} = K \times p_{hkl} \times L_\theta \times P_\theta \times A_\theta \times T_{hkl} \times E_{hkl} \times \left|F_{hkl}\right|^2$$

(Equation 2.12)

where K is the scale factor, p_{hkl} is the multiplicity factor which accounts for symmetrically equivalent points in the reciprocal lattice contributing to the same observed Bragg peak, L_θ is the geometric Lorentz factor which varies depending on the collection mode, P_θ is the polarisation factor for the scattered radiation which is often partially polarised during reflection (additional polarisation factor correction required when monochromator utilised), A_θ is the absorption factor accounting for the absorption of both incident and diffracted radiation by the heavier atoms in the sample, T_{hkl} is the preferred orientation factor representing deviation from random grain orientation and E_{hkl} is the extinction multiplier [7].

For all powder X-ray diffraction data collected using the Siemens D5000 diffractometer, correction for sample absorbance was necessary as the absorbance factor is considerable for data collected in transmission mode. Therefore the computer program "ABSORB" [17] was used to facilitate absorbance correction of the data before use in structural refinement.

The magnitude of the scattering of X-ray radiation by the electrons associated with a particular atom within a crystal structure is described by the scattering factor f_n which is in turn dependent on the number of electrons present in the atom. Thus with increasing atomic number, Z, the number of electrons in the atom increase and it follows that scattering from heavy atoms can dominate X-ray diffraction patterns whilst it is often difficult to draw reliable conclusions from X-ray diffraction data about lighter atoms. It should also be noted that considering the relative size of the electron cloud, there can be destructive interference between X-rays scattered from different areas of the electron cloud which results in the scattered intensity 'dropping off' as the value of 2θ increases.

2.3 Neutron Powder Diffraction

2.3.1 Principles of Neutron Powder Diffraction

A beam of neutrons in motion possesses wave-like properties as described by the de Broglie equation:

$$\lambda = \frac{h}{p}$$

(*Equation 2.13*)

where h is Planck's constant and p is the particle momentum ($p = mv$). Reactor source neutrons, produced by the fission of uranium, have high velocity therefore need to be slowed using heavy water in order for the wavelength of the neutron beam to be suitable for powder diffraction studies. Neutrons can also be produced *via* proton spallation whereby a metal target is bombarded with high-energy protons to generate a pulsed neutron beam. For spallation sources, the entire beam is utilised, at a fixed angle θ to the sample, and the intensity is recorded as a function of neutron time of flight. The proportional relationship between λ and t is simply illustrated by substituting for velocity ($v = xt^{-1}$) in the de Broglie equation:

$$\lambda = \frac{ht}{xm}$$

(*Equation 2.14*)

Unfortunately both nuclear and spallation sources are expensive and are only available at national facilities.

Neutron powder diffraction (NPD) techniques also utilise the Bragg description of radiation being reflected from different planes within a crystal structure. However, an important distinction between powder X-ray and powder neutron diffraction is that neutrons are scattered by the nuclei of atoms within the

crystal structure whereas X-ray are scattered by their electron clouds. When using X-rays to determine bond-length, the size of the electron cloud they are being scattered by can sometimes distort the determination of distance between the atoms. As neutrons are directly scattered by the nuclei, they can be used to determine bond lengths far more precisely. As neutron scattering lengths are similar for all elements, varying randomly between different nuclei rather than linearly with atomic number, the neutron is an excellent probe for lighter atoms, even in the presence of heavier atoms.

Neutrons possess spin and therefore a magnetic moment, thus are also scattered by paramagnetic atoms (those possessing unpaired electrons). The magnetic scattering of neutrons tells us about the alignment of electron spins and thus we can determine the magnetic ordering and magnetic unit cell of a crystal structure. Since this magnetic scattering occurs as a result of interaction with the electron cloud of an atom, the magnetic scattering drops off with increasing scattering angle due to the size of the electron cloud [8, 18, 19].

2.3.2 Instrumentation for Neutron Powder Diffraction

Neutron powder diffraction was carried out at the Institut Laue-Langevin, Grenoble using the high-resolution, two-axis powder diffractometer D2B (Ge monochromator, λ = 1.59432 Å). The Instiut Laue-Langvin is a reactor source of neutrons – its High Flux Reactor produces the most intense flux of neutrons currently available for diffraction studies (1.5×10^{15} neutrons per second per cm^2) [20].

Time of flight (TOF) neutron powder diffraction data were used in Chapter 5. These data were collected using Polaris at the ISIS pulsed spallation neutron source, Rutherford Appleton Laboratory, Oxford.

2.3.3 Integrated Intensity of Diffracted Neutrons

As neutrons are scattered both by the nuclei of atoms and *via* interaction with their electron density, the expression for the structure factor must contain both a nuclear and magnetic scattering factor. The components of the structure factor arising respectively from nuclear and magnetic neutron scattering is additive, thus the overall structure factor is given by:

$$\left|\mathrm{F}_{hkl}\right|^2 = \left|\mathrm{F}_{nuc}\right|^2 + \left|\mathrm{F}_{mag}\right|^2$$

(*Equation 2.15*)

Similar to the scattering of X-rays, the structure factor for nuclear neutron diffraction may be written as follows:

$$\mathrm{F}_{nuc} = \sum_{\mathrm{j}=1}^{n} g_{\mathrm{j}} t_{\mathrm{j}}(s) f_{\mathrm{j}} \exp[2\pi\mathrm{i}(hx_{\mathrm{j}} + ky_{\mathrm{j}} + lz_{\mathrm{j}})]$$

(*Equation 2.16*)

For neutrons, the atomic scattering factor f_{j} is independent of $\frac{\sin\theta_{hkl}}{\lambda}$. For nuclear neutron diffraction, the scattering power of an atom is dependent solely on the properties of the nucleus of the atomic species concerned and varies randomly, thus no form factor is required. The structure factor for magnetic neutron scattering is given by:

$$\mathrm{F}_{mag} = \sum_{\mathrm{j}=1}^{n} \boldsymbol{q}_{\mathrm{j}} p_{\mathrm{j}} \exp[2\pi\mathrm{i}(hx_{\mathrm{j}} + ky_{\mathrm{j}} + lz_{\mathrm{j}})]$$

(*Equation 2.17*)

where $\boldsymbol{q}$ is the magnetic interaction vector and p is the magnetic scattering length [18, 19].

The interactions of neutron spin with the spins of unpaired outer electrons on a scale comparable to neutron wavelength necessitate the use of a form factor for magnetic neutron scattering. The magnetic scattering length p is calculated from the magnitude of the spin quantum number of the scattering atom j, S_j, and its magnetic form factor f_{mag} *via* the following expression:

$$p = S_j f_{mag} \frac{e^2 \gamma}{m_e{}^2 c}$$

(*Equation 2.18*)

where e is the charge of an electron, γ is the magnetic moment of a neutron (in Bohr magnetons), m_e is the mass of an electron and c is the speed of light in a vacuum [21].

Similarly to XRD, the integrated intensity of a Bragg reflection from time of flight neutron diffraction data is proportional to the square of the structure factor and is given is by the following general expression:

$$I_{hkl} = \frac{K I_0(\lambda)\varepsilon(\lambda)\lambda^4 V_s A_{hkl}(\lambda) E_{hkl}(\lambda) j |F_{hkl}|^2 \cos\Delta\theta}{4 V_c{}^2 \sin^2\theta}$$

(*Equation 2.19*)

where K is a normalising constant, $I_0(\lambda)$ is the incident neutron flux at wavelength λ, $\varepsilon(\lambda)$ is the detector efficiency, A_{hkl} is the attenuation constant for reflection hkl, E_{hkl} is the extinction coefficient, V_s is the sample volume, V_c is the unit cell volume, j is the reflection multiplicity, F_{hkl} is the structure factor, $\Delta\theta$ is the angular width of the detector and 2θ is the Bragg angle [18, 22].

2.4 The Rietveld Method for Profile Refinement

High symmetry crystal structures yield simple powder diffraction patterns consisting of a small number of distinct, well-resolved peaks, hence the intensity of reflected radiation and 2θ positions are sufficiently accurate to solve the crystal structure directly. However, the larger the unit cell or the lower the symmetry within the crystal structure the more reflections are present in the powder diffraction pattern. Commonly, at certain reflection positions intensity peaks may be either coincident or in very close proximity to each other forming composite peaks. In this case, it is not possible to resolve the individual peak intensities from the composite peaks and a full profile refinement method is required to overcome such difficulties and thus solve the crystal structure.

A profile refinement method for the nuclear and magnetic refinement of powder neutron diffraction data was proposed by Rietveld [23, 24], which has subsequently been adapted for utilisation with powder X-ray diffraction data. Full pattern refinement methods such as the Rietveld, Pawley [25] and Le Bail [26] methods fit a calculated profile pattern to observed powder diffraction data in order to refine both structural and instrumental parameters.

In order to achieve the global minimum as opposed to a local false minimum, the Rietveld full pattern refinement method requires a model crystal structure including the space group, approximate lattice parameters and atom positions. This information is combined with instrument parameters such as wavelength of incident radiation to calculate a profile pattern. The overall line profile is analysed by assigning a Voigt profile calculated from a pseudo-Voigt approximation consisting of a weighted sum of Gaussian and Lorentzian peak symmetries to each peak position, allowing for overlapping Gaussian functions at composite peaks [7]. Commonly, the

peak shapes in powder X-ray diffraction data are a combination of both Gaussian and Lorentzian functions, whilst constant wavelength neutron powder diffraction gives largely Gaussian peaks and the pulse neutrons used in time of flight data often cause asymmetric peak broadening. The calculated profile pattern is compared with the observed data and the trial structure is modified to improve the fit between the calculated and observed profile patterns. The model structure is gradually refined until the best fit between the calculated profile pattern and the observed data is obtained.

The Rietveld method for whole pattern least-squares refinement uses the observed intensities of scattered radiation y_i for data points i in the powder diffraction pattern, where i may be in increments of neutron time of flight, Bragg angle 2θ or X-ray energy. The observed intensity at a data point i is related to the calculated intensity at the same point y_{ci} by the following series:

$$y_{c1} = ky_1$$

$$y_{c2} = ky_2$$

$$\ldots$$

$$y_{cn} = ky_n$$

(*Equation 2.20*)

where y_i is the observed intensity of data point i, y_{ci} is the calculated intensity of data point i and k is the pattern scale factor.

The Rietveld method employs a non-linear least-squares refinement in order to solve the above system of equations. As the scale on which the intensity of scattered radiation is measured is relative one, the pattern scale factor, k, is usually set at unity.

Therefore, the residual least-squares function is given by:

$$S_y = \sum_{i=1}^{n} w_i \left(y_i - y_{ci} \right)^2$$

(*Equation 2.21*)

where S_y is the residual, y_i is the observed intensity of data point i, y_{ci} is the calculated intensity of data point i and w_i is the weight assigned to i^{th} data point and in the absence of background is equal to y_i^{-1}.

The least-squares refinement aims to minimise the sum of the residual over all data points. The quality of fit for a Rietveld profile refinement is assessed visually by a difference plot of the calculated and observed profile patterns, which should ideally be a straight line. There are also several figures of merit known as reliability or R-factors that are used to evaluate the quality of fit: the profile residual (R_p), the weighted profile residual (R_{wp}), the Bragg residual (R_B) and the expected profile residual (R_{exp}).

$$\mathrm{R_p} = \frac{\sum_{i=1}^{n} \left| y_i - y_{ci} \right|}{\sum_{i=1}^{n} y_i}$$

(*Equation 2.22*)

$$\mathrm{R_{wp}} = \left[\frac{\sum_{i=1}^{n} \mathrm{w_i} \left(y_i - y_{ci} \right)^2}{\sum_{i=1}^{n} w_i \left(y_i \right)^2} \right]^{\frac{1}{2}}$$

(*Equation 2.23*)

$$R_B = \frac{\sum_{j=1}^{m} \left| I_j - I_{cj} \right|}{\sum_{j=1}^{m} I_j}$$

(*Equation 2.24*)

$$R_{exp} = \left[\frac{n-p}{\sum_{i=1}^{n} w_i (y_i)^2} \right]^{\frac{1}{2}}$$

(*Equation 2.25*)

where I_j is the observed integrated intensity of the j^{th} Bragg peak, I_{cj} is the calculated integrated intensity of the j^{th} Bragg peak, m is the number of independent Bragg reflections, n is the total number of data points in the observed powder diffraction pattern and p is the number of free least squares parameters.

The Bragg residual is not meaningful in Pawley or Le Bail methods, but is an important figure of merit in Rietveld refinements as it is independent of background. Hence, the Bragg residual is almost totally dependent on structural parameters and is a direct indication of the accuracy of the model crystal structure. Both the profile and weighted profile residuals may become unreliable when the background is high due to their large denominators, although the weighted profile residual is generally considered to be the most meaningful figure of merit overall as it has the residual least-squares function S_y as the numerator.

The goodness of fit (χ^2) is given by the following expression:

$$\chi^2 = \frac{\sum_{i=1}^{n} w_i \left(y_i - y_{ci}\right)^2}{n-p} = \left[\frac{R_{wp}}{R_{exp}}\right]^2$$

(*Equation 2.26*)

From *Equation 2.11*, it follows that the goodness of fit should approach unity when R_{wp} approaches R_{exp}, although in practice this is rarely achieved [7, 22-24].

2.5 Transmission Electron Microscopy

Electron diffraction and microscopy is often utilised to examine non-periodic structures such as crystal defects and can reveal valuable information about intergrowth phases and superstructures [3, 27]. In this body of work, conventional transmission electron microscopy (TEM) and high-resolution electron microscopy (HREM) have been used to investigate materials in which evidence has suggested the presence of a superstructure.

Electrons possess charge therefore a beam of electrons will interact with both the electron density and the coulombic potential of the nucleus of the atoms upon which they are incident [27]. Electrons interact very strongly with matter hence electron scattering is more intense than X-ray scattering and secondary diffraction (whereby the diffracted electron beam is in turn diffracted by another set of lattice planes) is commonplace [3].

The electrons used in transmission electron microscopy are generated by a heated filament in a thermionic electron gun and are then accelerated through a potential difference. These electrons are then focused by a series of electromagnetic fields referred to as ‘lenses’, these are used to control factors such as beam aperture,

resolution, final magnification and can toggle between direct image and diffraction modes.

The wavelength of the accelerated electrons are related to the potential difference by the de Broglie equation:

$$\lambda = \frac{h}{\sqrt{2m_e eV}}$$

(*Equation 2.27*)

where h is Planck's constant, m_e is the mass of an electron, e is the charge upon an electron and V is the potential difference through which the electrons are accelerated. At high voltages, the velocity of the accelerated electrons approaches the speed of light therefore m_e increases due to the effect of relativity [9].

2.6 X-ray Fluorescence Spectroscopy

X-ray fluorescence (XRF) is an X-ray emission technique commonly used for quantitative elemental analysis. The term fluorescence in this instance describes the process by which the target material absorbs high-energy X-rays and emits lower-energy X-rays. The sample is bombarded with high-energy X-rays such that electrons are emitted from the inner orbitals of the atom and outer shell electrons drop down to fill the vacancies. When this occurs, the excess energy is emitted as a discrete spectrum of low-energy X-rays. Each element possesses a characteristic X-ray emission spectrum; this technique can be used to identify all elements with $Z > 8$ within a sample. Comparing the peak intensities at the appropriate wavelengths with a calibration chart enables the quantitative analysis of the constituent elements of a sample [3].

2.7 Thermal Analysis

Thermal analysis measures the properties of solids, most commonly weight or the absorption/evolution of heat as a function of sample temperature.

Thermogravimetric analysis (TGA) records the weight of a sample as the temperature is increased and/or decreased at a controlled uniform rate. Oxidising or reducing atmospheres are often used depending on whether the aim is to quantify the oxidation of a material or the loss of water/oxygen or to study the complete decomposition of a material.

Differential thermal analysis (DTA) records the difference in temperature, ΔT, between the sample and a control material that remains inert upon heating and cooling. This area of thermal analysis is particularly useful for studying phase changes. Plotting ΔT against T shows clear exotherms or endotherms where phase changes occur, thus yielding information not only about the temperature ranges over which the phase changes occur but also the nature of these transitions.

All thermal analysis data presented here was obtained using a Rheometric Scientific STA 1500.

2.8 Magnetic Measurements

Zero-field cooled magnetisation data were recorded upon warming the sample from being cooled in the absence of a magnetic field; and field-cooled magnetisation data were recorded upon warming the sample that has been cooled in the presence of a magnetic field. Zero-field cooled (ZFC) and field-cooled (FC) measurements were performed between $\approx$ 2K and $\approx$ 300K under an applied field of 0.3 T. On certain samples, field sweep measurements were also performed at a temperature of 10K with an applied field sweeping between –7 T and 7 T.

All magnetisation data were collected *via* DC extraction whereby the magnetised sample is moved through the detection coils thus inducing a voltage in the detection coil set with amplitude proportional to the magnetic moment [28]. The magnetic susceptibility measurements reported here were performed using both a Quantum Design Model 6000 Physical Property Measurement System (PPMS) and a Quantum Design Magnetic Property Measurement System (MSPS) superconducting quantum interference device (SQUID) magnetometer.

2.9 References

1. L. E. Smart and E. A. Moore (2005) *Solid State Chemistry: An Introduction* 3rd edition (first published 1992) Boca Raton: Taylor & Francis.
2. M. T. Weller (1996) *Inorganic Materials Chemistry* (first published 1994) New York: Oxford University Press.
3. A. R. West (1985) *Solid State Chemistry and its Applications* John Wiley & Sons (Asia).
4. C. Greaves and M. G. Francesconi (1998) *Current Opinion in Solid State and Materials Science* **3** 2 132.
5. E. E. McCabe and C. Greaves (2007) *Journal of Fluorine Chemistry* **128** 448.
6. P. A. Tipler (1999) *Physics for Scientists and Engineers* 4th edition (first published 1976) New York: W. H. Freeman and Company.
7. V. K. Pecharsky and P. Y. Zavalij (2005) *Fundamentals of Powder Diffraction and Structural Characterisation of Materials* (first published 2003) New York: Springer.
8. J. P. Glusker and K. N. Trueblood (1985) *Crystal Structure Analysis: A Primer* 2nd edition (first published 1972) New York: Oxford University Press.
9. J.P. Eberhart trans J.P. Eberhart (1995) *Structural and Chemical Analysis of Materials* (first published 1989 in French, 1991 in English) Wiley.
10. J. R. Hook and H. E. Hall (2001) *Solid State Physics* 2nd edition (first published 1974) Wiley.
11. C. Kittel (1996) *Introduction to Solid State Physics* 7th edition (first published 1953) Wiley.
12. W. L. Bragg (1912) *Proceedings of the Cambridge Philosophical Society* **17** 43.
13. D. Louër and M. Louër (1972) *"INDEX"*, *Journal of Applied Crystallography* **5** 271, (modified by C. Greaves, The School of Chemistry, The University of Birmingham).
14. C. Greaves (1982) *"DSPACE"*, The School of Chemistry, The University of Birmingham.

15. M. F. Pye *"CELL"* Inorganic Chemistry Laboratory, The University of Oxford (modified by C. Greaves, The School of Chemistry, The University of Birmingham).
16. Quickdic [Internet: accessed 23/09/2008] available from http://www.quickdic.org/index_e.html
17. C. Greaves *"ABSORB"*, The School of Chemistry, The University of Birmingham.
18. R. I. Smith *Introduction to Neutron Diffraction*. In: A. C. Hannon (Ed.) *ISIS Neutron Training Course, Module 2: Neutron Diffraction*.
19. G. E. Bacon (1975) *Neutron Diffraction* (3rd edition) Oxford: Clarendon Press.
20. ILL Neutrons for Science: Technical Characteristics [Internet: accessed 24/09/2009] available from http://www.ill.eu/reactor-environment-safety/high-flux-reactor/technical-characteristics/
21. G. E. Bacon (1963) *Applications of Neutron Diffraction in Chemistry* Pergamon Press.
22. R. A. Young (Ed.) (1993) *The Rietveld Method* Oxford: Oxford University Press.
23. H. M. Rietveld (1967) *Acta Crystallographica* **22** 151.
24. H. M. Rietveld (1969) *Journal of Applied Crystallography* **2** 65.
25. G. S. Pawley and J. Pawley (1981) *Journal of Applied Crystallography* **14** 357.
26. A. Le Bail, H. Duroy and J. L. Fourquet (1988) *Materials Research Bulletin* **23** 447.
27. R. J. D. Tilley (2006) *Crystals and Crystal Structures* Wiley.
28. Quantum Design Physical Property Measurement System Magnetometry Brochure [Internet: accessed 29/07/2009] available from http://www.qd.usa.com/pdf/brochues/mag3-07.pdf

Chapter Three

Nuclear and Magnetic Characterisation of $Sr_2Co_2O_5$

3.1 Introduction

3.1.1 The Brownmillerite $Sr_2Co_2O_5$

Perovskite-related strontium cobaltite $SrCoO_{3-x}$ has been reported to exhibit three main structure types [1-3]. At temperatures higher than ~900°C, a cubic perovskite structure is adopted [1-3] with stoichiometry $SrCoO_{2.5}$ ($Sr_2Co_2O_5$) and containing a random arrangement of oxygen vacancies. On quenching from temperatures above ~910°C, the stoichiometry is retained but the oxygen vacancies order to give $Sr_2Co_2O_5$ with the brownmillerite structure [2], as shown in *Figure 3.1*. On slow cooling, the high temperature cubic perovskite form transforms at ~750°C to give the thermodynamically stable low temperature configuration, which comprises an intergrowth of two phases: rhombohedral $Sr_6Co_5O_{15}$ (2H $BaNiO_3$-type) and Co_3O_4 [4]. The existence of the rhombohedral and cubic structures is therefore largely dependent on temperature, and the brownmillerite-type phase $Sr_2Co_2O_5$ is metastable and provides the focus of this study.

The existence at room temperature of two different structures of strontium cobaltite was rationalised by Grenier *et al.* [2] in terms of the influence of the spin state of Co^{3+} on structure and magnetic behaviour. Quenching from 910ºC resulted in the

formation of a brownmillerite-type phase stabilised by high spin (HS) Co^{3+} cations in octahedral and tetrahedral coordination; both sites have four unpaired electrons with configurations $t_{2g}^4\ e_g^2$ and $e^3\ t_2^3$, respectively. Recent *ab initio* work [5] has supported the hypothesis that this material contains Co^{3+} in a high spin state. The magnetic behaviour of the low temperature phase was explained by the simultaneous presence of Co^{3+} in an intermediate spin (IS) state (two unpaired electrons) and a low spin (LS) state (no unpaired electrons) [6]; this was later characterised by Harrison *et al*. [4] as the Co-deficient phase $Sr_6Co_5O_{15}$ using a rhombohedral unit cell.

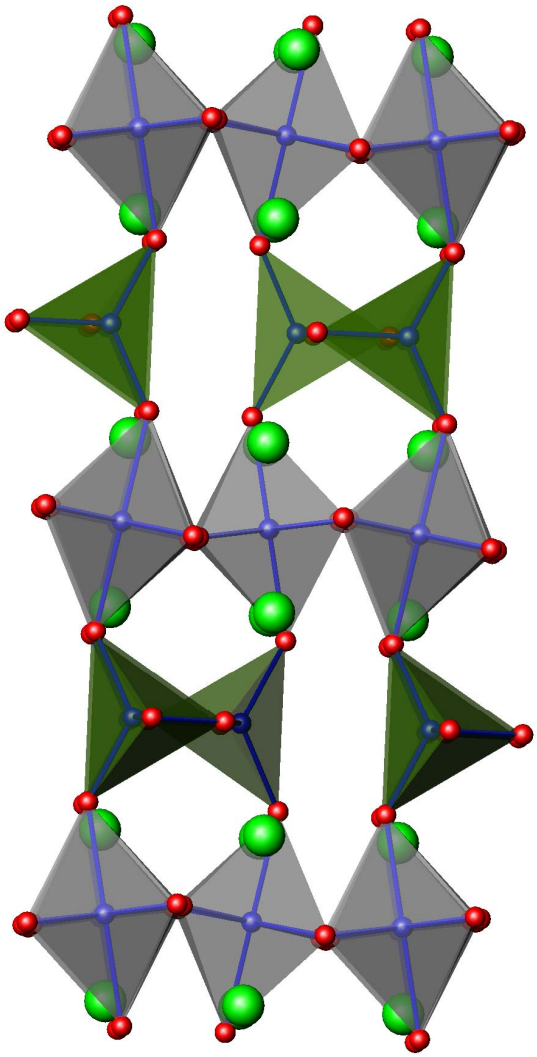

Figure 3.1 The crystallographic structure of brownmillerite $Sr_2Co_2O_5$ where Sr cations are shown in light green, Co cations are shown in blue and O anions are shown in red. CoO_6 octahedra are highlighted in grey whilst CoO_4 tetrahedra are highlighted in khaki.

The brownmillerite $Sr_2Co_2O_5$ can be described as having a perovskite-type structure with ordered oxygen vacancies in alternate perovskite layers such that the overall structure comprises a characteristic stacking of alternating layers of octahedral and tetrahedral cations; vertex-sharing CoO_4 tetrahedra form infinite chains and the oxygen vacancies form 1-D channels. The orthorhombic unit cell is related to the basic perovskite unit cell dimension, a_p, by $a \approx \sqrt{2}a_p$, $b \approx 4a_p$, $c \approx \sqrt{2}a_p$ and the oxygen deficient layers of CoO_4 tetrahedra are at $y = 0.25$ and $y = 0.75$.

Takeda *et al.* [7] determined that $Sr_2Co_2O_5$ with brownmillerite type structure is an antiferromagnet with a Néel temperature of 570 K. Neutron powder diffraction showed this material to exhibit a G-type magnetic structure ($\mu = 3.3(5)\ \mu_B$ at 77K) and the unit cell parameters at 168°C were reported as a =5.4761(3) Å, b = 15.8016(10) Å and c = 5.5819(3) Å after transposing for consistency with the space group *Imma*. The magnetic structure of $Sr_2Co_2O_5$ is shown in *Figure 3.2*, with Sr and O atoms omitted for clarity. It should be noted that Takeda *et al*. originally described this structure using the *Icmm* space group (the **cba** setting of *Imma*) and reported that the Co^{3+} spins are directed along the shortest axis (which in *Icmm* is the *c*-axis). For facile comparison with the space groups *I2mb*, *Pnma* and *Pcmb* in this chapter, the standard setting for this space group, *Imma*, has been used and therefore in this setting the Co^{3+} spins are directed along the *a*-axis.

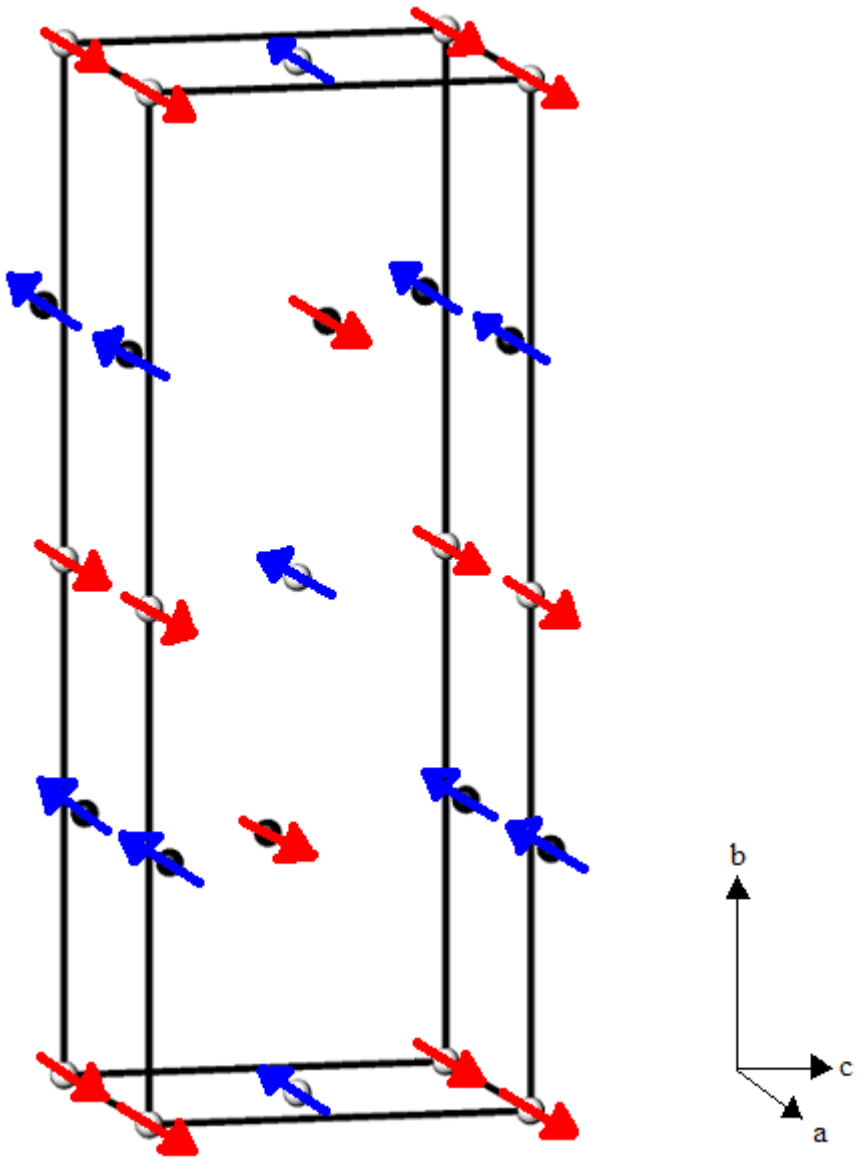

Figure 3.2 An illustration to demonstrate the G-type antiferromagnetic structure of $Sr_2Co_2O_5$ as described by Takeda *et al*. wherein the Co^{3+} spins are directed along the *a*-axis. Black atoms denote Co cations situated in the tetrahedral layers whilst white atoms represent Co cations situated in the octahedral layers.

3.1.2 Ordering of Tetrahedral Chains in Brownmillerites

Although the structures of brownmillerites (generic representation $A_2B_2O_5$) are very closely related, small differences in symmetry arise due to the orientation of the infinite chains of BO_4 tetrahedra within each BO□ layer and the relation between adjacent BO□ layers. It will be assumed that the chains of vacancies are parallel to [100] and the layers of BO_4 tetrahedra are perpendicular to [010]; displacements of O

and B atoms occur to provide pseudo-tetrahedral geometry for the B atoms, and these displacements can occur with two equivalent senses: [100] and [-100], as depicted in *Figure 3.3*. The resultant tetrahedral chains can be represented as L-chains or R-chains and order between these types of chain provides different structures [8, 9].

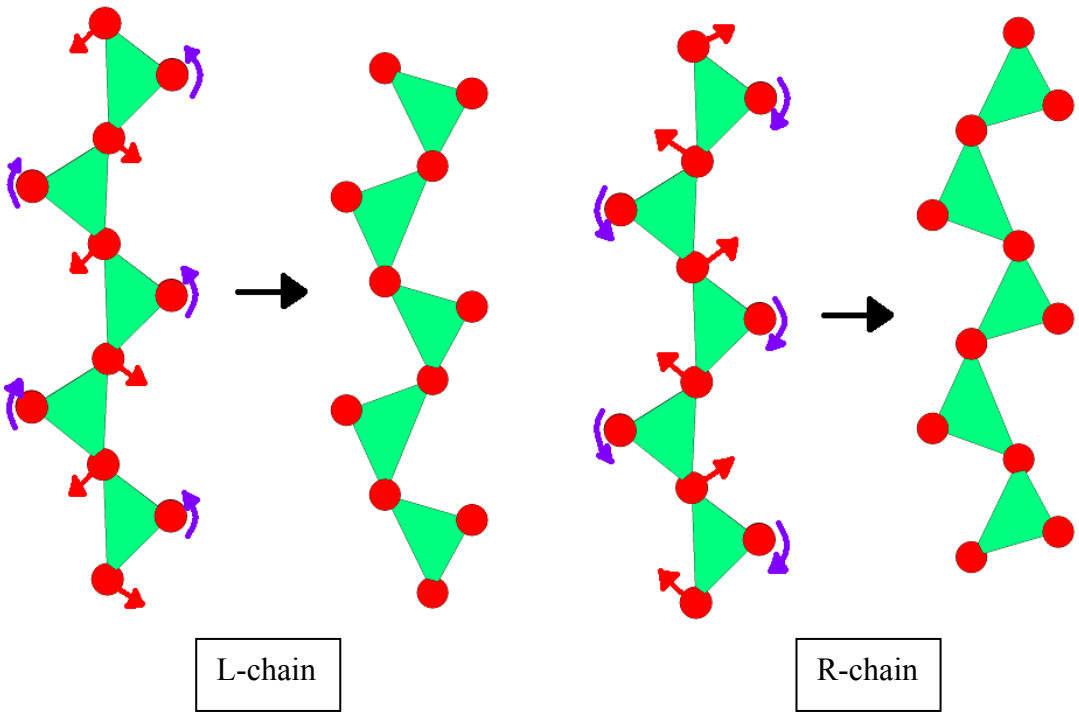

Figure 3.3 Diagram to illustrate how displacement of O atoms (shown by straight red arrows) and rotation of tetrahedra (shown by curved purple arrows) leads to 2-types of relative distortions, L- and R-chains,

Three basic structures contain only L-chains or R-chains within a given layer. If adjacent BO layers have the same chain orientation (only L- or R-chains throughout the structure), such as the chains shown in *Figure 3.4*, the arrangement is consistent with the non-centrosymmetric space group *I2mb*. If layers of L-chains alternate with layers of R-chains, the layers are connected by an inversion centre and the structure is centrosymmetric, space group *Pnma*, as illustrated by *Figure 3.5*. Finally, a totally disordered arrangement of the two possible layer types provides, on average, a random distribution of L- and R-chains throughout the structure and can be described by space group *Imma*.

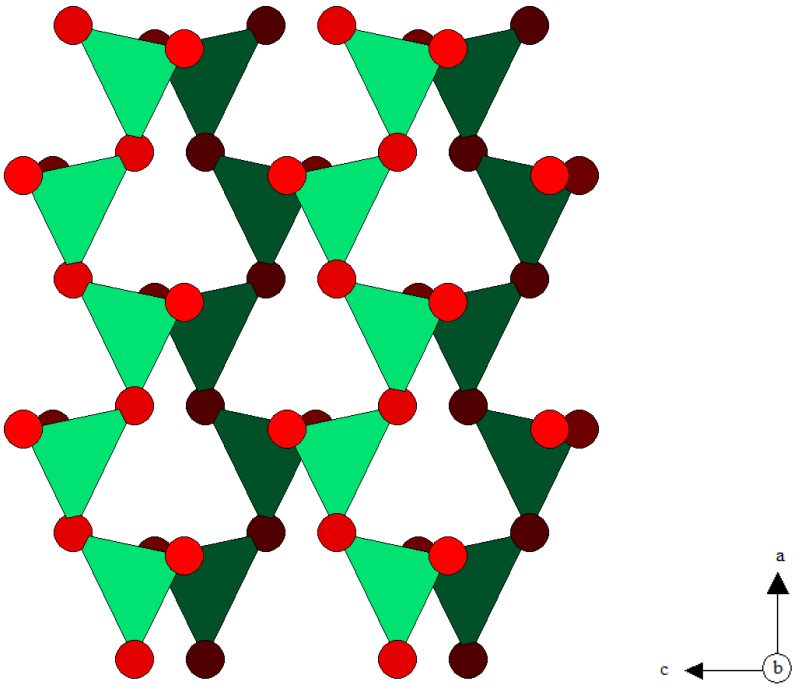

Figure 3.4 Identical interlayer tetrahedral chain orientation at $y = 0.25$ (light green) and $y = 0.75$ (dark green) as described by the space group *I2mb*.

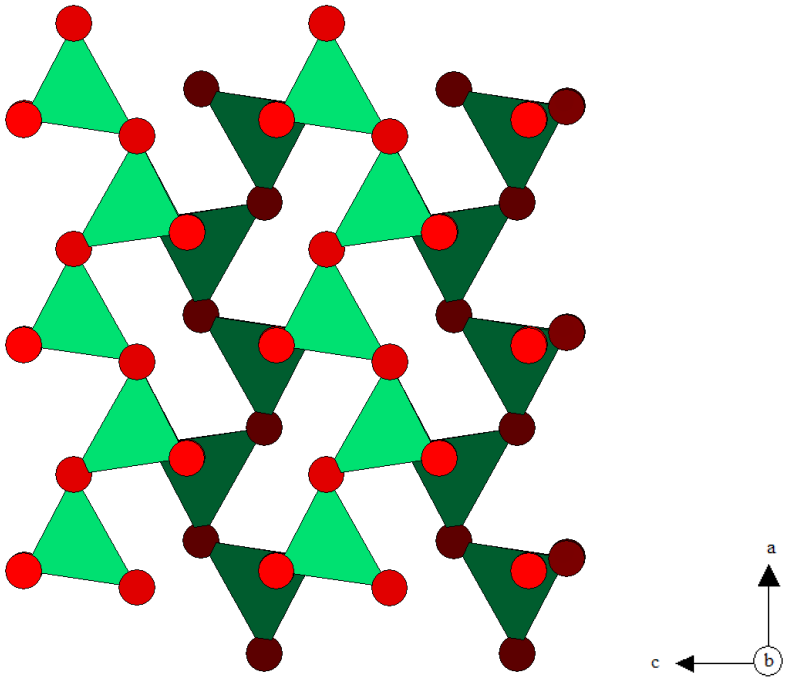

Figure 3.5 Interlayer alternation of tetrahedral chain orientation at $y = 0.25$ (light green) and $y = 0.75$ (dark green) as described by the space group *Pnma*.

A fourth type of chain order has recently been reported for the brownmillerite Sr_2MnGaO_5 [10, 11], which exhibits ordering of the Mn and Ga cations over the two

different coordination environments to yield a structure comprising alternating MnO_2 (octahedral Mn) and GaO (tetrahedral Ga) layers. Examination of this material by electron diffraction and high-resolution electron microscopy revealed that the local ordering of L- and R-chains leads to a superstructure recognisable by the doubling of one of the shorter orthorhombic axes. This corresponds to the alternation of L- and R-chains within a given layer, and hence a doubling of the *c*-axis such that the superstructure unit cell is related to the basic perovskite unit cell dimension, a_p, by $a \approx \sqrt{2}a_p$, $b \approx 4a_p$, $c \approx 2\sqrt{2}a_p$; this arrangement corresponds with space group *Pcmb* [12] (see *Figure 3.6*).

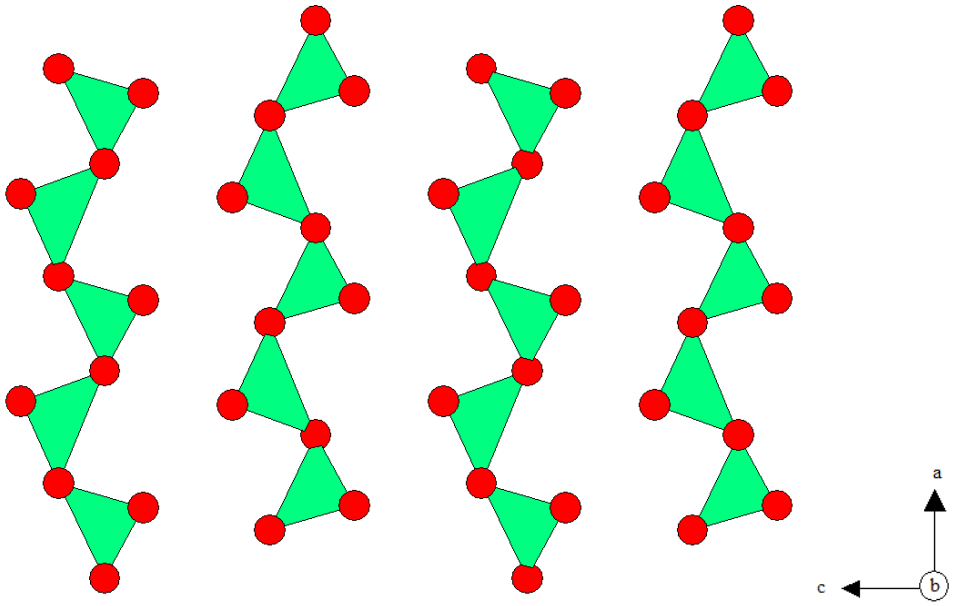

Figure 3.6 Intralayer alternation of tetrahedral chain orientation at $y = 0.25$ (light green) resulting in doubling of the *c*-parameter as described by the space group *Pcmb*.

Abakumov *et al.* [13] proposed that a possible driving force for the different tetrahedral chain ordering patterns observed in brownmillerites could be the minimisation of free energy due to the interaction between the dipole moments of tetrahedral chains. It was hypothesised that since the co-operative displacements of B and O result in a net shift of the chains relative to the rest of the structure and as the

BO layer is positively charged then it follows that each chain has a dipole associated with it. Thus, the chains will attempt to order in such a fashion as to minimise repulsions between dipoles (*i.e.* L-R-L-R- intralayer chain ordering) but this in turn causes the O atoms comprising the vertices of the tetrahedra to interfere with the geometry of the octahedral perovskite layers. Thus the type and observed range of chain ordering is a compromise between lowering the energy of the tetrahedral chains and introducing distortion of the BO_2 and AO layers, thus destabilising these regions of the structure.

Although $Sr_2Co_2O_5$ has previously been reported to crystallise in the disordered space group *Imma*, no detailed structural data have yet been reported on this phase, and the co-operative orientations of CoO_4 tetrahedral chain rotations has not been investigated. The aim of this study was therefore to use electron diffraction and neutron powder diffraction to probe the chain ordering in $Sr_2Co_2O_5$ and hence perform a full structural and magnetic characterisation of this material.

After the work contained in this chapter was completed, a further neutron diffraction study of $Sr_2Co_2O_5$ coupled with *ab-initio* band structure calculations by Muñoz *et al.* [14] was published. A comparison of the findings appearing in this chapter with this new research is discussed in greater detail in Section 3.4.

3.2 Experimental Procedure

A polycrystalline sample of brownmillerite $Sr_2Co_2O_5$ was synthesised by the standard solid-state reaction of stoichiometric quantities of high purity Sr_2CO_3 and Co_3O_4. The reagents were ground together and subjected to 2 heat treatments with intermediary grinding, consisting of 12 hours at 1150°C in air. The 2nd heat treatment was followed by immediately quenching from 1150°C into liquid nitrogen.

3.3 Results and Discussion

3.3.1 Investigation of the Phase Transitions of $Sr_2Co_2O_5$

The phase transitions of this system were investigated *via* thermogravimetric and differential thermal analysis. All samples were heated in air at a ramp rate of 10ºC min^{-1} from 25ºC to 1250ºC, held isothermally at 1250ºC for 20 minutes, then cooled to 25ºC at 10ºC min^{-1}.

Figure 3.7 shows the thermogravimetric and differential thermal analysis plots for a typical sample of brownmillerite-type $Sr_2Co_2O_5$. The weight increase accompanied by an exothermic transition at 580-680ºC corresponds to the absorption of oxygen and transition to the low-temperature hexagonal form $Sr_6Co_5O_{15}$ + ⅓Co_3O_4. From 700ºC the sample gradually loses weight again and between 900-940ºC an endothermic transition to the high temperature cubic phase is observed. Upon cooling, the sample begins to absorb oxygen again and adopts the low temperature hexagonal phase from around 750ºC.

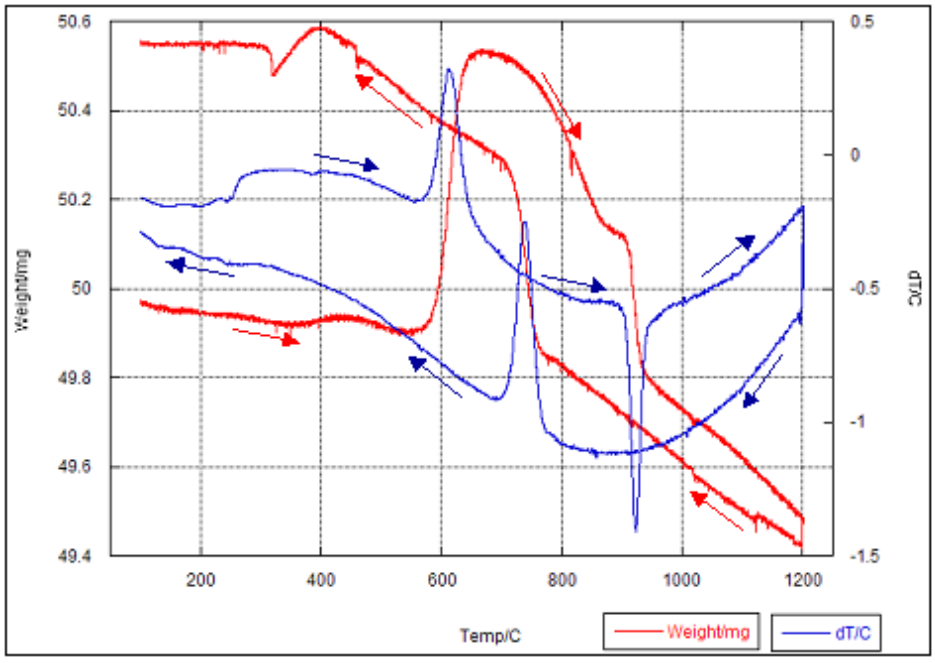

Figure 3.7 TGA differential thermal analysis plot illustrating the exothermic and endothermic transitions (blue line) and weight (red line) of $Sr_2Co_2O_5$ as a function of temperature.

XRD data collected between 26°C-1079°C confirm these phase transitions and the observation of the cubic phase above 940ºC confirms the findings of Rodriguez *et al.* [3] that oxygen vacancy ordering occurs upon quenching. A few selected XRD patterns are illustrated in *Figure 3.8*.

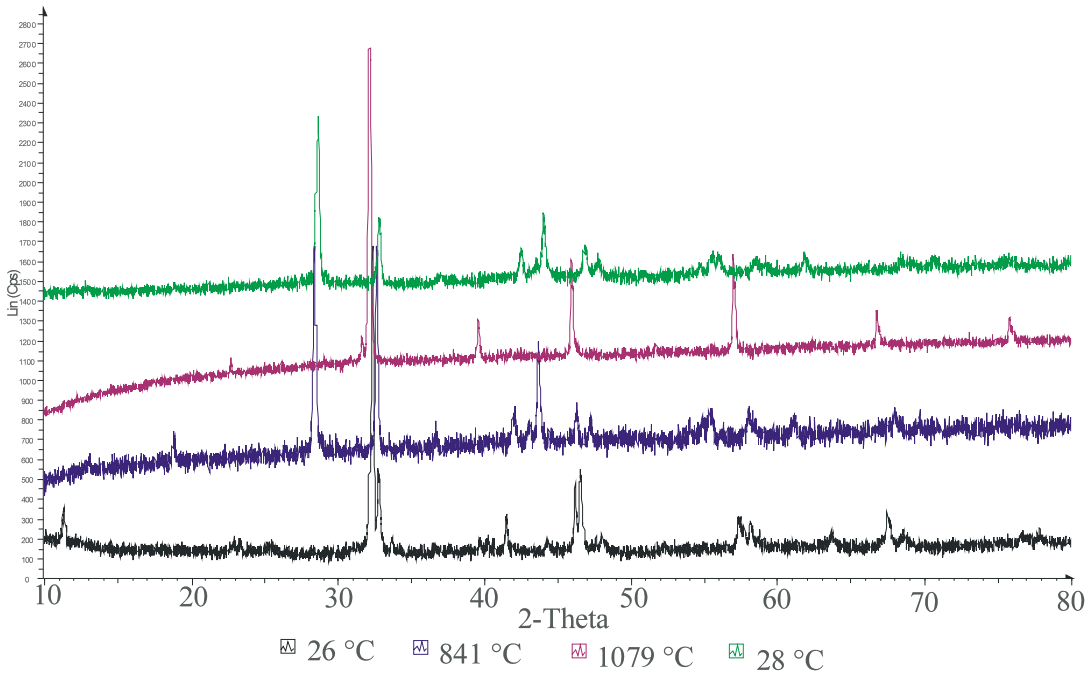

Figure 3.8 Selected variable temperature XRD data illustrating the phase transitions observed upon heating $Sr_2Co_2O_5$ in air. The black trace shows brownmillerite $Sr_2Co_2O_5$ prior to heating, the blue trace shows that the brownmillerite structure has been replaced by rhombohedral $Sr_6Co_5O_{15}$ + ⅓Co_3O_4 and the purple trace shows that $Sr_2Co_2O_5$ reverts to a cubic perovskite structure above 940ºC. The rhombohedral phase is formed upon cooling as this is more thermodynamically stable, as shown by the green trace; the brownmillerite phase may only be formed by quenching.

3.3.2 Preliminary Refinement Based on Room Temperature XRD Data in the Space Group *Imma*

A preliminary Rietveld structural refinement using the program "GSAS" was carried out on XRD data collected over a period of 10 hours. The model adopted for this refinement, using the space group *Imma*, converged with $\chi^2 = 1.835$, $R_p = 1.18\%$ and $R_{wp} = 1.53\%$. No detailed structural data have yet been reported on this phase, but

the refined lattice parameters, a = 5.4592(2) Å, b = 15.7841(7) Å and c = 5.5726(2) Å, are in agreement with the results of Rodriguez *et al.* [3]. The assignment of the disordered space group provided a reasonable fit to the experimental data (see *Figure 3.9*) with no obvious unindexed peaks.

The space groups *I2mb*, *Pnma*, *Pcmb* and *Imma* are commonly used to describe the subtle differences in symmetry displayed by brownmillerite structures, which may arise from the co-operative rotations of tetrahedral chains. One might expect to be able to assign the correct space group merely by examining the presence or absence of certain reflections, for example, *Pcmb* symmetry should produce a 1 0 0 reflection not predicted for *I2mb*, *Pnma* or *Imma* at $2\theta = 16.223$. However, it should be borne in mind that these space groups are used to differentiate between symmetry variations arising in the oxygen sublattice. As oxygen is a light atom and powder XRD is not sensitive enough to accurately determine the positions of light atoms such as oxygen, it is unlikely that XRD alone can be used to differentiate between these space groups, hence the assignment of *Imma* to allow for disorder in the oxygen sublattice. In general, unless there is real evidence to assign a lower symmetry space group, then it is preferable to use the highest symmetry space group. Although XRD is a poor probe for lighter atoms because the scattering length varies linearly in proportion to Z, neutron diffraction scattering lengths vary randomly thus can yield more accurate information about the oxygen ordering.

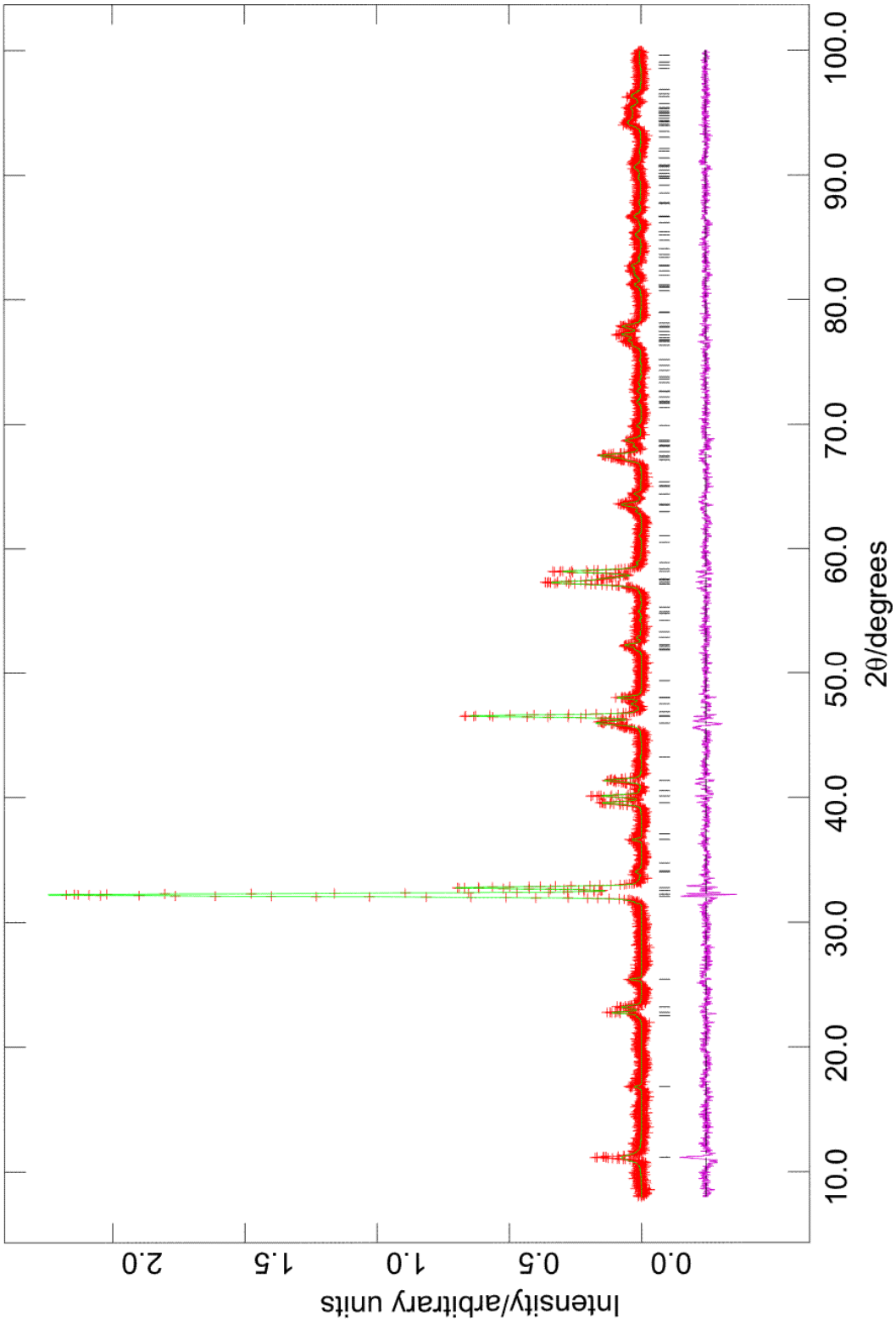

Figure 3.9 Observed (red +), calculated (green) and difference (pink) profiles of $Sr_2Co_2O_5$ as generated by the Rietveld profile refinement of XRD data in the space group *Imma* with peak positions indicated by black vertical lines.

3.3.3 TEM and HREM Studies

To explore the possibility of chain ordering more rigorously, the sample was examined by Dr Joke Hadermann (The University of Antwerp) using electron diffraction to determine the local symmetry more reliably.

The electron diffraction patterns were indexed using the brownmillerite structure with space group *Imma*. Crystals examined along [010] displayed sharp reflections at 0 0 1+1/2 indicating a doubling of the *c*-parameter and hence the presence of a superstructure, as shown in *Figure 3.10*. *Figures 3.11* and *3.12* show the electron diffraction pattern of $Sr_2Co_2O_5$ along the [101] and [100] zones respectively.

It was concluded that $Sr_2Co_2O_5$ displays the same superstructure as Sr_2MnGaO_5 arising from the alternation of L- and R- tetrahedral chain orientation along the *c*-axis with reflection conditions in agreement with the space group *Pcmb*. This observation, of course, relates to the length scale appropriate to electron diffraction, which is substantially smaller than that for XRD or NPD. Both XRD and NPD are bulk techniques, which provide valuable information about the average structures of powders whilst TEM and HREM examine single crystallites. The wavelength of electrons used for HREM are smaller than the wavelength of X-rays and neutrons used for powder diffraction studies (by a factor of approximately 50) therefore are more suited for examining structural features on a smaller length scale, hence assigning the space group symmetry on a local level.

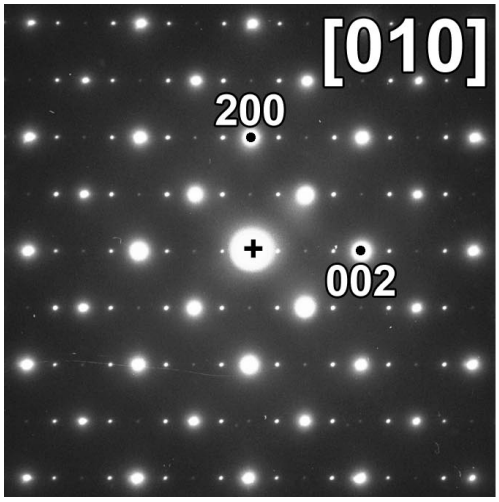

Figure 3.10 Electron diffraction pattern of $Sr_2Co_2O_5$ along the [010] zone.

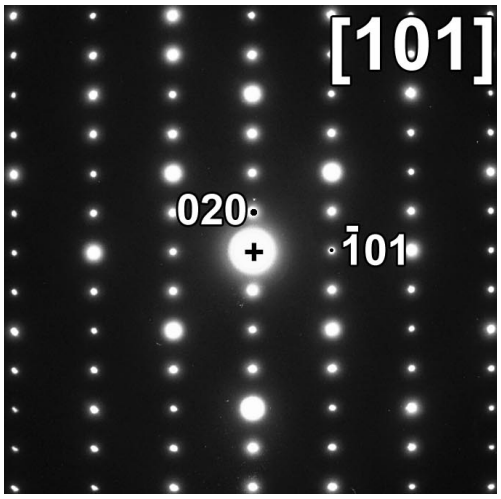

Figure 3.11 Electron diffraction pattern of $Sr_2Co_2O_5$ along the [101] zone.

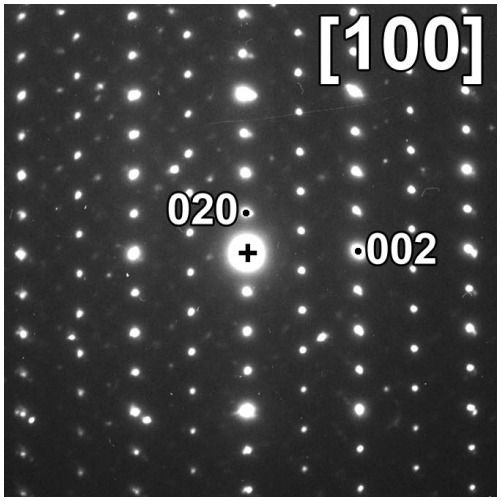

Figure 3.12 Electron diffraction pattern of $Sr_2Co_2O_5$ along the [100] zone.

High-resolution images of [010] (see *Figure 3.13*) show a periodicity estimated to be about 11Å along [001], confirming the approximate doubling of the *c*-parameter. This provided further support for a chain ordered superstructure similar to that observed in Sr_2MnGaO_5.

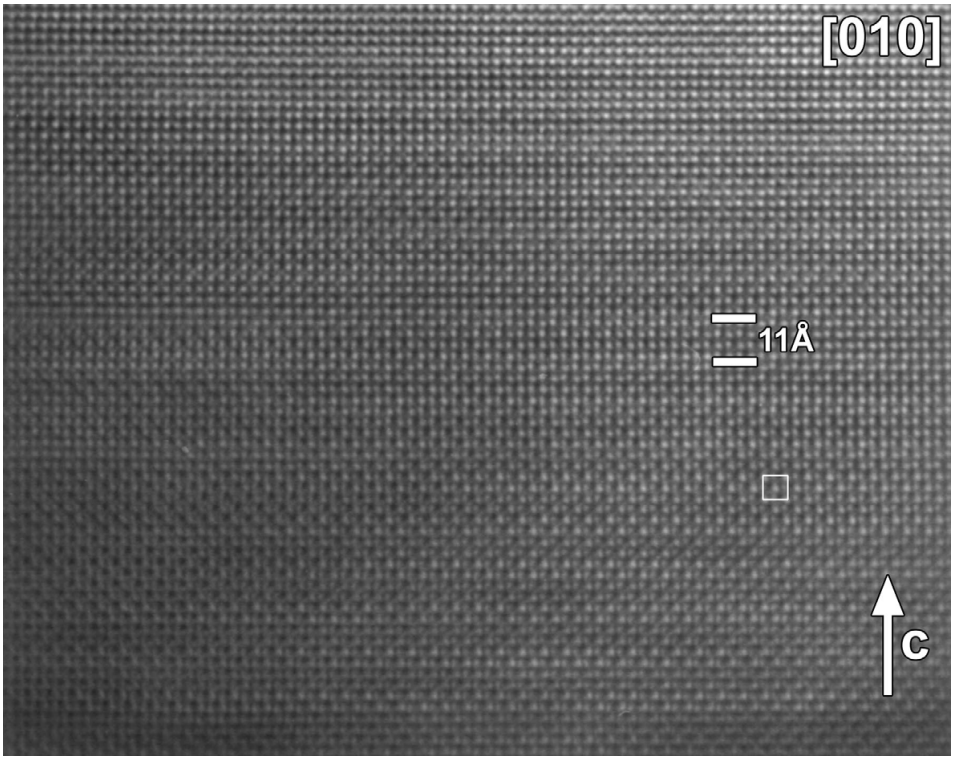

Figure 3.13 High-resolution electron microscope image of $Sr_2Co_2O_5$ viewed along the [010] zone illustrating a periodicity of approximately 11 Å.

3.3.4 Nuclear and Magnetic Refinement Based on NPD Data in the Space Group *Pcmb*

Neutron powder diffraction data were collected at 4K (to minimise temperature factor effects) in order to examine whether the *Pcmb* symmetry was still reflected on the longer length scale applicable to the neutron wavelength, and to provide more complete structural and magnetic characterisation. In order to account for the magnetic component of the NPD data, the refinement was carried out in terms of 2 phases, one purely nuclear and the other purely magnetic.

As indicated by electron diffraction, a structural model for $Sr_2Co_2O_5$ based on Sr_2MnGaO_5 was adopted for the nuclear component of the refinement, which allowed for the doubling of the *c*-parameter due to the L-R-L-R- ordering of chain orientations within the tetrahedral layer. The magnetic model was based upon G-type antiferromagnetic order with the Co^{3+} moments directed along the *a*-axis as proposed by Takeda *et al.* [7]. *Pcmb* was used as a fully ordered model for the magnetic unit cell (4 Co positions) with the lattice parameters of both the nuclear and the magnetic phases constrained to be equal.

The "GSAS" suite of programs [15] was used to carry out a Rietveld profile refinement with linear interpolation function background parameters, diffractometer zero point, histogram scale factor, lattice parameters, pseudo-Voigt peak profiles, atomic co-ordinates and isotropic thermal parameters refined. The temperature factors of the same atomic species were constrained to remain equal. The Rietveld profile refinement plot is shown in *Figure 3.14*.

The nuclear and magnetic refinement was possible in the space group *Pcmb*, consistent with doubling of the *c*-parameter (a = 5.4640(3) Å, b = 15.6485(8) Å, c = 11.1340(6) Å, $\chi^2 = 5.080$, $R_{wp} = 3.76\%$, $R_p = 2.76\%$,) and the presence of a superstructure. For the magnetic refinement, a single μ was assigned for both octahedral and tetrahedral Co with all moments aligned along the *a*-axis, giving a refined magnetic moment per $Co^{3+} = 2.80(4)\ \mu_B$ which is less than that determined by Takeda *et al.* ($\mu = 3.3(5)\ \mu_B$ at 77K) [7]. *Table 3.1* shows the refined atom parameters obtained from the powder neutron diffraction refinement using the *Pcmb* superstructure model. The bond lengths associated with the Co(1) and Co(3) octahedra are tabulated in *Table 3.2* and those for the Co(2) and Co(4) tetrahedra in *Table 3.3*.

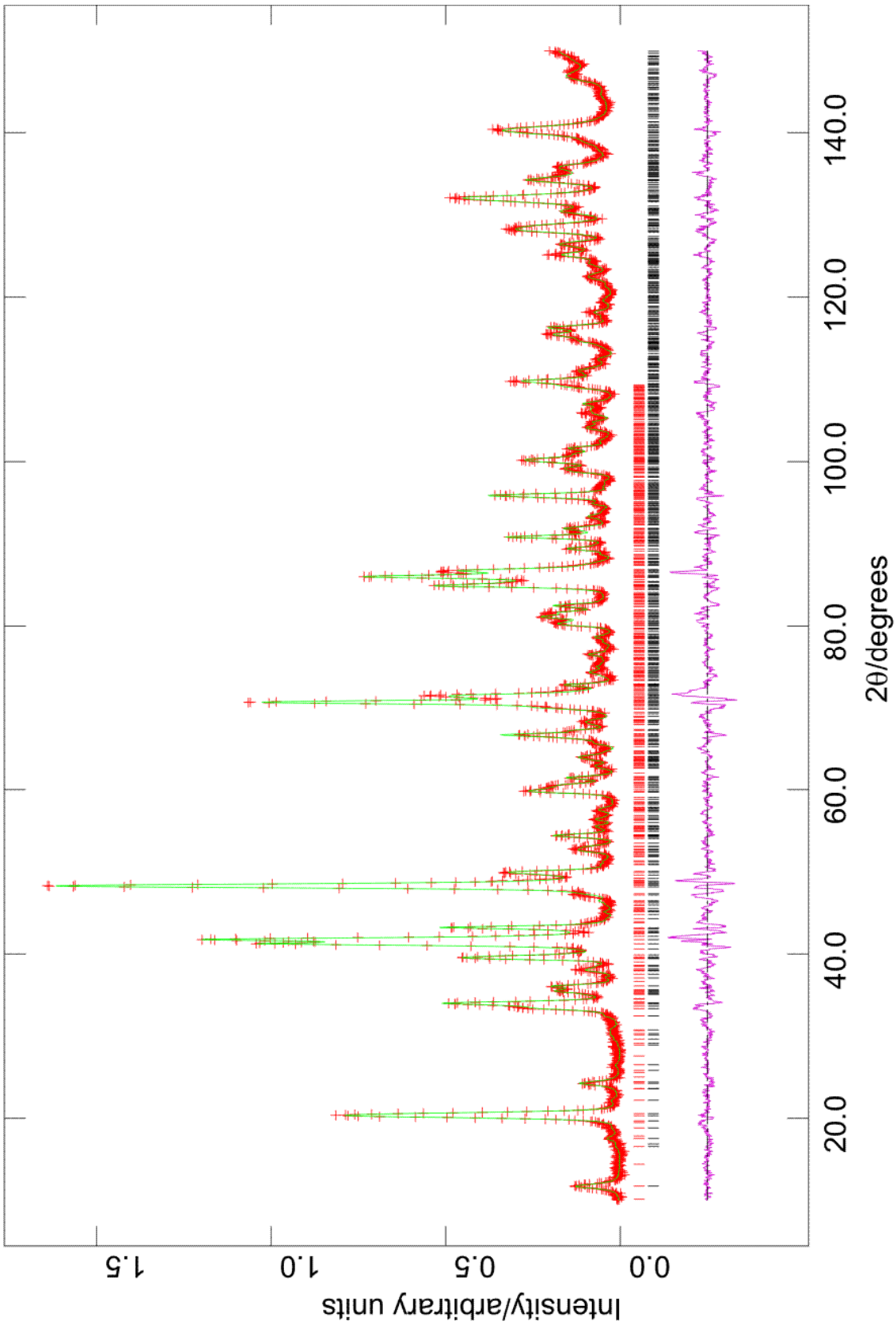

Figure 3.14 Observed (red +), calculated (green) and difference (pink) profiles of $Sr_2Co_2O_5$ as generated by the Rietveld profile refinement in the space group *Pcmb* of NPD data collected at 4K, with peak positions indicated by black vertical lines and magnetic reflections indicated by red vertical lines.

Table 3.1 Refined atom parameters of $Sr_2Co_2O_5$ from refinement of NPD data (collected at 4K) in the space group *Pcmb*.

Atom	Site Symmetry	*x*	*y*	*z*	$U_{iso} \times 100$ (Å^2)
Sr (1)	8e	0.006(2)	0.6114(4)	0.2571(9)	0.52(6)
Sr (2)	8e	0.502(2)	1.1134(4)	0.506(1)	0.52(6)
Co (1)	4a	0	0	0	0.7(2)
Co (2)	4d	0.459(4)	0.75	0.229(2)	0.7(2)
Co (3)	4c	0.493(6)	0	0.25	0.7(2)
Co (4)	4d	0.011(7)	0.75	0.048(2)	0.7(2)
O (1)	8e	0.257(2)	-0.0058(6)	0.1333(9)	0.73(6)
O (2)	8e	0.261 (2)	-0.0066(6)	0.6355(8)	0.73(6)
O (3)	8e	-0.000(2)	0.1459(4)	0.0233(6)	0.73(6)
O (4)	4d	0.848(2)	0.75	0.682(1)	0.73(6)
O (5)	8e	0.507(2)	0.6374(4)	0.2677(7)	0.73(6)
O (6)	4d	0.614 (2)	0.75	0.073(1)	0.73(6)

Table 3.2 Bond lengths for CoO_6 octahedra from the refinement of NPD data collected at 4K in the space group *Pcmb*.

Bond	Length in Å at 4K
Co(1)-O(1) [× 2] eq	2.05(1)
Co(1)-O(2) [× 2] eq	2.080(9)
Co(1)-O(3) [× 2] ap	2.298(6)
Co(3)-O(1) [× 2] eq	1.83(2)
Co(3)-O(2) [× 2] eq	1.86(3)
Co(3)-O(5) [× 2] ap	2.160(7)

Table 3.3 Bond lengths for CoO_4 tetrahedra from the refinement of $Sr_2Co_2O_5$ in the space group *Pcmb* using NPD data collected at 4K.

Bond	**Length in Å at 4K**
Co(2)-O(4)	1.75(2)
Co(2)-O(6)	1.93(2)
Co(2)-O(5) [× 2]	1.834(9)
Co(4)-O(4)	1.68(3)
Co(4)-O(6)	2.19(4)
Co(4)-O(3) [× 2]	1.81(1)

It is clear from these bond lengths that the Co(3) octahedra are markedly smaller than the Co(1) octahedral (~9%). In addition, the Co(4)-O(4) bond length was noted to be exceptionally shorter and the Co(4)-O(6) longer than the Co(2)-O(4) and Co(2)-O(6) bond lengths respectively. Upon moving the O(4) further away from, and the O(6) closer to, the Co(4) and then refining this parameter the O atoms rapidly returned to their former positions.

It was postulated that although $Sr_2Co_2O_5$ had previously been reported to be a high spin Co(III) material, the marked difference in bond lengths for both the 2 octahedral Co sites and the 2 tetrahedral Co sites respectively may have been indicative of the disproportionation of Co(III) to Co(II) and Co(IV). It was proposed that the marked differences in Co-O bond lengths could arise as a result of occupation of the octahedral Co(1) and tetrahedral Co(4) sites by Co(II) whilst the octahedral Co(3) and tetrahedral Co(2) sites were occupied by Co(IV). Hence, the magnetic model was modified to allow different values of M_x for the 4 different Co sites. This alteration had a negligible effect upon the refinement statistics (χ^2 = 5.067,

R_{wp} = 3.76%, R_p = 2.76%), although the Co(4)-O(4) bond length was noted to have approached the value of the Co(2)-O(4) bond length.

In order to ascertain the validity of this model, bond valence sum (BVS) calculations [16-18] were carried out on all 4 Co polyhedra in this structure for Co(II), Co(III) and Co(IV) with the results tabulated in *Table 3.4* (see *Appendix 3.1* for detailed calculations). These calculations used the bond lengths from the initial refinement with the magnetic moment for all Co^{3+} being kept equal at 2.80(4) μ_B, as this was in reasonable agreement with previously reported data for $Sr_2Co_2O_5$.

Table 3.4 Summary of the bond valence sums, V, calculated using NPD data collected at 4K for $Sr_2Co_2O_5$ refined in the space group *Pcmb*, based upon r_0 for Co(II)-O = 1.692, r_0 for Co(III)-O = 1.70 and r_0 for Co(IV)-O = 1.75.

Co-O Bond	Co Oxidation State	V
Co(1)-O	II	1.86
Co(1)-O	III	1.90
Co(1)-O	IV	2.18
Co(3)-O	II	3.20
Co(3)-O	III	3.26
Co(3)-O	IV	3.74
Co(2)-O	II	2.67
Co(2)-O	III	2.73
Co(2)-O	IV	3.13
Co(4)-O	II	2.78
Co(4)-O	III	2.84
Co(4)-O	IV	3.25

As shown by the data in *Table 3.4*, disproportionation of Co^{3+} to Co^{2+} on the Co(1) sites and Co^{4+} on the Co(3) sites could possibly explain the size difference between the Co(1) and Co(3) bond lengths. The bond valence sum calculations for the Co(1)-O bond for Co^{2+} give V = 1.86 which is in good agreement with the Co valency. Coupled with the result of bond valence sum calculations for the Co(3)-O bond for Co^{4+} which gave V = 3.74, this would support the theory of Co^{3+}

disproportionation to Co^{2+} and Co^{4+} on the Co(1) and Co(3) octahedral sites. However, there is no similar evidence to imply the occurrence of such behaviour on the Co(2) and Co(4) tetrahedral sites. Hence, on the basis of these calculations, there was not enough conclusive evidence to support the disproportionation model.

In order to further explore the apparent difference in size between octahedra centred around the Co(1) and Co(3) positions respectively as observed at 4K, the average Co-O bond lengths for all Co sites were calculated for NPD data collected at several different temperatures.

Table 3.5 Average bond lengths for Co(1) and Co(3) octahedra from NPD data collected between 4K and 300K refined in the space group *Pcmb*.

Temperature	**Average Co(1)-O Bond Length (Å)**	**Average Co(3)-O Bond Length (Å)**
4K	2.141(4)	1.95(1)
100K	2.138(6)	1.96(1)
200K	2.138(6)	1.96(1)
300K	2.138(6)	1.97(1)

The average octahedral bond lengths tabulated in *Table 3.5* clearly showed the trend of an approximate 9% contraction in average bond length of the Co(3)-O octahedra as compared with the Co(1)-O octahedra in the temperature range studied.

Table 3.6 Average bond lengths for Co(2) and Co(4) tetrahedra from NPD data collected between 4K and 300K refined in the space group *Pcmb*.

Temperature	Average Co(2)-O Bond Length (Å)	Average Co(4)-O Bond Length (Å)
4K	1.839(9)	1.87(1)
100K	1.921(9)	1.79(1)
200K	1.859(9)	1.86(1)
300K	1.93(1)	1.81(1)

However, the average Co-O bond lengths for Co on tetrahedral sites (see *Table 3.6*) only showed such a trend for data collected at 100K and 300K, with the 4K and 200K data tetrahedral bond lengths showing similarly sized tetrahedra on both the Co(2) and Co(4) site. This indicated that the observed difference in octahedral bond lengths about the Co(1) and Co(3) positions may well be an artefact of the space group symmetry used for the refinement allowing such elongations and contractions of bond length and hence cast significant doubt on the assignment of *Pcmb* as best describing the overall structure.

3.3.5 Nuclear and Magnetic Refinement Based on NPD Data in the Space Group *Imma*

Although the crystals of $Sr_2Co_2O_5$ examined using TEM and HREM clearly showed doubling of the *c*-parameter arising from the L-R-L-R- ordering of chains in the tetrahedral layer, there were aspects of the refinement of NPD data in the *Pcmb* space group which cast doubt upon the assignment of this space group for the overall crystal structure. The rather short refined bond length for Co(4)-O(4) coupled with the

longer Co(4)-O(6) refined bond length seemed unusual, as did the differing sizes of the Co-O polyhedra.

It was thought that the oddities in this refinement could relate to the assignment of the *Pcmb* space group being inappropriate. In fact, no evidence for cell doubling could be found from careful examination of the NPD data and refinements based upon these data were therefore carried out in the original, disordered space group *Imma*. As for the *Pcmb* refinement, the magnetic component of the data was modelled by using a 2-phase refinement whereby one phase was purely nuclear and the other purely magnetic. For this refinement, because *Imma* allows for the splitting of the Co cation sites due to disorder in the structure, the *P*1 space group (8 Co positions) was used to describe the magnetic phase as it allows for maximum Co flexibility, using the ordered Co array (*I*2*mb* symmetry) for this model.

The refinement statistics for the 4K data set ($\chi^2 = 5.315$, $R_{wp} = 3.86\%$, $R_p = 2.83\%$) were slightly inferior to those obtained using the *Pcmb* superstructure model ($\chi^2 = 5.080$, $R_{wp} = 3.76\%$, $R_p = 2.76\%$), however the difference in visual goodness of fit is negligible (see *Figure 3.15*) and the number of refined structural parameters is reduced from 33 to 15. *Table 3.7* contains the atom parameters for $Sr_2Co_2O_5$ obtained from the refinement of NPD data collected at 4K in the space group *Imma.* The refined magnetic moment was $\mu = 3.00(4)\ \mu_B$ which is in better agreement with that determined by Takeda *et al*. ($\mu = 3.3(5)\ \mu_B$ at 77K) than the value from the refinement in *Pcmb* ($\mu = 2.80(4)\ \mu_B$). A detailed analysis of the magnetic symmetry was not required as it has already been reported, however it is important for NPD data to model the magnetic structure correctly as there is a large magnetic component to the neutron scattering for this material thus a good refinement based on the NPD data cannot be obtained without taking this into account.

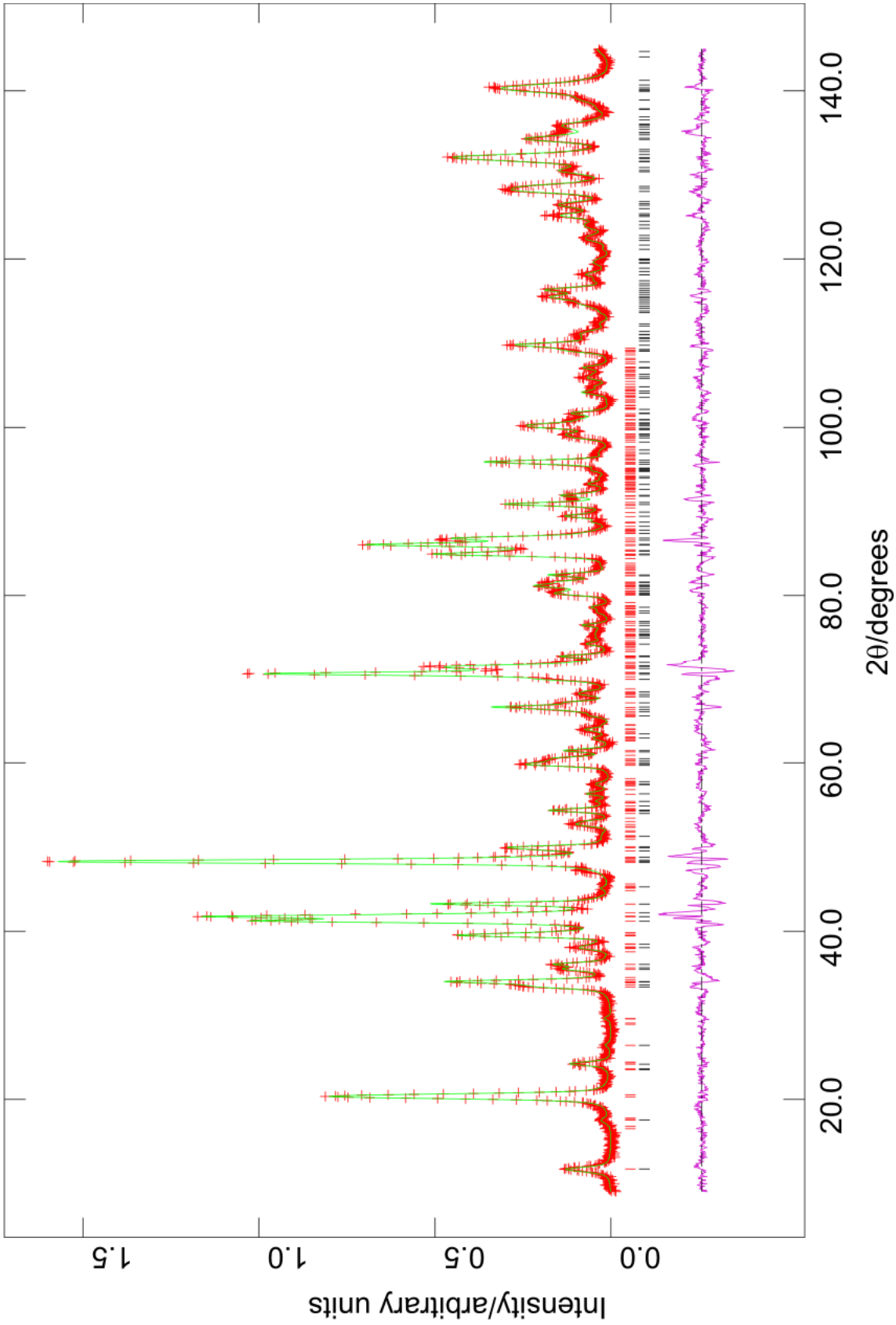

Figure 3.15 Observed (red +), calculated (green) and difference (pink) profiles of $Sr_2Co_2O_5$ as generated by the Rietveld profile refinement in the space group *Imma* of NPD data collected at 4K, with peak positions indicated by black vertical lines and magnetic reflections indicated by red vertical lines.

Table 3.7 Table of atomic parameters from the refinement of $Sr_2Co_2O_5$ in the space group *Imma* using NPD data collected at 4K.

Atom	Site Symmetry	*x*	*y*	*z*	Occupancy	$U_{iso} \times 100$ (Å^2)
Sr	8h	0	0.6120(1)	0.5125(5)	1	0.66(6)
Co(1)	4a	0	0	0	1	1.93(2)
Co(2)	8i	0.480(6)	0.25	0.565(2)	0.5	2.1(4)
O(1)	8g	0.25	0.9936(2)	0.25	1	0.96(8)
O(2)	8h	0	0.1419(2)	0.0433(5)	1	0.86(8)
O(3)	8i	0.1389(9)	0.25	0.6420(9)	0.5	0.71(1)

Table 3.8 Table of refined lattice parameters from NPD data collected between 4K and 300K refined in the space group *Imma.*

Temperature	*a* (Å)	*b* (Å)	*c* (Å)
4K	5.4639(3)	15.6486(8)	5.5667(3)
100K	5.4638(3)	15.660(1)	5.5669(4)
200K	5.4671(3)	15.694(1)	5.5684(4)
300K	5.4702(3)	15.733(1)	5.5706(4)

Table 3.9 Table of selected bond lengths for NPD data collected between 4K and 300K refined in the space group *Imma.*

Bond	Bond Length (Å) at 4K	Bond Length (Å) at 100K	Bond Length (Å) at 200K	Bond Length (Å) at 300K
Co(1)-O(1) [× 4] eq	1.9527(2)	1.9526(2)	1.954(2)	1.9543(2)
Co(1)-O(2) [× 2] ap	2.235(3)	2.241(3)	2.248(3)	2.249(3)
Co(2)-O(2) [× 2]	1.803(5)	1.806(5)	1.808(5)	1.794(5)
Co(2)-O(3)	1.85(2), 1.89(1)	1.83(2), 1.89(1)	1.81(2), 1.91(1)	1.85(2), 1.95(1)

Table 3.10 Average bond lengths for Co(1)-O octahedra and Co(2)-O tetrahedra from NPD data collected between 4K and 300K refined in the space group *Imma*

Temperature	Average Co(1)-O Bond Length (Octahedra) (Å)	Average Co(2)-O Bond Length (Tetrahedra) (Å)
4K	2.0468(9)	1.835(5)
100K	2.049(1)	1.831(5)
200K	2.052(1)	1.834(5)
300K	2.053(1)	1.847(6)

The bond valence sum calculations were re-worked using the bond lengths derived from the refinement of NPD data in the *Imma* space group and assuming all Co to be Co^{3+}. *Table 3.11* summarises the results of these calculations, which show that the values of V for all Co sites are reasonably close to 3, although V = 2.49 for the octahedral site is still somewhat low. However, the bond lengths from the refinement of NPD data in *Imma* are more feasible for Co^{3+} than those obtained from refinement of NPD data in the *Pcmb* space group.

Table 3.11 Summary of the bond valence sums, V, calculated using NPD data collected at 4K for $Sr_2Co_2O_5$ refined in the space group *Imma*, based upon r_0 for Co(III)-O = 1.70.

Co-O Bond	Co Oxidation State	V
Co(1)-O	III	2.49
Co(2)-O	III	2.78

The fairly low value of V for Co(1) combined with the high refined U_{iso} of 1.9(2) suggests slightly more flexibility is required to describe the local symmetry which would be consistent with the assignment of *Pcmb*. However, although electron diffraction studies irrefutably showed intralayer chain ordering consistent with the space group *Pcmb* in the grains examined, it would seem that on the larger scale applicable to X-ray and neutron powder diffraction the bond valence sum calculations support the argument that the overall structure is best described by the disordered space group *Imma*.

Table 3.12 Magnetic moment M_x from NPD data collected on $Sr_2Co_2O_5$ between 4K and 300K refined in the space group *Imma.*

Temperature	Refined Moment M_x/ μ_B
4K	3.00(4)
100K	2.77(4)
200K	2.61(4)
300K	2.33(5)

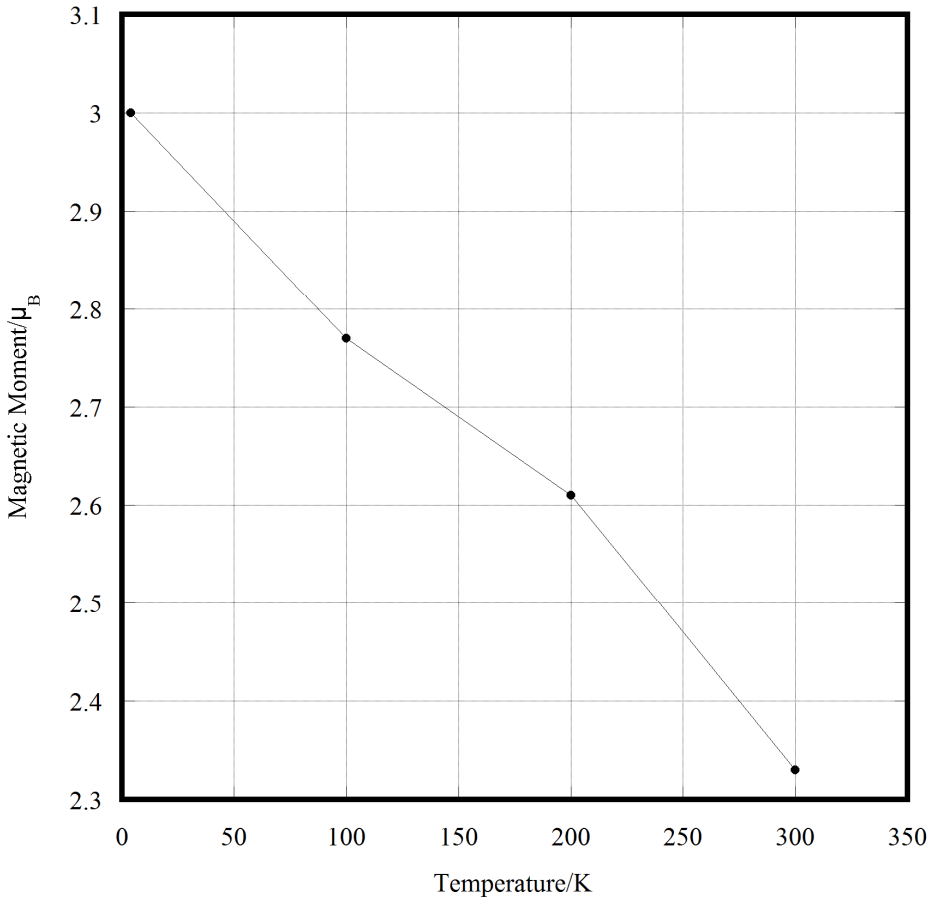

Figure 3.16 Plot of magnetic moment M_x against T from the refinement of $Sr_2Co_2O_5$ in the space group *Imma*.

The refined neutron magnetic moments M_x for data collected at T = 4K, 100K, 200K and 300K as shown in *Figure 3.16* show a general decrease with increasing temperature which confirm antiferromagnetic ordering in this region. It is possible these data could be extrapolated using the mean field approximation whereby M_z should decease smoothly to 0 at $T = T_N$ to provide an estimate for T_N for this particular sample, although T_N is already known for this material ($T_N \approx 570K$). However, it was not possible to fit these data to mean field theory, and taking into account that data were only collected at 4 different temperatures then even if it were possible to extrapolate T_N from the M_z values obtained, it is unlikely that an accurate estimate would result.

3.3.6 Characterisation of Magnetic Properties

Zero-field cooled and field-cooled DC magnetisation data were collected on $Sr_2Co_2O_5$ in an applied field of 3000 Oe (0.3 T) from ~2K to ~320K *Figure 3.17* shows a plot of the magnetic susceptibility χ_m against temperature.

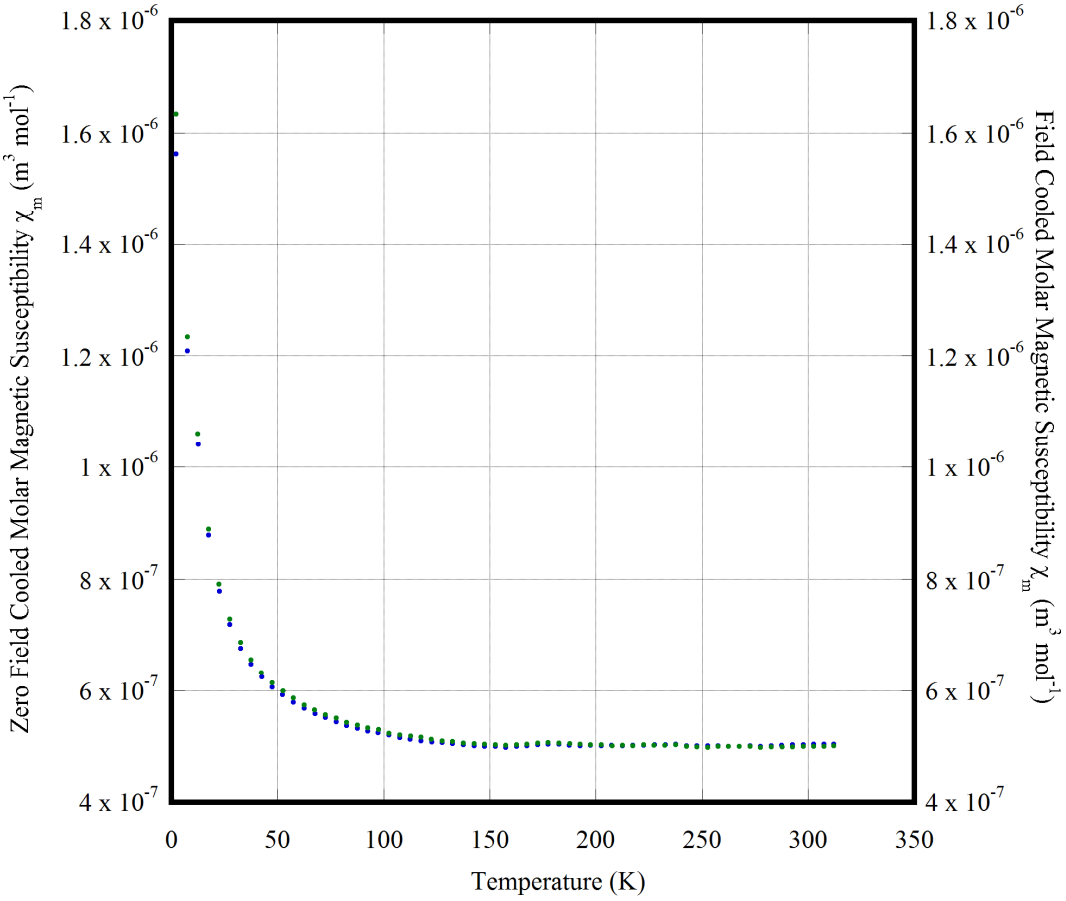

Figure 3.17 Plot of zero-field cooled and field-cooled magnetic susceptibility (χ) against temperature.

The zero-field cooled and field-cooled data slightly diverge from one another below 100K with a slight paramagnetic upturn in magnetic susceptibility at low temperature. These data support the findings by Takeda *et al.* [7] that $Sr_2Co_2O_5$ exhibits antiferromagnetic ordering of Co cations below its Néel temperature T_N = 570 K.

3.4 Conclusions

Choosing a space group which best describes a brownmillerite structure can often prove very difficult. There are subtle differences in symmetry in the space groups *I2mb, Pnma* and *Pcmb* each of which allow order in the tetrahedral layers to differing extents and the space group *Imma* is used to describe the brownmillerite structure wherein the chain orientation within the tetrahedral layers is disordered.

A recent study by Muñoz *et al*. [14] reported that the correct space group for $Sr_2Co_2O_5$ was *Ima2* (standard setting of *I2mb*, the **bac** setting which has been used in previous discussions to facilitate comparison with other space groups discussed) that being a fully ordered brownmillerite wherein all tetrahedral chains possessed identical orientation. Refinements of NPD data were carried out using both the *Ima2* (non-centrosymetric, structure is comprised entirely of L- or R-chains exclusively) and the *Pnma* (centrosymmetric, layers of all L-chains alternating with layers of all R-chains) space groups. Due to the reflections for $h + k + l = 2n + 1$ (which is forbidden for *Ima2*) being too weak to be observed, the fits and statistics for both refinements were good hence both were deemed to have equal merit based on these data. The assignment of the *Ima2* space group for $Sr_2Co_2O_5$ was based on *ab initio* calculations that suggested that *Ima2* was the more stable crystal structure. These calculations were based upon density field theory (DFT) calculations, which make predictions on the energy of the structure based on nuclear charge and intersite e^- repulsions using parameters obtained from refinements of NPD data. It was shown that a structure based on the *Ima2* space group was more stable than a *Pnma*-based structure by 34 meV per Co. This is the equivalent of 3.28 kJ mol^{-1} per Co which equates to 6.56 kJ mol^{-1} per unit cell.

Muñoz *et al*. reported that for their sample the ZFC and FC magnetisation data diverges below ~200K and proposed it was not due to any change in the magnetic structure of brownmillerite but as a result of the presence of small ferromagnetic clusters. Several forms of $SrCoO_{3-x}$ are known in addition to the brownmillerite phase [19-21] and ferromagnetic behaviour has been widely reported in cubic $SrCoO_{3-x}$ phases [22-24]. Although not considered in the paper, it is feasible that this noticeable divergence and the observation of hysteresis behaviour upon performing field sweep measurements may have been due to the sample studied containing some small quantity of $SrCoO_{3-x}$. Quenching is necessary in order to stabilise the brownmillerite phase at room temperature and it is sometimes difficult to prepare a homogenous phase in this manner, particularly where the rate of cooling can affect the oxygen content or even the structure of the product. As the rhombohedral phase $Sr_6Co_5O_{15}$ produced upon slow cooling has been reported to be antiferromagnetic [25] it is unlikely that this phase is the cause of the anomalous magnetic data.

From the calculations presented by Muñoz *et al*. [14] the case for *Ima2* being the more stable structure is strong and there is no reason to disagree with this conclusion from the evidence presented. However, the assignment of a space group is ultimately dependent on the length scale of the measurement and the size of the domain of the structure. For example, Muñoz *et al*. [14] did not consider the *Pcmb* space group, which is unsurprising for, as has been discussed in this chapter, the intrachain ordering is only visible on the small length scale associated with transmission electron microscopy. However, the paper did not endeavour to refine the structure in *Imma*. Realistically, neither *Ima2* (or *Ibm2*), *Pnma*, or *Pcmb* mean anything on the scale applicable to X-ray and neutron powder diffraction, as these techniques are largely insensitive to the existence of small domains exhibiting local

order and due to defects in breaking up such ordered regions, the bulk structure of the material will not display long-range order. Muñoz *et al*. [14] did not report a refinement of their NPD data using the *Imma* space group, or any *ab initio* calculations allowing for a disordered structure, although such a study may well present interesting results.

As the electron diffraction presented in Section 3.3.3 showed no evidence for *Ima2* (or *I2mb* for consistency with the axes used in Section 3.1) in the sample used in this chapter, refinements of XRD and NPD data were only carried out using the *Pcmb* and *Imma* space groups. This chapter found that electron diffraction provided evidence that $Sr_2Co_2O_5$ contained interlayer chain ordering thus making a strong case for the assignment of the *Pcmb* space group. However, X-ray and neutron powder diffraction data were unable to confirm that this assignment was representative of the material as a whole. Therefore, the space group *Imma*, which allows for disorder of the chain orientations in the tetrahedral layers was deemed to be the most accurate representation of the structure of $Sr_2Co_2O_5$.

It is interesting to note that utilising the larger unit cell consistent with the assignment of the *Pcmb* space group resulted in unreliable Co-O bond lengths, which could have been interpreted as indicative of charge segregation over the Co sites. This stresses that great care must be taken in interpreting the rationalisation of M-O bonds and hence the designation of charge ordering in this structure. In particular, careful consideration is required in order to assign the correct space group for the structural technique used.

3.5 References

1. H. Watanabe and T. Takeda (1970) *Ferrites: Proceedings of the International Conferenc*e 588.
2. J. C. Grenier, S. Ghodbane, G. Demazeau, M. Pouchard and P. Hagenmuller (1979) *Materials Research Bulletin* **14** 831.
3. J. Rodriguez, J. M. Gonzalez-Calbet, J. C. Grenier, J. Pannetier and M. Anne (1987) *Solid State Communications* **62** 4 231.
4. W. T. A. Harrison, S. L. Hegwood and A. J. Jacobson (1995) *Chemical Communications* 1953.
5. V. Pardo, V. M. Botta, D. Baldomir, J. Rivas, A. Piñeiro, C. de la Calle, J. A. Alonso and J. E. Arias (2008) *Physica B* **403** 1636.
6. J. C. Grenier, L. Fournès, M. Pouchard and P. Hagenmuller (1986) *Materials Research Bulletin* **21** 441.
7. T. Takeda, Y. Yamaguchi and H. Watanabe (1972) *Journal of the Physical Society of Japan* **33** 4 970.
8. T. Krekels, O. Milat, G. van Tendeloo, S. Amelinckx, T. G. N. Babu, A. J. Wright and C. Greaves (1993) *Journal of Solid State Chemistry* **105** 313.
9. S. Lambert, H. Leligny, D. Grebille, D. Pelloquin and B. Raveau (2002) *Chemistry of Materials* **14** 1818.
10. A. J. Wright, H. M. Palmer, P. A. Anderson and C. Greaves (2001) *Journal of Materials Chemistry* **11** 1324.
11. A. M. Abakumov, M. G. Rosova, B. Ph. Pavlyuk, M. V. Lobanov, E. V. Antipov, O. I. Lebedev, G. van Tendeloo, O. L. Ignatchik, E. A. Ovtchenkov, Yu. A. Koksharov and A. N. Vasil'ev (2001) *Journal of Solid State Chemistry* **160** 353.
12. A. M. Abakumov, A. M. Alekseeva, M. G. Rosova, E. V. Antipov, O. I. Lebedev and G. van Tendeloo (2003) *Journal of Solid State Chemistry* **174** 319.
13. A. M. Abakumov, A. S. Kalyuzhnaya, M. G. Rosova, E. V. Antipov, J. Hadermann and G. van Tendeloo (2005) *Solid State Sciences* **7** 801.
14. A Muñoz, C. de la Calle, J. A. Alonso, P. M. Botta, V. Pardo, D. Baldomir and J. Rivas (2008) *Physical Review B* **78** 054404.

15. A. C. Larson and R. B. Von Dreele (1990) *Generalised Structure Analysis System,* Los Alamos National Laboratory.
16. D. Altermatt and I. D. Brown (1985) *Acta Crystallographica* **B41** 240.
17. I. D. Brown (1989) *Journal of Solid State Chemistry* **82** 122.
18. N. E. Brese and M. O'Keeffe (1991) *Acta Crystallographica* **B47** 192.
19. A. Nakatsuka, A. Yoshiasa, N. Nakayama, T. Mizota and H. Takei (2004) *Acta Crystallographica* **C60** i59.
20. R. Le Toquin, W. Paulus, A. Cousson, C. Prestipino and C. Lamberti (2006) *Journal of the American Chemical Society* **128** 13161.
21. L. Karvonen, H. Yamauchi and M. Karppinen (2008) *Chemistry of Materials* **20** 7143.
22. H. Taguchi, M. Shimada and M. Koizumi (1979) *Journal of Solid State Chemistry* **29** 221.
23. H. Watanabe, Y. Yamaguchi, H. Oda and H. Takei (1986) *Journal of Magnetism and Magnetic Materials* **15-18** 521.
24. P. Bezdicka, A. Wattiaux, J. C. Grenier, M. Pouchard and P. Hagenmuller (1993) *Zeitschrift für Anorgische und Allgemeine Chemie* **619** 7.
25. J. Sun, G. Li, Z. Li, L. You and J. Lin (2006) *Inorganic Chemistry* **45** 8394.

Chapter Four

Fluorination Study of the Brownmillerite Materials $Sr_2Fe_2O_5$, Sr_2CoFeO_5 and $Sr_2Co_2O_5$

4.1 Introduction

4.1.1 Fluorination of $LaACuGaO_5$ (A = Ca, Sr)

Ordered vacancy perovskite-related materials such as brownmillerites are good candidates for anion insertion studies. The first brownmillerite system shown to be amenable to low-temperature fluorine insertion reactions was $LaACuGaO_5$ (A = Ca, Sr) [1]. $LaSrCuGaO_5$ [2] and $LaCaCuGaO_5$ [3] both adopt an orthorhombic unit cell with space group *Ima2*, with lattice parameters approximately related to that of the basic perovskite subcell, a_p, by $a \approx \sqrt{2}a_p$, $b \approx 4a_p$ and $c \approx \sqrt{2}a_p$ when transposed for consistency with *I2mb* (the **cab** setting of *Ima2* as discussed in Section 3.1). Both phases exhibit a brownmillerite structure formed by alternating layers of corner-sharing CuO_6 octahedra and GaO_4 tetrahedra stacked along the *b* axis, with the La and Ca/Sr cations statistically occupying the 10-fold cavities within the structure. The CuO_2 layers within the $LaACuGaO_5$ (A = Ca, Sr) structure are buckled due to the ordering of oxygen vacancies in the GaO□ layer. This causes the rotation of the CuO_6

octahedra about the [010] direction of the perovskite subcell and hence a significant distortion of the equatorial Cu coordination [3].

Upon fluorination with XeF_2, both $LaCaCuGaO_5$ and $LaSrCuGaO_5$ were shown to form low fluorine-content phases that retained an orthorhombic unit cell with space group *Ima2* but for the purposes of the discussion in this chapter is transposed to *I2mb* for facile comparison with related space groups used to describe brownmillerite structures, such as *Imma*. A comparison of the $(a - c)/(a + c)$ ratio of the starting materials and their respective fluorinated phases showed a decrease in this measure of orthorhombicity with increasing fluorine content. For $LaSrCuGaO_5$, it was shown that not only did the degree of orthorhombicity decrease with increasing fluorine content, but also that with sufficient fluorine insertion this phase undergoes a transformation to a tetragonal structure with cell parameters $a \approx a_p$ and $c \approx 2a_p$. Studies of this tetragonal phase using HREM were able to assign the space group *P4/mmm* [1].

Upon fluorination of the strontium phase $LaSrCuGaO_5$, F anions are inserted into the vacant anion positions in the GaO□ layers and simultaneously F anions replace some O anions in this layer in a ratio of $2F^-$ to one replaced O^{2-}, resulting in a Ga coordination number > 4. This mechanism is accompanied by a random occupation of the anion positions in the Ga layers by O, F and anion vacancies (□) leading to tetragonal symmetry. Electron microscopy shows different superstructures due to local ordering of anions and vacancies.

Formation of the tetragonal perovskite structure for the fluorinated phase requires an increase in the coordination number of the A cation from 10 to 12. Although the larger Sr^{2+} cation ($r_{Sr(II)} = 1.44$ Å) readily forms the tetragonal structure, in this situation it is not feasible for the smaller Ca^{2+} cation ($r_{Ca(II)} = 1.35$ Å) to

increase its coordination number to 12 and thus the fluorination of $LaCaCuGaO_5$ is unable to produce a tetragonal phase [1].

4.1.2 Fluorination of Sr_2MnGaO_5

Sr_2MnGaO_5 is a brownmillerite consisting of alternating MnO_2 and $GaO\square$ layers [4, 5]. Initially, Abakumov *et al.* [5] had proposed the fully ordered (all chain orientations identical) *I2mb* model for the structure of Sr_2MnGaO_5 whilst Wright *et al.* [6] had characterised Sr_2MnGaO_5 using the disordered space group *Imma*. Both studies deduced that Sr_2MnGaO_5 is an antiferromagnet with magnetic moments aligned normal to the MnO_2 planes, with some degree of canting due to the tilting of the MnO_6 octahedra. Examination of this material using electron diffraction and HREM revealed that within a given layer the infinite chains of vertex-linked GaO_4 tetrahedra alternated between L- and R-chain orientation [7]. This intralayer ordering results in a superstructure whereby one of the shorter orthorhombic axes is doubled, consistent with the assignment of the space group *Pcmb*, as discussed in more detail in Section 3.1.

The space groups *Pnma* (interlayer alternation of L- and R-chains), *I2mb* (all chains possessing the same orientation) and *Imma* (complete long-range disorder of chain orientation) all are energetically similar as the transformation or L- to R- chains and *vice versa* does not significantly alter the coordination environment of the Ga cations nor do the interatomic distances alter significantly therefore the Madelung energy of all 3 models of chain ordering are of very similar values. Hence, although it has subsequently been shown that there is some degree of intralayer ordering of chain orientation, the use of the *Imma* space group, which allows full disorder of the chain orientation, is adequate for the purposes of this discussion.

Abakumov *et al.* [5] demonstrated that Sr_2MnGaO_5 is amenable to oxygen insertion to form $Sr_2MnGaO_{5+\delta}$ with the increase in δ accompanied by a gradual decrease of orthorhombic distortion. This is shown by the observed symmetry change from *Imma* ($a \approx c \approx \sqrt{2}a_p$, $b \approx 4a_p$) for $0.03 \leq \delta \leq 0.13$, to *Bmmm* ($a \approx c \approx \sqrt{2}a_p$, $b \approx 2a_p$) for $0.41 \leq \delta \leq 0.46$, and finally to tetragonal *P4/nmm* ($a \approx a_p$, $c \approx 2a_p$) for $\delta = 0.505$. For oxygen contents between $\delta = 0.13$ and $\delta = 0.41$ a mixture of oxidised and reduced phases was noted to have formed. The insertion of oxygen anions into the GaO□ layers to form $GaO_{1+\delta}$ was shown to alter the magnetic structure from an antiferromagnetic G-type structure to the antiferromagnetic C-type structure whereby the Mn magnetic moments are aligned antiferromagnetically in the MnO_2 planes but these planes are in turn ferromagnetically coupled [8].

For $Sr_2MnGaO_{5+\delta}$, XRD and ED data suggested that increasing the oxygen content causes the Ga coordination number to increase from 4 to 5, rather than from 4 to 6 (*i.e.* forming thicker octahedral layers/extra octahedral layers in the brownmillerite OTOTOT stacking sequence, for example OOOTOOOTOOOT). These XRD and ED observations were supported by BVS calculations and it was shown that oxygen atoms form a distorted trigonal bipyramid about the Ga cations [8].

It has also been shown that the fluorination of Sr_2MnGaO_5 produces a tetragonal phase where $a \approx a_p$ and $c \approx 2a_p$. The structure was found to consist of alternating layers of MnO_2, SrO and $GaO_{0.78}F_{1.22}$ ($GaO_{1-x}F_{1+x}$) with the Ga atoms situated in slightly elongated octahedra, with the MnO_6 octahedra apical compressed (a reversal of the apical elongation seen in the starting material Sr_2MnGaO_5 resulting from Jahn-Teller distortions) [8, 9]. The atomic coordinates were transformed from perovskite structure and full occupancy assigned to all anion positions giving the general composition $Sr_2MnGa(O,F)_6$ with the structure being described by the space

group *P4/nmm*. Lattice parameters were reported as $a = 3.85559(2)$ Å and $c = 7.78289(6)$ Å [9].

The main structural difference between O-doped $Sr_2MnGaO_{5.5}$ and the fluorinated phase $Sr_2MnGaO_{4.78}F_{1.22}$ is that the latter structure has full occupancy of all the anion positions with the formation of an octahedral environment around the Ga atoms.

4.1.3 $Sr_2Fe_2O_5$ and Fluorination of $SrFeO_{3-\delta}$ to form $SrFeO_2F$

$Sr_2Fe_2O_5$ crystallises with a brownmillerite structure, described by Greaves *et al.* [10] using the space group *Icmm* (equivalent to *Imma* as previously discussed in Section 3.1) to account for disorder in the displacements of the Fe cations in the FeO□ layers. The lattice parameters obtained from the least squares analysis of NPD data were $a = 5.503(7)$ Å, $b = 15.582(2)$ Å and $c = 5.6727(7)$ Å, transposed for consistency with *Imma*.

Gallagher *et al.* [11] proposed that $Sr_2Fe_2O_5$ was isostructural with brownmillerite $Ca_2Fe_2O_5$, based on the Mössbauer spectra showing the presence of equivalent amounts of iron occupying both octahedrally and tetrahedrally coordinated sites. The hyperfine splitting on these spectra also indicated that $Sr_2Fe_2O_5$ displayed antiferromagnetic ordering in the temperature range 4–600K, thus deduced the Néel temperature must be in excess of 600K. However, a study of single crystal XRD data [12] found that the symmetry of $Sr_2Fe_2O_5$ was best described using the space group *Ibm2* (the **bac** setting of *Ima2*) whereby all the tetrahedral chains possess the same orientation.

Takeda *et al.* [13] reported $Sr_2Fe_2O_5$ is an antiferromagnet with $T_N \approx 700$K, exhibiting a G-type magnetic structure similar to that observed for $Ca_2Fe_2O_5$ [14, 15]

with Fe^{3+} spin directions aligned antiferromagnetically along the *a* axis (for the *Imma* space group, or the *c* axis if using *Icmm*) with the refined neutron magnetic moment $\mu = 4.5(3)\ \mu_B$ [13]. In their NPD study of polycrystalline $Sr_2Fe_2O_5$ at different temperatures, Schmidt and Campbell [16] reported the lattice parameters $a = 5.5265(3)$ Å, $b = 15.5823(8)$ Å and $c = 5.6685(4)$ Å from the refinement of room temperature NPD data using the space group *Ibm2* (transposed for consistency with *I2mb*). The G-type magnetic structure as proposed by Takeda *et al.* [13] was used as a model for the magnetic reflections, with both octahedral and tetrahedral Fe^{3+} moments constrained along the *a*-axis.

Interestingly, whilst $Sr_2Fe_2O_5$ is an antiferromagnetic insulator, the Fe^{4+} phase $SrFeO_3$ is a metallic antiferromagnet below 134 K with a helical spin magnetic structure [17]. At room temperature, $SrFeO_3$ is a simple cubic perovskite best described using the primitive space group *Pm-3m* with the lattice parameter from the refinement of NPD data $a = 3.851(1)$ Å [18]. However, it was recently shown in an electron diffraction study by D'Hondt *et al.* [19] that similarly to Sr_2MnGaO_5, $Sr_2Fe_2O_5$ also exhibits L-R-L-R- ordering of tetrahedral chains within any given layer, necessitating a doubling of the *c*-axis. These observations do not support the assignment of the *Ibm2* space group for $Sr_2Fe_2O_5$, as relatively large local areas of other ordered stacking sequences, for example *Pcmb*, are observed using high resolution electron microscopy. However, it is acknowledged that when using a bulk technique for structural characterisation such as NPD, the use of the disordered *Imma* structure is correct, as the stacking sequences observed *via* electron microscopy do not provide long-range order.

In their study of the fluorinated materials $Sr_3Fe_2O_6F_{0.87}$, Sr_2FeO_3F and $Ba_2InFeO_5F_{0.68}$, Case *et al.* [20] also briefly reported that the fluorination of $Sr_2Fe_2O_5$

resulted in the formation of 2 cubic perovskite phases formed in an approximately 1:1 ratio with the respective lattice parameters a = 3.95 Å and a = 3.87 Å. The compositions of the phases were not known nor were any reasons identified for the formation of a 1:1 mixture of these 2 phases upon fluorination of $Sr_2Fe_2O_5$.

The cubic phase $SrFeO_2F$ was prepared by Berry *et al.* [21] *via* the low temperature fluorination of the oxygen-deficient perovskite-related material $SrFeO_{3-\delta}$. The starting material $SrFeO_{3-\delta}$ used in this study was shown to display a slightly orthorhombic unit cell with the following lattice parameters: a = 5.474(1) Å, b = 5.469(1) Å and c = 7.706(1) Å, this was attributed to the degree of oxygen deficiency in the sample. Fluorination of this phase produced a material with the cubic unit cell parameter a = 3.956(1) Å. Upon comparing the primitive perovskite subcells for each sample, fluorination leads to a significant increase in cell parameter. The larger unit cell was attributed to the partial replacement of O^{2-} anions by F^- anions and hence a reduction of the Fe oxidation state and lengthening of the bond distances.

The study by Berry *et al.* [21] found that the novel Fe^{3+} perovskite $SrFeO_2F$ can be formed *via* the fluorination of $SrFeO_{3-\delta}$ (a mixed Fe^{3+}/Fe^{4+} perovskite). This raises the question of whether the low-temperature fluorination of $Sr_2Fe_2O_5$ (as first attempted by Case *et al.* [20]) may be used to form a cubic perovskite $Sr_2Fe_2O_5F$ phase with an average oxidation state of $Fe^{3.5+}$ as opposed to the purely Fe^{3+}-containing phase $SrFeO_2F$. A further study of the fluorination of $Sr_2Fe_2O_5$ has therefore been conducted.

4.1.4 Brownmillerite-Structured $Sr_2Co_2O_5$

As discussed in some detail in Chapter 3, $Sr_2Co_2O_5$ has been shown in the bulk phase to display similar disorder to $Sr_2Fe_2O_5$ and is best described using the

space group *Imma*. The lattice parameters obtained from refinement of neutron powder diffraction data collected at 4K were $a = 5.4639(3)$ Å, $b = 15.6486(8)$ Å and $c = 5.5667(3)$ Å. Many $SrCoO_{3-x}$ cubic perovskite phases exist and are commonly prepared *via* electrochemical oxidation [22]. Almost stoichiometric $SrCoO_{3-x}$ has been synthesised using high oxygen pressures [23] and electrochemical oxidation [24] and this phase has been shown to be ferromagnetic. However, it appears that the preparation of the pure Co^{4+}-containing phase $SrCoO_3$ is not as facile as preparation of fully stoichiometric $SrFeO_3$.

4.1.5 The Mixed Co/Fe Brownmillerite Sr_2CoFeO_5

Due to the close similarities of the nuclear and magnetic structures of $Sr_2Fe_2O_5$ and $Sr_2Co_2O_5$, it was proposed by Battle *et al.* [25] that the preparation of the mixed transition metal phase Sr_2CoFeO_5 should be relatively facile and likely to also form a brownmillerite structure. Indeed, the crystal and magnetic structure reported by Battle *et al.* [26] confirmed that Sr_2CoFeO_5 possessed a brownmillerite structure with the refined lattice parameters $a = 5.5017(2)$ Å, $b = 15.5615(5)$ Å and $c = 5.6243(2)$ Å, as transposed for consistency with the space group *Imma*. It was determined that samples quenched from 1200ºC contained Fe and Co cations randomly distributed over the octahedral and tetrahedral sites, whereas annealing an aliquot under flowing argon at 800ºC induced a partial ordering whereby Co^{3+} showed a slight preference (57:43) for the tetrahedral sites. The structural and magnetic characterisation from NPD data was carried out on the partially ordered phase and the neutron magnetic moments were reported as $\mu = 3.2(1)\ \mu_B$ and $\mu = 2.9(1)\ \mu_B$ for the octahedral and tetrahedral sites respectively. It was noted that these values are lower than the expected moment for high spin $3d^5$ Fe^{3+} ($\approx 4.4\ \mu_B$) or $3d^6$ Co^{3+} ($> 4\ \mu_B$) cations, although the percentage

error in the refined moments was ≈ 15% due to uncertainty in the form factor used and the relatively small proportion of reflections in the diffraction pattern arising from magnetic scattering. For $Sr_2Fe_2O_5$ and $Sr_2Co_2O_5$, lower than expected neutron magnetic moments were previously reported ($\mu = 4.0(1)\ \mu_B$ [10] and $\mu = 3.3(5)\ \mu_B$ [27] respectively, separate moments for octahedral and tetrahedral cations were not refined). As this behaviour is not observed in the ordered phase $Ca_2Fe_2O_5$ where the spins are aligned along the *a*-axis in the space group *Pnma* [15] with the observed neutron magnetic moment $\mu = 4.5(2)\ \mu_B$ [14], it was proposed that such phenomena were due to the moments in the disordered phases having moments along both *a* and *c* with only the components aligned in the *a* direction (if using the standard *Imma* space group) showing any long range order [26].

It is interesting to note that for both $Sr_2Fe_2O_5$ and Sr_2CoFeO_5, the use of the disordered space group *Imma* (with half-occupied 8i sites) has been necessary to describe the bulk phase, but it has been acknowledged that there is most likely some degree of additional order over smaller length scales. These observations are similar to the findings of Chapter 3, where a higher degree of order was observed in $Sr_2Co_2O_5$ using electron microscopy techniques, but was shown not to be applicable on the length scale pertinent to neutron powder diffraction.

Thus $Sr_2Fe_2O_5$, $Sr_2Co_2O_5$ and Sr_2CoFeO_5 all possess brownmillerite structures that are best described using the *Imma* space group which allows disorder onto the half occupied 8i sites. All three phases exhibit strong antiferromagnetic coupling between nearest neighbour transition metal cations arising from a G-type antiferromagnetic structure whereby the magnetic moment are aligned along the short, *a*-axis.

This chapter examines whether it is possible to fill the oxygen vacancies in these materials with fluorine to produce cubic perovskite-type materials with mixed valency transition metal cations.

4.2 Experimental Procedure

All fluorinated brownmillerite samples synthesised during the course of this study were prepared *via* low-temperature solid-gas fluorine insertion reactions, as described in Section 2.1.2.

$Sr_2Co_2O_5$ was prepared in the same way as detailed in Chapter 3 (see Section 3.2). The optimum conditions for preparing fluorinated samples was found to be a 15 minute pulse of $10\%F_{2(g)}/90\%N_{2(g)}$ at 200ºC (as described in Section 2.1.2(a)) followed by grinding and annealing for 90 minutes in static $10\%F_{2(g)}/90\%N_{2(g)}$ at 220ºC (as described in Section 2.1.2(b)).

$Sr_2Fe_2O_5$ was prepared from stoichiometric amounts of dried $SrCO_3$ and Fe_2O_3, ground together and subjected to 2 separate heat treatments of 12 hours at 1300ºC under $N_{2(g)}$ with intermediate grinding, then an additional 12 hours at 800ºC under $N_{2(g)}$ with no grinding. All fluorinated samples produced were approximately 1:1 mixtures of 2 cubic perovskite phases with lattice parameter $a \approx$ 3.87 Å and $a \approx$ 3.95 Å. Varying the reaction conditions had no effect on the ratio of the product phases. The optimum conditions for sample crystallinity and minimising SrF_2 in the sample were 2 hours at 250ºC under static $10\%F_{2(g)}/90\%N_{2(g)}$ with intermediate grinding of the sample, followed by another 2 hours at 265ºC under static $10\%F_{2(g)}/90\%N_{2(g)}$.

Sr_2CoFeO_5 was prepared from stoichiometric amounts of dried $SrCO_3$, Co_3O_4 and Fe_2O_3 ground together and pressed into a pellet. This was then subjected to 2 heat

treatments of 12 hours at 1200ºC each followed by immediately quenching in liquid nitrogen. The optimum conditions for fluorination of this phase were found to be heat treatments of 2 hours at 220ºC and 230ºC followed by an additional 2 heat treatments of 2 hours at 250ºC, all carried out under static $10\%F_{2(g)}/90\%N_{2(g)}$ (as described in Section 2.1.2(b)) with intermediate grinding.

Additional information regarding the fluorine-insertion reactions discussed in this chapter may be found in *Appendix 4.1*, *Appendix 4.2* and *Appendix 4.3* for the fluorination of $Sr_2Fe_2O_5$, Sr_2CoFeO_5 and $Sr_2Co_2O_5$ respectively.

4.3 Results and Discussion

4.3.1 Characterisation of Fluorinated $Sr_2Fe_2O_5$

4.3.1.1 2-Phase Rietveld Profile Refinement Based on XRD Data

Examination of the fluorinated material using XRD confirmed the findings of Case *et al.* [20], that two cubic perovskite phases are formed with the approximate lattice parameters $a = 3.87$ Å and $a = 3.95$ Å (2dp), accompanied by a small SrF_2 impurity. The experimental conditions (temperature and reaction time) were varied to investigate whether the yield of either cubic phase could be improved. However, this ratio of these 2 cubic perovskite phases remained approximately 1:1 in the range where fluorination was successful, and harsher conditions caused larger amounts of SrF_2 to be formed during the reaction.

Comparing the lattice parameters of these cubic perovskite phases with literature, phase 1 ($a = 3.95$ Å) was attributed to $SrFeO_2F$ [21] and phase 2 ($a = 3.87$ Å) to $SrFeO_{3-\delta}$ (as the lattice parameter of $SrFeO_3$ was reported by Takeda *et al.* as $a = 3.85$ Å [17], the slightly larger unit cell $a = 3.87$ Å is consistent with a slightly reduced phase). As the fluorinated material also contained a small amount of SrF_2, the

GSAS suite of programs [28] was used to carry out a 3-phase Rietveld profile refinement on XRD data. For least-squares refinement, the primitive cubic space group *Pm-3m* was used for $SrFeO_2F$ and $SrFeO_{3-\delta}$, whilst the *Fm-3m* space group was used for SrF_2. For simplicity, the thermal parameters were constrained to U_{iso} = 1.00 x 100 $Å^2$ whilst the phase fraction was permitted to vary. The least-squares refinement converged with the following statistics: $\chi^2 = 2.147$, $R_{wp} = 2.97\%$ and $R_p = 2.26\%$, and visually provided a good fit between observed and calculated values. The refined lattice parameters for $SrFeO_2F$ and $SrFeO_{3-\delta}$ were $a = 3.9481(3)$ Å and $a = 3.8775(3)$ Å respectively, with the slight expansion in lattice parameter for $SrFeO_{3-\delta}$ *cf.* $SrFeO_3$ in accordance with this phase containing mixed Fe^{3+}/Fe^{4+}. The refined phase fractions $SrFeO_2F$:$SrFeO_{3-\delta}$:SrF_2 were 1:1.0775:0.0431, approximately equating to ≈ 2% SrF_2 impurity in the sample.

These data show that the formation of 2 distinct cubic perovskite phases with similar lattice parameters as reported by Case *et al.* [20] are reproducible and hence there must be an explanation for the fluorination of $Sr_2Fe_2O_5$ resulting in an approximately 1:1 mixture of these phases. This phenomenon was further explored in Section 4.3.1.2 using Madelung energy calculations.

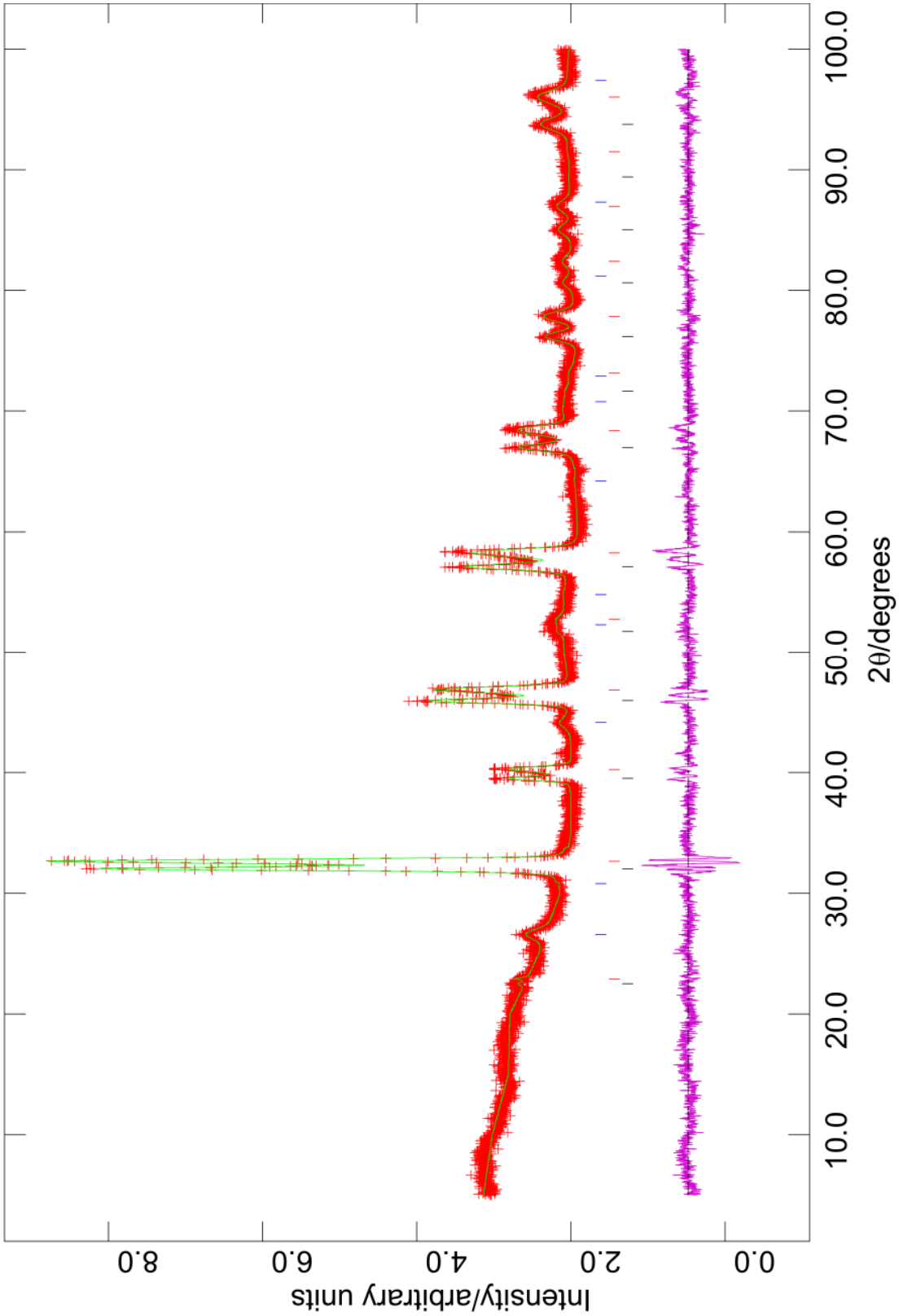

Figure 4.1 Observed (red +), calculated (green) and difference (pink) profiles of fluorinated $Sr_2Fe_2O_5$, as generated by the 3 phase Rietveld profile refinement of XRD data where phase 1 = $SrFeO_2F$ (black vertical lines), phase 2 = $SrFeO_{3-\delta}$ (red vertical lines) and phase 3 = SrF_2 (blue vertical lines).

4.3.1.2 Madelung Energy Calculations

Using the lattice parameters obtained from the Rietveld refinement of XRD data, the Madelung energies were calculated using the Ewald method [29] for two possible models of fluorine insertion into $Sr_2Fe_2O_5$. Model A assumes that a 1:1 stoichiometric mixture of the Fe^{3+}-containing $SrFeO_2F$ (a = 3.9481(3) Å) and the Fe^{4+}-containing $SrFeO_3$ (a = 3.8775(3) Å) is formed upon fluorination ($SrFeO_3$ was used as opposed to $SrFeO_{3-\delta}$ purely for ease of calculation), whereas model B uses 2 moles of a hypothetical intermediate using a mean unit cell parameter a = 3.9128 Å. The Madelung energy for model A was calculated as –29111.95 kJ mol^{-1} whilst model B yielded a Madelung energy of -28806.42 kJ mol^{-1}. Therefore these calculations support the hypothesis that the formation of a 1:1 mixture of $SrFeO_2F$ and $SrFeO_3$ is more energetically favourable than complete formation of an intermediate fluorinated product. It is likely that the driver behind this phase separation into purely Fe^{3+}-containing $SrFeO_2F$ and Fe^{4+}-containing $SrFeO_{3-\delta}$ is the enhanced lattice energy for Fe^{4+} oxides.

4.3.2 Characterisation of Fluorinated Sr_2CoFeO_5

4.3.2.1 Rietveld Profile Refinement Based on XRD Data

Low-temperature fluorine insertion reactions of the mixed cobalt and iron brownmillerite Sr_2CoFeO_5 resulted in the formation of a single cubic perovskite phase ($a \approx$ 3.87 Å) accompanied by a small SrF_2 impurity. From the Madelung energy calculations for fluorine insertion into $Sr_2Fe_2O_5$ one might expect a similar phase separation whereby a 1:1 mixture of Co^{3+}-containing $SrCoO_2F$ and Fe^{4+}-containing $SrFeO_{3-\delta}$ is formed due to the Fe oxidising more readily. However, as the starting material Sr_2CoFeO_5 contains randomly distributed Co and Fe, the cation migration

required to produce such a phase separation is not energetically favourable. It was proposed that the structure of the observed fluorinated cubic phase was closely related to $SrFeO_2F$ with Co and Fe disordered over all the Fe (B) sites, and will henceforth be referred to as $SrCo_{0.5}Fe_{0.5}O_{2.5}F_{0.5}$.

The "GSAS" suite of programs [28] was used to carry out a Rietveld profile refinement of XRD data using the space group *Pm-3m*. The background was fitted using a linear interpolation function, simultaneously refining 51 parameters including parameters including diffractometer zero point, histogram scale factor, phase fraction, lattice parameter, isotropic temperature factors and profile parameters.

The refinement converged with $\chi^2 = 1.128$, $R_{wp} = 3.06\%$ and $R_p = 4.07\%$, and a good fit between the calculated profiles and the experimental data (*Figure 4.2*). The atom parameters are shown in *Table 4.1*, with the high values of U_{iso} most likely reflecting an incorrect estimation of absorption effects. The refined lattice parameter for the $SrCo_{0.5}Fe_{0.5}O_{2.5}F_{0.5}$ phase ($a = 3.872(2)$ Å) was close to that observed/literature value for $SrFeO_{3-\delta}$ ($a = 3.85$ Å [17]) and the literature value for $SrCoO_{3-x}$ ($a = 3.835(2)$ Å [24]). The phase fraction refined to a ratio of $SrCo_{0.5}Fe_{0.5}O_{2.5}F_{0.5}$:$SrF_2$ of $1:8.7031\times10^{-2}$, thus the sample contained approximately 8% SrF_2 impurity.

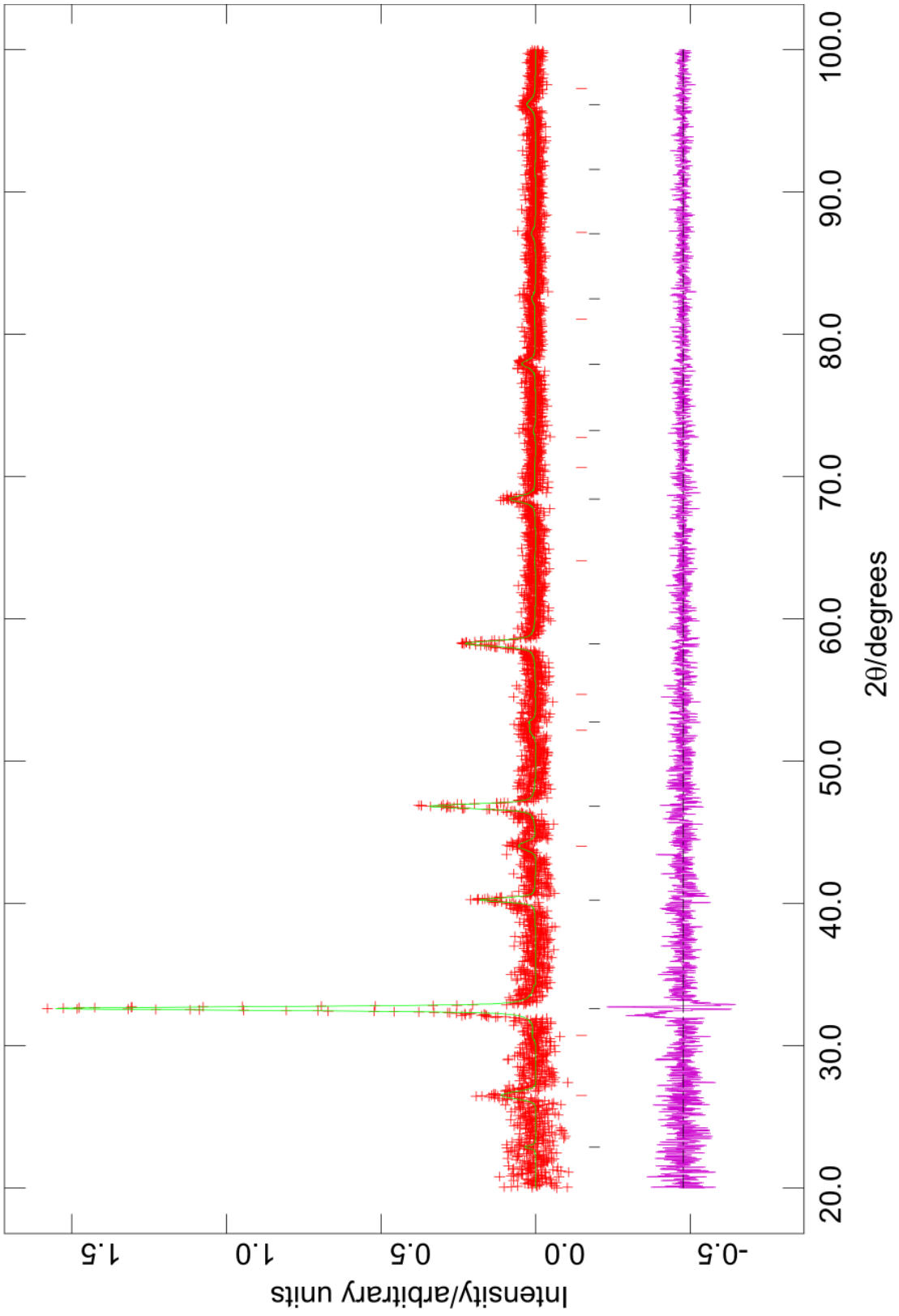

Figure 4.2 Observed (red +), calculated (green) and difference (pink) profiles of fluorinated Sr_2CoFeO_5, as generated by the 2 phase Rietveld profile refinement of XRD data where phase 1 = $SrCo_{0.5}Fe_{0.5}O_{2.5}F_{0.5}$ (black vertical lines) and phase 2 = SrF_2 (red vertical lines).

Table 4.1 Refined atom and lattice parameters of $SrCo_{0.5}Fe_{0.5}O_{2.5}F_{0.5}$ from refinement of XRD data in the space group *Pm-3m* (a = 3.872(2) Å).

Atom	Site Symmetry	*x*	*y*	*z*	U_{iso} x 100 (Å^2)
Sr	1a	0	0	0	4.3(3)
Co/Fe	1b	0.5	0.5	0.5	5.6(5)
O/F	3c	0	0.5	0.5	6.4(7)

4.3.2.2 Magnetic Measurements

Zero-field-cooled (ZFC) and field-cooled (FC) DC magnetisation data were collected on $SrCo_{0.5}Fe_{0.5}O_{2.5}F_{0.5}$ in an applied field of 0.3T from ≈ 2K to ≈ 300K. The fluorinated phase appears to show a canted antiferromagnetic transition below 150K (as the ZFC drop-off is consistent with ferromagnetic as opposed to spin glass-type behaviour) and the ZFC and FC data diverge below 75K.

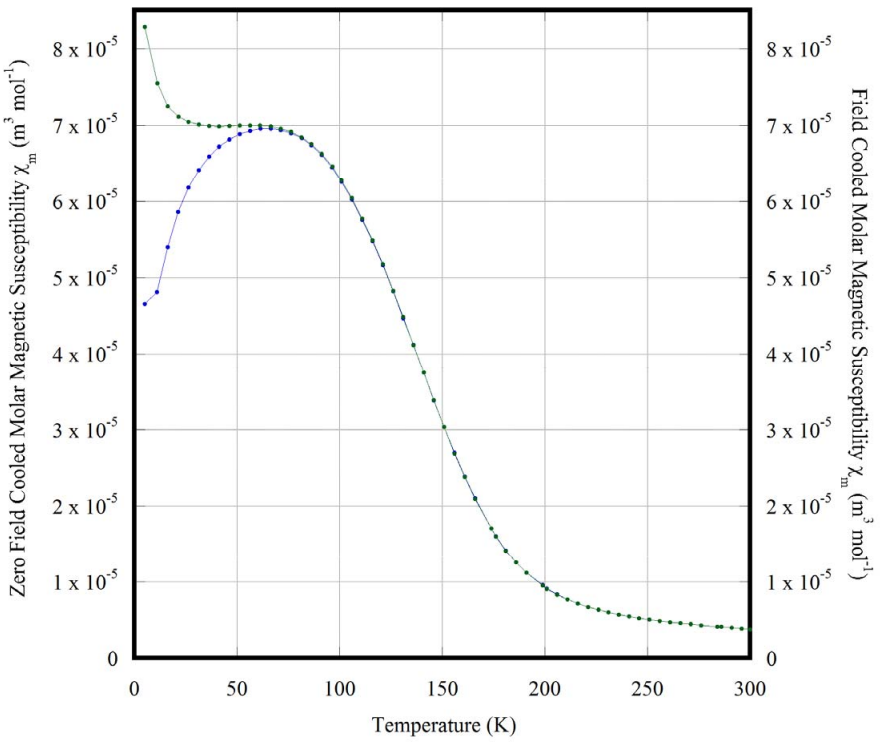

Figure 4.3 Plot of zero-field cooled (blue) and field-cooled (green) magnetic susceptibility (χ) against temperature.

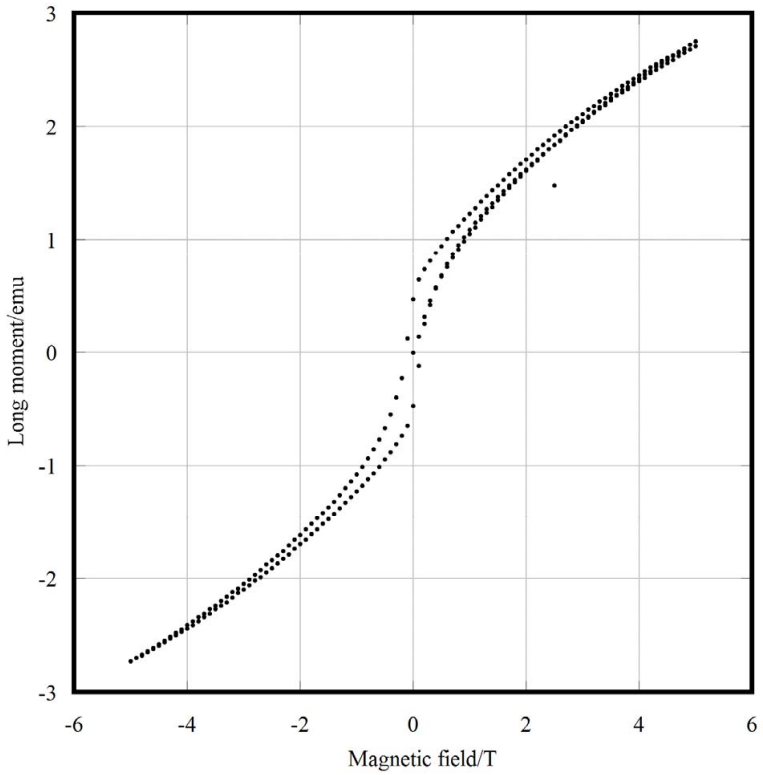

Figure 4.4 Plot of magnetic moment against applied field for field sweep measurements performed at 10K.

Field sweep measurements were collected between –0.5 and +0.5T at 10K, showing a small degree of hysteresis, which supports the existence of a ferromagnetic component to the magnetic structure of $SrCo_{0.5}Fe_{0.5}O_{2.5}F_{0.5}$ at 10K.

It is likely that this magnetic behaviour arises from complex exchange interactions between Co and Fe cations, but this is difficult to predict, as the oxidation states of these cations in this material are currently unknown. As Fe oxidises more readily than Co, it is probable that there is a greater proportion of Co^{3+} and Fe^{4+} in $SrCo_{0.5}Fe_{0.5}O_{2.5}F_{0.5}$, however techniques such as Mössbauer and X-ray absorption near edge structure (XANES) spectroscopy could be used in the future to elucidate the transition metal oxidation states present and thus aid understanding of the magnetic behaviour of $SrCo_{0.5}Fe_{0.5}O_{2.5}F_{0.5}$.

4.3.3 Characterisation of Fluorinated $Sr_2Co_2O_5$

4.3.3.1 Rietveld Profile Refinement Based on XRD Data

A Rietveld least-squares profile refinement of XRD data using the primitive cubic space group *Pm-3m* converged with $\chi^2 = 1.783$, $R_{wp} = 1.64$ and $R_p = 1.20$ with good visual agreement between observed and calculated profiles (*Figure 4.5*). The refined lattice parameter for the fluorinated phase $SrCoO_{2.5}F_{0.5}$, $a = 3.8574(3)$ Å, is similar to the literature value for $SrCoO_{3-x}$ ($a = 3.835(2)$ Å [24]). For refined atom parameters, please refer to *Appendix 4.4*.

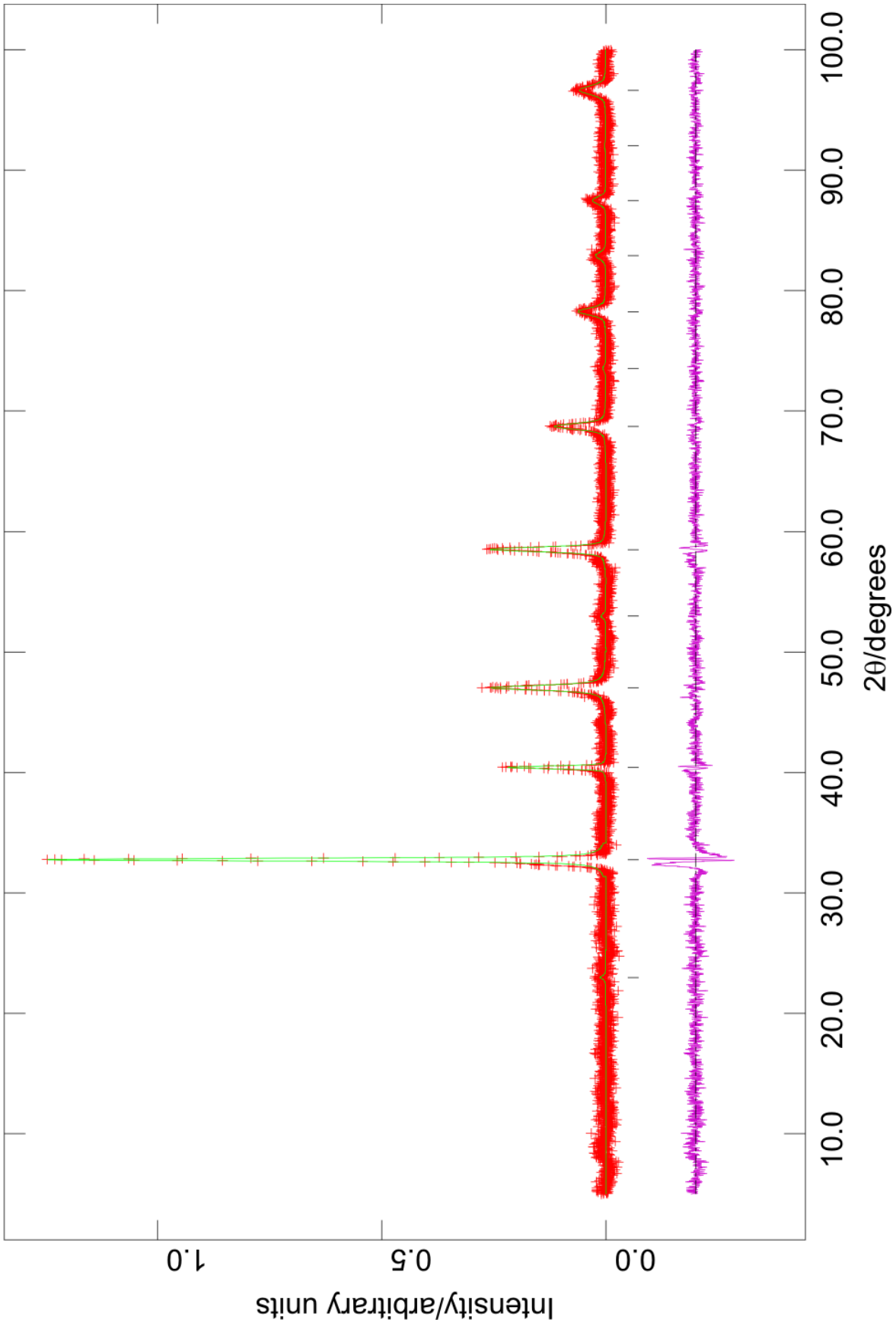

Figure 4.5 Observed (red +), calculated (green) and difference (pink) profiles of fluorinated $Sr_2Co_2O_5$, as generated by Rietveld profile refinement of XRD data with peak positions indicated by black vertical lines.

4.3.3.2 Nuclear and Magnetic Refinement Based on NPD Data

Neutron powder diffraction data were collected at 4K (to minimise temperature factor effects) in order to provide more complete structural and magnetic characterisation of $SrCoO_{2.5}F_{0.5}$. Unfortunately, although not apparent in XRD data, NPD data revealed that the sample also contained some unfluorinated starting material $Sr_2Co_2O_5$. As magnetic reflections due to both $SrCoO_{2.5}F_{0.5}$ and $Sr_2Co_2O_5$ were present, a 4-phase Rietveld profile refinement was necessary to fit the data.

The visual fit of the observed and calculated profiles were good, with reasonable refinement statistics ($\chi^2 = 2.230$, $R_{wp} = 2.78$ and $R_p = 2.09$) and a refined phase fraction of $SrCoO_{2.5}F_{0.5}$: $Sr_2Co_2O_5$ of 1:0.17049. This suggests that the presence of $Sr_2Co_2O_5$ is most likely due to fluorination readily occurring on the surface of grains, leaving small cores of unfluorinated material. For refined atom parameters, please refer to *Appendix 4.5*.

Although the sample of $SrCoO_{2.5}F_{0.5}$ contained a significant impurity of $Sr_2Co_2O_5$, it is clear that no phase segregation to Co^{3+}-containing $SrCoO_2F$ and Co^{4+}-containing $SrCoO_3$ occurs for the fluorination of $Sr_2Co_2O_5$, as might be expected from the observed fluorination of $Sr_2Fe_2O_5$. This may be because oxidation to Co^{4+} is rather difficult *cf.* oxidation to Fe^{4+} (hence fully oxidised $SrCoO_3$ may only be formed under high oxygen pressure or *via* electrochemical oxidation).

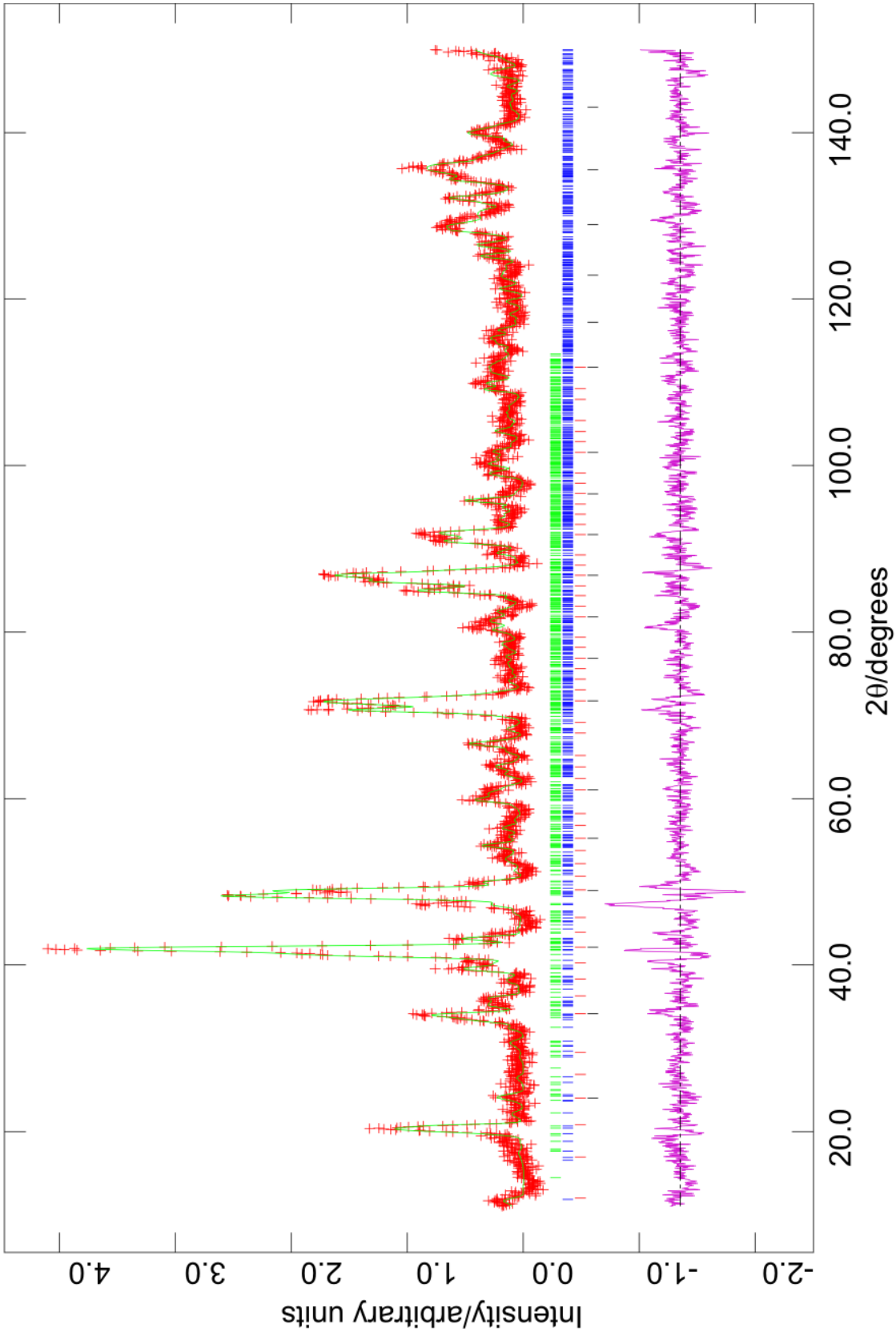

Figure 4.6 Observed (red +), calculated (green) and difference (pink) profiles of fluorinated $Sr_2Co_2O_5$, as generated by the Rietveld profile refinement of NPD data, where phase 1 = $SrCoO_{2.5}F_{0.5}$ (black vertical lines), phase 2 = $SrCoO_{2.5}F_{0.5}$ magnetic reflections (red vertical lines), phase 3 = $Sr_2Co_2O_5$ (blue vertical lines) and phase 4 = $Sr_2Co_2O_5$ magnetic reflections.

4.3.3.3 Magnetic Measurements

ZFC and FC DC magnetisation data were collected on fluorinated $Sr_2Co_2O_5$ in an applied field of 0.3T from ≈ 2K to ≈ 300K. The fluorinated phase appears to show a canted antiferromagnetic transition below 150K and the zero-field cooled and field-cooled data diverge below 50K. This is comparable to the behaviour of the mixed Co/Fe phase $Sr(Co,Fe)O_{2.5}F_{0.5}$ discussed in Section 4.3.2.2 and also rather similar to the transition observed by Muñoz *et al.* [30] for $Sr_2Co_2O_5$, albeit with a less pronounced divergence of ZFC data from FC data.

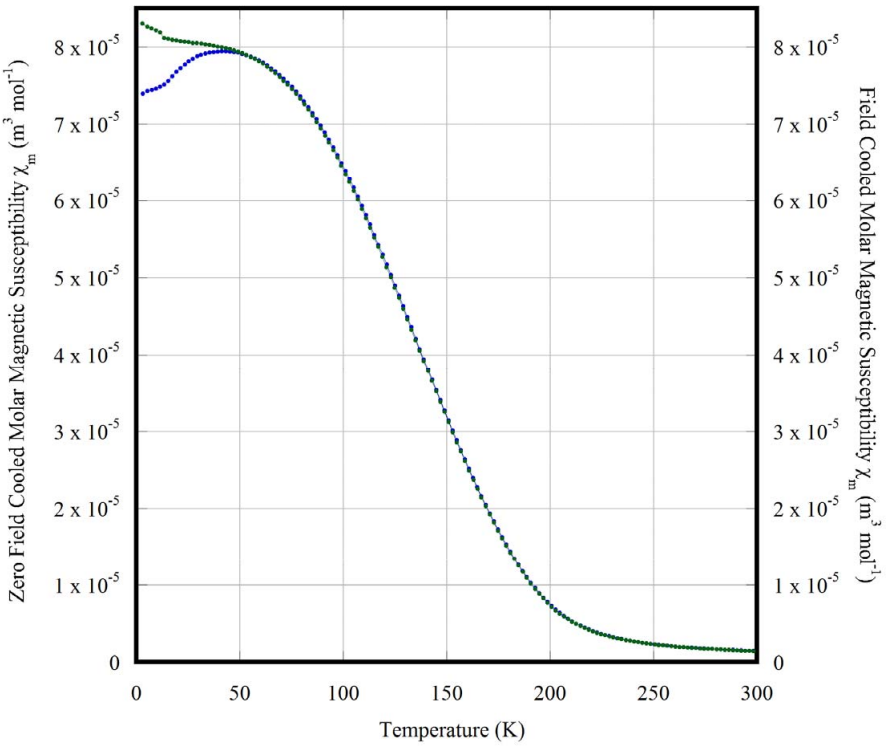

Figure 4.7 Plot of zero-field cooled (blue) and field-cooled (green) magnetic susceptibility (χ) against temperature.

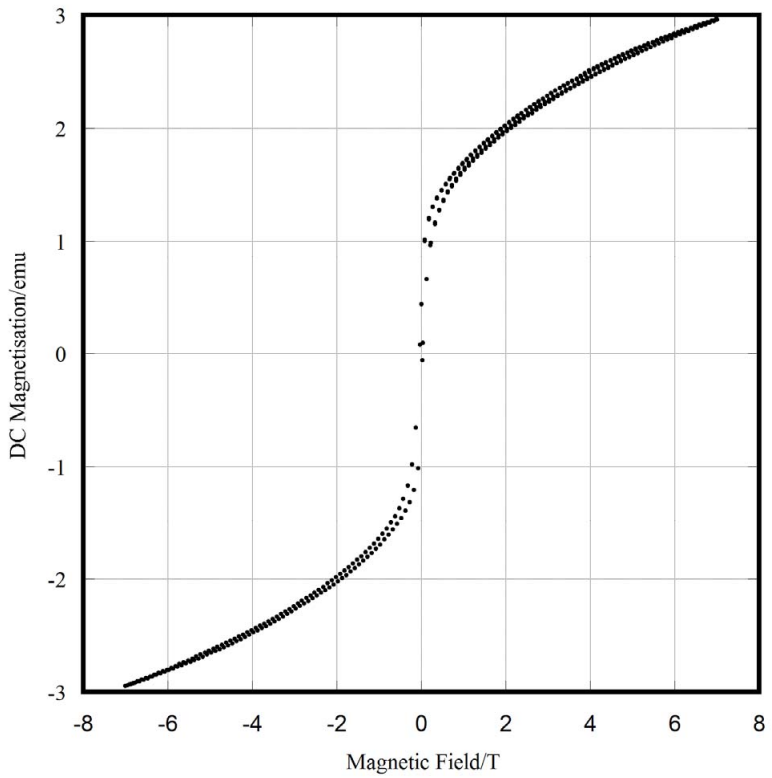

Figure 4.8 Plot of magnetic moment against applied field for field sweep measurements performed at 10K.

Field sweep measurements were collected between –0.7 and +0.7T at 10K, showing a small degree of hysteresis, similar to the observations for $SrCo_{0.5}Fe_{0.5}O_{2.5}F_{0.5}$, thus verifying the presence of a ferromagnetic component.

4.4 Conclusions

The brownmillerite materials $Sr_2Fe_2O_5$, Sr_2CoFeO_5 and $Sr_2Co_2O_5$ possess ordered oxygen vacancy structures that are amenable to fluorine insertion reactions. Interestingly, due to the readiness of Fe^{3+} to oxidise to form Fe^{4+}, the fluorination of $Sr_2Fe_2O_5$ results in a phase segregation to form a 1:1 mixture of the Fe^{3+}-containing phase $SrFeO_2F$ and Fe^{4+}-containing $SrFeO_3$. Madelung energy calculations confirmed that this was indeed more energetically favourable than the formation of a hypothetical intermediate phase with nominal composition $SrFeO_{2.5}F_{0.5}$.

The fluorination of the Co-containing phases Sr_2CoFeO_5 and $Sr_2Co_2O_5$ in both cases results in the formation of fluorinated phases with primitive cubic structures. Phase segregation is not observed in Sr_2CoFeO_5 as the Co and Fe cations are randomly distributed throughout the starting material and thus phase segregation to form $SrCoO_2F$ and $SrFeO_3$ would require extremely facile cation migration in order to be viable. Due to the difficulty in oxidising Co^{3+} to Co^{4+}, similarly phase separation upon the fluorination of $Sr_2Co_2O_5$ is not energetically feasible. Both $SrCo_{0.5}Fe_{0.5}O_{2.5}F_{0.5}$ and $SrCoO_{2.5}F$ display canted ferromagnetic behaviour, which most likely arises from complex exchange interactions between transition metal cations with mixed 3+/4+ oxidation states. However, the samples produced during the course of this study were not pure enough to derive accurate estimations of oxygen and fluorine contents therefore there is some uncertainty about the transition metal oxidation states in these materials and thus the mechanism for the observed canted ferromagnetism.

4.5 References

1. J.Hadermann, G. van Tendeloo, A. M. Abakumov, B. Ph. Pavlyuk, M. Rozova and E.V. Antipov (2000) *International Journal of Inorganic Materials* **2** 493.
2. J. T. Vaughey, J. B. Wiley and K. R. Poeppelmeier (1991) *Zeitschrift für Anorgische und Allgemeine Chemie* **598/599** 327.
3. G. Roth, P. Adelmann, R. Knitter, S. Massing and T. H. Wolf (1992) *Journal of Solid State Chemistry* **99** 376.
4. A. J. Wright, H. M. Palmer, P. A. Anderson and C. Greaves (2001) *Journal of Materials Chemistry* **11** 1324.
5. A. M. Abakumov, M. G. Rozova, B. Ph. Pavlyuk, M. V. Lobanov, E. V. Antipov, O. I. Lebedev, G. van Tendeloo, O. L. Ignatchik, E. A. Ovtchenkov, Yu. A. Koksharov and A. N. Vasil'ev (2001) *Journal of Solid State Chemistry* **160** 353.
6. A. J. Wright, H. M. Palmer, P. A. Anderson and C. Greaves (2002) *Journal of Materials Chemistry* **12** 978.
7. A. M. Abakumov, A. M. Alekseeva, M. G. Rosova, E. V. Antipov, O. I. Lebedev and G. van Tendeloo (2003) *Journal of Solid State Chemistry* **174** 319.
8. E. V. Antipov, A. M. Abakumov, A. M. Alekseeva, M. G. Rozova, J. Hadermann, O. I. Lebedev and G. van Tendeloo (2004) *Physica Status Solidi (a)* **201** 7 1403.
9. A. M. Alekseeva, A. M. Abakumov, M. G. Rozova, E. V. Antipov and J. Hadermann (2004) *Journal of Solid State Chemistry* **177** 731.
10. C. Greaves, A. J. Jacobson, B. C. Tolfield and B. E. F. Fender (1975) *Acta Crystallographica* **B31** 641.
11. P. K. Gallagher, J. B. MacChesney and D. N. E. Buchann (1964) *The Journal of Chemical Physics* **41** 8 249.
12. M. Harder and H. K. Müller-Buschbaum (1980) *Zeitschrift für Anorgische und Allgemeine Chemie* **464** 169.
13. T. Takeda, Y. Yamaguchi, H. Watanabe, S. Tomiyoshi and H. Yamamoto (1969) *Journal of the Physical Society of Japan* **26** 1320.

14. T. Takeda, Y. Yamaguchi, S. Tomiyshi, M. Fukase, M. Sugimoto and H. Watanabe (1968) *Journal of the Physical Society of Japan* **24** 3 446.
15. P. Berastegui, S.-G. Eriksson and S. Hull (1999) *Materials Research Bulletin* **34** 2 303.
16. M. Schmidt and S. J. Campbell (2001) *Journal of Solid State Chemistry* **156** 292.
17. T. Takeda, Y. Yamaguchi and H. Watanabe (1972) *Journal of the Physical Society of Japan* **33** 4 967.
18. J. P. Hodges, S. Short, J. D. Jorgensen, X. Xiong, B. Dabrowski, S. M. Mini and C. W. Kimball (2000) *Journal of Solid State Chemistry* **151** 190.
19. H. D'Hondt, A. M. Abakumov, J. Hadermann, A. S. Kalyuzhnaya, M. G. Rozova, E. V. Antipov and G. van Tendeloo (2008) *Chemistry of Materals* **20** 7188.
20. G. S. Case, A. L. Hector, W. Levason, R. L. Needs, M. F. Thomas and M. T. Weller (1999) *Journal of Materials Chemistry* **9** 2821.
21. F. J. Berry, X. Ren, R. Heap, P. Slater and M. F. Thomas (2005) *Solid State Communications* **134** 621.
22. R. Le Toquin, W. Paulus, A. Cousson, C. Prestipino and C. Lamberti (2006) *Journal of the American Chemical Society* **128** 13161.
23. H. Watanabe and T. Takeda (1970) *Ferrites: Proceedings of the International Conferenc*e 588.
24. P. Bezdicka, A. Wattiaux, J. C. Grenier, M. Pouchard and P. Hagenmuller (1995) *Zeitschrift für Anorgische und Allgemeine Chemie* **619** 7.
25. P. D. Battle, T. C. Gibb and S. Nixon (1988) *Journal of Solid State Chemistry* **73** 330.
26. P. D. Battle, T. C. Gibb and P. Lightfoot (1988) *Journal of Solid State Chemistry* **76** 334.
27. T. Takeda, Y. Yamaguchi and H. Watanabe (1972) *Journal of the Physical Society of Japan* **33** 4 970.
28. A. C. Larson and R. B. Von Dreele (1990) *Generalised Structure Analysis System,* Los Alamos National Laboratory.
29. J. W. Weenk and H. A. Harwig (1977) *Journal of the Physics and Chemistry of Solids* **38** 1047, (program adapted by C. Greaves, The School of Chemistry, The University of Birmingham).

30. A Muñoz, C. de la Calle, J. A. Alonso, P. M. Botta, V. Pardo, D. Baldomir and J. Rivas (2008) *Physical Review B* **78** 054404.

Chapter Five

Synthesis and Characterisation of the Fluorinated Single-Layer Manganite $Sr_2MnO_{3.5+x}F_y$

5.1 Introduction

5.1.1 The Structure of Sr_2MnO_4

Sr_2MnO_4 was initially synthesized by Balz and Plieth [1] in their 1955 study of the single layered (n = 1) Ruddlesden-Popper phase K_2NiF_4 and materials they found to be isostructural with it. The pure Mn^{4+}-containing Sr_2MnO_4 was reported here to adopt body centred tetragonal symmetry in the *I*4/*mmm* space group with the lattice parameters a = 3.79 Å and c = 12.43 Å [1]. The crystallographic structure of Sr_2MnO_4 is composed of single layers of corner-linked octahedral MnO_6 units separated by a stratum of rock salt structured SrO. Within the systematic study of strontium-manganese oxides by Mizutani *et al*. in 1971 [2], it was postulated that Sr_2MnO_4 possessed two allotropic forms: low temperature α-Sr_2MnO_4 and β-Sr_2MnO_4 (as reported by Balz and Plieth [1]), which required temperatures in excess of 1500˚C to form. However, Kriegel and Feltz [3] later showed that the α -Sr_2MnO_4 form was in fact a mixture of SrO and a previously unknown monoclinic compound $Sr_7Mn_4O_{15}$

crystallising in the space group $P2_1/c$ with lattice parameters $a = 6.8178(6)$ Å, $b = 9.6224(8)$ Å, $c = 10.380(1)$ Å and $\beta = 91.886(7)°$. Hence it should be clarified here that in the literature published between 1971-1992, the term β-Sr_2MnO_4 is used as opposed to simply Sr_2MnO_4.

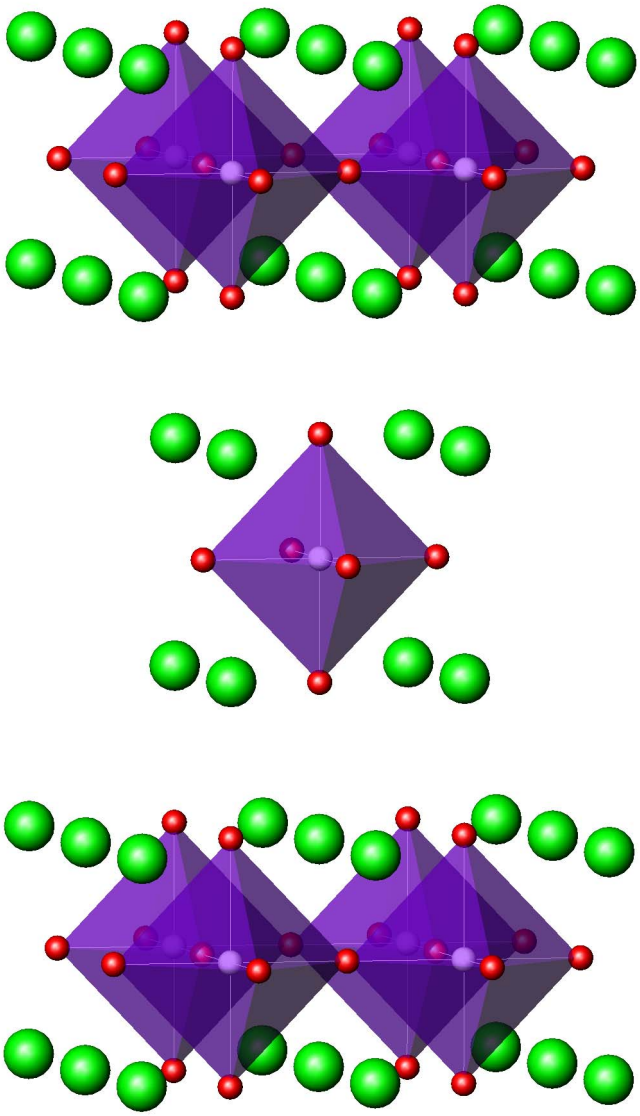

Figure 5.1 The structure of Sr_2MnO_4. The white spheres denote Mn atoms, green spheres Sr atoms, red spheres O atoms and the MnO_6 octahedra are shaded in purple.

Kriegel *et al.* [4] found that synthesising Sr_2MnO_4 at 1510˚C in an argon atmosphere made it possible to introduce anion defects and hence mixed Mn^{3+}/Mn^{4+} cation valences in this material. The removal of oxygen anions produced the reduced

phase $Sr_2MnO_{3.84(1)}$ formed by a statistical distribution of basal O vacancies in the equatorial positions in the MnO_6 octahedra, thus retaining the K_2NiF_4 structure. The defects lead to a distorted tetragonal pyramidal coordination of Mn^{3+} cations. Single crystal X-ray diffraction was used to obtain the lattice parameters of this reduced phase, which were reported as a = 3.8058(3) Å and c = 12.5319(11) Å.

5.1.2 Magnetic Structure of β-Sr_2MnO_4/$Sr_2MnO_{3.84}$

Characterisation of the magnetic properties and structure of Sr_2MnO_4 was carried out by Bouloux *et al.* [5] in 1981. The material was found to exhibit antiferromagnetic ordering below the Néel temperature T_N = 170(5) K. The magnetic structure of Sr_2MnO_4 was reported to be similar to that of K_2NiF_4 with doubling of the magnetic unit cell parameter a thus the magnetic and crystallographic structures are related by $a_{magn} = 2a_{cryst}$ and $c_{magn} = c_{cryst}$. The magnetic moments of the Mn^{4+} cations are aligned parallel to the c axis. *Figure 5.2* depicts the magnetic structure of Sr_2MnO_4 wherein each Mn^{4+} cation is antiferromagnetically aligned with its 4 surrounding neighbours within the $[MnO_4]_n$ layer and each translation of ½, ½, ½ results in an identical layer. The structural refinement carried out on data collected at 4.2 K gave a magnetic moment of 2.42(5) μ_B for the Mn^{4+} ions.

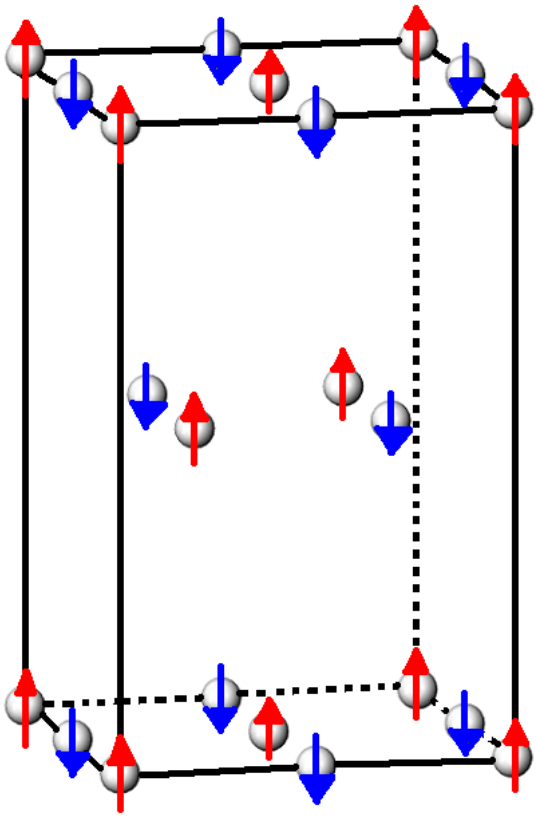

Figure 5.2 The magnetic structure of Sr_2MnO_4 with the red and blue arrows highlighting the spin direction of Mn^{4+} cations aligned in the direction of the *c* axis.

5.1.3 The Structure of $Sr_2MnO_{3.5+x}$

The further reduction of Sr_2MnO_4 to form $Sr_2MnO_{3.5+x}$ with a view to creating a new ordered oxygen vacancy structure was achieved by Gillie *et al.* [6, 7]. Neutron powder diffraction was used to examine the defect structure of this material more thoroughly, but discrepancies in the fit of the Rietveld structural refinement of these data utilising the *I*4/*mmm* space group necessitated a lower symmetry model. Study of this material using electron microscopy revealed the presence of superstructure and a lower symmetry space group. The oxygen vacancy ordering scheme was deduced by comparison with the oxygen deficient perovskite phases $SrMnO_{2.5}$ [8-10], $CaMnO_{2.5}$ [11], $Ca_2MnO_{3.5}$ [12] and $SrCuO_{2.5}$ [13]. In these isostructural materials, corner connected MnO_5 square pyramids form an ordered oxygen defect arrangement of psuedo-

hexagonal channels. The Mn^{3+} ions adopt a square pyramidal co-ordination and exhibit antiferromagnetic coupling with three neighbouring Mn^{3+} ions.

A model for the oxygen vacancy structure of $Sr_2MnO_{3.5+x}$ was proposed that was consistent with the unit cell derived from electron diffraction. This structure consisted of elongated psuedo-hexagonal channels similar to those exhibited by $SrMnO_{2.5}$, $CaMnO_{2.5}$ and $Ca_2MnO_{3.5}$. Rietveld structural refinement using this model gave a good fit to the data, thus the crystal structure was solved in the primitive monoclinic space group $P2_1/c$ with the lattice parameters a = 6.8524(3) Å, b = 10.8131(4) Å, c = 10.8068(4) Å and β = 113.247(4) Å [6, 7].

The equatorial oxygen vacancies introduced by reduction to the composition $Sr_2MnO_{3.5+x}$ form an ordered defect superstructure within the perovskite layer. The Mn^{3+} cations form MnO_5 square pyramids corner-linked through oxygen anions. A view of the bc-plane of the monoclinic supercell is shown in *Figure 5.3*.

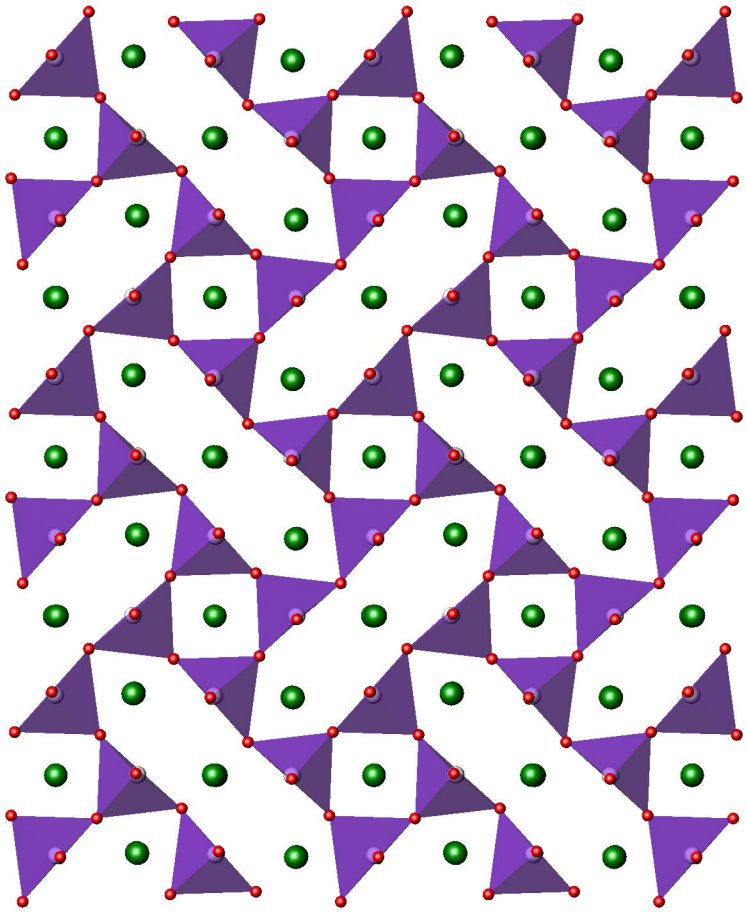

Figure 5.3 Structure of $Sr_2MnO_{3.5+x}$. The blue spheres denote Mn atoms, green spheres Sr atoms, red spheres O atoms and the MnO_5 polyhedra are shaded in purple.

The transformation to a lower symmetry space group was necessary to account for the defect superstructure. The monoclinic unit cell is related to the body-centred tetragonal sub-cell vectors ($\mathbf{a}_t$, $\mathbf{b}_t$, $\mathbf{c}_t$) by $\mathbf{a} = ½(-\mathbf{a}_t-\mathbf{b}_t+\mathbf{c}_t)$; $\mathbf{b} = 2(-\mathbf{a}_t+\mathbf{b}_t)$; $\mathbf{c} = 2(\mathbf{a}_t+\mathbf{b}_t)$. Hence, the a_tb_t tetragonal plane translates to the bc-plane in the monoclinic super-cell, where the a-axis links the adjacent perovskite block layers.

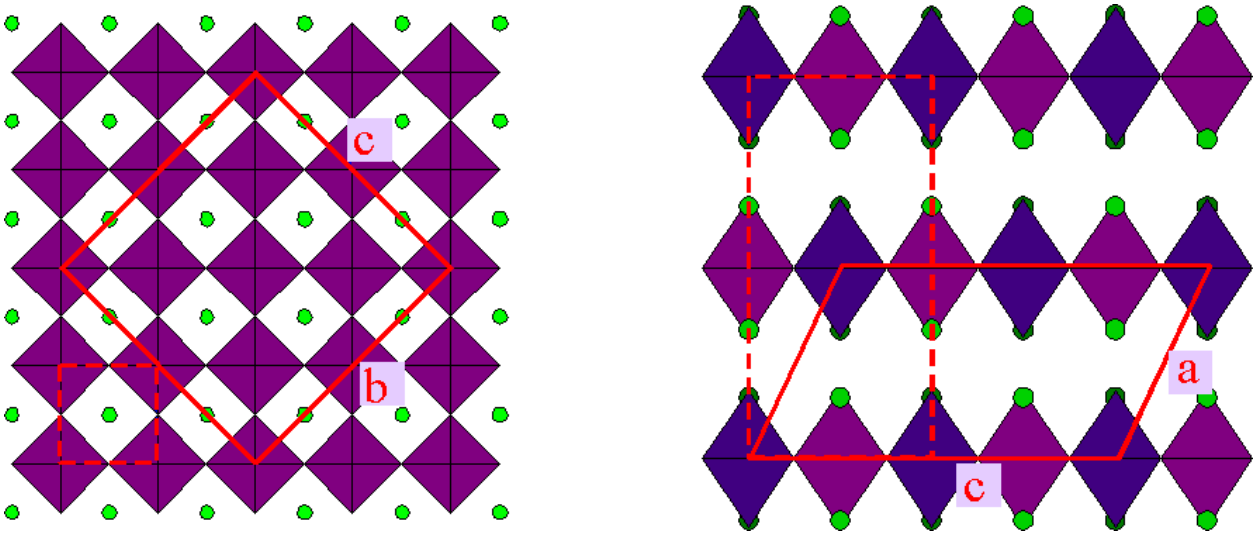

Figure 5.4 Figure illustrating the relationship between the *I4/mmm* tetragonal sub cell and the larger $P2_1/c$ monoclinic unit cell. The diagram on the left shows the bc-plane of the monoclinic super cell (solid red lines) and the a_tb_t-plane of the tetragonal sub cell (dotted red lines), whilst the diagram on the right depicts the monoclinic ac-plane and the tetragonal a_tc_t plane, superimposed on the K_2NiF_4-type tetragonal model.

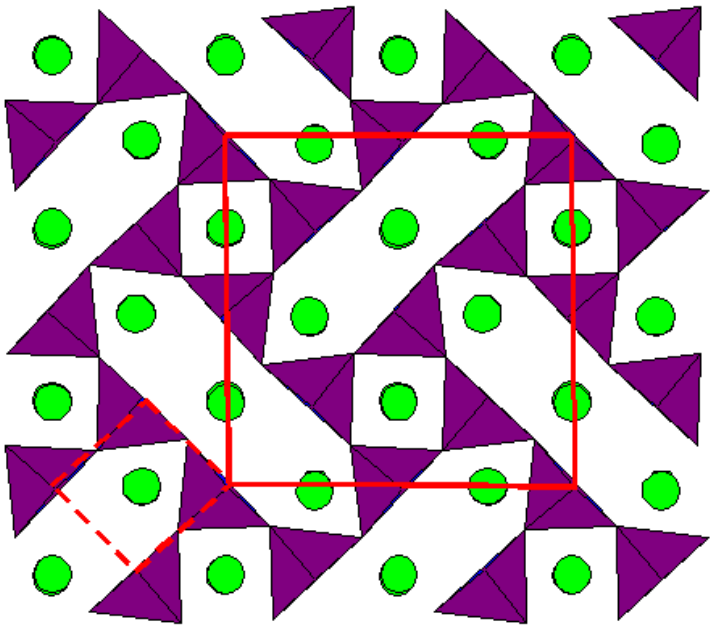

Figure 5.5 The K_2NiF_4-type tetragonal sub-cell (dotted red line) and monoclinic super-cell (solid red line) shown against the bc-plane of the monoclinic model.

5.1.4 Magnetic Structure of $Sr_2MnO_{3.5+x}$

Gillie *et al.* [6, 7] reported that the plot of magnetic susceptibility against temperature showed a broad peak approximately centred around 280 K, below which $Sr_2MnO_{3.5+x}$ displays antiferromagnetic ordering. The characterisation of the magnetic structure of this material *via* powder neutron diffraction by Gillie *et al.* [6, 7] found this behaviour to arise from clusters of four ferromagnetically aligned MnO_5 square pyramids corner-linked through oxygen anions arranged antiferromagnetically to the neighbouring clusters of MnO_5.

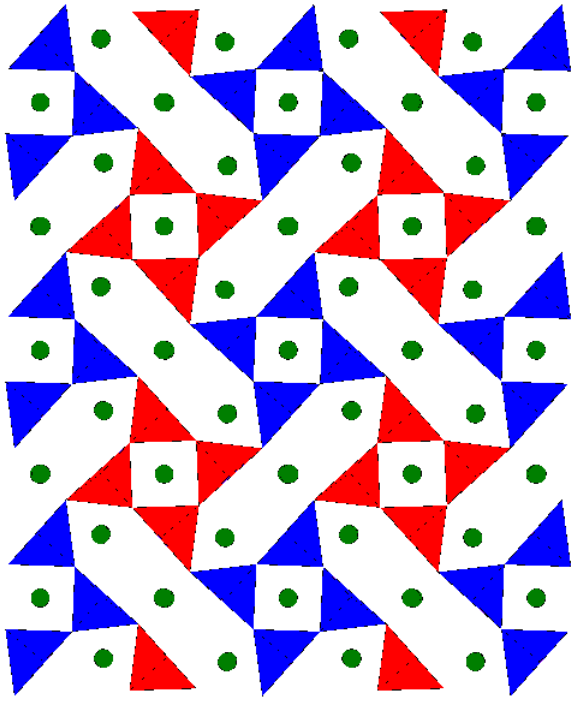

Figure 5.6 Magnetic structure of $Sr_2MnO_{3.5+x}$ where all corner-linked MnO_5 units highlighted in red are ferromagnetically aligned with one another whilst all blue MnO_5 units are ferromagnetically aligned with the opposite spin such that the red and blue clusters display antiferromagnetic ordering.

In accordance with the Curie-Weiss law, the inverse susceptibility plotted against temperature is linear above this transition with a paramagnetic moment of 6.34 μ_B per Mn as reported by Gillie *et al.*, which is significantly greater than the expected spin-only value (Mn^{3+} = 4.90 μ_B, Mn^{4+} = 3.87 μ_B) [6, 7]. This can most likely

be attributed to clusters of predominantly ferromagnetic interactions resulting from the mixed Mn^{3+}/Mn^{4+} oxidation state.

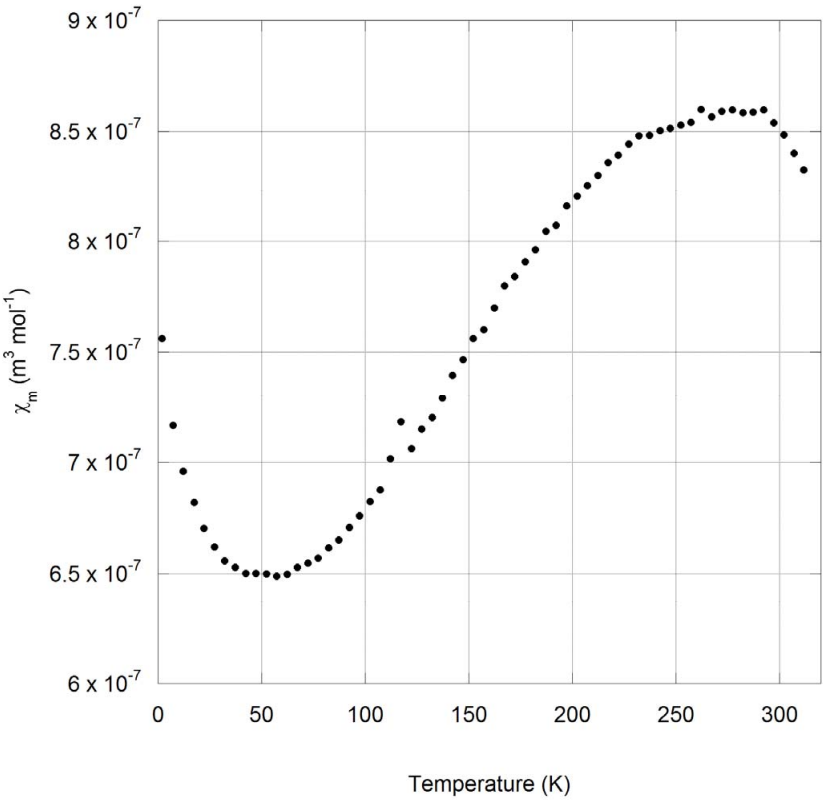

Figure 5.7 Zero field cooled magnetic susceptibility of $Sr_2MnO_{3.5+x}$ recorded using a field of 0.3T.

5.1.5 Fluorination of $Sr_3Mn_2O_{6+x}$

The reduced double-layer manganite $Sr_3Mn_2O_{6+x}$ was found to crystallize in the tetragonal space group *P*4/*mbm* exhibiting a similar oxygen vacancy superstructure to that observed for $Sr_2MnO_{3.5+x}$ and the lattice parameters a = 10.8686(2) Å and c = 20.2051(3) Å [14].

Gillie [7] demonstrated that staged fluorine insertion into this material was entirely feasible, synthesizing *I*-centred tetragonal $Sr_3Mn_2O_6F_x$ phases with x = 1, 2, 3 thus attaining a variety of manganese oxidation states. From consideration of the change in c from the parent oxide, it was concluded that the x = 1 phase was produced by the filling of all the equatorial oxygen vacancies by fluorine atoms. The x = 2

phase resulted from the random distribution of fluorine anions throughout both interstitial rocksalt and equatorial sites, whilst the fully fluorinated $x = 3$ phase arose from the complete occupation of all these sites. The $x = 3$ phase $Sr_3Mn_2O_6F_3$ is illustrated in *Figure 5.8*. The apical Mn-O bond lengths are distorted such that the Mn cation is situated closer to the interstitial rocksalt sites, which is akin to the shortening of the Mn-O bonds observed for the staged Ruddlesden-Popper structure $La_{1.2}Sr_{1.8}Mn_2O_7F$ [15]. In this material, electrostatic Mn-F attractions coupled with O-F repulsions result in an extremely short Mn-O bond length for the apical bond directed towards the interstitial fluorine sites, and a similar process was discussed to be responsible for the distortion of the Mn-O bond length in $Sr_3Mn_2O_6F_3$.

5.1.6 Fluorination of $SrMnO_{2.5}$

Lobanov *et al*. [16] recognised that the anion-deficient structure of $SrMnO_{2.5}$ provided an appropriate matrix for low-temperature fluorine insertion reactions and synthesised the novel oxyfluoride $Sr_2Mn_2O_{5-x}F_{1+x}$ using XeF_2 as a fluorinating agent. The starting material $SrMnO_{2.5}$ was reported to possess an orthorhombic crystal structure in the space group *Pbam* with lattice parameters $a = 5.5307(4)$ Å, $b = 10.7829(8)$ Å and $c = 3.8145(3)$ Å [10]. Upon fluorination, it was shown that the fluorine anions fill the equatorial vacancies such that the Mn cations are octahedrally co-ordinated. The fluorinated phase $Sr_2Mn_2O_{5-x}F_{1+x}$ undergoes a tetragonal distortion of the perovskite structure originating from the apical elongation Jahn-Teller distortion of the $Mn(O,F)_6$ octahedra. There was no evidence for any remaining superstructure in the fluorinated phase, thus characterisation was carried out in the space group *P*4/*mmm* with the refined lattice parameters reported as $a = 3.8069(8)$ Å and $c = 3.989(2)$ Å [16].

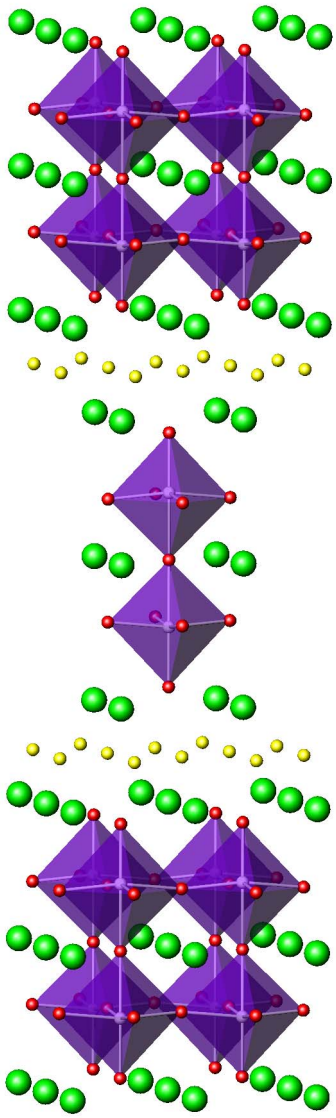

Figure 5.8 Structure of $Sr_3Mn_2O_6F_3$ with MnO_5F octahedra in purple, Mn atoms in white, O atoms in red (although note there is a statistical distribution of O and F over the equatorial sites in the MnO_5F octahedra), Sr atoms in green, with interstitial F atoms in yellow.

As both the single and double layer manganites share the same oxygen defect superstructure, and it has been previously shown that a *chimie douce* approach to fluorination has met with success in both $Sr_3Mn_2O_{6+x}$ and $SrMnO_{2.5}$ (exhibiting a similar superstructure) it was postulated that $Sr_2MnO_{3.5+x}$ would also be a suitable candidate for the creation of an ordered array of fluorine anions *via* low temperature fluorine insertion.

5.2 Experimental Procedures

5.2.1 Synthesis of the Starting Material $Sr_2MnO_{3.5+x}$

The starting material $Sr_2MnO_{3.5+x}$ was prepared from the solid state reaction of stoichiometric amounts of $SrCO_3$ and Mn_2O_3 under reducing conditions [6, 7]. The sample was sintered at 1350ºC under an atmosphere of flowing $N_{2(g)}$ for 36 hours with intermediate grinding, then annealed for 12 hours at 550ºC under an atmosphere of flowing $10\%H_{2(g)}/90\%N_{2(g)}$.

5.2.2 Fluorination *via* Solid-Gas Reaction

Based on previous studies of the fluorination of $Sr_3Mn_2O_6$[7], phases of the composition $Sr_2MnO_{3.5+x}F_y$ were produced by several 2 hour heat treatments of polycrystalline $Sr_2MnO_{3.5+x}$ at 200ºC in a static atmosphere of 10% $F_{2(g)}/90\%N_{2(g)}$. Please refer to Section 2.1.2 for diagrams of the solid-gas fluorination apparatus and in-depth methodology.

5.3 Results and Discussion

5.3.1 Characterization of the Starting Material $Sr_2MnO_{3.5+x}$

5.3.1.1 Verification of Oxygen Content Prior to Fluorination *via* TGA

$Sr_2MnO_{3.5+x}$ was oxidized to form Sr_2MnO_4 by heating to 600ºC in pure $O_{2(g)}$ at a ramp rate of 5ºC min^{-1} then held isothermally for 20 minutes.

Also, thermogravimetric decomposition under 10% $H_{2(g)}/90\%N_{2(g)}$ to form SrO and MnO was used to verify the oxygen content of the starting material $Sr_2MnO_{3.5+x}$.

TGA established that the actual composition of the starting material was $Sr_2MnO_{3.53(5)}$

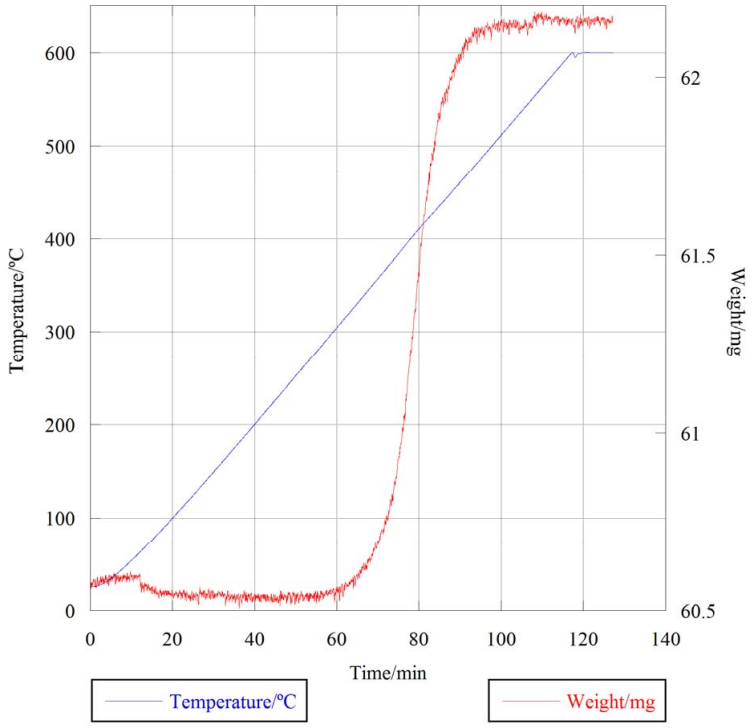

Figure 5.9 Typical thermogravimetric plot showing the oxidation of $Sr_2MnO_{3.5+x}$ to form Sr_2MnO_4.

5.3.1.2 Rietveld Refinement Based on XRD Data in the Space Group *I*4/*mmm*

The "GSAS" suite of programs [17] was employed to refine powder X-ray diffraction data collected on the starting material $Sr_2MnO_{3.5+x}$. The space group adopted for this refinement was *I*4/*mmm*, despite the proper symmetry reported by Gillie *et al*. being the monoclinic space group $P2_1/c$. The body centred tetragonal model was deemed appropriate for this refinement, as XRD data are insensitive to the order of oxygen atoms in such materials. Thus this technique could not reveal the network of ordered oxygen vacancies within $Sr_2MnO_{3.5}$, only that the O(1) equatorial positions were not fully occupied thus the MnO_2 planes contained oxygen vacancies. The expansion in the lattice parameters *cf.* Sr_2MnO_4 to $a = 3.8208(5)$ Å and $c = 12.590(3)$ Å is consistent with the reduction from Mn^{4+} to Mn^{3+} as this would

increase the cationic radii of the manganese and is in agreement with the literature values [6, 7].

The Rietveld structural refinement generated by "GSAS" calculated both the model X-ray diffraction pattern and the difference between this and the experimentally observed data. The corresponding fitting factors for this refinement were $\chi^2 = 1.119$, $R_{wp} = 8.99\%$ and $R_p = 6.77\%$. The refined fractional occupancy of the O(1) site was 0.80(2), suggesting the composition $Sr_2MnO_{3.60(4)}$, although the thermal parameters were constrained for the anions in this refinement, and as these two parameters are highly correlated this composition cannot be relied upon without other evidence. The tetragonal model was a good fit for this powder X-ray diffraction data, but it should be borne in mind that in reality the structural arrangement is far more complex and the lower symmetry monoclinic space group $P2_1/c$ is necessary in order to fully describe the oxygen vacancy superstructure and the magnetic ordering in this phase, particularly when considering NPD data.

5.3.2 Characterisation of the Fluorinated Phase $Sr_2MnO_{3.5+x}F_y$

An increase in sample mass upon heating in an atmosphere composed of $10\%F_{2(g)}/90\%N_{2(g)}$ indicated that low temperature fluorine insertion had met with some degree of success. Powder X-ray diffraction of samples that had been treated with fluorine showed peaks shifting to lower angles in accordance with an increase in the *c* parameter. Thermal decomposition products after thermogravimetric reduction were identified by XRD as MnO, SrF_2 and SrO, the latter rapidly forming $Sr(OH)_2H_2O$ upon exposure to air.

5.3.2.1 Rietveld Refinement Based on XRD Data in the Space Group *I*4/*mmm*

The Rietveld refinement was carried out in the *I*4/*mmm* space group, as the oxygen defect super-cell reflections could not be detected by powder X-ray diffraction.

Upon fluorination, the *a* parameter has essentially remained constant (*a* = 3.82069(5) Å), whilst the *c* parameter has increased slightly from 12.590(3) Å to 12.6309(4) Å. The refined fractional occupancy of the equatorial anion position of 0.87(2) suggests the material is not fully fluorinated to form $Sr_2Mn(O,F)_4$, and instead forms a phase of approximately $Sr_2Mn(O,F)_{0.75}$, hence around 50% fluorinated. However, as the thermal parameter values and fractional occupancy for XRD data are highly correlated, at this stage and without further supporting evidence, the refined fractional occupancy can only be regarded as a guide.

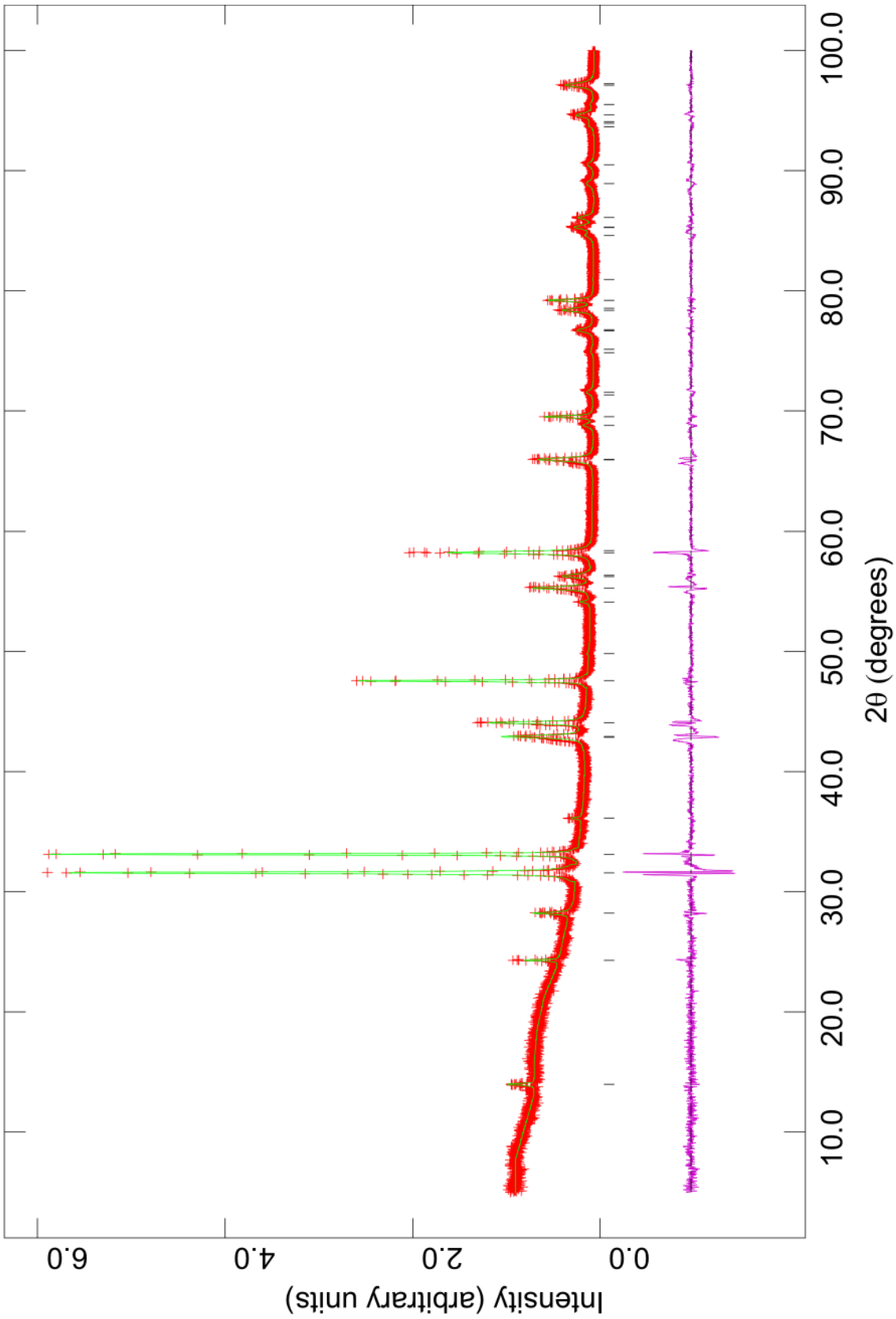

Figure 5.10 Observed (red +), calculated (green) and difference (pink) profiles of $Sr_2MnO_{3.5+x}F_y$ as generated by the Rietveld profile refinement of XRD data with peak positions indicated by black vertical lines.

Table 5.1 Refined atom and lattice parameters of $Sr_2MnO_{3.5+x}F_y$ from refinement of XRD data in the space group *I4/mmm*.

Atom	Site Symmetry	*x*	*y*	*z*	Occupancy	$U_{iso} \times 100$ (Å^2)
Sr	4e	0	0	0.3535(2)	1	0.19(6)
Mn	2a	0	0	0	1	0.1(1)
O(1)	4c	0	0.5	0	0.87(2)	1.3(5)
O(2)	4e	0	0	0.1534(9)	1	1.4(3)

Generally, the refinement of XRD data in the space group *I*4/*mmm* provided a reasonable fit, converging with $\chi^2 = 3.136$, however the R_p and R_{wp} values (6.36% and 9.66% respectively) seemed slightly high.

Two possible models for fluorination were proposed. Should the fluorine atoms fill the equatorial oxygen vacancies thus forming an ordered fluorine array, the fluorinated manganite would also display $P2_1/c$ symmetry with an ordered fluorine superstructure. However, if the fluorine atoms adopted apical positions, the vacancy superstructure would be destroyed and thus the fluorinated material would crystallise in the *I*4/*mmm* space group, effectively Sr_2MnO_4 with the apical O(2) positions preferentially occupied by F. Ascertaining whether the fluorine adopted apical or equatorial positions and thus which model for fluorine insertion was reliable would require utilising several techniques (such as Madelung energy calculations and TEM) in addition to XRD and NPD, on account of the similar scattering lengths of O and F.

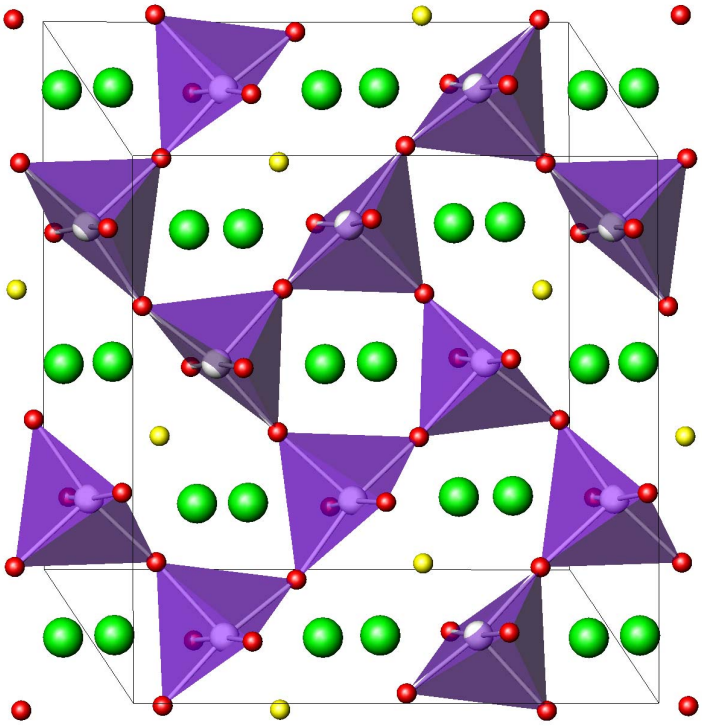

Figure 5.11 Illustration to demonstrate fluorine atoms (yellow) occupying the equatorial oxygen vacancies in the monoclinic bc plane, thus still conforming to $P2_1/c$ symmetry (based upon nominal stoichiometry $Sr_2Mn(O,F)_4$).

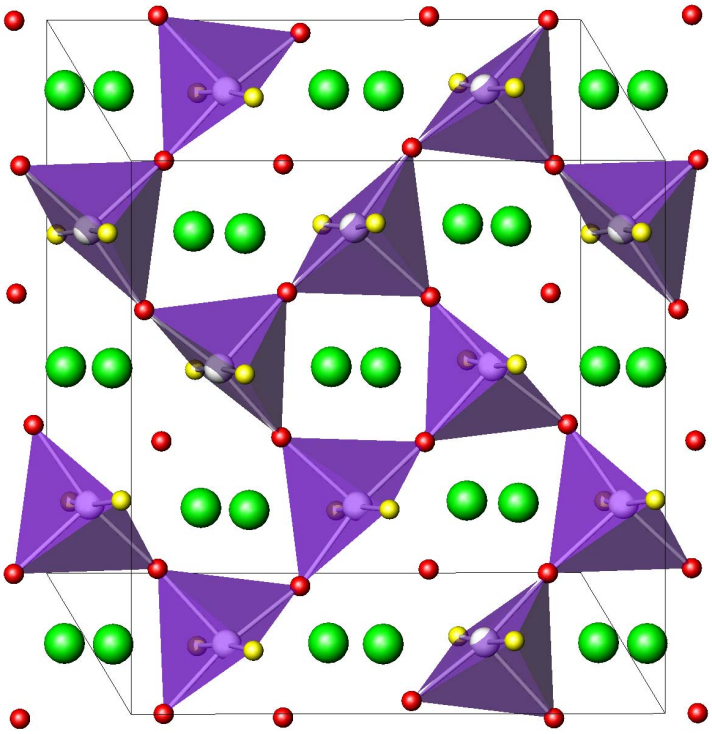

Figure 5.12 Should fluorine atoms displace oxygen atoms from their apical positions thus causing the oxygen atoms to fill the equatorial vacancies, then the fluorinated material would revert to *I4/mmm* symmetry (based upon nominal stoichiometry $Sr_2Mn(O,F)_4$).

5.3.2.2 Estimation of Fluorine Content Using TGA

As the fluorine content of the sample could not be precisely determined from the XRD refinement, TGA studies were carried out to establish the sample composition.

$Sr_2MnO_{3.5+x}F_y$ was fully decomposed upon heating to 1000ºC in a flowing atmosphere of $10\%H_{2(g)}/90\%N_{2(g)}$. From the change in mass, the original composition of this particular sample was calculated to be $Sr_2MnO_{3.53(5)}F_{0.39(5)}$. This was supported within error by oxidation studies.

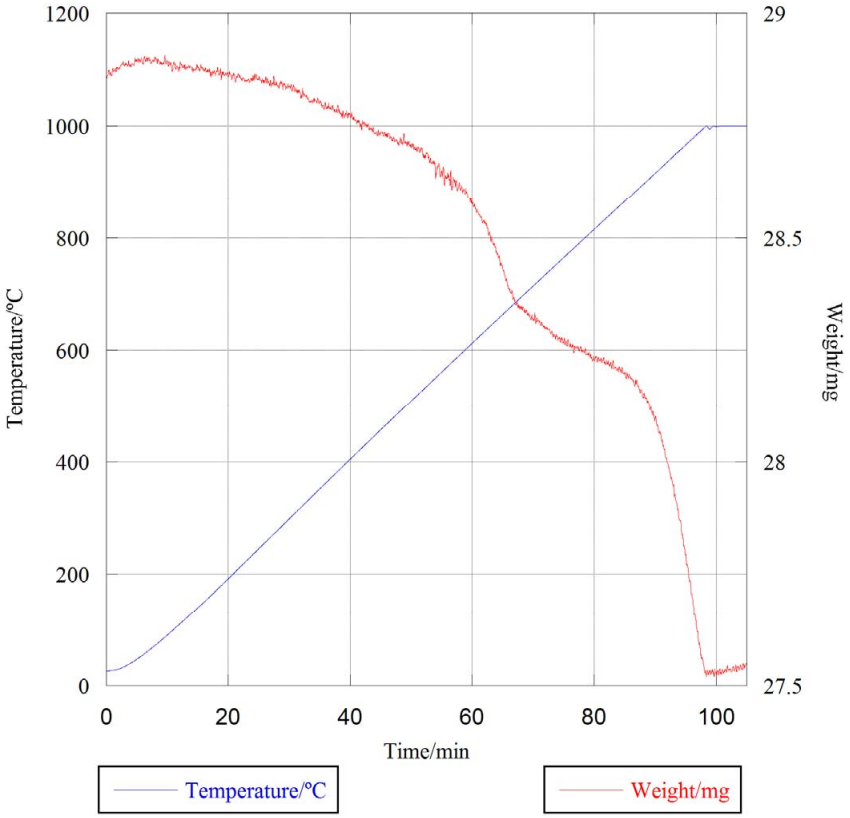

Figure 5.13 Plot representing the thermogravimetric decomposition of $Sr_2MnO_{3.5+x}F_y$ to form MnO, SrF_2 and SrO.

5.3.2.3 Bond Valence Sum Calculations

Bond valence sum calculations were carried out to estimate the average Mn oxidation state for the two different anion distribution models and thus infer whether the F anions are more likely to be situated in equatorial or apical positions (please

refer to *Appendix 5.1* for detailed calculations). The valence sum calculated for apical F was $V_{ap} = 3.71$ and that calculated for equatorial F was $V_{eq} = 3.75$. Seeing as the valence sums of the two different models are rather similar, all that can really be inferred from these values is that they suggest an average composition of approximately $Sr_2MnO_{3.75}F_{0.25}$, a higher O content than expected from TGA studies. This is probably due to the expression used to calculate these valence sums which did not take into account vacancies and assumed an overall composition of $Sr_2Mn(O,F)_4$. The composition found experimentally using TGA ($Sr_2MnO_{3.53(5)}F_{0.39(5)}$) would correspond to an average Mn oxidation state of $Mn^{3.45+}$. Although the valence sum calculated using apical fluorine ($V_{ap} = 3.71$) was marginally closer to the experimentally determined Mn oxidation state, as the expression for mixed M^{3+}/M^{4+} bond valence sums cannot account for vacancies then this calculation alone cannot be taken as evidence that inserted fluorine anions adopt apical positions. Furthermore, if one considers the bond lengths used for these calculations (from the refinement based upon XRD data: Mn-O(1)eq = 1.91035(3) Å, Mn-O(2)ap = 1.938(11) Å) it is clear that the error lies in the second decimal place in the apical Mn-O bond thus it follows that bond valence sum calculations cannot be used reliably in this case to distinguish between the two models for fluorine insertion as they are effectively identical when the error is taken into account.

5.3.2.4 Madelung Energy Calculations

The Madelung energy of a solid related to the electronic charge on its ions is described by the Coulombic term in the Born-Lande equation. However, this description does not account for deformations of the ions in the crystalline field. The Madelung energies shown below were calculated for both apical and equatorial

fluorine positions using the computer program "MAD" which utilises the Ewald method [18].

Apical F: E_M = -18471.52 kJ mol^{-1} (2dp)

Equatorial F: E_M = -18261.07 kJ mol^{-1} (2dp)

The Madelung energy calculations suggest that fluorine is more likely to favour the apical sites.

5.3.2.5 Verifying Sample Composition *via* XRF

Initially, XRF data could only accurately report the Sr:Mn ratio and overestimated the percentage by mass of oxygen and fluorine. The analysis for this sample was reworked assuming that the correct ratio of Sr, Mn and O were present according to the expected formula of the compound, $Sr_2MnO_{3.5}F_y$. Therefore, the percent by mass of fluorine was reported as 1.77% which yielded a fluorine content consistent with a composition of $Sr_2MnO_{3.5}F_{0.28}$ and this was in reasonable agreement with that derived from TGA.

5.3.2.6 Nuclear Refinement Based on Time of Flight NPD Data Collected at 4K

Time of flight (TOF) NPD data were collected using the POLARIS powder diffractometer at the ISIS spallation neutron source at the Rutherford Appleton Laboratory. Although the starting material $Sr_2MnO_{3.5+x}$ was shown to crystallise in the monoclinic space group $P2_1/c$, because the magnetic peaks and the peaks resulting from the oxygen defect superstructure are very low intensity, an acceptable fit may also be obtained using the tetragonal space group *I4/mmm* [6, 7]. Madelung energy calculations suggested that fluorine anions were likely to favour the apical sites and

displace the apical oxygen anions into the equatorial vacancies in $Sr_2MnO_{3.53(5)}F_{0.39(5)}$, hence an initial refinement of the data was carried out in *I4/mmm* (see *Appendix 5.2*).

Another refinement was carried out using the same space group but splitting the anion sites to allow for the presence of interstitial fluorine. A linear interpolation function was used for the background with 58 parameters including diffractometer constant, histogram scale factor, lattice parameters, profile parameters and atomic co-ordinates. It was also necessary to include the absorption/reflectivity correction in the refinement due to the propensity of Mn nuclei to absorb thermal neutrons. The isotropic temperature factors for the 3 anion sites were constrained to remain equal.

This provided a significantly better visual fit to the data (see *Figure 5.14*) and the refinement statistics ($\chi^2 = 8.286$, $R_{wp} = 1.56\%$ and $R_p = 2.50\%$) were better than those achieved without splitting the anion sites. The refined lattice parameters were $a = 3.81639(13)$ Å and $c = 12.6029(7)$ Å. The refined atom parameters are tabulated in *Table 5.2*.

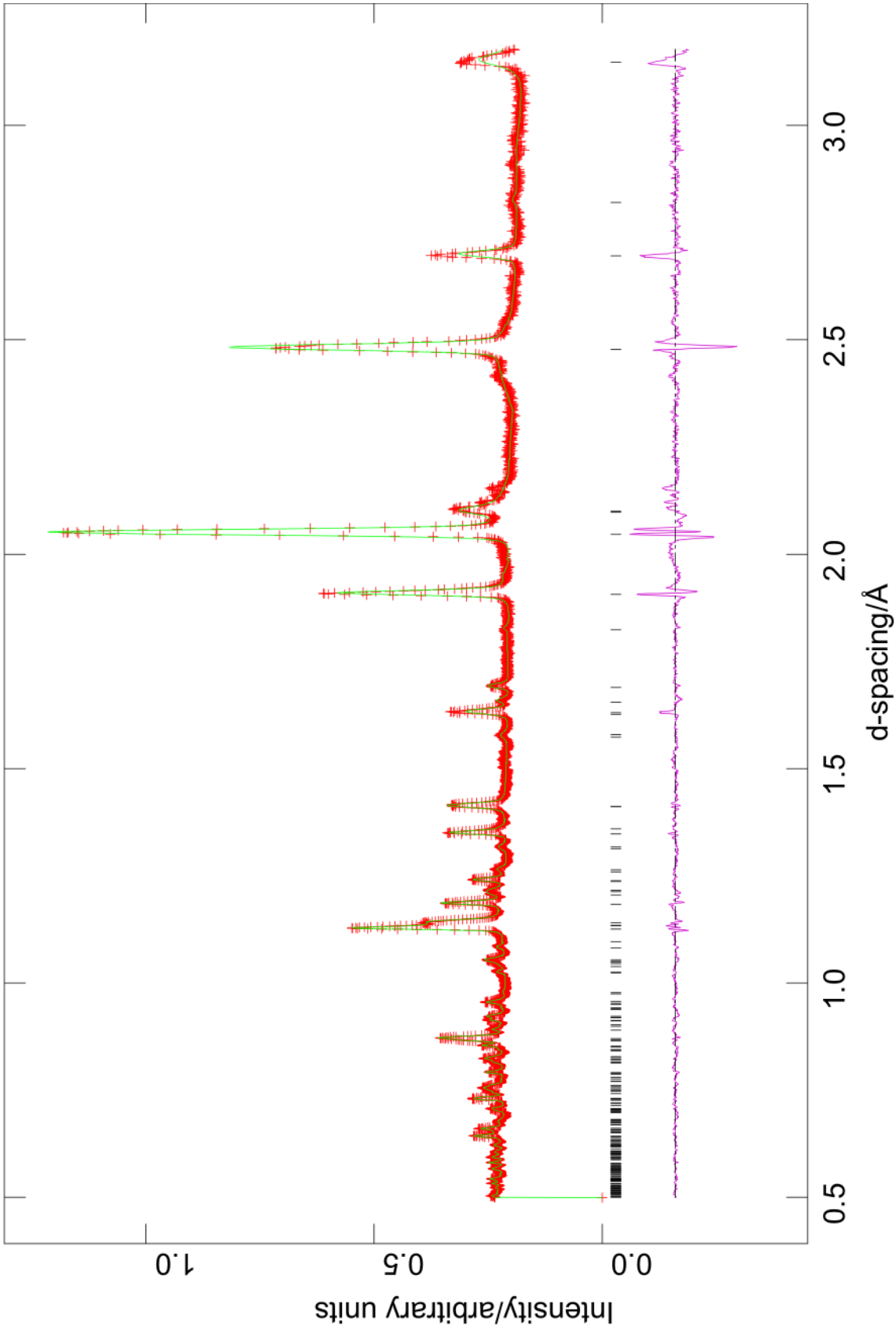

Figure 5.14 Observed (red +), calculated (green) and difference (pink) profiles of $Sr_2MnO_{3.53(5)}F_{0.39(5)}$ as generated by the Rietveld profile refinement of TOF NPD data collected at 2K, with peak positions indicated by black vertical lines.

Table 5.2 Refined atom parameters of $Sr_2MnO_{3.53(5)}F_{0.39(5)}$ from refinement of TOF NPD data collected at 2K in the space group *I4/mmm*.

Atom	Site Symmetry	*x*	*y*	*z*	Occupancy	$U_{iso} \times 100$ (Å^2)
Sr	4e	0	0	0.3563(1)	1	0.69 (3)
Mn	2a	0	0	0	1	0.15(5)
O(1)	8j	-0.017(2)	0.5	0	0.386(5)	0.64(5)
O(2)	16n	0.039(1)	0	0.1567(2)	0.25	0.64(5)
O(3)	16n	0.443(4)	0	0.248(5)	0.031(2)	0.64(5)

In order to definitively assign monoclinic or tetragonal symmetry to the fluorinated phase and to elucidate whether some fluorine was being inserted into interstitial sites, crystallites of $Sr_2MnO_{3.53(5)}F_{0.39(5)}$ were examined using TEM.

5.3.2.7 Examination of $Sr_2MnO_{3.53(5)}F_{0.39(5)}$ *via* TEM

Transmission electron microscopy was carried out by Dr Joke Hadermann at EMAT, Antwerp. This revealed two levels of fluorination within the sample of $Sr_2MnO_{3.53(5)}F_{0.39(5)}$. Some sections still retained the monoclinic superstructure (*Figure 5.15*) and small amounts of fluorine. The pieces containing more fluorine showed reflections according to the tetragonal sub-cell (*i.e.* smaller spots at ¼ of the distance between bright spots disappeared), thus had reverted to K_2NiF_4-type structure as seen for Sr_2MnO_4.(*Figure 5.16*) The higher levels of fluorination resulted in loss of superstructure and in these sections the *c* parameter varied between 12.7-13.1 Å, supporting the improvement in fit observed in the TOF NPD data upon the inclusion of interstitial sites.

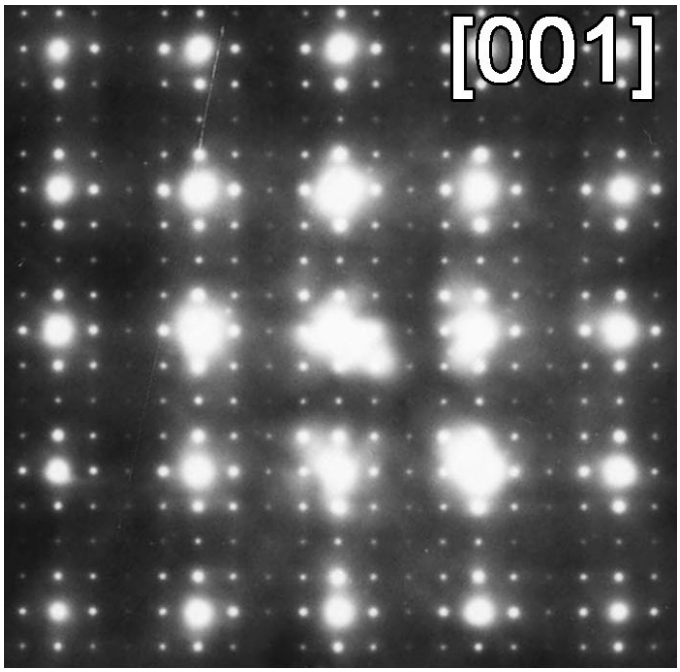

Figure 5.15 Electron diffraction pattern of $Sr_2MnO_{3.5+x}F_y$ along the $[001]_t$ zone.

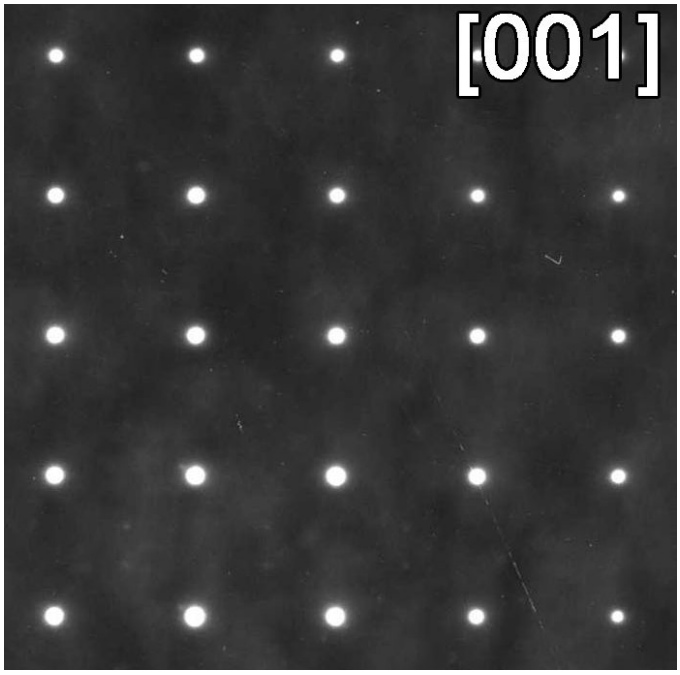

Figure 5.16 Electron diffraction pattern of $Sr_2MnO_{3.5+x}F_y$ along the $[001]_t$ zone.

These images suggest that when sufficient fluorine is introduced to this material, the fluorine atoms displace apical oxygen atoms, which subsequently fill the equatorial oxygen vacancies.

The observable asymmetry in the 2 most intense peaks in the original XRD refinement support the conclusion drawn from TEM that two phases were present in the crystallites studied: a high-fluorine content phase with K_2NiF_4-type structure and essentially unfluorinated $Sr_2MnO_{3.53(5)}$. As the composition derived from TGA assumed no presence of starting material, the formula $Sr_2MnO_{3.53(5)}F_{0.39(5)}$ is essentially an average between $Sr_2MnO_{3.53(5)}$ and a higher fluorine content phase that has lost all vacancy superstructure and may be described as $Sr_2Mn(O,F)_4$.

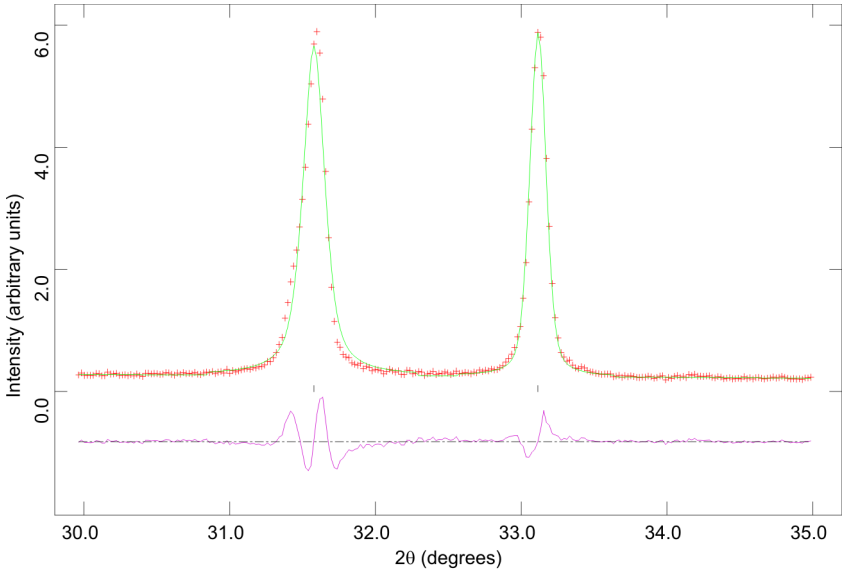

Figure 5.17 Close-up on the 2θ = 30º-35º region of the Rietveld profile refinement showing the 1 0 3 and the 1 1 0 peaks.

.

Visual inspection of the profile fitting shows the greatest deviation between observed and calculated values occurs at the two most intense peaks at 2θ ~ 31.5°and 2θ ~ 33° (the 1 0 3 and the 1 1 0 peaks), as shown in *Figure 5.17*.

5.3.2.8 2-Phase Rietveld Refinement Based on XRD Data

Further to the TEM images showing some crystallites with $P2_1/c$ symmetry and the observed asymmetry in the most intense XRD peaks, it was postulated that some unfluorinated starting material remained in the sample. Thus a 2-phase Rietveld refinement of the XRD data was carried out, with phase 1 assumed to be fully fluorinated $Sr_2Mn(O,F)_4$ with no equatorial anion vacancies and phase 2 was designated $Sr_2MnO_{3.5+x}$ with the O(1) occupancy allowed to vary. Both phases were assigned the space group *I4/mmm*.

A linear interpolation function was used for the background with 62 parameters including histogram scale factor, phase fraction, lattice parameters, profile parameters and atomic co-ordinates. The isotropic temperature factors for both phases were constrained to be equal for the same atom position. It was clear that the refinement statistics ($\chi^2 = 1.447$, $R_{wp} = 6.56\%$, $R_p = 4.65\%$) were significantly improved by the inclusion of the unfluorinated phase. Upon visual inspection of the profile refinement plot (*Figure 5.18*), there is a marked improvement in the agreement between observed and calculated profiles. The phase fraction of $Sr_2Mn(O,F)_4$ to $Sr_2MnO_{3.5+x}$ derived from the 2 phase refinement was 1:0.87416.

The refined *a* parameters for both the fluorinated phase $Sr_2Mn(O,F)_4$ ($a = 3.8210(1)$ Å) and the starting material $Sr_2MnO_{3.5+x}$ ($a = 3.8209(1)$ Å) were very similar, whilst $Sr_2Mn(O,F)_4$ showed a slight expansion in *c* ($c = 12.686(1)$ Å) when compared to the refined value for $Sr_2MnO_{3.5+x}$ ($c = 12.6086(4)$ Å). The refined atom parameters for the $Sr_2Mn(O,F)_4$ and $Sr_2MnO_{3.5+x}$ phases are shown in *Table 5.3* and *Table 5.4* respectively. The refined fractional occupancy of the O(1) position for $Sr_2MnO_{3.5+x}$ of 0.69(3) (*Table 5.4*) is in reasonable agreement with that reported by Gillie [7] of 0.723(6).

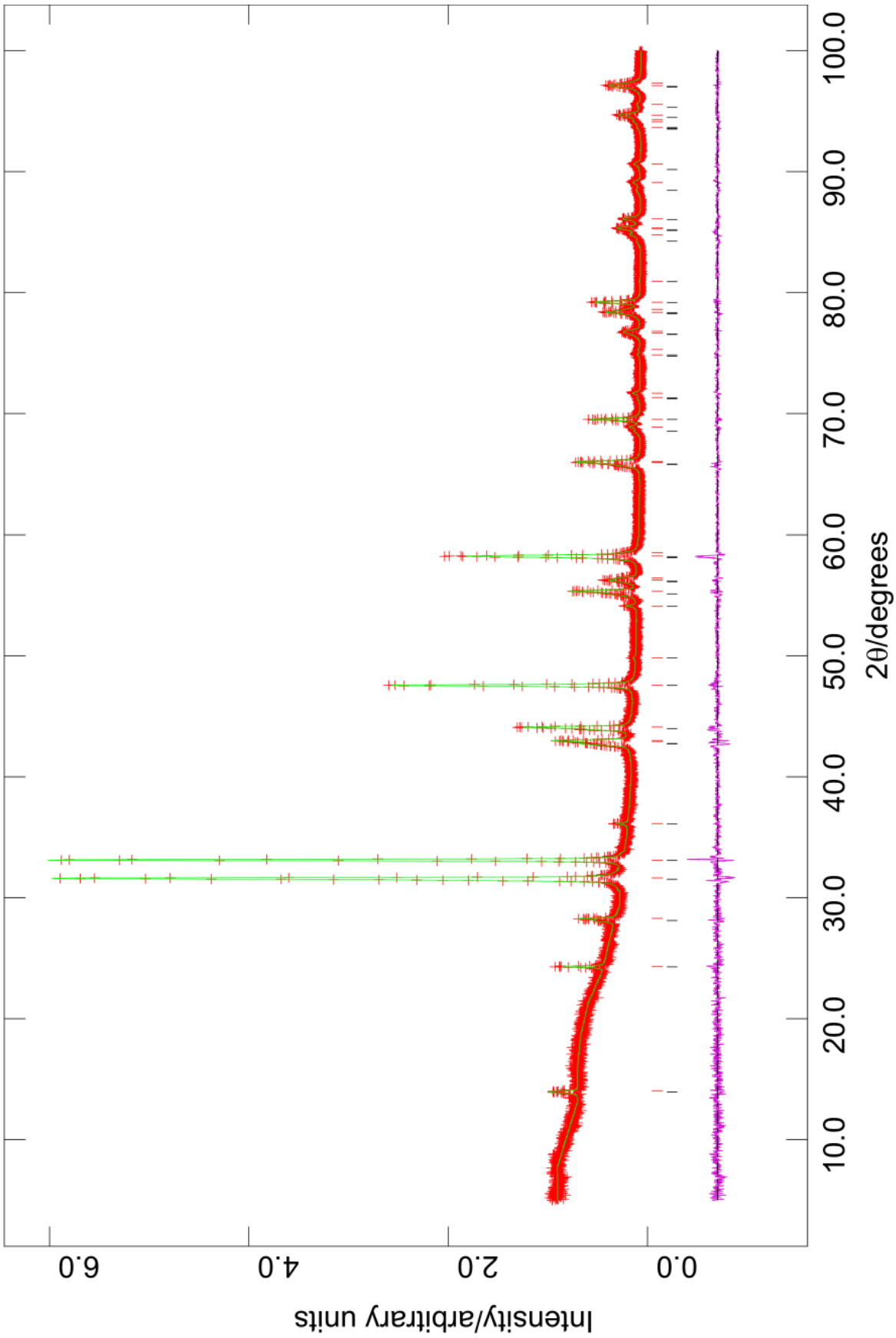

Figure 5.18 Observed (red +), calculated (green) and difference (pink) profiles as generated by a 2 phase Rietveld profile refinement of XRD data with peak positions indicated by black vertical lines.

Table 5.3 Refined atom and lattice parameters of $Sr_2Mn(O,F)_{4)}$ from refinement of XRD data in the space group *I4/mmm* (*a* = 3.8210(1) Å, *c* = 12.686(1) Å).

Atom	Site Symmetry	*x*	*y*	*z*	Occupancy	$U_{iso} \times 100$ (Å^2)
Sr	4e	0	0	0.3558(2)	1.0	0.16(4)
Mn	2a	0	0	0	1.0	0.04(7)
O(1)	4c	0	0.5	0	1.0	0.7(3)
O(2)	4e	0	0	0.155(1)	1.0	0.9(2)

Table 5.4 Refined atom and lattice parameters of $Sr_2MnO_{3.5+x}$ from refinement of XRD data in the space group *I4/mmm* (*a* = 3.8209(1) Å, *c* = 12.6086(4) Å).

Atom	Site Symmetry	*x*	*y*	*z*	Occupancy	$U_{iso} \times 100$ (Å^2)
Sr	4e	0	0	0.3529(2)	1.0	0.16(4)
Mn	2a	0	0	0	1.0	0.04(7)
O(1)	4c	0	0.5	0	0.69(3)	0.7(3)
O(2)	4e	0	0	0.156(1)	1.0	0.88(17)

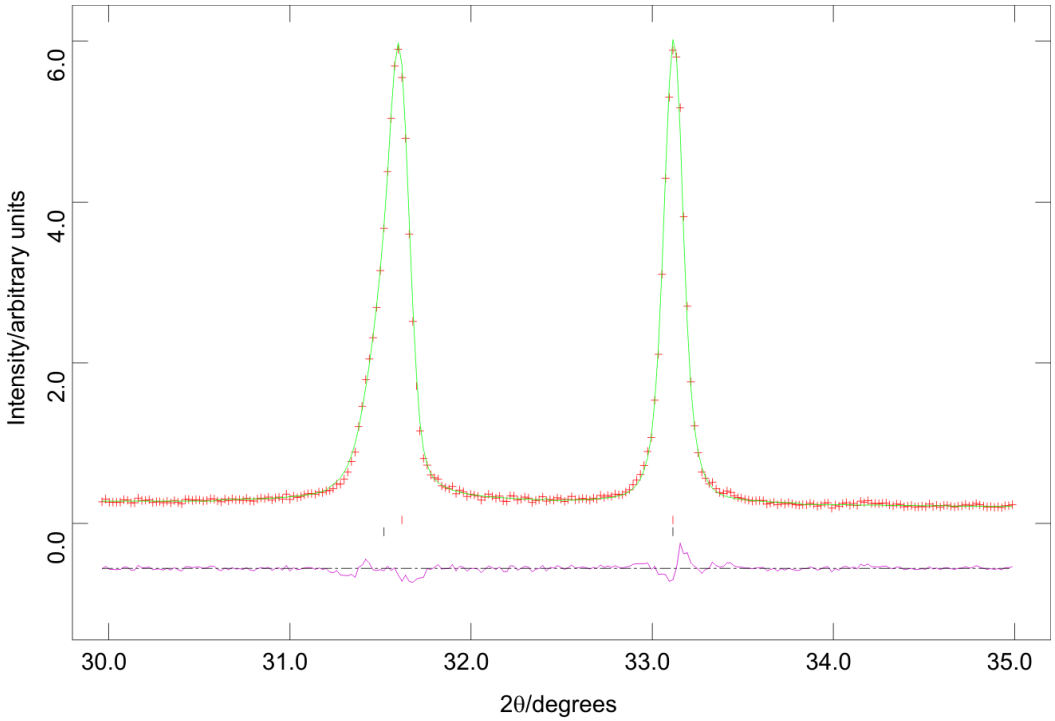

Figure 5.19 Close-up on the 2θ = 30º-35º region of the 2-phase Rietveld profile refinement showing the 1 0 3 and the 1 1 0 peaks.

Visual inspection of the 2-phase refinement of the XRD data shows a clear improvement in fit, which is particularly apparent in the more satisfactory fitting of the asymmetry in the most intense peaks (1 0 3 and 1 1 0 respectively), as shown in *Figure 5.19*.

As the inclusion of the starting material in the refinement of XRD data provided a marked improvement in fit, a 2-phase refinement based upon the TOF NPD data was also carried out. However, the inclusion of $Sr_2MnO_{3.5+x}$ failed to noticeably enhance the fit (see *Appendix 5.3*) and the resulting refinement statistics were similar to those obtained from the single-phase refinement. It was necessary to apply constraints to this refinement in order to keep the profile parameters for both phases equal. Relaxing these constraints resulted in an unstable refinement. It was apparent that the structural similarity of the 2 phases made them very hard to

differentiate between using TOF NPD, which is possibly due to the resolution of the TOF NPD technique.

5.3.2.9 Magnetic Measurements

Zero-field cooled and field-cooled DC magnetisation data were collected on several samples of $Sr_2MnO_{3.5+x}F_y$ in an applied field of 3000 Oe (0.3 T) from ≈ 2K to ≈ 320K. The zero-field cooled and field-cooled data (as shown in *Figure 5.20*) diverge below ≈ 20K, hence $Sr_2MnO_{3.5+x}F_y$ was observed to exhibit spin glass type behaviour. The plot of inverse susceptibility against temperature, shown in *Figure 5.21*, was still linear above the transition thus obeying the Curie-Weiss law. The gradient from this plot was used to calculate a paramagnetic moment of $9.82\mu_B$ *per* Mn. This high figure can most likely be attributed to small clusters of predominantly ferromagnetic interactions resulting from the mixed Mn^{3+}/Mn^{4+} oxidation state.

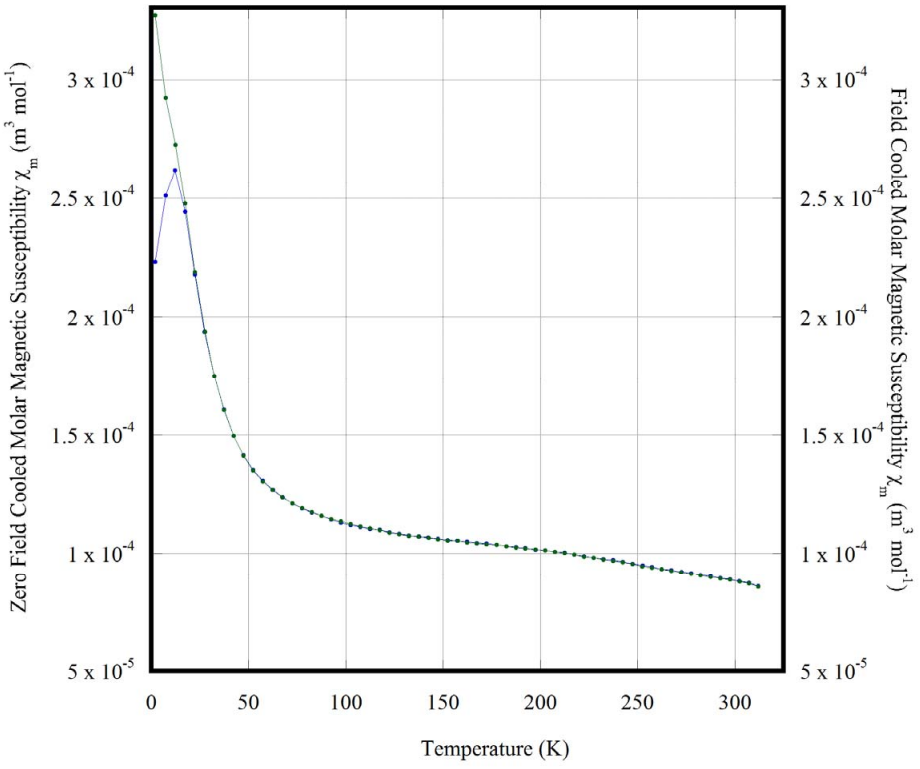

Figure 5.20 Plot of zero-field cooled (blue) and field-cooled (green) magnetic susceptibility (χ) against temperature.

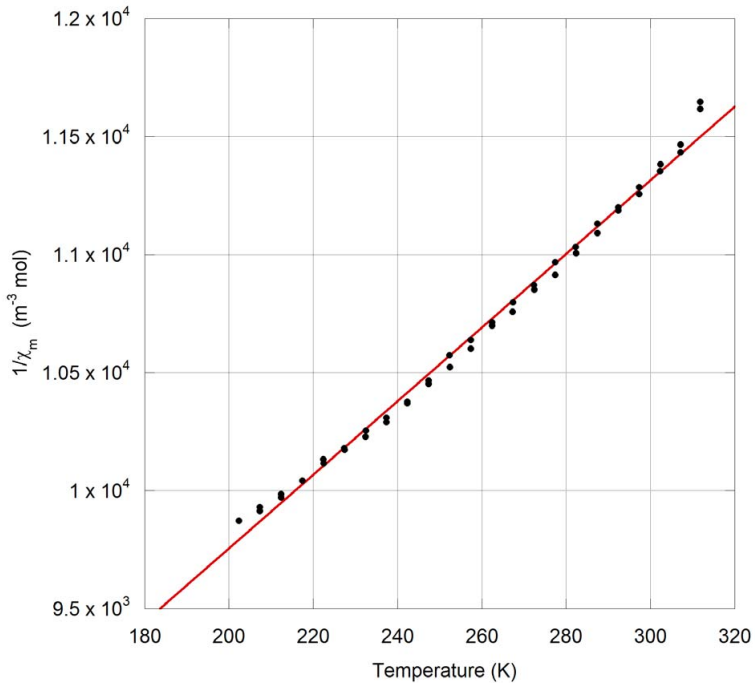

Figure 5.21 Plot of inverse magnetic susceptibility (1/ χ) against T.

5.4 Conclusions

Fluorine insertion into $Sr_2MnO_{3.5+x}F_y$ has been shown to produce both a low fluorine content phase retaining the monoclinic superstructure and a higher fluorine content phase reverting to the tetragonal K_2NiF_4-type structure.

As NPD data showed that the oxygen vacancy superstructure was no longer present in the bulk phase this supported the hypothesis that fluorine insertion to the fully stoichiometric composition $Sr_2Mn(O,F)_4$ resulted in a reversion to the K_2NiF_4 structure. However, as both the X-ray and neutron scattering lengths for oxygen and fluorine are very similar, it is hard to contrast between these 2 species using these techniques. The notion that the inserted fluorine adopted apical positions was suggested by TEM and Madelung energy calculations. Thus, it appears that fluorine insertion into this material facilitates an anion rearrangement whereby fluorine atoms displace apical oxygen atoms, as opposed to simply filling the equatorial oxygen vacancies present in the starting material.

The data presented in this chapter were collected on a sample containing uneven fluorination. Whilst the evidence collated using a variety of techniques suggests that the inserted fluorine displaces oxygen atoms from their apical positions thus instigating a return to K_2NiF_4 symmetry, it would be preferable to repeat the refinement on a single phase sample in order to obtain more reliable refined parameters. The sample used in this chapter was quite large, and even with multiple fluorine treatments contained some areas of lower fluorine content – it is likely the homogeneity in fluorine content of future samples could be improved by fluorinating smaller amounts of the starting material. This work could also be expanded to encompass materials displaying a similar oxygen defect structure.

5.5 References

1. D. Balz and K. Plieth (1955) *Zeitschrift für Elektrochemie* **59** 6 545.
2. N. Mizutani, A. Kitazawa, N. Onkuma and M. Kato (1971) *Kogyo Kagaku Zasshi* **73** 6 1087.
3. R. Kriegel and A. Feltz (1992) *Zeitschrift für Anorgische und Allgemeine Chemie* **617** 99.
4. R. Kriegel, H. Borrmann, A. Simon and A. Feltz (1993) *Zeitschrift für Naturforschung* **48B** 15.
5. J.-C. Bouloux, J.-L. Soubeyroux, G. Le Flem and P. Hagenmuller (1981) *Journal of Solid State Chemistry* **38** 34.
6. L. J. Gillie, A. J. Wright, J Hadermann, G. Van Tendeloo and C. Greaves (2002) *Journal of Solid State Chemistry* **167** 145.
7. L. J. Gillie (2003) *Ph.D Thesis*, The University of Birmingham.
8. V. Caignaert, N. Nguyen, M. Hervieu and B. Raveau (1985) *Materials Research Bulletin* **20** 479.
9. V. Caignaert (1997) *Journal of Magnetism and Magnetic Materials* **166** 117.
10. T. Mori, K. Inoue, N. Kamegashira, Y. Yamaguchi and K. Ohoyama (2000) *Journal of Alloys and Compounds* **296** 92.
11. K. R. Poeppelmeier, M. E. Leonowicz, J. C. Scanlon, J. M Longo and Y. B. Yelon (1985) *Journal of Solid State Chemistry* **45** 71.
12. M. E. Leonowicz, K. R. Poeppelmeier and J. M. Longo (1985) *Journal of Solid State Chemistry* **59** 71.
13. B.-H. Chen and D. Walker (1996) *Journal of Solid State Chemistry* **121** 498.
14. L. J. Gillie, A. J. Wright, J. Hadermann, G. Van Tendeloo and C. Greaves (2003) *Journal of Solid State Chemistry* **175** 188.
15. L. D. Aikens, L. J. Gillies, R. K. Li and C. Greaves (2002) *Journal of Materials Chemistry* **12** 264.
16. M. V. Lobanov, A. M. Abakumov, A. V. Sidorva, M. G. Rozova, O. G. D'Yachenko, E. V. Antipov, J. Hadermann and G. Van Tendeloo (2002) *Solid State Sciences* **4** 19.

17. A. C. Larson and R. B. Von Dreele (1990) *Generalised Structure Analysis System,* Los Alamos National Laboratory.
18. J. W. Weenk and H. A. Harwig (1977) *Journal of the Physics and Chemistry of Solids* **38** 1047, (adapted by C. Greaves, The School of Chemistry, The University of Birmingham).

Chapter Six

Synthesis and Characterisation of the Quaternary Nitride-Fluoride $Ce_2MnN_3F_{2-\delta}$

6.1 Introduction

Synthesis of the novel nitride-fluoride phase $Ce_2MnN_3F_{2-\delta}$ was achieved in collaboration with D. A. Headspith and M. G. Francesconi from The University of Hull. The synthesis of the starting material Ce_2MnN_3 was carried out entirely at The University of Hull, whilst the subsequent low-temperature solid-gas fluorine insertion reactions were done at The University of Birmingham. All magnetic data were collected at The University of Birmingham, as was the XRD data that are presented in this chapter. Both parties conducted aspects of the structural refinements, which were based on XRD and NPD data.

6.1.1 The T- and T'-Type Structures: La_2CuO_4 and Nd_2CuO_4

The structure of La_2CuO_4 was first reported and characterised by Longo *et al.* using the space group *Fmmm* with lattice parameters a = 5.363(5) Å, b = 5.409(5) Å and c = 13.17(1) Å [1]. This structure is often described as an orthorhombic distortion of K_2NiF_4 [2] with 2 apical Cu-O bonds elongated and 4 equatorial Cu-O bonds

compressed due to Jahn-Teller effects. The orthorhombic La_2CuO_4 unit cell is related to the tetragonal K_2NiF_4 unit cell parameters a_t, and c_t by $a \approx \sqrt{2}a_t$, $b \approx \sqrt{2}a_t$ and $c \approx c_t$.

Nd_2CuO_4 was reported to crystallise in the *I*4/*mmm* space group with lattice parameters a = 3.945 Å, and c = 12.171 Å [3]. The contraction in *c*-parameter compared to La_2CuO_4 (c = 13.17 Å) is chiefly due to the absence of apical oxygen positions in Nd_2CuO_4, although the smaller size of the Nd cation is also a contributing factor. La_2CuO_4-type structures are often referred to as T structures whereas Nd_2CuO_4-type structures are known as T' structures.

The adoption of the T or the T' structure in A_2BO_4 materials is closely related to the size of the A cation as demonstrated by Bringley *et al*. for the mixed rare earth systems $La_{2-x}RE_xCuO_4$ (RE = Nd-Y) [4]. This work reported that a perovskite-like tolerance factor t could be applied to establish stability limits for the T structure ($0.87 \leq t \leq 0.99$) and the T' structure ($0.83 \leq t \leq 0.86$) with the smaller rare earth cations ($t \leq 0.83$) unable to form stable $(RE)_2CuO_4$ compounds [4]. The La_2CuO_4- and Nd_2CuO_4-type structures are shown in *Figure 6.1* and *Figure 6.2*, respectively.

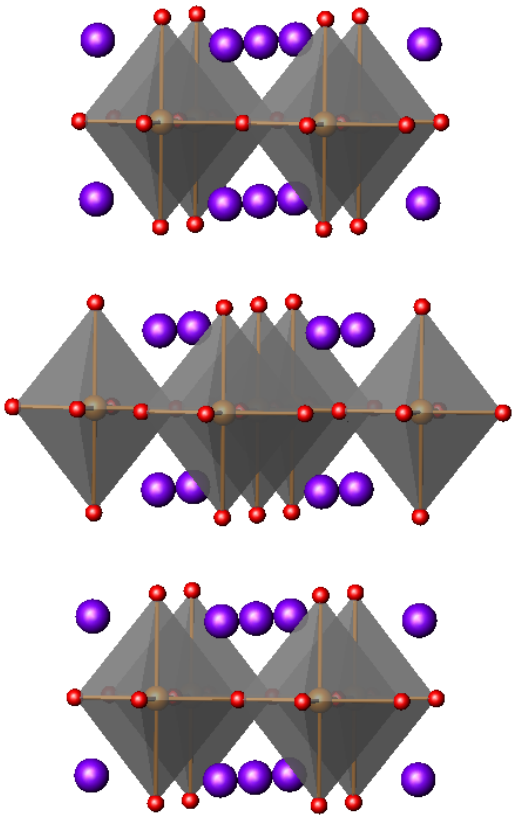

Figure 6.1 The structure of La_2CuO_4 (T-type) with La shown as purple spheres, O as red spheres, Cu as orange spheres, Cu-O bonds highlighted in orange and CuO_6 octahedra shaded in grey.

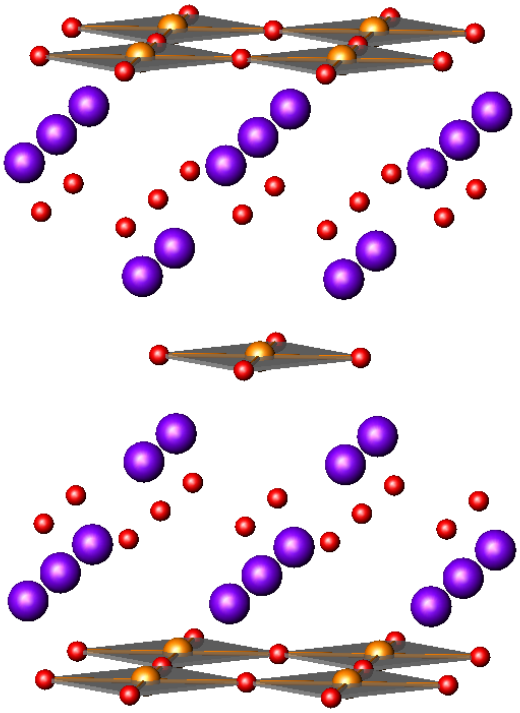

Figure 6.2 The structure of Nd_2CuO_4 (T'-type) with Nd shown as purple spheres, O as red spheres, Cu as orange spheres, Cu-O bonds highlighted in orange and CuO_4 square planar units shaded in grey.

6.1.2. The Structure of Sr_2CuO_3

The synthesis of the ternary cuprate Sr_2CuO_3 and subsequent determination of its structure by investigation of single crystal X-ray data was first described by Teske and Müller-Buschbaum in 1969 [5]. It was reported to crystallize with orthorhombic symmetry in the space group *Immm* with the lattice parameters $a = 12.68$ Å, $b = 3.91$ Å and $c = 3.48$ Å, with the synthesis and characterisation of an isostructural Ca analogue, Ca_2CuO_3 [6] reported shortly afterwards. In a later powder neutron diffraction study of the structures of some ternary copper (II) oxides by Weller and Lines [7], the lattice parameters of Sr_2CuO_3 were determined with higher accuracy and were given as $a = 12.7163(2)$ Å, $b = 3.9159(1)$ Å and $c = 3.5032(1)$ Å.

Sr_2CuO_3 is fundamentally composed of isolated linear chains formed from square planar CuO_4 polyhedra that are exclusively corner-linked. This linear arrangement of corner-linked CuO_4 units gives rise to infinite 1-dimensional $[CuO_3]_n^{4-}$ chains. A framework of trigonal prisms consisting of neighbouring O^{2-} surrounding Sr^{2+} holds these linear chains of CuO_4 units together [5, 8]. The full crystallographic structure of Sr_2CuO_3 is shown in *Figure 6.3*.

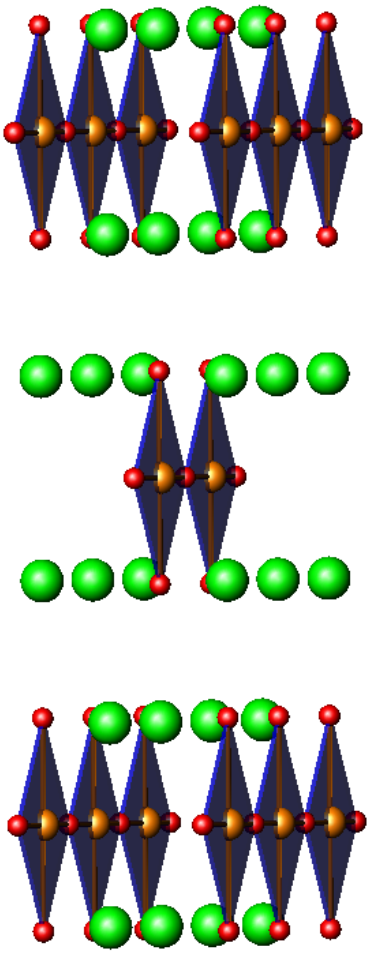

Figure 6.3 The crystallographic structure of Sr_2CuO_3. The green spheres represent Sr cations. The orange spheres represent Cu cations, the red spheres represent O anions and the CuO_4 square planar units are highlighted in blue.

6.1.3 Fluorine Insertion to form Superconducting $Sr_2CuO_2F_{2+\delta}$

The low-temperature reaction of Sr_2CuO_3 with gaseous fluorine by Al Mamouri *et al*. produced the first known superconducting oxide-fluoride phase $Sr_2CuO_2F_{2+\delta}$ crystallising in the space group *Fmmm* with lattice parameters a = 5.394(1) Å, b = 5.513(1) Å and c = 13.468(3) Å [9].

The structure of Sr_2CuO_3 is essentially an oxygen deficient La_2CuO_4-type structure where the oxygen defects in the equatorial plane leave chains of corner-linked square planar CuO_4, as opposed to CuO_6 octahedra. Upon the fluorination of La_2CuO_4 to form $La_2CuO_4F_\delta$, the F^- ions are simply incorporated into interstitial sites

and function as electronic dopants by inducing hole states in the CuO_2 planes already present in the La_2CuO_4 structure whereas $Sr_2CuO_2F_{2+\delta}$ is formed by the F anions preference for apical sites instigating a significant structural rearrangement (rather than merely acting as an electronic dopant) by which oxygen migrates to the equatorial sites thus adopting La_2CuO_4-type structure [10, 11].

Fluorine insertion into Sr_2CuO_3 involves three concurrent processes: direct substitution of F^- for O^{2-}, interstitial F^- insertion and most notably a structural rearrangement to form the superconducting phase $Sr_2CuO_2F_{2+\delta}$. As F^- ions have a preference for apical sites, they displace the O^{2-} ions from the apical sites that they occupy in Sr_2CuO_3 to the equatorial sites in the fluorinated phase. This substitution of F^- into the apical sites once occupied by the O^{2-} ions results in $Sr_2CuO_2F_{2+\delta}$ containing planes as opposed to 1-dimensional chains of CuO_4. In addition to this, F^- ions are also incorporated into interstitial sites, depending on the extent of the fluorination [12]. The dopant effect of insertion of fluorine into Sr_2CuO_3 causes partial oxidation of Cu^{2+} cations to create a mixed Cu^{2+}/Cu^{3+} oxidation state in 2-dimensional planes of CuO_4 polyhedra thus providing the electronic and structural prerequisites for superconductivity.

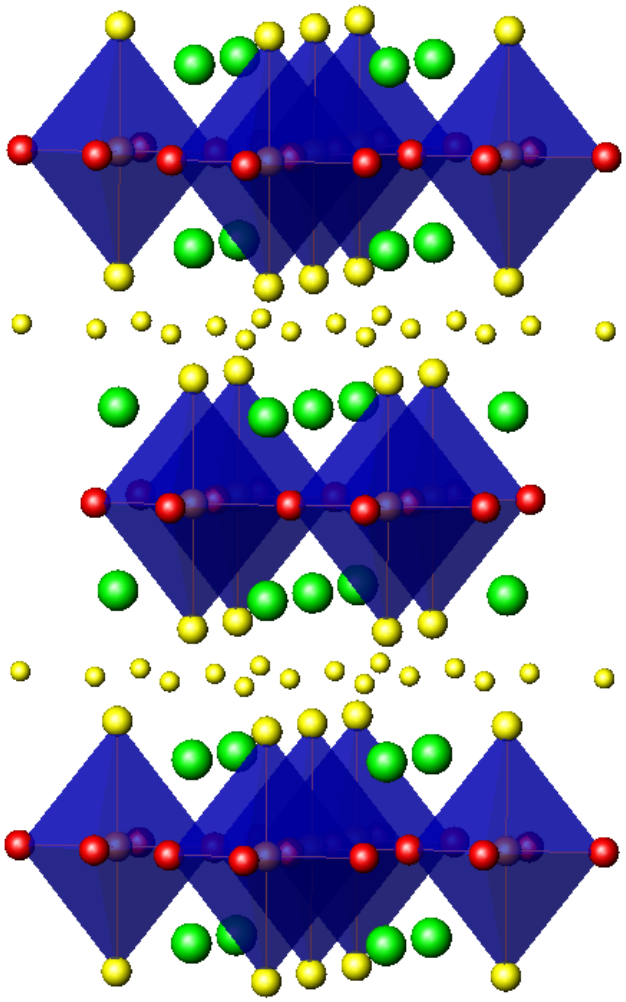

Figure 6.4 The crystallographic structure of $Sr_2CuO_2F_{2+\delta}$. The green spheres represent Sr cations, orange spheres represent Cu cations, red spheres represent O anions, yellow spheres represent F anions (smaller spheres denote interstitial F) and the $Cu(O,F)_6$ octahedra are highlighted in blue.

The superconducting properties of the $Sr_2CuO_2F_{2+\delta}$ phase can be tuned by controlling levels of fluorine insertion (and hence Cu oxidation state) and have also been shown to be further enhanced by doping to form $Sr_{2-x}A_xCuO_2F_{2+\delta}$ where A= Ca, Ba [13-15].

Other ternary oxides isostructural with Sr_2CuO_3 such as the Ca analogue Ca_2CuO_3 and $Ba_{2-x}Sr_xPdO_3$ ($0 < x < 1$) have also been shown to be amenable to low temperature fluorine insertion reactions [16, 17]. However, in the fluorinated phases $Ca_2CuO_2F_{2+\delta}$ and $Ba_{2-x}Sr_xPdO_2F_2$ ($0 \leq x \leq 1.5$), the Cu and Pd cations retain square

planar coordination hence adopting a Nd_2CuO_4 (T'-type) structure instead of the predicted La_2CuO_4 (T-type) structure.

In $Ca_2CuO_2F_{2+\delta}$, unlike $Sr_2CuO_2F_{2+\delta}$, the apical oxygen anions are again displaced to fill the equatorial positions, but the F^- anions are preferentially located at sites between the Ca bilayers characteristic of the Nd_2CuO_4-type structure with some interstitial F^- anions also occupying apical positions. Likewise, for $Ba_{2-x}Sr_xPdO_2F_2$ ($0 \leq x \leq 1.5$), it was reported that the F^- anions are located within the Ba/Sr layers with the T' structure which is also consistent with the preference of Pd^{2+} cations for square planar coordination.

Al-Mamouri *et al*. carried out a structural refinement of $Ca_2CuO_2F_{2+\delta}$ based on NPD data in the space group *I*4/*mmm* using the Nd_2CuO_4 (T'-type) structure as a model, and reported the following lattice parameters: $a = 3.850(1)$ Å and $c = 11.842(3)$ Å [16].

The assignment of the T-type structure to $Sr_2CuO_2F_{2+\delta}$ and the T'-type structure for $Ca_2CuO_2F_{2+\delta}$ is further supported by consideration of the *c* parameter in both cases before and after fluorination. The fluorination of Sr_2CuO_3 ($c = 12.716$Å [7]) to produce $Sr_2CuO_2F_{2+\delta}$ ($c = 13.468$ Å [9]) shows a clear expansion in *c*-parameter, whereas the fluorination of the Ca analogue Ca_2CuO_3 ($c = 12.234$ Å [6]) to give $Ca_2CuO_2F_{2+\delta}$ ($c = 11.842$ Å [16]) clearly shows a contraction in the *c*-parameter consistent with a T'-type structure.

6.1.4 Ce_2MnN_3: A Nitride Analogue of Sr_2CuO_3

A variety of anion insertion reactions have been demonstrated in other ternary oxides with La_2CuO_4 related structures and such reactions are a common approach to inducing or improving useful properties of the starting material such as

superconductivity. Few studies to date have focused on using anion insertion to tune the structural and electronic properties of ternary nitrides, although some single crystal nitride-chlorides have been synthesised such as K_2OsNCl_5 [18], $LiBa_4[Mo_2N_7]BaCl_2$ [19], $Ba_4[WN_4]Cl_2$ [20], $Ba_{25}Nb_5N_{19}Cl_{18}$ [21], and $Ba_3Ta_3N_6Cl$ [22].

It is known that a handful of ternary nitrides are isostructural with Sr_2CuO_3 and may be similarly amenable to fluorine insertion reactions. Benz and Zachariason synthesised Th_2CrN_3, Th_2MnN_3, U_2CrN_3 and U_2MnN_3 and found this family of materials to adopt an anion-deficient orthorhombic La_2CuO_4 related structure analogous to Sr_2CuO_3 [23]. These materials were produced from the solid state reaction in 1 atm $N_{2(g)}$ of the actinide mononitride (ThN or UN) with the transition metal (Cr or Mn). However, due to the intrinsic radioactivity of thorium and uranium, these materials were deemed unsuitable for fluorination studies. It was shown by Niewa *et al*. that cerium could be used in lieu of uranium to prepare Ce_2CrN_3 and Ce_2MnN_3 which were shown to be isostructural with U_2CrN_3 and U_2MnN_3 [24].

The structure of Ce_2MnN_3 is therefore structurally related to Sr_2CuO_3, with Sr and Cu replaced by Ce and Mn respectively. Similarly to Sr_2CuO_3, the structure of Ce_2MnN_3 is made up of infinite chains of corner-linked MnN_4 units and was also assigned the space group *Immm* [24], although the square planar geometry is slightly distorted as the bond length between Mn and bridging N atoms is shorter than the bond length between Mn and terminal N atoms.

In order to fully understand the electronic effects of fluorine insertion into Ce_2MnN_3, it is first necessary to clarify the oxidation states of Ce and Mn in this material. Assuming a formal charge of N^{3-} for the anion, several permutations exist for the cation oxidation states, the most plausible of which are $(Ce^{IV})_2Mn^{I}N_3$, $(Ce^{III})_2Mn^{III}N_3$ and $Ce^{III}Ce^{IV}Mn^{II}N_3$. The effective magnetic moment was reported by

Niewa *et al*. to be $\mu_{eff} = 0.53\ \mu_B$. The magnetic moment calculated for Ce^{3+} (f^1) is $\mu_{eff} = 2.54\ \mu_B$ whilst Mn^{3+} (d^4) has $\mu_{eff} = 4.90$ (high spin, $t_{2g}^3 e_g^1$) or $\mu_{eff} = 2.83$ (low spin, t_{2g}^4), hence $(Ce^{III})_2Mn^{III}N_3$ does not fit the experimental data. The assignment $Ce^{III}Ce^{IV}Mn^{II}N_3$ is also unlikely as although Ce^{4+} has an f^0 configuration ($\mu_{eff} = 0$), Mn^{2+} (d^5) has $\mu_{eff} = 5.92$ (high spin, $t_{2g}^3 e_g^2$) or $\mu_{eff} = 1.73$ (low spin, t_{2g}^5). From this data it was deduced that the oxidation states $(Ce^{IV})_2Mn^{I}N_3$ seemed most feasible, with Ce^{4+} (f^0, $\mu_{eff} = 0$) and Mn^{+} (d^6) in a low spin configuration (t_{2g}^6, $\mu_{eff} = 0$) and the small experimentally observed magnetic moment was thought to be due to an impurity [24]. The assignment of Ce^{4+} and low spin Mn^{+} has also been supported by X-ray Absorption spectroscopy and computer modelling *via* the Linear Muffin-Tin Orbital method [25, 26].

As the structure-type of Ce_2MnN_3 has previously been shown to be highly amenable to low-temperature solid-gas fluorine insertion reactions, it was postulated that a similar approach could be utilised to control the Mn oxidation state. Assuming that the oxidation states of Ce and N remain invariable upon fluorination, it could be possible to oxidise Mn to prepare $(Ce^{IV})_2Mn^{II}N_3F$, $(Ce^{IV})_2Mn^{III}N_3F_2$, $(Ce^{IV})_2Mn^{IV}N_3F_3$ or to induce a mixed Mn oxidation state depending on the extent of fluorine insertion.

6.2 Experimental Procedures

6.2.1 Synthesis of Ce_2MnN_3

The starting material Ce_2MnN_3 was prepared *via* high temperature solid state reaction by D. A. Headspith and M. G. Francesconi at The University of Hull. A stoichiometric mixture of Ce and Mn metal powders (Aldrich, 99.99%) were reacted in a niobium crucible inside the quartz tube of an upright tube furnace under nitrogen gas, which was passed through Varian gas clean filters in order to remove any traces

of oxygen and moisture. Once the reaction vessel was in place, the system was flushed with nitrogen for 30 minutes before heating to the reaction temperature of 900°C. The polycrystalline mixture was held at 900°C for 36 hours, then ground and reacted under the same conditions until a homogenous sample was achieved. Although Ce_2MnN_3 is stable in air, where possible the sample was stored and handled within an argon filled glove box ($O_2 \leq$ 0.1 ppm, $H_2O \leq$ 0.1 ppm).

6.2.2 Synthesis of $Ce_2MnN_3F_{2-\delta}$

Finding the optimum conditions for the fluorination of Ce_2MnN_3 proved to be a rather difficult process, as this nitride was highly responsive to the presence of $F_{2(g)}$, rapidly forming CeF_3 and MnF_2 upon the smallest change in reaction temperature or duration. Both the pulse method (as described in Section 2.1.2(a)) and reaction with static fluorine (as described in Section 2.1.2(b)) were investigated over a range of conditions, the former synthesis route meeting with the most success.

Solid-gas reactions of Ce_2MnN_3 with $10\%F_{2(g)}/90\%N_{2(g)}$ using the pulse method typically used < 0.1 g Ce_2MnN_3, in a nickel boat. For diagrams of the solid-gas fluorination apparatus please see *Figure 2.1* and *Figure 2.2*. The sample was placed in the nickel reaction tube, which was subsequently sealed, before the system was flushed with dry nitrogen for 30 minutes. The temperature of the tube furnace was raised to the desired reaction temperature under nitrogen, then once the temperature was stable the gas was switched to the $10\%F_{2(g)}/90\%N_{2(g)}$ mixture. The solid-gas reaction was carried out for the desired amount of time, after which the gas flow was switched back to dry nitrogen. The temperature of the tube furnace was allowed to cool to room temperature after the last of the $10\%F_{2(g)}/90\%N_{2(g)}$ mixture had passed through the system.

The initial synthetic strategy was to use the same conditions as had been reported for the fluorination of Sr_2CuO_3 (15 minute reaction with $10\%F_{2(g)}/90\%N_{2(g)}$ at 230°C). It transpired that such conditions were far too harsh for Ce_2MnN_3, resulting in the formation of an amorphous phase. Numerous experiments were carried out varying the duration of reaction from 10-30 minutes in the temperature range 40-230°C and it was found that it was only possible to produce the fluorinated phase within a small range of reaction conditions.

Significant amounts of the fluorinated phase $Ce_2MnN_3F_{2-\delta}$ were produced during reactions carried out in the temperature range 90-115°C with $10\%F_{2(g)}/90\%N_{2(g)}$ pulses lasting for 15 minutes. However, in all samples produced, some unfluorinated starting material remained. Such temperatures are low, even for low-temperature fluorination reactions, hence starting material impurities were not unexpected.

Fluorination for periods of time in excess of 15 minutes increased the amount of amorphous material in the samples and showed no improvement in the quantity of $Ce_2MnN_3F_{2-\delta}$ produced. Annealing in $N_{2(g)}$ between 150-250°C caused the sample to decompose with the primary product being CeF_3. In the course of this study, the solid-gas reaction conditions used to maximise yield of the target phase $Ce_2MnN_3F_{2-\delta}$ whilst avoiding formation of the amorphous phase, CeF_3 and MnF_2 were a 15 minute pulse of $10\%F_{2(g)}/90\%N_{2(g)}$ at 95°C. Unfortunately, despite the investigation of a sizeable range of reaction conditions, the synthesis of a pure fluorinated phase $Ce_2MnN_3F_{2-\delta}$ has yet to be achieved, thus it should be borne in mind that all results discussed contain a significant amount of Ce_2MnN_3 in the sample and all refinements are 2-phase in order to account for the presence of unfluorinated Ce_2MnN_3.

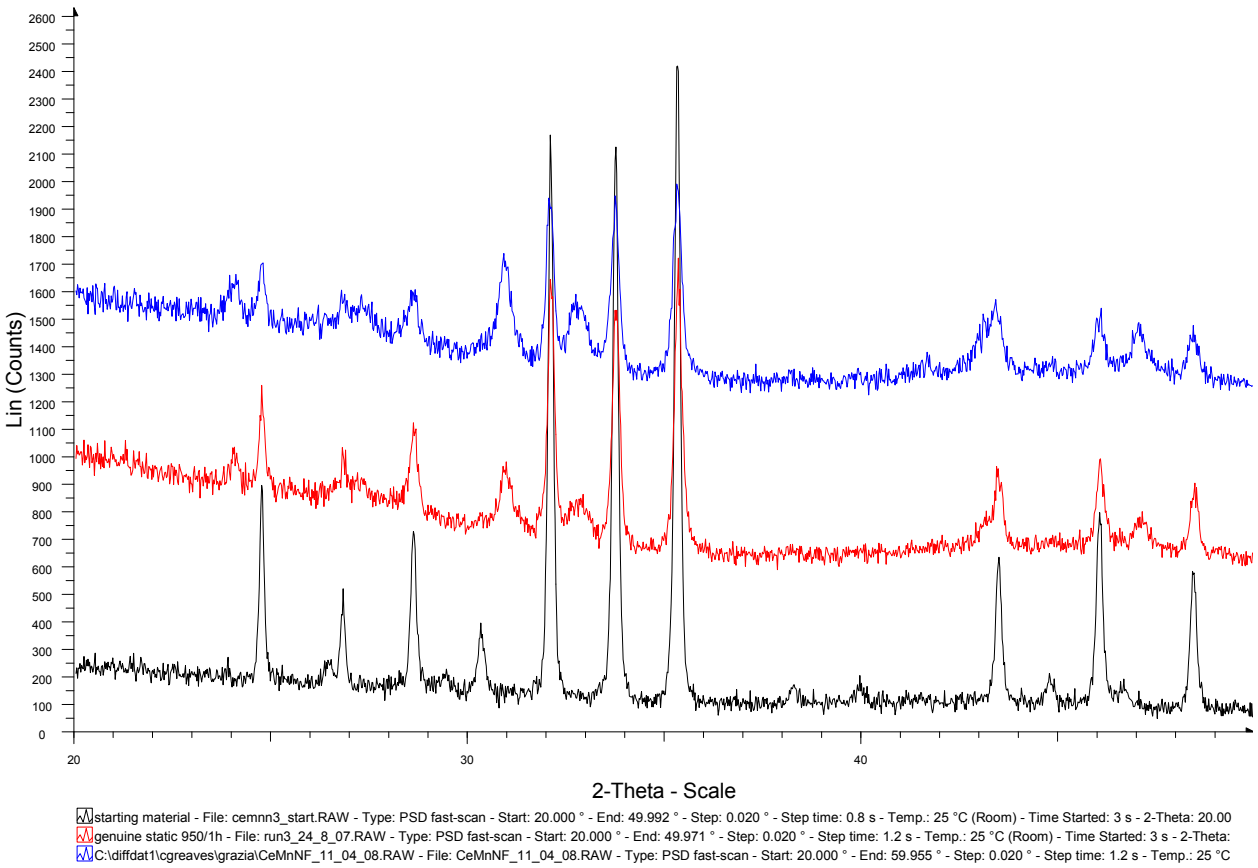

Figure 6.5 Stacked XRD plots showing the starting material Ce_2MnN_3 (black trace), a typical result with approximately ⅓ $Ce_2MnN_3F_{2-\delta}$ and ⅔ unfluorinated Ce_2MnN_3 (red trace) and a sample with approximately ½ $Ce_2MnN_3F_{2-\delta}$ and ½ unfluorinated Ce_2MnN_3 (blue trace).

Table 6.1 A selection of fluorination conditions explored for Ce_2MnN_3.

Temperature	Duration	Conditions	Observations
210°C	15 minutes	Flowing $10\%F_{2(g)}/90\%N_{2(g)}$	Mostly CeF_4
180°C	15 minutes	Flowing $10\%F_{2(g)}/90\%N_{2(g)}$	Mostly CeF_4
100°C	15 minutes	Flowing $10\%F_{2(g)}/90\%N_{2(g)}$	Mostly CeF_4
100°C	10 minutes	Static $10\%F_{2(g)}/90\%N_{2(g)}$	Mostly Ce_2MnN_3, MnF_2
40°C	10 minutes	Static $10\%F_{2(g)}/90\%N_{2(g)}$ *	Ce_2MnN_3
70°C	20 minutes	Flowing $10\%F_{2(g)}/90\%N_{2(g)}$ †	Mostly Ce_2MnN_3, MnF_2
80°C	30 minutes, 20 minutes	Flowing $10\%F_{2(g)}/90\%N_{2(g)}$, Static $10\%F_{2(g)}/90\%N_{2(g)}$	Ce_2MnN_3
90°C	30 minutes, 60 minutes	Flowing $10\%F_{2(g)}/90\%N_{2(g)}$, Static $10\%F_{2(g)}/90\%N_{2(g)}$ ‡	Ce_2MnN_3, CeF_3 after annealing
95°C	60 minutes	Static $10\%F_{2(g)}/90\%N_{2(g)}$	Ce_2MnN_3, $Ce_2MnN_3F_{2-\delta}$
95°C	300 minutes	Static $10\%F_{2(g)}/90\%N_{2(g)}$	Ce_2MnN_3, $Ce_2MnN_3F_{2-\delta}$, amorphous material
100°C	120 minutes	Static $10\%F_{2(g)}/90\%N_{2(g)}$	Ce_2MnN_3, $Ce_2MnN_3F_{2-\delta}$, amorphous material
95°C	15 minutes	Flowing $10\%F_{2(g)}/90\%N_{2(g)}$	Ce_2MnN_3, $Ce_2MnN_3F_{2-\delta}$
97°C	15 minutes	Flowing $10\%F_{2(g)}/90\%N_{2(g)}$	Ce_2MnN_3, $Ce_2MnN_3F_{2-\delta}$

* *annealed in Ar(g) for 300 minutes at 100°C*
† *annealed in Ar(g) for 300 minutes at 150°C*
‡ *annealed in N_2(g) for 300 minutes at 200°C*

Table 6.1 gives an insight into the breadth of reaction conditions that Ce_2MnN_3 was subjected to, using both static and flowing $10\%F_{2(g)}/90\%N_{2(g)}$. Even using the optimised fluorination conditions (15 minute pulses of $10\%F_{2(g)}/90\%N_{2(g)}$ in the temperature range 95-115ºC), the phase composition of the products still varied between approximately ⅓ $Ce_2MnN_3F_{2-\delta}$: ⅔ Ce_2MnN_3 and ½ $Ce_2MnN_3F_{2-\delta}$: ½ Ce_2MnN_3, a phenomenon most likely attributable to minute differences in the flow rate of $10\%F_{2(g)}/90\%N_{2(g)}$.

6.3 Results and Discussion

The results described in the following section were obtained from a full collaboration involving The University of Birmingham and The University of Hull. Powder XRD data were collected at The University of Birmingham, with refinements based on these XRD data performed independently both at The University of Birmingham and The University of Hull. NPD data were collected jointly at the Institut Laue-Langevin and these data were used by The University of Hull to determine the important structure type. Consideration of magnetic results obtained by the author showed that the composition implied by the structure was, however, not compatible with susceptibility data, and a further NPD refinement that focused on the anion site occupancies was performed.

6.3.1 Preliminary Refinement Based on XRD Data Using K_2NiF_4 Model

Examination of the fluorinated samples *via* XRD showed the presence of 2 phases. One set of peaks was clearly due to residual Ce_2MnN_3 in the sample, whereas the other set of peaks could not be identified using the JCPDS database of known XRD patterns [27]. Thus, this set of peaks was attributed to a hitherto unknown compound and were indexed on a tetragonal unit cell, using the computer program INDEX [28]. It was postulated that this tetragonal phase was a novel quaternary nitride-fluoride $Ce_2Mn(N,F)_x$ with a K_2NiF_4 related structure, since the *c* parameter increased by ≈ 5% compared with Ce_2MnN_3.

A preliminary structure refinement using XRD data was carried out using the GSAS suite of programs [29] with K_2NiF_4 as a model for the fluorinated phase. As the X-ray scattering lengths of N and F are very similar, XRD data could not yield any accurate information about N/F distribution or stoichiometry, hence the structural

refinement of XRD data was based on a stoichiometry $Ce_2Mn(N,F)_4$ with all anions modelled as O. The refined atom parameters are shown in *Table 6.2*.

Table 6.2 Table of atomic parameters from the refinement of $Ce_2Mn(N,F)_4$ XRD data in the space group *I*4/*mmm* modelled on the K_2NiF_4 structure. Thermal parameters were set at zero for this refinement due to uncertainty in the absorption correction.

Atom	**Site Symmetry**	***x***	***y***	***z***	**Occupancy**
Ce	4e	0	0	0.3630(4)	1
Mn	4e	0	0	0.0323(12)	0.5
N/F(eq)	4c	0.5	0	0	1
N/F(ap)	4e	0	0	0.1516(30)	1

The background was subtracted for the profile refinement plot shown in *Figure 6.6* as it was rather uneven due to some unknown amorphous material. Please refer to *Appendix 6.1* for the profile refinement plot without the background subtraction. Although the isotropic thermal parameters were constrained to be equal for all atoms, the value refined to a slightly negative value; hence, U_{iso} was fixed at zero for this preliminary refinement. Transmission XRD data is quite sensitive to uncertainty in the correction for sample absorption, which in this case seemed to be reflected in the tendency towards negative thermal parameters.

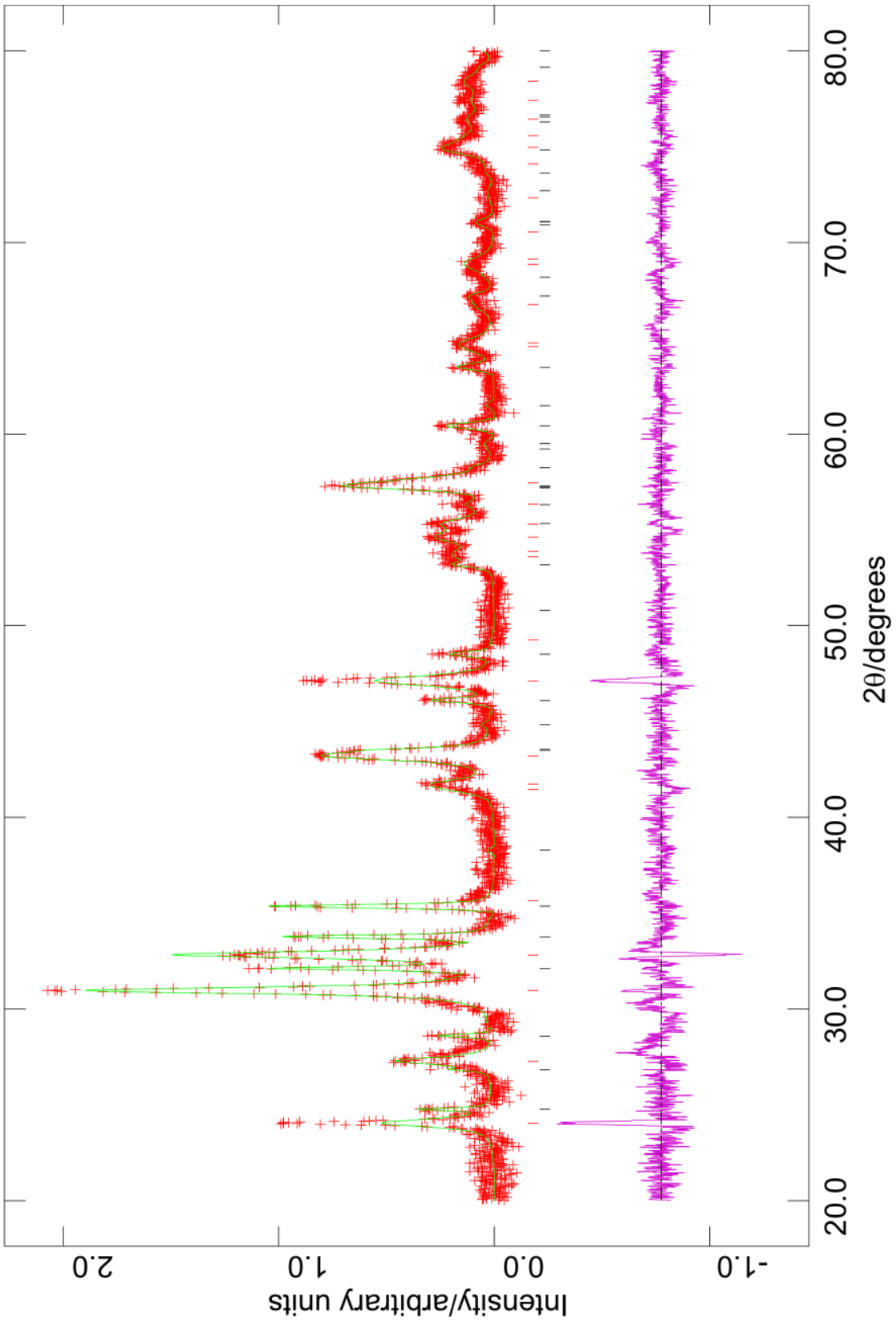

Figure 6.6 Observed (red +), calculated (green) and difference (pink) profiles of $Ce_2Mn(N,F)_4$ as generated by the Rietveld profile refinement of XRD data using a K_2NiF_4 model. Red vertical lines highlight the positions of the $Ce_2Mn(N,F)_4$ diffraction peaks whilst black vertical lines correspond to residual Ce_2MnN_3.

This preliminary refinement converged with $\chi^2 = 1.969$, $R_p = 3.12\%$ and $R_{wp} = 4.15\%$, and confirmed that the fluorinated phase does indeed adopt a K_2NiF_4-related tetragonal structure with refined lattice parameters $a = 3.8516(5)$ Å and $c = 13.0501(25)$ Å, showing an increase in the c parameter relative to Ce_2MnN_3 ($c = 12.4601$ Å). Comparing the atom parameters with those of K_2NiF_4 [2] it is apparent that the refined Mn position is slightly displaced from the ideal (0, 0, 0) site, suggesting that the Mn ions are situated in an asymmetrical environment. This would be consistent with fluorine insertion occurring in alternate layers within the structure as observed in the isostructural staged materials $LaSrMnO_4F$ [30] and $Sr_2TiO_3F_2$ [31] whilst the Mn is situated in an asymmetrical octahedral co-ordination environment containing both N and F.

6.3.2 Refinement Based on XRD Data Using Staged $LaSrMnO_4F$ Model

The refinement of XRD data using K_2NiF_4 as a structural model gave a reasonable fit to the experimental data, although it was apparent that the assignment of a model allowing for staged fluorine insertion would better describe the actual structure of the fluorinated phase. Hence this refinement was modelled on the structure previously observed in the staged materials $LaSrMnO_4F$ and $Sr_2TiO_3F_2$, whereby fluorine insertion occurs in interstitial sites in alternate rocksalt layers. All anions were modelled as O for this refinement due to the limitations of XRD data with respect to distinguishing between N and F. The interstitial site is labelled (int), (eq) denotes the equatorial sites in the $Mn(N,F)_6$ octahedra, (ap1) describes the apical site directed towards the interstitial site and (ap2) the apical site facing away from the interstitial site. Again, the background was subtracted from the profile refinement plot and thermal parameters were constrained to zero.

Visually, this model could be seen to produce a better fit to the experimental data (as shown in *Figure 6.7*), which is reflected in the improved refinement statistics: $\chi^2 = 1.773$, $R_p = 3.04\%$ and $R_{wp} = 3.94\%$. The refined lattice parameters were $a = 3.8496(5)$ Å and $c = 13.042(3)$ Å and atomic parameters are shown in *Table 6.3*.

Table 6.3 Table of atomic parameters from the refinement of $Ce_2Mn(N,F)_4$ XRD data in the space group *P*4/*nmm* modelled on the $LaSrMnO_4F$ structure.

Atom	Site Symmetry	*x*	*y*	*z*	Occupancy
Ce(1)	2c	0.75	0.75	0.123(1)	1
Ce(2)	2c	0.75	0.75	0.3893(8)	1
Mn	2c	0.25	0.25	0.282(2)	1
N/F (eq)	4f	0.25	0.75	0.25(1)	1
N/F (ap1)	2c	0.25	0.25	0.12(1)	1
N/F (ap2)	2c	0.25	0.25	0.409(7)	1
N/F (int)	2a	0.25	0.75	0	1

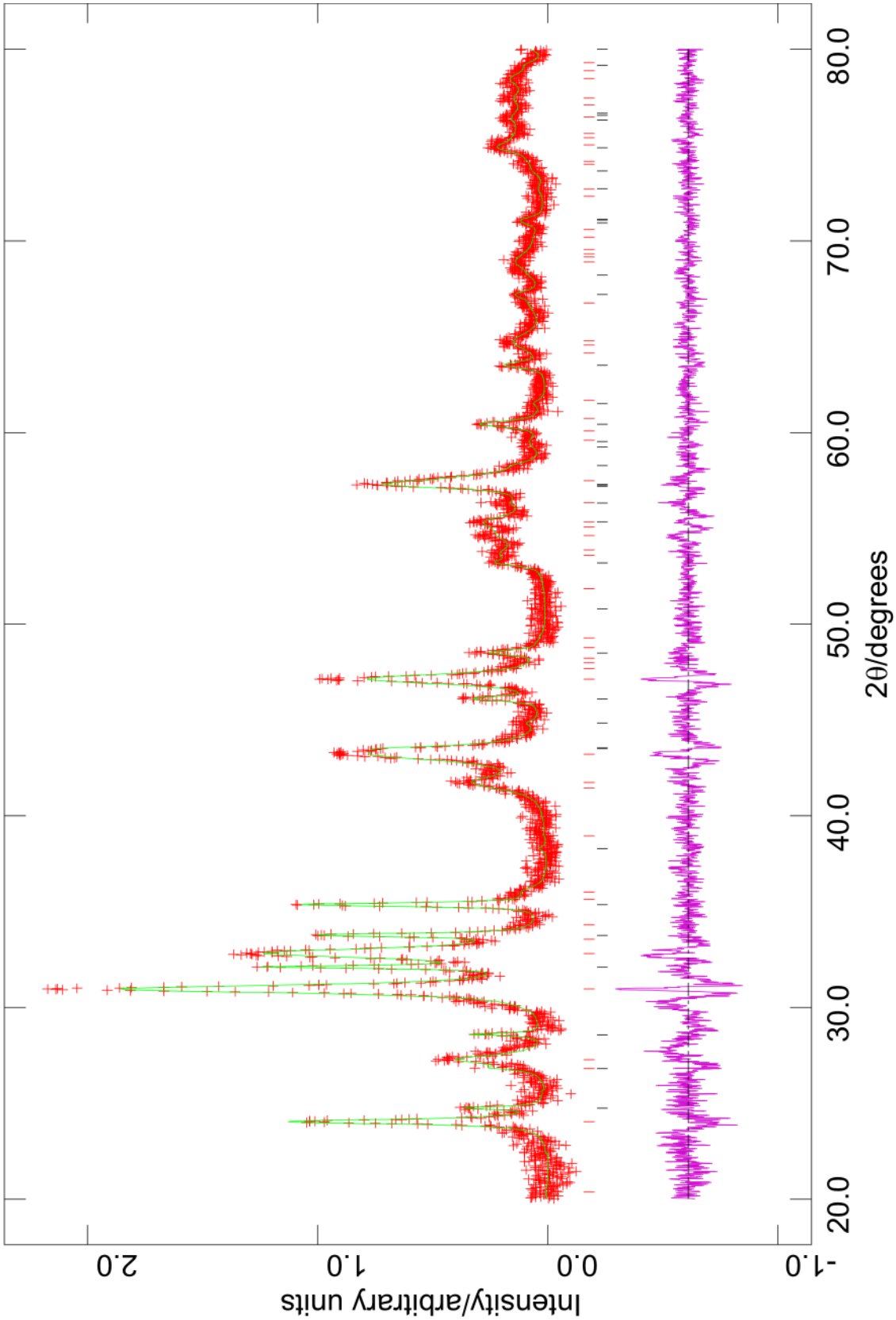

Figure 6.7 Observed (red +), calculated (green) and difference (pink) profiles of $Ce_2Mn(N,F)_4$ as generated by the Rietveld profile refinement of XRD data using a $LaSrMnO_4F$. Red vertical lines highlight the positions of the $Ce_2Mn(N,F)_4$ diffraction peaks whilst black vertical lines correspond to residual Ce_2MnN_3

6.3.3 Nuclear Refinement Based on NPD Data Using Staged $LaSrMnO_4F$ Model

NPD data were collected in a joint experiment at the Institut Laue-Langevin, Grenoble, in order to confirm the findings from the refinements of XRD data that the fluorinated phase adopts a staged $LaSrMnO_4F$-type structure, and to study the anion distribution within this material. The University of Hull conducted a full examination of all possible structural models including that involving staged insertion and concluded that the staged model was the preferred choice. In this model, all allowed anion sites were fully occupied, corresponding with a composition $Ce_2MnN_3F_2$, a Mn(III) phase, and each Mn was coordinated by five N atoms (four equatorial and one apical) and one apical F atom.

Magnetic susceptibility data on the two-phase mixture, collected and analysed by the author, was incompatible with a pure Mn(III) phase ($Ce_2MnN_3F_2$), and suggested a mixed Mn(II)/Mn(III) material, as discussed in detail in Section 6.3.4. The author therefore re-examined the NPD data using the results from The University of Hull, but focused on the anion site occupancies. The refinement converged with $\chi^2 = 1.370$, $R_p = 1.43\%$, $R_{wp} = 1.80\%$ and confirmed that the interstitial F site was probably only partially occupied, with the refinement suggesting a site occupancy of 0.83(4). The visual fit of the calculated profiles with the experimental data (as shown in *Figure 6.8*) is very good, supporting the structural model. The refined atom parameters are tabulated in *Table 6.4* and selected bond lengths in *Table 6.5*.

Table 6.4 Table of atomic parameters from the refinement of $Ce_2Mn(N,F)_4$ NPD data in the space group *P*4/*nmm* modelled on the $LaSrMnO_4F$ structure.

Atom	Site Symmetry	*x*	*y*	*z*	$U_{iso} \times 100$ (Å^2)	Occupancy
Ce(1)	2c	0.75	0.75	0.128(2)	0.2(3)	1
Ce(2)	2c	0.75	0.75	0.391(2)	0.2(3)	1
Mn	2c	0.25	0.25	0.284(2)	0.2(3)	1
N(1)	4f	0.25	0.75	0.272(1)	4.4(3)	1
N(2)	2c	0.25	0.25	0.422(2)	4.4(3)	1
F(1)	2c	0.25	0.25	0.118(2)	4.4(3)	1
F(2)	2a	0.25	0.75	0	4.4(3)	0.83(4)

Table 6.5 Selected bond lengths from the refinement of $Ce_2Mn(N,F)_4$ NPD data in the space group *P*4/*nmm* modelled on the $LaSrMnO_4F$ structure.

Bond	Length in Å
Mn-N(1) eq [× 4]	1.934(2)
Mn-F(1) ap1	2.18(4)
Mn-N(2) ap2	1.80(4)
F(1) ap1-F(2) int	2.47(2)
Ce(1)-F(2) int [× 4]	2.55(1)
Ce(1)-F(1) ap1 [× 4]	2.728(2)
Ce(2)-N(2) ap2 [× 4]	2.754(5)
Ce(2)-N(2) ap2	2.44(3)
Ce(2)-N(1) [× 4]	2.48(2)

These data suggest that the interstitial F(2) site is ≈ 83% occupied, however it should be noted that the site fractional occupancy is closely correlated with the isotropic temperature factor, thus cannot be relied upon for an accurate estimate of overall stoichiometry in this case. The large refined value of U_{iso} ($\approx 4.4 \times 100$ Å^2) is suggestive of some degree of disorder within the material such as the aforementioned partial occupancy of the F(2) site, a small degree of N/F substitution, mixed Mn valency or a combination of such factors.

Although the exact fluorine content cannot be accurately derived from refinement of the NPD data alone, it is likely that the interstitial F(2) site is partially occupied thus implying a generic stoichiometry of $Ce_2MnN_3F_{2-\delta}$.

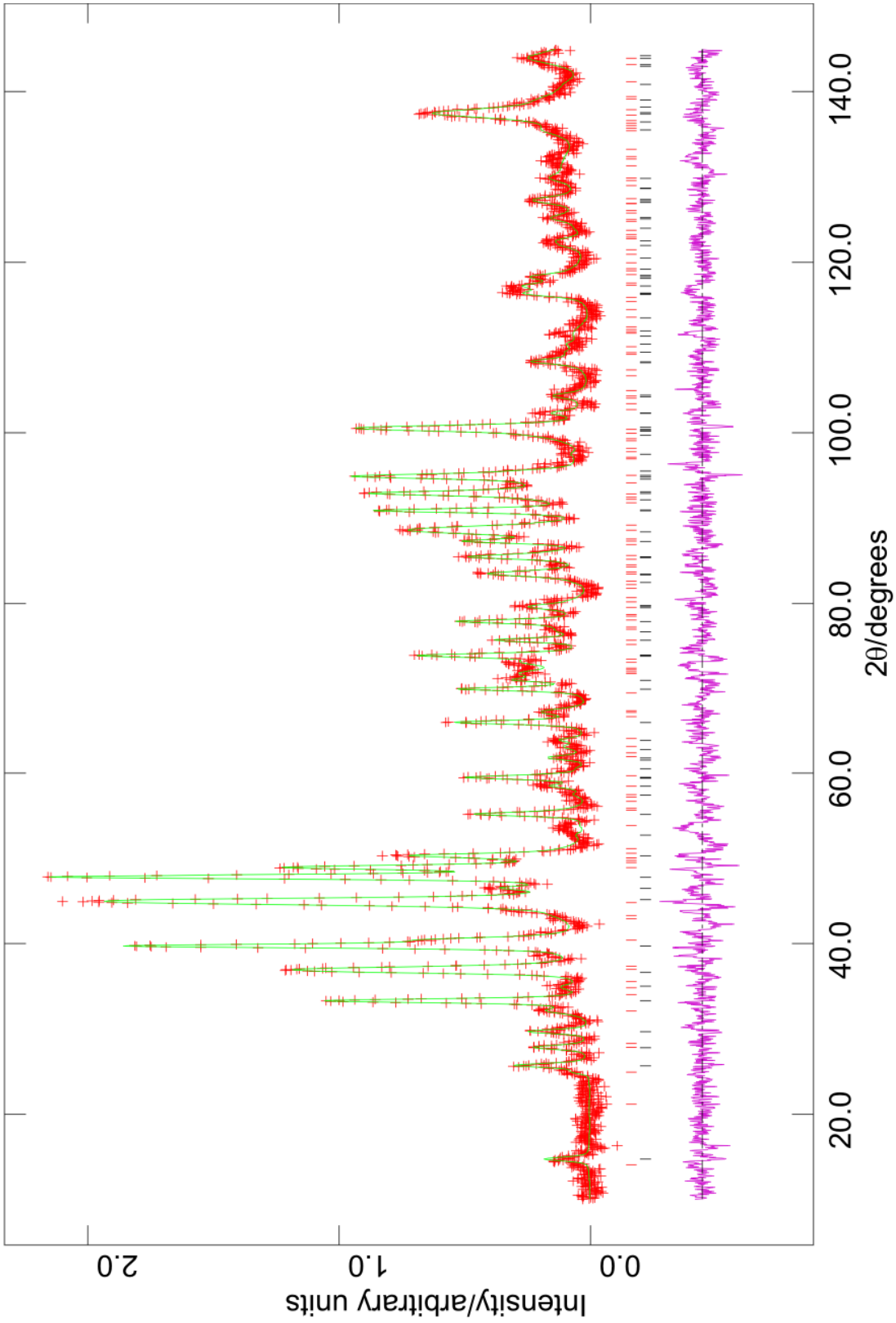

Figure 6.8 Observed (red +), calculated (green) and difference (pink) profiles of $Ce_2Mn(N,F)_4$ as generated by the Rietveld profile refinement of NPD data using a $LaSrMnO_4F$ model. Red vertical lines highlight the positions of the $Ce_2Mn(N,F)_4$ diffraction peaks whilst black vertical lines correspond to residual Ce_2MnN_3

As has been previously mentioned, due to the synthetic difficulties encountered during the fluorination stage, it was not possible to synthesise a pure sample of $Ce_2MnN_3F_{2-\delta}$. From the NPD data, the refined phase fraction of $Ce_2MnN_3F_{2-\delta}$ and Ce_2MnN_3 corresponded to the sample containing 49.4(9) mol % of starting material. It is important that the fit of the calculated and observed NPD profiles for the unfluorinated Ce_2MnN_3 are taken into consideration and a comparison with known literature values are made in order to support the assignment of the staged $LaSrMnO_4F$ model to the fluorinated phase. The refined atomic parameters for Ce_2MnN_3 refined in the space group *Immm* are tabulated in *Table 6.6*; demonstrating that the values obtained for U_{iso} are sensible and the refined atomic parameters concur with those expected for this phase.

Table 6.6 Table of atomic parameters from the refinement of residual Ce_2MnN_3 in the 2-phase refinement of $Ce_2Mn(N,F)_4$ NPD data in the space group *Inmm*. The structural refinement parameters reported by Niewa *et al*. [24] are included in italics for facile comparison.

Atom	**Site Symmetry**	***x***	***y***	***z***	**Occupancy**	**$U_{iso} \times 100$ (Å^2)**
Ce	4i	0	0	0.3537(3)	1	0.1(1)
Mn	2a	0	0	0	1	0.4(2)
N(1)	2b	0	0.5	0.5	1	0.5(1)
N(2)	4i	0	0	0.1640(2)	1	1.4(1)
Ce	*4i*	*0*	*0*	*0.35332(9)*	*1*	*2.4*
Mn	*2a*	*0*	*0*	*0*	*1*	*2.7*
N(1)	*2b*	*0*	*0.5*	*0.5*	*1*	*2.1*
N(2)	*4i*	*0*	*0*	*0.1638(2)*	*1*	*1.9*

The refined lattice parameters for Ce_2MnN_3 were a = 3.7534(2) Å, b = 3.4459(2) Å and c = 12.4740(7) Å, which were in good agreement with those initially reported by Niewa *et al.* (*a* = 3.74994(6) Å, *b* = 3.44450(6) Å and *c* = 12.4601(2) Å) [24]. This agreement of the structural data with literature values for Ce_2MnN_3 combined with the excellent visual fit of the 2-phase Rietveld refinement lends confidence to the assignment of the staged $LaSrMnO_4F$ model for the structure of $Ce_2MnN_3F_{2-\delta}$.

Madelung energy calculations were carried out at The University of Hull on various anion stoichiometries and distributions permitted within the staged $LaSrMnO_4F$ model to investigate which would be more feasible. This information was provided by The University of Hull, and the calculations were repeated using the composition $Ce_2MnN_3F_2$ and the final refined atomic positions shown in *Table 6.4*. A model unit cell of $Ce_2Mn(N,F)_4$ with the $LaSrMnO_4F$ structure is shown in *Figure 6.9*. The Ce and Mn positions are denoted by purple and black spheres respectively. The four anion sites are each assigned different colours: the interstitial sites (int) are shown in yellow, equatorial sites (eq) blue, the apical site facing the interstitial site (ap1) is represented by red spheres and the other apical site (ap2) by green spheres.

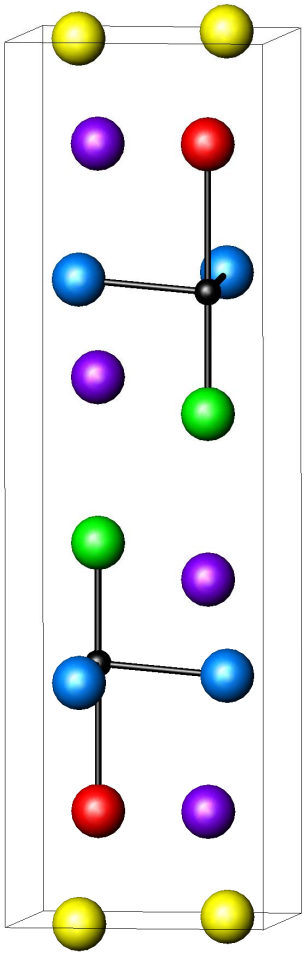

Figure 6.9 The model unit cell of $Ce_2Mn(N,F)_4$ with the $LaSrMnO_4F$ structure used for Madelung energy calculations. Mn sites are shown in black, whilst the anion sites are denoted interstitial (yellow), equatorial (blue), apical 1 (red) and apical 2 (green).

Models 1-4, described in *Table 6.7*, investigated the anion distribution within the stoichiometry $Ce_2Mn^{III}N_3F_2$. Models 1, 2 and 3 assumed the equatorial sites to be occupied solely by N^{3-} and the interstitial sites by F^-, the only difference being the distribution of N^{3-} and F^- over the apical sites. Model 1 placed F^- in the ap1 position and N^{3-} in ap2, model 2 placed N^{3-} in the ap1 position and F^- in ap2 and model 3 assumed N^{3-} and F^- were disordered over the apical sites. Model 4 on the other hand placed F^- in the equatorial sites with N^{3-} adopting the interstitial and both apical sites. The Madelung energies shown in *Table 6.7* were calculated using the computer program "MAD" which utilises the Ewald method [32].

Table 6.7 Table of Madelung energies calculated for possible anion distribution models in $Ce_2Mn(N,F)_4$.

Model	Equatorial Site	Apical Site 1	Apical Site 2	Interstitial Site	Madelung Energy (kJ mol^{-1})
1. $Ce_2Mn^{III}N_3F_2$	N^{3-}	F^-	N^{3-}	F^-	-34862.99
2. $Ce_2Mn^{III}N_3F_2$	N^{3-}	N^{3-}	F^-	F^-	-30186.73
3. $Ce_2Mn^{III}N_3F_2$	N^{3-}	N^{3-}/ F^-	N^{3-}/ F^-	F^-	-33425.96
4. $Ce_2Mn^{III}N_3F_2$	F^-	N^{3-}	N^{3-}	N^{3-}	-23544.57

The Madelung energy calculations confirmed the results obtained from The University of Hull using the stoichiometric anion formulation: model 1 is the most stable with N occupying all the equatorial sites and the apical 2 position, whilst F is inserted in a staged fashion into interstitial sites in alternate rocksalt layers. The apical 1 F sites are adjacent to the layers containing these interstitial sites.

The Madelung energy calculations support the chemically logical hypothesis that if interstitial fluorine anions are inserted into alternate interstitial layers, then the apical N in the MnN_5F octahedra will point away from the extra electron density, leaving the apical F facing the interstitial F.

The structure of the fluorinated phase is comprised of corner-linked MnN_5F octahedra stacked along the *c* axis with F^- inserted in a staged fashion into interstitial sites situated in alternate layers with rocksalt structure. Upon comparison of the starting material Ce_2MnN_3 with $Ce_2MnN_3F_{2-\delta}$ (*see Figure 6.10* and *Figure 6.11*) it is evident that several notable structural rearrangements occur upon fluorination. In Ce_2MnN_3, the Ce is situated on a single site forming a trigonal prism with neighbouring N atoms, the triangular faces of which link together the isolated 1-

dimensional chains of distorted square planar MnN_4 units. Upon the insertion of fluorine, the Ce adopts two distinct crystallographic sites. Ce(1) is adjacent to the interstitial fluorine position F(2) and co-ordinated to 8 N anions at the base of a rectangular anti-prism, whilst Ce(2) is closest to the vacant interstitial position and is co-ordinated to 9 anions in a similar arrangement to K in K_2NiF_4.

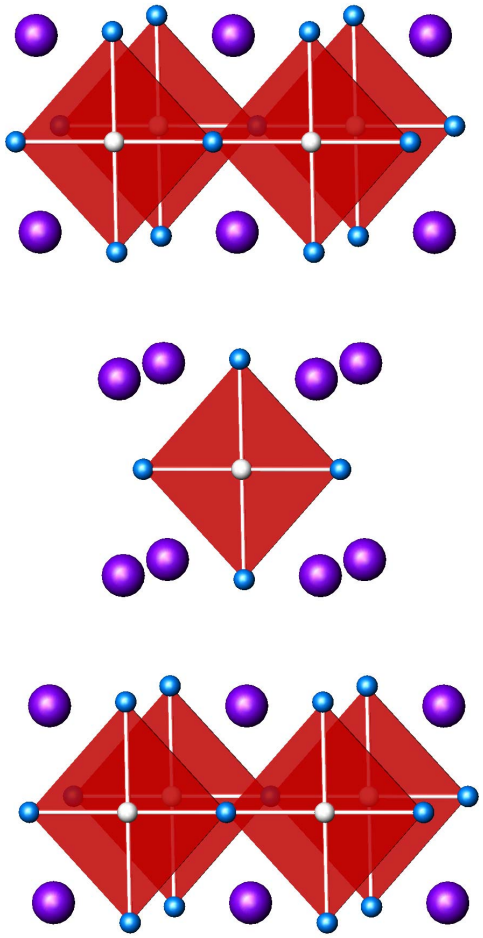

Figure 6.10 The structure of Ce_2MnN_3 with Ce shown in purple, Mn in white, N in blue and Mn-N square planar units highlighted in red.

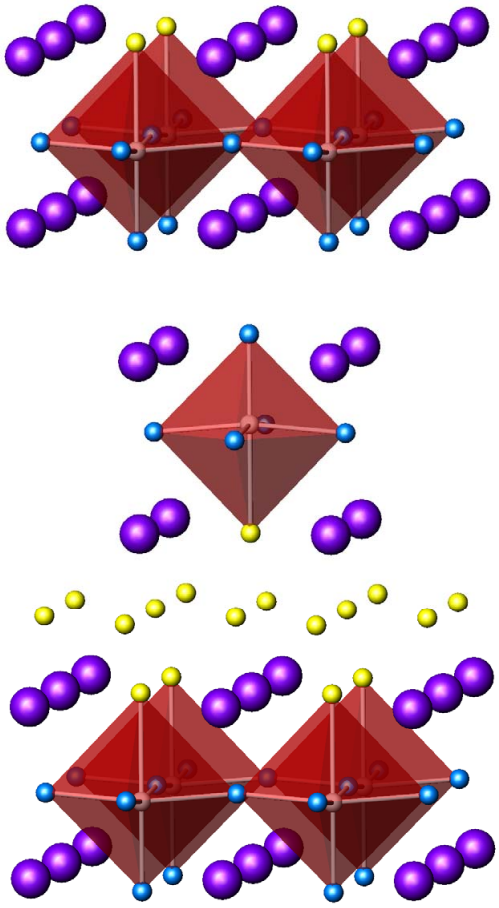

Figure 6.11 The structure of $Ce_2MnN_3F_{2-\delta}$ with Ce shown in purple, Mn in white, N in blue, F in yellow and MnN_5F octahedra highlighted in red

6.3.4 Magnetic Characterisation of $Ce_2MnN_3F_{2-\delta}$

Neutron powder diffraction data collected at room temperature contained no magnetic peaks, indicating the absence of magnetic ordering. In order to examine the magnetic susceptibility of $Ce_2MnN_3F_{2-\delta}$, zero-field cooled and field-cooled DC magnetisation data were collected in an applied field of 3000 Oe (0.3 T) between ≈ 2K and ≈ 273K. From the refinement of NPD data this sample was known to be comprised of an approximately 1:1 ratio of unreacted Ce_2MnN_3 and the fluorinated phase $Ce_2MnN_3F_{2-\delta}$, thus magnetic data was also collected on the starting material. Niewa *et al.* reported Ce_2MnN_3 to be a Pauli paramagnet, displaying a Curie tail that was attributed to impurities or defects; these observations were echoed in the data

collected. This data gave an effective paramagnetic moment of 0.62(1) μ_B per Mn, which was in good agreement with the figure of 0.53 μ_B per Mn reported previously [24].

The magnetic data collected on the mixed phase were fitted using *Equation 6.1*, which is the sum of the Curie-Weiss equation with a temperature independent component and the fitted function is shown in *Figure 6.12*.

$$\chi = \chi_0 + \frac{C}{T - \theta}$$

(*Equation 6.1*)

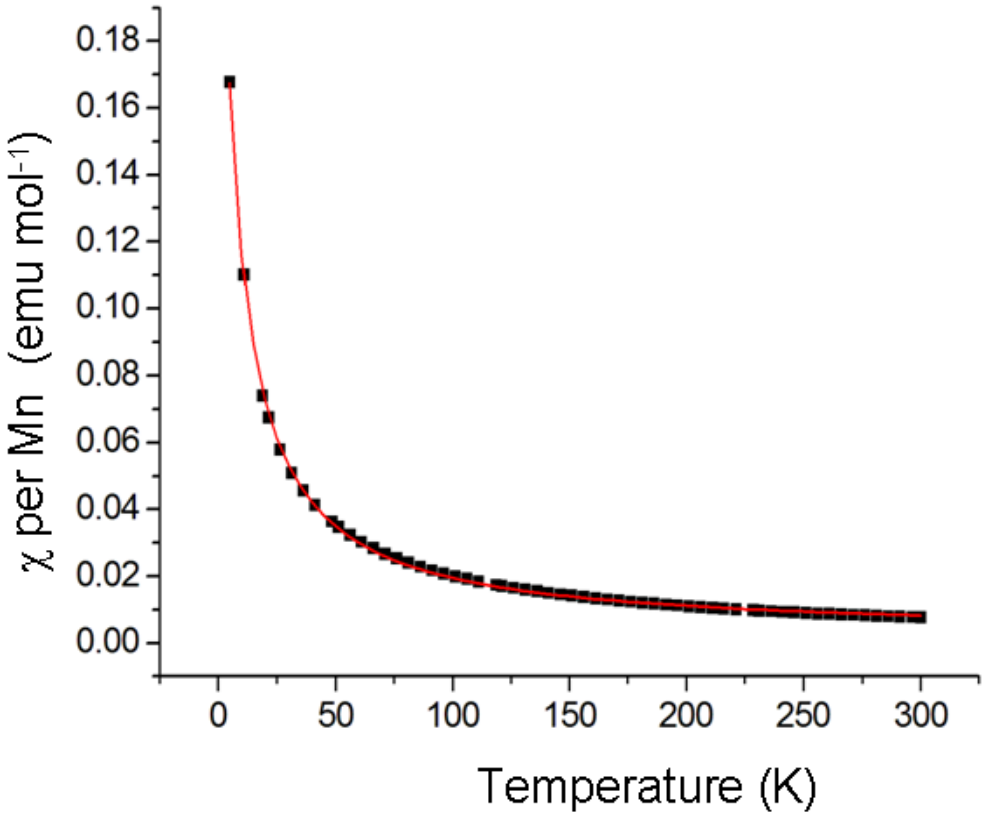

Figure 6.12 Magnetic susceptibility (χ) against temperature with a fit line (shown in red) based on the Curie-Weiss equation with a temperature independent component.

The fitted function assigned the following values to the 3 unknowns in the equation: χ_0 = 0.0023(1) emu mol^{-1}, C = 1.83(1) emu K mol^{-1} and θ = -6.1(1) K and yielded the composite moment for the mixed phase material of μ_{eff} = 3.82(2) μ_B per Mn. From this, the effective magnetic moment solely ascribed to $Ce_2MnN_3F_{2-\delta}$, was calculated to be μ_{eff} = 5.38(3) μ_B per Mn.

This value falls between that expected for Mn^{3+} (4.9 μ_B) and Mn^{2+} (5.9 μ_B) in an octahedral co-ordination thus implying a mixed Mn^{2+}/Mn^{3+} valency. The presence of mixed valence Mn would be consistent with a slightly fluorine deficient phase as suggested by the refinement of NPD data.

6.4 Conclusions

It has been demonstrated that fluorination of the ternary nitride Ce_2MnN_3 *via* low-temperature solid-gas reaction although not facile, is entirely feasible. The fluorination of ternary oxides is nowadays an extensively researched and well-documented field; this study has shown that ternary nitrides can also undergo such reactions to form nitride-fluorides.

The novel nitride-fluoride material $Ce_2MnN_3F_{2-\delta}$ has been synthesised and characterised, revealing a unique mechanism of fluorine insertion including a structural rearrangement from the starting material. The two fluorine anions simultaneously expand the co-ordination of manganese from four to six and occupy interstitial sites in alternate layers, adopting a $LaSrMnO_4F$-type staged structure.

Neutron powder diffraction data was indicative of a slight fluorine deficiency with the occupation of the interstitial fluorine sites refining to ≈ 83%. The composition $Ce_2MnN_3F_{1.83}$ would correspond to an average Mn oxidation state of $Mn^{2.83+}$, thus containing more Mn^{3+} than Mn^{2+}. Although the average Mn oxidation

state from the refinement of NPD data is larger than that suggested by the magnetic data, it is still consistent with $Ce_2MnN_3F_{2-\delta}$ containing mixed Mn^{2+} and Mn^{3+}. The effective magnetic moment μ_{eff} = 5.38(3) μ_B per Mn lies midway between the expected values for Mn^{3+} and Mn^{2+} suggesting a mixed Mn valency, namely $Ce_2(Mn^{III},Mn^{II})N_3F_{2-\delta}$. This reinforces the assertion that the material is slightly fluorine deficient.

6.5 References

1. J. M. Longo and P. M. Raccah (1973) *Journal of Solid State Chemistry* **6** 526.
2. D. Balz (1953) *Die Naturewissen* **40** 241.
3. H. Müller-Buschbaum and W. Wollschläger (1975) *Zeitschrift für Anorganische und Allgemeine Chemie* **414** 76.
4. J. F. Bringley, S. S. Trail and B. A. Scott (1990) *Journal of Solid State Chemistry* **86** 310.
5. C. L. Teske, & H. Müller-Buschbaum (1969) *Zeitschrift für Anorganische und Allgemeine Chemie* **371** 325.
6. C. L. Teske and H. Müller-Buschbaum (1970) *Zeitschrift für Anorganische und Allgemeine Chemie* **379**, 234.
7. M. T. Weller and D. R. Lines (1989) *Journal of Solid State Chemistry* **82** 21.
8. H. Müller-Buschbaum (1977) *Angewandte Chemie International Edition* **16** 674.
9. M. Al-Mamouri, P. P. Edwards, C. Greaves and M. Slaski (1994) *Nature* **369** 382.
10. B. M. Tissue, K. M. Cirillo, J. C. Wright, M. Daeumling and D. C. Larbalestier (1988) *Solid State Communications* **65** 1 51.
11. B. Chevalier, A. Tressaud, B. Lepine, K. Amine, J. M. Dance, L. Lozano, E. Hickey and J. Etorneau (1990) *Physica C* **167** 97.
12. C. Greaves and M. G. Francesconi (1998) *Current Opinion in Solid State & Materials Science* **3** 132.
13. P. R. Slater, P. P. Edwards, C. Greaves, I. Gameson, M. G. Francesconi, J. P. Hodges, M. Al-Mamouri and M. Slaski (1995) *Physica C* **241** 151.
14. P. R. Slater, J. P Hodges M. G. Francesconi, P. P. Edwards, C. Greaves, I. Gameson and M Slaski (1995) *Physica C* **253** 16.
15. M. G. Francesconi, P. R. Slater, J. P. Hodges, C. Greaves, P. P. Edwards, M. Al-Mamouri and M. Slaski (1998) *Journal of Solid State Chemistry* **135** 17.
16. M. Al-Mamouri, P. P. Edwards, C. Greaves, P. R. Slater and M. Slaski (1995) *Journal of Materials Chemistry* **5** (6) 913.

17. T. Baikie, E. L. Dixon, J. F. Rooms, N. A. Young and M. G. Francesconi (2003) *Chemical Communications* 1580.
18. D. Bright and J. A. Ibers (1969) *Inorganic Chemistry* **8** (4) 709.
19. A. Gudat, R. Kniep and J. Maier (1992) *Zeitschrift Naturforsch B* **47** 1363.
20. C. Wachsmann and H. Jacobs (1996) *Zeitschrift für Anorganische und Allgemeine Chemie* (1996) **622** 885.
21. M. G. Francesconi, M. G. Barker and C. Wilson (2002) *Chemical Communications* 1358.
22. A. J. D. Barnes, T. J. Prior and M. G. Francesconi (2007) *Chemical Communications* 4638.
23. R. Benz and W. H. Zachariasen (1970) *Journal of Nuclear Materials* **37** 109.
24. R. Niewa, G. V. Vajenine, F. J. DiSalvo, H. Luo and W. B.Yelon (1998) *Zeitschrift Naturforsch B* **53** 63.
25. R. Niewa, Z. Hu, C. Grazioli, U. Rößler, M. S. Golden, M.Knupfer J. Fink, H. Giefers, G. Wortmann, F. M. F. de Groot and F. J. DiSalvo (1999) *Journal of Alloys and Compounds* **346** 129.
26. G. A. Landrum, R. Dronskowski, R. Niewa and F. J. DiSalvo *Chemistry – A European Journal* **5** (2) 515.
27. International Centre for Diffraction Data (ICDD) database, Powder Diffraction File: PDF-2 (Sets 1-14).
28. D. Louër and M. Louër (1972) *"INDEX"*, *Journal of Applied Crystallography* **5** 271, (program modified by C. Greaves, The School of Chemistry, The University of Birmingham).
29. A. C. Larson and R. B. Von Dreele (1990) *Generalised Structure Analysis System,* Los Alamos National Laboratory.
30. L. D. Aikens, R. K. Li and C. Greaves (2000) *Chemical Communications* 2129.
31. P. R. Slater and R. K. B. Gover (2001) *Journal of Materials Chemistry* 12 291.
32. J. W. Weenk and H. A. Harwig (1977) *Journal of the Physics and Chemistry of Solids* **38** 1047, (adapted by C. Greaves, The School of Chemistry, The University of Birmingham).

Chapter Seven

Conclusions and Further Work

This investigation has focused on anion-deficient perovskites and perovskite-related phases and their potential for undergoing fluorine insertion reactions. The ordering in the oxygen-vacancy layers in the perovskite-related brownmillerite $Sr_2Co_2O_5$ was studied and fluorine insertion reactions in this class of materials were explored using $Sr_2Co_2O_5$, $Sr_2Fe_2O_5$ and Sr_2CoFeO_5. Low-temperature fluorination of K_2NiF_4-type structures was also investigated, whereby $Sr_2MnO_{3.5+x}$, (which exhibits an oxygen defect superstructure) and the ternary nitride Ce_2MnN_3 (isostructural with Sr_2CuO_3) were shown to undergo structural rearrangements upon fluorination.

7.1 Nuclear and Magnetic Characterisation of $Sr_2Co_2O_5$

The brownmillerite phase $Sr_2Co_2O_5$ has previously been described by Takeda *et al.* [1] using the space group *Imma*, which allows for disorder onto the half occupied 8i sites arising from the random orientation of tetrahedral chains throughout the structure. In a recent study by Muñoz *et al*. [2], the ordered *I2mb* space group whereby all tetrahedral chain possess identical orientations was assigned based on *ab initio* calculations. Since related brownmillerite materials such as Sr_2MnGaO_5 have been shown upon closer examination using TEM and HREM to exhibit a variety of inter- and intra-plane chain ordering patterns, electron microscopy techniques were used to

study $Sr_2Co_2O_5$ in order to elucidate the chain ordering in the tetrahedral layers at the local level.

TEM and HREM images were indicative of a superstructure consisting of L-R-L-R- intra-plane ordering of tetrahedral chains, necessitating a doubling of the *c*-parameter and the assignment of the space group *Pcmb*. However, Rietveld refinement based on NPD data using the space group *Pcmb* yielded an unusually short refined bond length for Co(4)-O(4) coupled with a longer Co(4)-Co(6) refined bond length, and the Co-O polyhedra from this refinement were rather dissimilar in size. Although the *Pcmb* space group permitted such elongations and contractions in bond length, there was no evidence from the NPD data that such distortions were actually present in the structure. It was postulated that the idiosyncrasies in the refinement were artefacts from the doubling of the unit cell along *c*, thus *Pcmb* did not provide a satisfactory description of the overall structure of $Sr_2Co_2O_5$.

Another refinement based on NPD data was carried out using the disordered space group *Imma*, and this provided a good fit with more feasible bond lengths. Although the L-R-L-R intralayer ordering of tetrahedral chains (and thus the assignment of the *Pcmb* space group) was incontrovertible on the basis of electron microscopy alone, on the larger scale pertinent to X-ray and neutron powder diffraction the overall structure of $Sr_2Co_2O_5$ is still best described using the disordered space group *Imma*.

In order to determine the extent to which *ab initio* work such as that carried out by Muñoz *et al.* would support the assignment of the fully ordered cell doubling model, it would be interesting to carry out DFT calculations based upon *Pcmb.* Such calculations can only be based on fully ordered models, but a comparison between the stability of *I2mb* and *Pcmb* could be useful. This theoretical treatment cannot take into

account entropy nor the length over which ordering is occurring, thus consideration of the disordered *Imma* model would be very difficult as it is most likely stabilised by entropy.

7.2 Fluorination Study of the Brownmillerite Materials $Sr_2Fe_2O_5$, Sr_2CoFeO_5 and $Sr_2Co_2O_5$

The brownmillerites $Sr_2Fe_2O_5$, Sr_2CoFeO_5 and $Sr_2Co_2O_5$ were investigated with a view to using fluorine insertion reactions to fill the oxygen vacancies in these materials, thus forming cubic perovskite-type phases with mixed 3+/4+ B cation oxidation states.

Fluorination of $Sr_2Fe_2O_5$ was shown to consistently form approximately equal amounts of two cubic perovskite phases. These were attributed to $SrFeO_2F$ [3] and a phase closely related to $SrFeO_3$ [4] (with undetermined oxygen content) by comparison of the lattice parameters with literature values and the assignments of these phases was supported by Madelung energy calculations using $SrFeO_3$ for simplicity. This phase separation to form the fluorinated Fe^{3+} phase and the highly oxidised Fe^{4+} phase in *lieu* of the mixed Fe^{3+}/Fe^{4+} intermediate $SrFeO_{2.5}F_{0.5}$ is most likely driven by the enhanced lattice energy for Fe^{4+} oxides.

The mixed Co/Fe brownmillerite Sr_2CoFeO_5 has been shown to be amenable to fluorine insertion reactions, forming a new cubic perovskite phase closely related to $SrFeO_2F$ with the nominal composition $SrCo_{0.5}Fe_{0.5}O_{2.5}F_{0.5}$. Magnetic measurements appeared to show a canted ferromagnetic transition below 150K and the appearance of hysteresis in field sweep measurements performed at 10K supported the existence of a ferromagnetic component to the magnetic structure of $SrCo_{0.5}Fe_{0.5}O_{2.5}F_{0.5}$. As the exact oxygen and fluorine content of this phase is unknown, it is difficult to know the

oxidation state of the B cations. Even with accurate data on the anion composition, as Co is more likely to favour the 3+ oxidation state and oxidation to 4+ is more facile for Fe, other techniques such as Mössbauer and X-ray absorption near edge structure (XANES) spectroscopy would need to be used to determine precise oxidation states for the B cations and thus examine the complex exchange interactions between them.

The new cubic perovskite of nominal composition $SrCoO_{2.5}F_{0.5}$ was formed *via* fluorine insertion into the brownmillerite $Sr_2Co_2O_5$. Unfortunately, examination of this material using NPD showed that the product contained an impurity of unfluorinated starting material, although this was not apparent in XRD data thus a purer sample will be required in future to enable complete characterisation of this phase. It was apparent that, unlike the observations for $Sr_2Fe_2O_5$, no phase segregation to Co^{3+}-containing $SrCoO_2F$ and Co^{4+}-containing $SrCoO_3$ occurs for the fluorination of $Sr_2Co_2O_5$. This can be rationalised by considering the readiness of oxidation to 4+; whilst the lattice energy for Fe^{4+} oxides is favourable, the same cannot be said for Co^{4+} (as fully oxidised $SrCoO_3$ forms even less readily than $SrFeO_3$), hence the fluorinated intermediate $SrCoO_{2.5}F_{0.5}$ is more energetically favourable than phase segregation to form $SrCoO_2F$ and $SrCoO_3$. Similarly to the mixed Co/Fe perovskite $SrCo_{0.5}Fe_{0.5}O_{2.5}F_{0.5}$, magnetic measurements showed a canted ferromagnetic transition below 150K and a small degree of hysteresis was observed during field sweep measurements conducted at 10K. In future, NPD data collected on a pure sample combined with TGA measurements could help to confirm the anion composition whilst X-ray absorption near edge structure (XANES) and Mössbauer spectroscopy could be used to determine the Co oxidation state and hence explain the magnetic behaviour of this phase.

7.3 Synthesis and Characterisation of the Fluorinated Single-Layer Manganite $Sr_2MnO_{3.5+x}F_y$

In addition to brownmillerites, fluorine insertion into other perovskite-related ordered vacancy materials is also feasible, as shown by the synthesis of the novel oxide-fluoride $Sr_2MnO_{3.5+x}F_y$. The starting material $Sr_2MnO_{3.5+x}$ contains MnO_5 square pyramids, which are corner-linked to form a defect arrangement of psuedo-hexagonal channels of oxygen vacancies in the monoclinic bc plane [5]. Bond valence sum and Madelung energy calculations based on XRD data suggested that, rather than fill these equatorial O vacancies, the F anions would preferentially adopt apical positions causing the vacancies to be filled by the displaced O anions instead and thus reverting to a fully anion-stoichiometric K_2NiF_4-type structure. Rietveld profile refinement based on NPD data using the space group *I4/mmm* provided a good fit between observed and calculated values with reasonable refinement statistics. Transmission electron microscopy confirmed that the fluorinated phase was indeed of the K_2NiF_4-type structure, but some sections within the sample also contained unfluorinated starting material retaining the oxygen-defect monoclinic superstructure. Thus it has been shown that the single-layer manganite $Sr_2MnO_{3.5+x}F_y$ undergoes a structural rearrangement instigated by the preference of F anions for apical sites, but a pure sample would be preferable for any further characterisation work on this phase, such as magnetic measurements.

7.4 Synthesis and Characterisation of the Quaternary Nitride-Fluoride $Ce_2MnN_3F_{2-\delta}$

The first known superconducting oxide-fluoride was $Sr_2CuO_2F_{2+\delta}$, which was prepared *via* solid-gas fluorination of Sr_2CuO_3 [6] of which Ce_2MnN_3 is a nitride

analogue. In a similar fashion, the novel nitride-fluoride material $Ce_2MnN_3F_{2-\delta}$ has been synthesised and characterised.

Initially, a refinement based on XRD data was carried out using a K_2NiF_4-type structure, but it became apparent that the Mn cations were situated in asymmetrical environments, hence a staged $LaSrMnO_4F$ structure provided a better model for the fluorinated phase. Madelung energy calculations were utilised in order to assign the correct anion stoichiometries and distributions and predicted that fluorine is inserted in a staged fashion into interstitial sites in alternate rocksalt layers and the apical sites that face these interstitial sites whilst N occupies all the equatorial sites and the apical position facing away from the interstitial sites. This was verified by Rietveld profile refinement based on NPD data. Thus the structure of $Ce_2MnN_3F_{2-\delta}$ comprises corner-linked MnN_5F octahedra with F anions occupying interstitial rocksalt sites in alternate layers. This phase is formed by way of a significant structural rearrangement instigated by F anions, whereby two fluorine anions simultaneously expand the co-ordination of manganese from four to six and occupy interstitial sites in alternate layers, adopting a $LaSrMnO_4F$-type staged structure.

As synthesis of the fluorinated phase could only be achieved in a very narrow range of temperatures, which are low even compared with other solid-gas fluorination reactions, starting material impurities were inevitable. Ideally, future work should focus on the isolation of the $Ce_2MnN_3F_{2-\delta}$ phase. Considering the amount of time already spent optimising the fluorination conditions for this material is it unlikely that the yield can be significantly improved unless a smaller particle size is used. However, this may not be a trivial matter as the air and moisture sensitivity of the nitride would necessitate any milling to take place within a glove box.

7.5 Final Remarks

The investigation of chain order in brownmillerite-type materials has shown that the degree of order observed in a material often depends on the length scale pertinent to the experimental technique used. Fluorination studies of these materials have shown that whilst it is sometimes straightforward to insert fluorine into existing oxygen vacancies, sometimes energetic considerations mean that the outcomes of fluorine-insertion reactions are more unusual.

Studying the low-temperature fluorination of $Sr_2Fe_2O_5$, $Sr_2Co_2O_5$, Sr_2CoFeO_5, $Sr_2MnO_{3.5+x}$ and Ce_2MnN_3 has shown that there are clear differences in the types of fluorinated products synthesised. Whilst fluorine insertion in vacancy perovskite materials such as the brownmillerite phases presented here is limited to the simple filling of anion vacancies coupled with a corresponding increase in the oxidation state of the B cation, in layered materials fluorine anions are also able to occupy interstitial sties. For instance, upon fluorination of the K_2NiF_4-related oxygen defect perovskite $Sr_2MnO_{3.5+x}$, both equatorial perovskite and interstitial sites are available and there is some evidence to suggest that fluorine tends to partially occupy interstitial sites whilst there are still vacancies in the perovskite layer. This could possibly relate to entropy considerations. The mixed O^{2-}/F^- in the conventionally co-ordinated sites provides an inherent and high degree of configurational entropy, but this will be enhanced by the additional partial occupancy of interstitial sites.

For layered K_2NiF_4-related phases, depending on the oxidation state preferences of the transition metal, it is possible to synthesise phases in which the interstitial sites are half filled but in a staged way - alternating layers of interstitial sites that are either completely full or completely empty. An example is the Mn(IV) compound $LaSrMnO_4F$ [7]. It is interesting to note that the fluorine insertion reactions

of the isostructural materials Sr_2CuO_3 and Ce_2MnN_3 occur in slightly different ways. Upon fluorination of Sr_2CuO_3 to form $Sr_2CuO_2F_{2+\delta}$, F^- anions displace O^{2-} anions from their apical positions thus the displaced O anions adopt equatorial positions and some O^{2-} is lost from the structure. In this phase, there is a small occupation of interstitial sites by fluorine but this is not significant enough to cause any staged fluorine insertion effects. In the case of Ce_2MnN_3, there is still a local rearrangement of N^{3-} anions to fill the equatorial vacancies but the amount of N in the structure remains constant, hence a greater occupancy of interstitial sites in this material (refined fractional occupancy = 0.83(4)). It is likely that this is due to the larger ionic radii of N^{3-} anions *cf*. O^{2-} anions. Since the fluorination reactions take place at low temperatures there is insufficient energy for any of the larger N^{3-} anions to diffuse out of the structure, hence no N is lost and more fluorine is inserted into interstitial sites which leads to a staged structure. Although the size differences between the O^{2-} and N^{3-} anions influence the structure of the final product, this study has shown that in addition to the fluorination of ternary oxides, low-temperature fluorination reactions may also be used to form nitride-fluorides, creating a plethora of opportunities to expand our understanding of anion manipulation in perovskite-related materials.

7.6 References

1. T. Takeda, Y. Yamaguchi and H. Watanabe (1972) *Journal of the Physical Society of Japan* **33** 4 970.
2. A Muñoz, C. de la Calle, J. A. Alonso, P. M. Botta, V. Pardo, D. Baldomir and J. Rivas (2008) *Physical Review B* **78** 054404.
3. F. J. Berry, X. Ren, R. Heap, P. Slater and M. F. Thomas (2005) *Solid State Communications* **134** 621.
4. T. Takeda, Y. Yamaguchi and H. Watanabe (1972) *Journal of the Physical Society of Japan* **33** 4 967.
5. L. J. Gillie, A. J. Wright, J Hadermann, G. Van Tendeloo and C. Greaves (2002) *Journal of Solid State Chemistry* **167** 145.
6. M. Al-Mamouri, P. P. Edwards, C. Greaves and M. Slaski (1994) *Nature* **369** 382.
7. L. D. Aikens, R. K. Li and C. Greaves (2000) *Chemical Communications* 2129.

List of Publications Resulting from this Thesis

1. "Synthesis and Characterisation of the Quaternary Nitride-Fluoride $Ce_2MnN_3F_{2-\delta}$"

   D. A. Headspith, M. G. Francesconi, E. C. Sullivan and C. Greaves

   (2009) *Dalton Transactions* 9273.

2. "Structural and Magnetic Characterisation of the Brownmillerite $Sr_2Co_2O_5$"

   E. C. Sullivan, J. Hadermann and C. Greaves

   In Preparation.

Appendix 3.1 Bond valence sum calculations using bond lengths obtained from Rietveld profile refinement calculated using NPD data collected at 4K for $Sr_2Co_2O_5$ refined in the space group *Pcmb*,

Refined bond lengths:
Co(1)-O(1): $r = 2.050(11)$
Co(1)-O(2): $r = 2.072(11)$
Co(1)-O(3): $r = 2.300(7)$

r_0 values:
Co(II)-O: $r_0 = 1.692(5)$
Co(III)-O: $r_0 = 1.70$
Co(IV)-O: $r_0 = 1.75$

$$S = \exp\left[\frac{r_0 - r}{B}\right] \qquad \text{where B} = 0.37$$

Co(1) based on Co(II)

Co(1)-O(1) $S = \exp\left[\frac{1.692 - 2.050}{0.37}\right] = 0.380006254 \times 2$

Co(1)-O(2) $S = \exp\left[\frac{1.692 - 2.072}{0.37}\right] = 0.358069911 \times 2$

Co(1)-O(3) $S = \exp\left[\frac{1.692 - 2.300}{0.37}\right] = 0.193351936 \times 2$

V = 1.86

Co(1) based on Co(III)

Co(1)-O(1) $S = \exp\left[\frac{1.7 - 2.050}{0.37}\right] = 0.388312074 \times 2$

Co(1)-O(2) $S = \exp\left[\frac{1.7 - 2.072}{0.37}\right] = 0.365896268 \times 2$

Co(1)-O(3) $S = \exp\left[\frac{1.7 - 2.300}{0.37}\right] = 0.197578042 \times 2$

V = 1.90

Co(1) based on Co(IV)

Co(1)-O(1) $S = \exp\left[\frac{1.75 - 2.050}{0.37}\right] = 0.444497516 \times 2$

Co(1)-O(2) $S = \exp\left[\frac{1.75 - 2.072}{0.37}\right] = 0.418838334 \times 2$

Co(1)-O(3) $S = \exp\left[\frac{1.75 - 2.300}{0.37}\right] = 0.226165898 \times 2$

V = 2.18

Co(3) based on Co(II)

Co(3)-O(1) $S = \exp\left[\frac{1.692-1.820}{0.37}\right] = 0.707550732 \times 2$

Co(3)-O(2) $S = \exp\left[\frac{1.692-1.875}{0.37}\right] = 0.60981808 \times 2$

Co(3)-O(5) $S = \exp\left[\frac{1.692-2.16}{0.37}\right] = 0.282277439 \times 2$

V = 3.20

Co(3) based on Co(III)

Co(3)-O(1) $S = \exp\left[\frac{1.7-1.820}{0.37}\right] = 0.723015712 \times 2$

Co(3)-O(2) $S = \exp\left[\frac{1.7-1.875}{0.37}\right] = 0.623146912 \times 2$

Co(3)-O(5) $S = \exp\left[\frac{1.7-2.16}{0.37}\right] = 0.288447194 \times 2$

V = 3.26

Co(3) based on Co(IV)

Co(3)-O(1) $S = \exp\left[\frac{1.75-1.820}{0.37}\right] = 0.827629913 \times 2$

Co(3)-O(2) $S = \exp\left[\frac{1.75-1.875}{0.37}\right] = 0.71331095 \times 2$

Co(3)-O(5) $S = \exp\left[\frac{1.75-2.16}{0.37}\right] = 0.330183041 \times 2$

V = 3.74

Co(2) based on Co(II)

Co(2)-O(4) $S = \exp\left[\frac{1.692-1.757}{0.37}\right] = 0.838890011$

Co(2)-O(6) $S = \exp\left[\frac{1.692-1.971}{0.37}\right] = 0.470455429$

Co(2)-O(5) $S = \exp\left[\frac{1.692-1.834}{0.37}\right] = 0.681278714 \times 2$

V = 2.67

Co(2) based on Co(III)

Co(2)-O(4) $S = \exp\left[\frac{1.7-1.757}{0.37}\right] = 0.857225683$

Co(2)-O(6) $S = \exp\left[\frac{1.7-1.971}{0.37}\right] = 0.480738203$

Co(2)-O(5) $S = \exp\left[\frac{1.7-1.834}{0.37}\right] = 0.696169466 \times 2$

V = 2.73

Co(2) based on Co(IV)

Co(2)-O(4) $S = \exp\left[\frac{1.75-1.757}{0.37}\right] = 0.98125892$

Co(2)-O(6) $S = \exp\left[\frac{1.75-1.971}{0.37}\right] = 0.550296917$

Co(2)-O(5) $S = \exp\left[\frac{1.75-1.834}{0.37}\right] = 0.796899244 \times 2$

V = 3.13

Co(4) based on Co(II)

Co(4)-O(4) $S = \exp\left[\frac{1.692-1.675}{0.37}\right] = 1.047017814$

Co(4)-O(6) $S = \exp\left[\frac{1.692-2.16}{0.37}\right] = 0.282277439$

Co(4)-O(3) $S = \exp\left[\frac{1.692-1.812}{0.37}\right] = 0.723015712 \times 2$

V = 2.78

Co(4) based on Co(III)

Co(4)-O(4) $S = \exp\left[\frac{1.7-1.675}{0.37}\right] = 1.069902548$

Co(4)-O(6) $S = \exp\left[\frac{1.7-2.16}{0.37}\right] = 0.288447194$

Co(4)-O(3) $S = \exp\left[\frac{1.7-1.812}{0.37}\right] = 0.738818712 \times 2$

V = 2.84

Co(4) based on Co(IV)

Co(4)-O(4) $S = \exp\left[\frac{1.75-1.675}{0.37}\right] = 1.224708312$

Co(4)-O(6) $S = \exp\left[\frac{1.75-2.16}{0.37}\right] = 0.330183041$

Co(4)-O(3) $S = \exp\left[\frac{1.75-1.812}{0.37}\right] = 0.845719472 \times 2$

V = 3.25

Appendix 4.1 Stacked XRD plots showing the starting material $Sr_2Fe_2O_5$ (black trace), a typical result obtained after unsuccessful attempted low-temperature fluorination reaction whereby there was no evidence to suggest fluorine insertion (red trace) and the 2 distinct cubic phases produced *via* low-temperature fluorine insertion (blue trace).

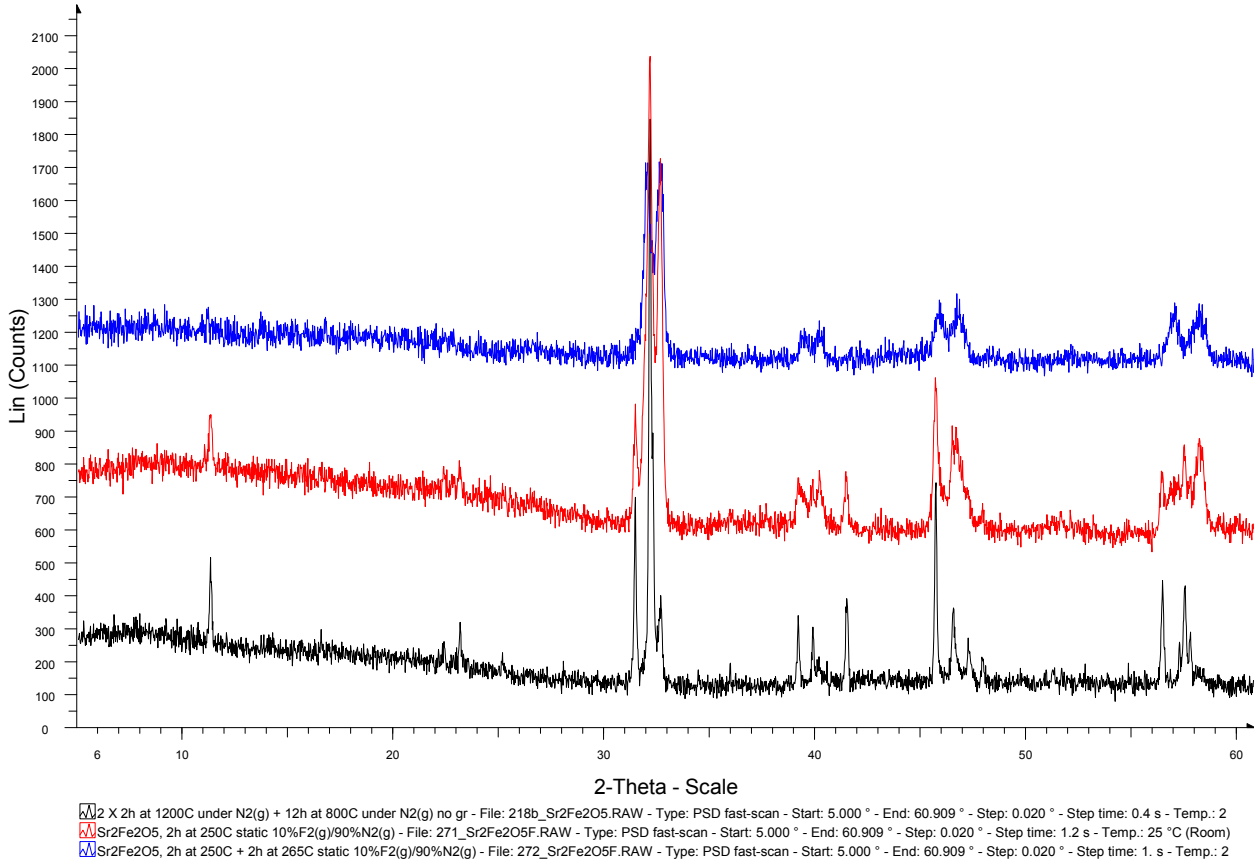

A selection of fluorination conditions explored for $Sr_2Fe_2O_5$.

Temperature	Duration	Conditions	Observations
200°C	30 minutes	Flowing $10\%F_{2(g)}/90\%N_{2(g)}$	No noticeable reaction.
220°C	90 minutes	Static $10\%F_{2(g)}/90\%N_{2(g)}$	No noticeable reaction
220°C	90 minutes, grind, 150 minutes	Static $10\%F_{2(g)}/90\%N_{2(g)}$	No noticeable reaction
230°C	120 minutes	Static $10\%F_{2(g)}/90\%N_{2(g)}$	No noticeable reaction
250°C	120 minutes	Static $10\%F_{2(g)}/90\%N_{2(g)}$	No noticeable reaction
250°C, 265°C	120 minutes, grind, 120 minutes	Static $10\%F_{2(g)}/90\%N_{2(g)}$	2 cubic phases formed

Appendix 4.2 Stacked XRD plots showing the starting material Sr_2CoFeO_5 (black trace), a typical result obtained after unsuccessful attempted low-temperature fluorination reaction whereby there was no evidence to suggest fluorine insertion (red trace) and the cubic phase produced *via* low-temperature fluorine insertion (blue trace).

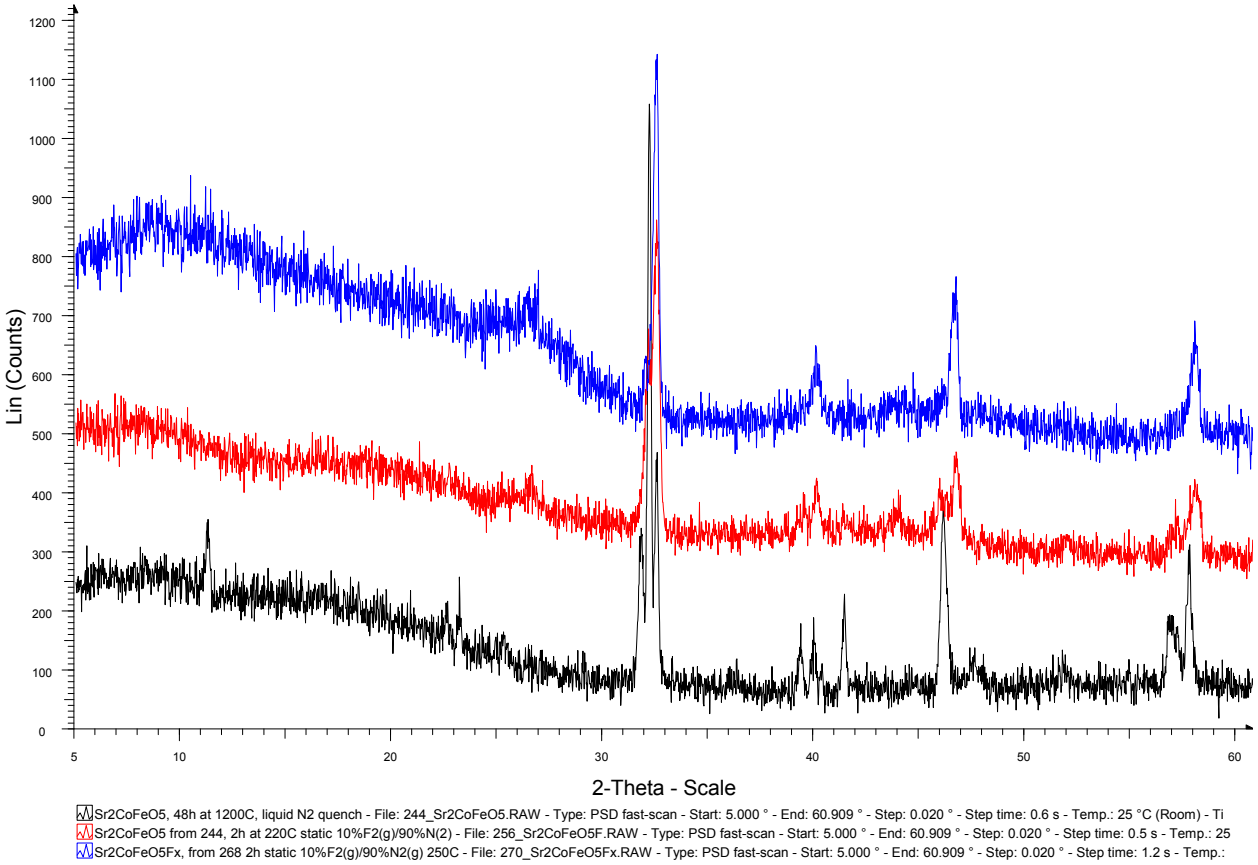

A selection of fluorination conditions explored for Sr_2CoFeO_5.

Temperature	Duration	Conditions	Observations
220°C	120 minutes	Static 10%$F_{2(g)}$/90%$N_{2(g)}$	No noticeable reaction.
220°C, 230°C	120 minutes, grind, 120 minutes	Static 10%$F_{2(g)}$/90%$N_{2(g)}$	No noticeable reaction
220°C, 230°C, 250°C	120 minutes, grind, 120 minutes, grind, 120 minutes	Static 10%$F_{2(g)}$/90%$N_{2(g)}$	No noticeable reaction
220°C, 230°C, 2 × 250°C	120 minutes each temperature, intermediate grinding	Static 10%$F_{2(g)}$/90%$N_{2(g)}$	Cubic phase formed
2 × 250°C	120 minutes, grind, 120 minutes	Static 10%$F_{2(g)}$/90%$N_{2(g)}$	No noticeable reaction

Appendix 4.3 Stacked XRD plots showing the starting material $Sr_2Co_2O_5$ (black trace), a typical result obtained after unsuccessful attempted low-temperature fluorination reaction whereby there was no evidence to suggest fluorine insertion (red trace) and the cubic phase produced *via* low-temperature fluorine insertion (blue trace).

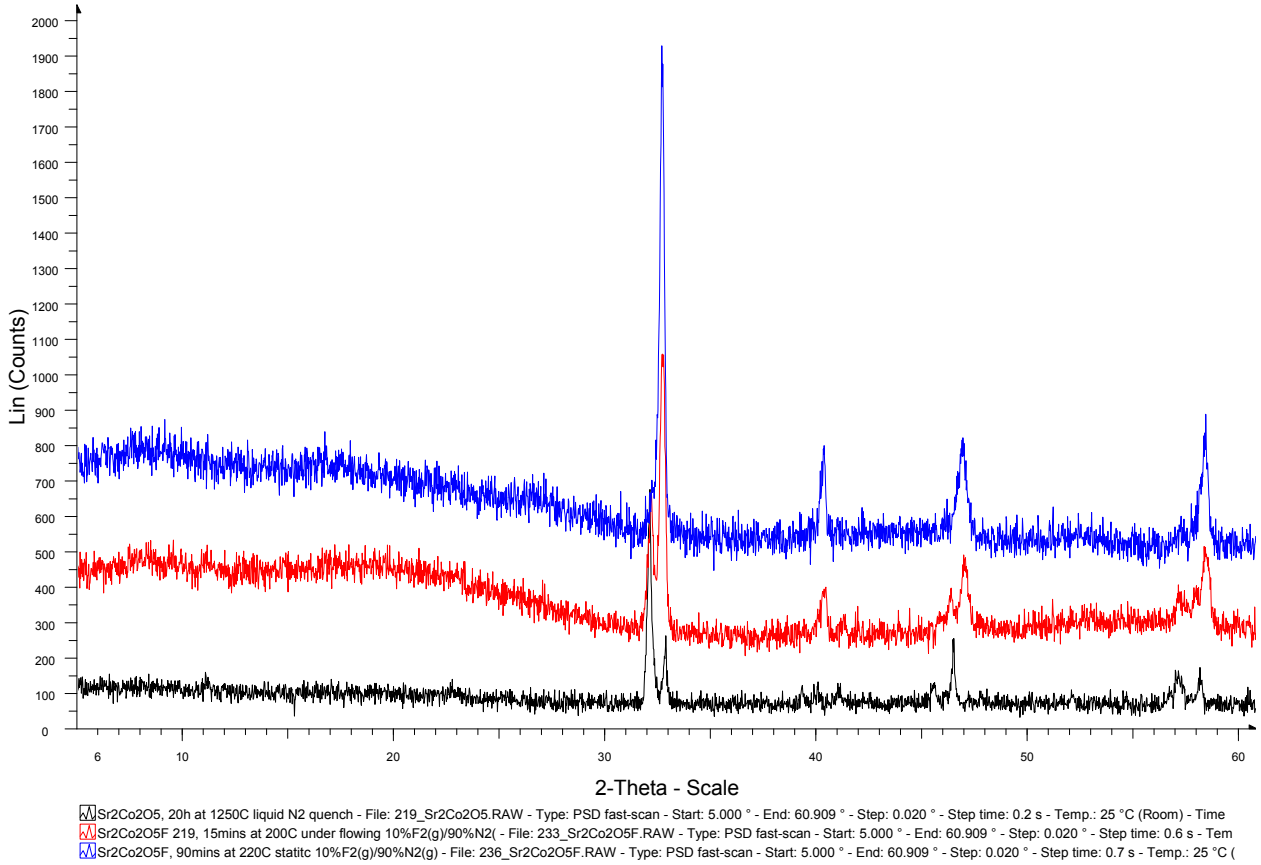

A selection of fluorination conditions explored for $Sr_2Co_2O_5$.

Temperature	Duration	Conditions	Observations
250°C	12 hours	$CuF_{2(s)}$	No noticeable reaction.
275°C	48 hours	$CuF_{2(s)}$	No noticeable reaction
3000°C	48 hours	$CuF_{2(s)}$	Large amount of amorphous material
200°C	15 minutes	Flowing $10\%F_{2(g)}/90\%N_{2(g)}$)	No noticeable reaction
220°C	90 minutes	Static $10\%F_{2(g)}/90\%N_{2(g)}$	Cubic phase formed
220°C	120 minutes	Static $10\%F_{2(g)}/90\%N_{2(g)}$	Cubic phase formed but large amount of amorphous material

Appendix 4.4 Refined atom and lattice parameters of $SrCoO_{2.5}F_{0.5}$ from refinement of XRD data in the space group *Pm-3m* (*a* = 3.8574(3) Å).

Atom	**Site Symmetry**	***x***	***y***	***z***	**U_{iso} × 100 (Å^2)**
Sr	1a	0	0	0	1.2(2)
Co	1b	0.5	0.5	0.5	1.6(2)
O/F	3c	0	0.5	0.5	0.8(3)

Appendix 4.5 Refined atom and lattice parameters of $SrCoO_{2.5}F_{0.5}$ from refinement of NPD data in the space group *Pm-3m* (a = 3.8533(5) Å). Thermal parameters were fixed at 0.01 $Å^2$ as the presence of an impurity of the starting material $Sr_2Co_2O_5$ necessitated a 4-phase refinement and independent variation of these parameters destabilised the refinement.

Atom	**Site Symmetry**	***x***	***y***	***z***	**U_{iso} × 100 ($Å^2$)**
Sr	1a	0	0	0	1
Co	1b	0.5	0.5	0.5	1
O/F	3c	0	0.5	0.5	1

Appendix 5.1 Bond valence sum calculations using bond lengths obtained from Rietveld profile refinement using the space group *I*4/*mmm* based on XRD data.

Refined bond lengths:
Mn-O(1) eq: $r = 1.91035(3)$
Mn-O(2) ap: $r = 1.938(11)$

r_0 values:
Mn(III)-O: $r_0 = 1.760(5)$
Mn(IV)-O: $r_0 = 1.753(6)$ [1]
Mn(III)-F: $r_0 = 1.66$
Mn(IV)-F: $r_0 = 1.71$ [2]

$$S = \exp\left[\frac{r_0 - r}{B}\right] \qquad \text{where B} = 0.37$$

Mn(III)-Oap $S = \exp\left[\frac{1.70 - 1.938}{0.37}\right] = 0.618114798$

Mn((IV)-Oap $S = \exp\left[\frac{1.753 - 1.938}{0.37}\right] = 0.606530659$

Mn(III)-Oeq $S = \exp\left[\frac{1.760 - 1.910}{0.37}\right] = 0.666706469$

Mn(IV)-Oeq $S = \exp\left[\frac{1.753 - 1.910}{0.37}\right] = 0.65421167$

Mn(III)-Fap $S = \exp\left[\frac{1.66 - 1.938}{0.37}\right] = 0.47172865$

Mn(IV)-Fap $S = \exp\left[\frac{1.71 - 1.938}{0.37}\right] = 0.539983758$

Mn(III)-Feq $S = \exp\left[\frac{1.66 - 1.910}{0.37}\right] = 0.508812512$

Mn(IV)-Feq $S = \exp\left[\frac{1.71 - 1.910}{0.37}\right] = 0.582433338$

Fap: $V_3 = (1 \times \text{Mn(III)-Fap}) + (1 \times \text{Mn(III)-Feq}) + (4 \times \text{Mn(III)-Oeq}) = 3.647367638$
Fap: $V_4 = (1 \times \text{Mn(IV)-Fap}) + (1 \times \text{Mn(IV)-Feq}) + (4 \times \text{Mn(IV)-Oeq}) = 3.739263776$
Feq: $V_3 = (1 \times \text{Mn(III)-Feq}) + (3 \times \text{Mn(III)-Oeq}) + (2 \times \text{Mn(III)-Oap}) = 3.745161515$
Fap: $V_4 = (1 \times \text{Mn(IV)-Feq}) + (3 \times \text{Mn(IV)-Oeq}) + (2 \times \text{Mn(IV)-Oap}) = 3.758129666$

For mixed M^{2+}/M^{3+} $y = (V_2 - 1)/(V_2 + 1 - V_3)$

where y = proportion of M^{3+}
V_2 = valence sum calculated with M^{2+}
V_3 = valence sum calculated with M^{3+} [3]

Thus it follows that for mixed M^{3+}/M^{4+} $y = (V_3 - 3)/(V_3 + 1 - V_4)$

where y = proportion of M^{4+}

V_3 = valence sum calculated with M^{3+}

V_4 = valence sum calculated with M^{4+} [3]

Fap:

$y = (V_3 - 3)/(V_3 + 1 - V_4) = 0.71287841$

$1 - y = 0.287121589$

$4y + 3(1 - y) = 3.712878407$

Feq:

$y = (V_3 - 3)/(V_3 + 1 - V_4) = 0.754951844$

$1 - y = 0.245048155$

$4y + 3(1 - y) = 3.754951842$

Appendix 5.2 Observed (red +), calculated (green) and difference (pink) profiles of $Sr_2MnO_{3.53(5)}F_{0.39(5)}$ as generated by Rietveld profile refinement based on TOF NPD data collected at 4K (Lattice parameters: a = 3.82926(17) Å and c = 12.6179(8) Å, Refinement statistics: χ^2 = 10.54, R_{wp} = 2.98% and R_p = 5.13%).

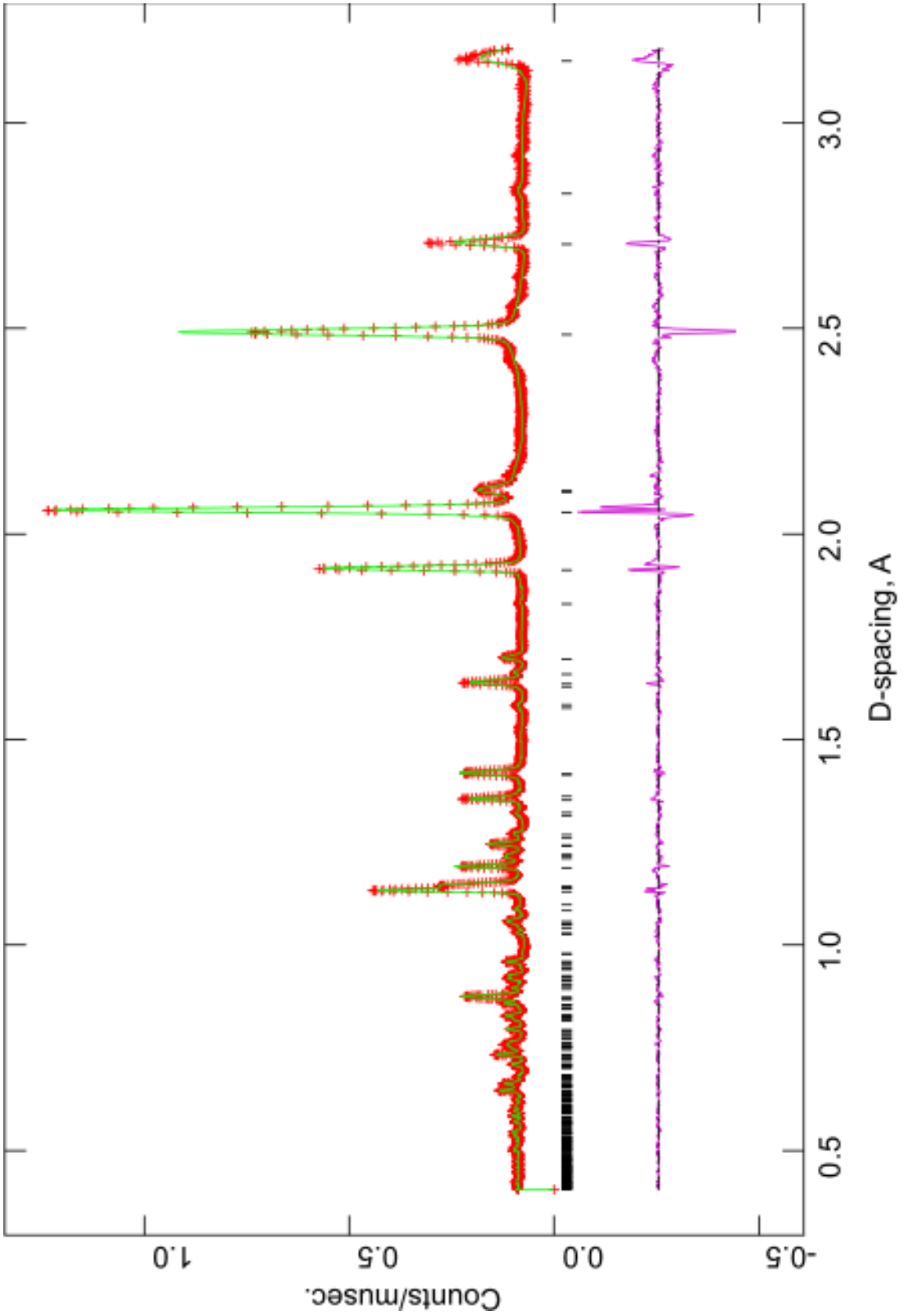

Appendix 5.3 Observed (red +), calculated (green) and difference (pink) profiles as generated by 2-phase Rietveld profile refinement based on TOF NPD data collected at 4K (Refinement statistics: $\chi^2 = 9.528$, $R_{wp} = 2.99\%$ and $R_p = 4.68\%$).

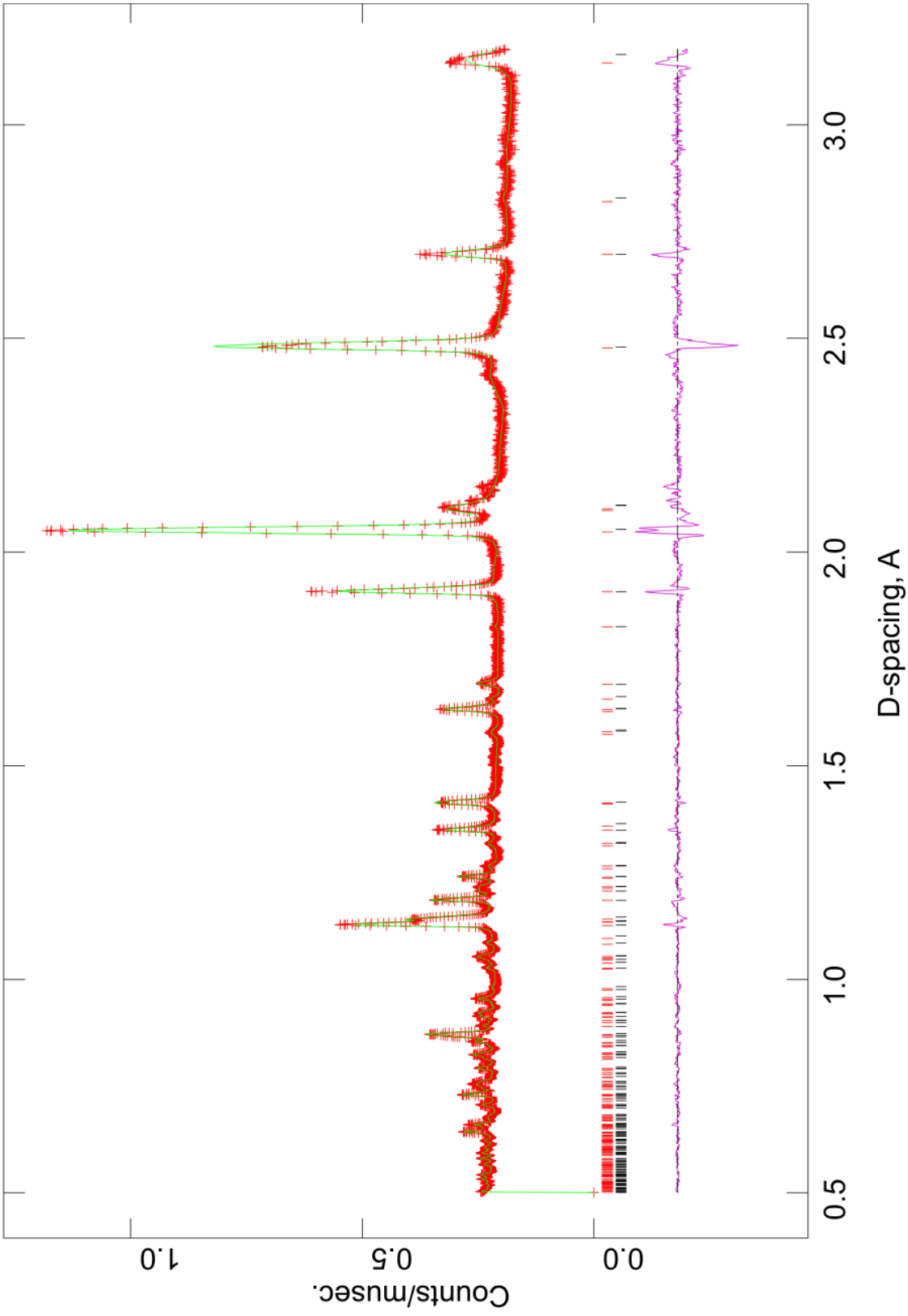

Refined atom and lattice parameters of $Sr_2Mn(O,F)_4$ from refinement of TOF NPD data in the space group *I4/mmm* (*a* = 3.82(7) Å, *c* = 12.6(2) Å).

Atom	Site Symmetry	*x*	*y*	*z*	Occupancy	$U_{iso} \times 100$ (Å^2)
Sr	4e	0	0	0.3609(4)	1.0	0.74(3)
Mn	2a	0	0	0	1.0	0.06(5)
O(1)	4c	0	0.5	0	1.0	1.26(5)
O(2)	4e	0	0	0.1568(6)	1.0	1.67(5)

Refined atom and lattice parameters of $Sr_2MnO_{3.5+x}$ from refinement of TOF NPD data in the space group *I4/mmm* (*a* = 3.81(7) Å, *c* = 12.56(23) Å).

Atom	Site Symmetry	*x*	*y*	*z*	Occupancy	$U_{iso} \times 100$ (Å^2)
Sr	4e	0	0	0.3543(2)	1.0	0.74(3)
Mn	2a	0	0	0	1.0	0.06(5)
O(1)	4c	0	0.5	0	0.73(1)	1.26(5)
O(2)	4e	0	0	0.1552(4)	1.0	1.67(5)

Appendix 6.1 Observed (red +), calculated (green) and difference (pink) profiles of $Ce_2Mn(N, F)_4$ as generated by the Rietveld profile refinement of XRD data using a K_2NiF_4 model, without background subtracted. Red vertical lines highlight the positions of the $Ce_2Mn(N,F)_4$ diffraction peaks whilst black vertical lines correspond to residual Ce_2MnN_3.

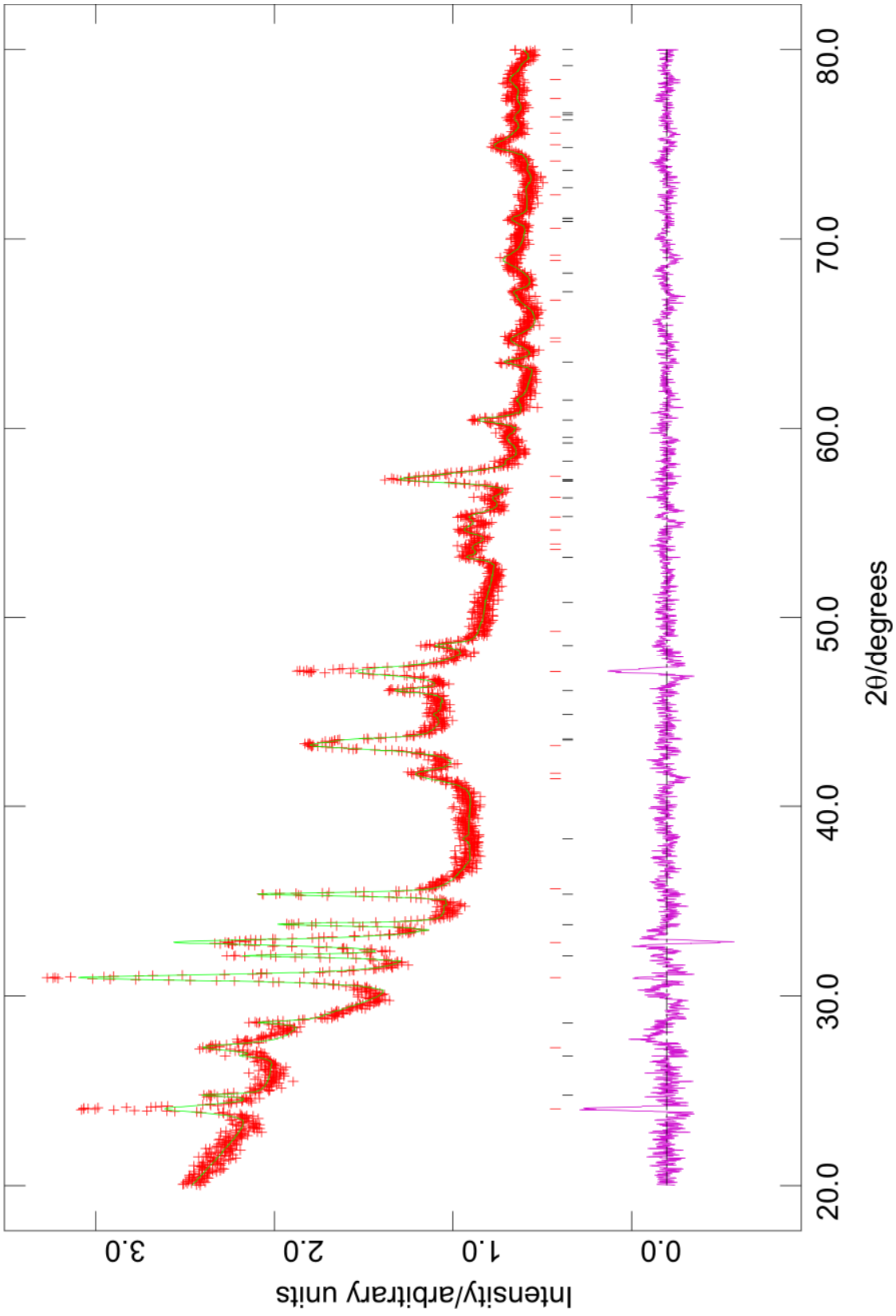

References

1. Brown and Altermatt (1985) *Acta Crystallographica* **B41** 244.
2. Brese and O'Keeffe (1991) *Acta Crystallographica* **B47** 192.
3. Brown (1989) *Journal of Solid State Chemistry* **82** 122.